

Structure and Bonding 154

Series Editor: D.M.P. Mingos

D. Michael P. Mingos *Editor*

Nitrosyl Complexes in Inorganic Chemistry, Biochemistry and Medicine II

 Springer

154

Structure and Bonding

Series Editor:

D.M.P. Mingos, Oxford, United Kingdom

Editorial Board:

F.A. Armstrong, Oxford, United Kingdom

X. Duan, Beijing, China

L.H. Gade, Heidelberg, Germany

K.R. Poeppelmeier, Evanston, IL, USA

G. Parkin, New York, USA

M. Takano, Kyoto, Japan

For further volumes:

<http://www.springer.com/series/430>

Aims and Scope

The series *Structure and Bonding* publishes critical reviews on topics of research concerned with chemical structure and bonding. The scope of the series spans the entire Periodic Table and addresses structure and bonding issues associated with all of the elements. It also focuses attention on new and developing areas of modern structural and theoretical chemistry such as nanostructures, molecular electronics, designed molecular solids, surfaces, metal clusters and supramolecular structures. Physical and spectroscopic techniques used to determine, examine and model structures fall within the purview of *Structure and Bonding* to the extent that the focus is on the scientific results obtained and not on specialist information concerning the techniques themselves. Issues associated with the development of bonding models and generalizations that illuminate the reactivity pathways and rates of chemical processes are also relevant

The individual volumes in the series are thematic. The goal of each volume is to give the reader, whether at a university or in industry, a comprehensive overview of an area where new insights are emerging that are of interest to a larger scientific audience. Thus each review within the volume critically surveys one aspect of that topic and places it within the context of the volume as a whole. The most significant developments of the last 5 to 10 years should be presented using selected examples to illustrate the principles discussed. A description of the physical basis of the experimental techniques that have been used to provide the primary data may also be appropriate, if it has not been covered in detail elsewhere. The coverage need not be exhaustive in data, but should rather be conceptual, concentrating on the new principles being developed that will allow the reader, who is not a specialist in the area covered, to understand the data presented. Discussion of possible future research directions in the area is welcomed.

Review articles for the individual volumes are invited by the volume editors.

In references *Structure and Bonding* is abbreviated *Struct Bond* and is cited as a journal.

D. Michael P. Mingos
Editor

Nitrosyl Complexes in Inorganic Chemistry, Biochemistry and Medicine II

With contributions by

P.K. Allan • P.C. Ford • L.R. Holloway • N. Lehnert •
L. Li • D.M.P. Mingos • K.M. Miranda • R.E. Morris •
J.C.M. Pereira • D.J. Salmon • W.R. Scheidt •
W.B. Tolman • M.W. Wolf

 Springer

Editor

D. Michael P. Mingos
Inorganic Chemistry Laboratory
University of Oxford
Oxford
United Kingdom

ISSN 0081-5993

ISSN 1616-8550 (electronic)

ISBN 978-3-642-41159-5

ISBN 978-3-642-41160-1 (eBook)

DOI 10.1007/978-3-642-41160-1

Springer Heidelberg New York Dordrecht London

Library of Congress Control Number: 2014940510

© Springer-Verlag Berlin Heidelberg 2014

This work is subject to copyright. All rights are reserved by the Publisher, whether the whole or part of the material is concerned, specifically the rights of translation, reprinting, reuse of illustrations, recitation, broadcasting, reproduction on microfilms or in any other physical way, and transmission or information storage and retrieval, electronic adaptation, computer software, or by similar or dissimilar methodology now known or hereafter developed. Exempted from this legal reservation are brief excerpts in connection with reviews or scholarly analysis or material supplied specifically for the purpose of being entered and executed on a computer system, for exclusive use by the purchaser of the work. Duplication of this publication or parts thereof is permitted only under the provisions of the Copyright Law of the Publisher's location, in its current version, and permission for use must always be obtained from Springer. Permissions for use may be obtained through RightsLink at the Copyright Clearance Center. Violations are liable to prosecution under the respective Copyright Law.

The use of general descriptive names, registered names, trademarks, service marks, etc. in this publication does not imply, even in the absence of a specific statement, that such names are exempt from the relevant protective laws and regulations and therefore free for general use.

While the advice and information in this book are believed to be true and accurate at the date of publication, neither the authors nor the editors nor the publisher can accept any legal responsibility for any errors or omissions that may be made. The publisher makes no warranty, express or implied, with respect to the material contained herein.

Printed on acid-free paper

Springer is part of Springer Science+Business Media (www.springer.com)

Preface

Volumes 153 and 154 of *Structure and Bonding* have been devoted to nitrosyl complexes of the transition metals and their implications to catalysis, biochemistry and medicine. It is surprising that this topic has not been the subject of previous volumes of *Structure and Bonding* since their structural and chemical properties have attracted great interest from coordination and organometallic chemists. In the 1960s and 1970s the renaissance of coordination chemistry led to the detailed study of nitrosyl complexes and the emergence of new spectroscopic and structural techniques defined the metrics of nitric oxide when coordinated to transition metals and established that unlike CO and CN^- NO adopted alternative coordination geometries with transition metals. This ambivalence caused some interest and controversy in the inorganic community, but the research was considered to be of academic rather than practical importance. However, the discovery in the 1980s that NO played a very important role as a messenger molecule in biology provided the impetus for the widespread resurgence of interest in this molecule and its coordination chemistry. NO is produced in vivo by the nitric oxide synthase (NOS) family of enzymes and plays a key role in the nerve-signal transduction, vasodilation, blood clotting and immune response by white blood cells. In these biological processes the coordination of nitric oxide to metal centres is crucial and therefore their detailed study is essential for an understanding of nitric oxide's functions at the molecular level. These volumes provide contemporary reviews of these important developments by leading experts in the field.

The first volume starts with an introductory chapter by myself on "Historical Introduction to Nitrosyl Complexes" recounts the discovery of nitric oxide and its complexes and serves as a general broad introduction to the two volumes. This is followed by a pair of chapters by Dr. Hanna Lewandowska on the "Coordination Chemistry of Nitrosyls and Its Biological Implications" and the "Spectroscopic Characterization of Nitrosyl Complexes." A comprehensive overview is presented of the biologically relevant coordination chemistry of nitrosyls and its biochemical consequences in the first chapter. Representative classes of metal nitrosyls are introduced along with the structural and bonding aspects that may have

consequences for the biological function of these complexes. The biological targets and functions of nitrogen (II) oxide are also introduced. The second chapter reviews structural and spectroscopic data and provides descriptions of the spectroscopic characteristics of nitrosyl complexes. The results of IR, Raman, UV–Vis, EPR Mössbauer, magnetic circular dichroism, NRVS, X-ray absorption spectroscopy are reviewed and conclusions concerning the structure and reactivities of nitrosyls are summarised. The study of nitrosyl complexes has not only had implications for biology but also homogeneous catalysis and Professor Heinz Berke and Dr. Yangfeng Jiang have reviewed recent developments in this field in the chapter entitled “Nitrosyl Complexes in Homogeneous Catalysis.” The ability of nitric oxide to coordinate in a flexible fashion has considerable implications for lowering the kinetic barriers of reactions of organic molecules at metal centres and Berke and Jiang give many examples of this characteristic.

Cellular actions are coordinated by sending signals to each other. This intercellular signalling is achieved by using neurotransmitters. Molecules which behave as neurotransmitters are compounds produced by neurons and stored in vesicles until stimulation of the neurons triggers their release. They bind to specific membrane receptors in a neighbouring cell to produce a physiological effect. ‘Gasotransmitters’ are a group of small gaseous molecules that exhibit a similar signalling function in the body but through a different mechanism. They function without receptors because they are freely permeable to cell membranes. The molecule must be produced within the body for a specific biological function. Three gasotransmitter molecules have been proposed – nitric oxide, carbon monoxide and hydrogen sulphide. They modulate cellular functions by influencing a range of intercellular signalling processes. The significance of this discovery was recognised by the award of the 1998 Nobel Prize for physiology to Murad, Furchgott and Ignarro for the discovery of the endogenous production of NO. In addition to the three accepted gasotransmitter molecules, recent reports suggest that the small gaseous sulphur dioxide molecule may also play a gasotransmitter role within the body, and other gases such as carbonyl sulphide and nitrous oxide have been suggested for investigation. Therefore the second volume highlights general electronic features of ambivalent molecules and the specific role of nitric oxide in biology and medicine.

The second volume also starts with an introductory chapter by myself on “Ambivalent Lewis Acid/Bases with Symmetry Signatures and Isolobal Analogies.” This review emphasises that the nitric oxide belongs to an important class of ambivalent molecules which have the potential to act as messenger molecules in biology. The ambivalence of ligands may also have implications for understanding intermediates in nitrogen fixation processes. The subclass also encompasses ambiphilic molecules such as SO₂ and I₂. Professor Lijuan Li has contributed a chapter on “Synthesis of Nitrosyl Complexes” which reviews the synthesis of dinitrosyl complexes, particularly of iron, which are relevant to understanding their important biological role. Professors Peter Ford et al. have reviewed the photochemistry and reactivities of nitrosyl complexes in their chapter entitled “Mechanisms of NO Reactions Mediated by Biologically Relevant Metal Centres.” They illustrate how understanding the basic coordination chemistry of nitric oxide is so important for

understanding its biological role. They discuss the applications of both thermal and photochemical methodologies for investigating such reactions which provide quantitative data on fundamental reactions involving NO. Professor William Tolman and Deborah Salmon have reviewed “Synthetic Models of Copper Nitrosyl Species Proposed as Intermediates in Biological Denitrification” and thereby emphasise that iron is not the only metal which is important in defining the role of NO in biology. Professor Robert Scheidt and Nicolai Lehnert have contributed much to our understanding of the structures of porphyrin nitrosyl complexes over the last 40 years and the bonding of nitric oxide to transition metals and their chapter with Dr. Mathew Wolf on “Heme Nitrosyl Structures” summarises our current understanding of the geometric and electronic structures of ferrous and ferric heme-nitrosyls. In detail and in-depth correlations are made between these properties and the reactivities of these biologically important complexes. The second volume finishes with a very timely chapter on the “Medical Applications of Solid Nitrosyl Complexes” by Professors Russell Morris and Phoebe Allan. They review endogenous production and biological effects of nitric oxide before discussing the exogenous dosage of nitric oxide as a medical device. They summarise recent research work on chemical donors, e.g. polymers, porous materials, particularly zeolites and metal-organic frameworks, as delivery vessels for NO.

Those of us who are old enough to remember performing the “brown-ring test” in qualitative inorganic chemistry practical exams will realise that the subject has come a long way in the last 50 years. There is, however, still much to learn about the biological and catalytic implications of the fascinating NO molecule and I am sure that future generations will realise its potential through interdisciplinary studies.

Oxford, UK
June 2013

D. Michael P. Mingos

Contents

Ambivalent Lewis Acid/Bases with Symmetry Signatures and Isolobal Analogies	1
D. Michael P. Mingos	
The Preparation, Structural Characteristics, and Physical Chemical Properties of Metal-Nitrosyl Complexes	53
Lauren R. Holloway and Lijuan Li	
Mechanisms of Nitric Oxide Reactions Mediated by Biologically Relevant Metal Centers	99
Peter C. Ford, Jose Clayston Melo Pereira, and Katrina M. Miranda	
Synthetic Models of Copper–Nitrosyl Species Proposed as Intermediates in Biological Denitrification	137
Debra J. Salmon and William B. Tolman	
Structure and Bonding in Heme–Nitrosyl Complexes and Implications for Biology	155
Nicolai Lehnert, W. Robert Scheidt, and Matthew W. Wolf	
Medical Applications of Solid Nitrosyl Complexes	225
Phoebe K. Allan and Russell E. Morris	
Index	257

Ambivalent Lewis Acid/Bases with Symmetry Signatures and Isolobal Analogies

D. Michael P. Mingos

Abstract This review proposes that the nitric oxide belongs to an important subclass of ambivalent molecules, which includes transition metals and main group molecules (or ions). The subclass encompasses amphiphilic molecules such as SO_2 and I_2 , a range of ligands with nitrogen or oxygen donor atoms and some transition metal complexes in low oxidation states. Adducts of these ambivalent molecules display geometric signatures, which reflect the number of electrons which they formally donate or accept. A frontier molecular orbital analysis is presented which rationalises the observed geometric preferences. The *symmetry signatures* may be observed at the ligand, at the metal or at the ligand and the metal simultaneously. The geometric changes associated with transition metal complexes may be interpreted using the *Complementary Spherical Electron Density Model*. Bringing together a significant and important group of ligands with **ambivalent symmetry signatures** provides the opportunity for developing a deeper understanding of their biological and catalytic functions and provides a more detailed understanding of their chemical similarities and differences.

The *isolobal* analogy has been widely used to provide bridges between coordination, organometallic and organic chemistry and between main group and transition metal polyhedral molecules. In this review it is extended to highlight important analogies between nitrosyl and related ligands. Detailed DFT molecular orbital calculations on some specific examples are used to highlight the basis of the isolobal analogy and its limitations.

Keywords Ambiphilic · Ambivalent · Amphoteric valence tautomerism · Bent nitrosyls · Electronic structure · Imido · Iodine · Isolobal · Linear nitrosyls · Nitric oxide · Nitrido · Nitrosonium · Non-innocent ligands · Nonlinear nitrosyls · Spectroscopy · Sulphur dioxide

D.M.P. Mingos (✉)

Inorganic Chemistry laboratory, Oxford University, South Parks Road, Oxford OX1 3QR, UK
e-mail: michael.mingos@seh.ox.ac.uk

Contents

1	Introduction	2
2	Ligands with Symmetry Signatures	9
2.1	Ambivalent Ligands	9
2.2	Ambiphilic Ligands	15
2.3	Ambiphilic and Ambivalent Metal Complexes	20
2.4	Valence Tautomerism	25
2.5	π -Bonded Alternative Geometries	26
2.6	Summary	28
3	Isolobal Analogies for Nitrosyl Complexes	29
3.1	Introduction	29
3.2	Theoretical Underpinning of the Isolobal Analogy	35
3.3	Sixteen-Electron Isolobal Analogies	38
3.4	Isolobal Analogies for Bent Nitrosyl Complexes	39
3.5	<i>Isolobal</i> 19-Electron Complexes	41
3.6	Trans-Influences in Isolobal Complexes	43
3.7	Isolobal Poly(Nitrosyls) and Poly-Nitrido-Oxo and Imido Complexes	45
3.8	Summary	46
	References	48

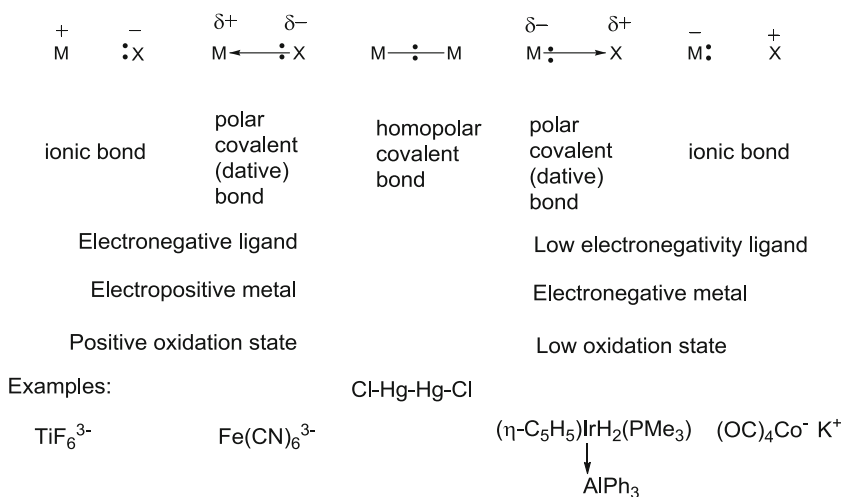
Abbreviations

acac	Acetylacetonate
Ar	Aryl
<i>t</i> -Bu	<i>Tert</i> -butyl
CSEDM	Complementary Spherical Electron Density Model
Cp	Cyclopentadienyl
DFT	Density functional theory
dppe	Bis(diphenylphosphino)ethane
dppm	Bis(diphenylphosphino)methane
EAN	Effective atomic number
Et	Ethyl
Me	Methyl
Mes	Mesityl 2,4,6-trimethylphenyl (not methanesulphonyl)
Ph	Phenyl
Pr	Propyl
<i>i</i> -Pr	Isopropyl
Tol	4-Methylphenyl
VSEPR	Valence Shell Electron Pair Repulsion (Theory)

1 Introduction

Since the discovery that nitric oxide plays many roles in biology, there has been an exponential growth of interest in its biochemistry and the study of nitrosyl transition metal complexes and particularly biomimetic complexes of iron and copper. It has

also renewed interest in a range of small molecules such as SO_2 , H_2S , CO , COS and N_2O which may also function as neurotransmitter molecules in biology [1, 2]. The biological role of these *gasotransmitters* is in many cases dependent on their basic coordination chemistries with transition metals. Their ability to coordinate to transition metals with specific and variable geometries can trigger what at first seem to be subtle effects, but which result in important changes at the molecular level for biology. Small changes in the effective size of the metal (via spin changes) may be amplified into large changes in the protein environment which may result in important allosteric effects. Similarly, relatively small changes in *trans* influences of a ligand bound to a metal may result in major geometric changes between the protein and the metal. The modulation of the redox properties of the metallo-protein can also dramatically influence the rates of reaction involving the protein and substrate. All or some of these effects are crucially important if the ligands are to function effectively and exclude other competing substrates. Consequently it is important to understand those factors which enable ligands to alter their geometries on coordination to transition metals. The aim of this chapter is to emphasise that nitric oxide belongs to a wider group of ligands which have alternative geometric signatures and electron-donating properties. These are described as ***ambivalent ligands with symmetry signatures***. Seeking patterns in their common properties may lead to a more general understanding of the geometries and strengths of interactions between the signalling molecules and metal sites in metallo-proteins and the use of complexes containing these ligands in homogeneous catalysis.

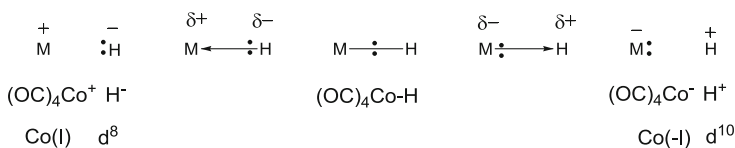


1

The initial Lewis bond description of Werner coordination complexes was based on the assumption that the ligand is an electron pair donor to the Lewis acidic metal cation. As coordination chemistry has developed, it has become increasingly clear that the metal–ligand bond types cover the whole range of possibilities shown in **1**.

The Pauling electronegativities of the transition metals range from 1.5 to 1.9 (first row) and 1.3 to 2.54 (third row) and may be compared with the following electronegativities for common ligands: H (2.20), CH₃ (2.31), CN (3.32), NH₂ (2.47) and OH (2.82) [3]. The earlier transition metals are significantly less electronegative than these ligands and therefore the bond descriptions on the left-hand side are an appropriate starting point for an initial description of the bond. The later transition metals have electronegativities, which are comparable to H, CH₃ and NH₂ and consequently the bonding approximates more closely to either a homopolar description, or indeed for a boron or aluminium Lewis acid adducts, then the polar covalent bond shown on the right-hand side may represent a more appropriate starting point. The completely ionic description of the bond on the far right-hand side is only achieved for an alkali metal salt of a metal carbonyl anion.

Of course a completely rigorous description of the polarity of the bond may only be obtained by sophisticated molecular orbital calculations or spectroscopic/X-ray diffraction measurements which are able to accurately plot the electron distribution in the bond. This electron distribution is influenced by the oxidation state of the metal and the electronic properties of the spectator ligands attached to the metal. An electron pair bond persists across most of the spectrum of bond types illustrated, but its electron distribution is asymmetric and concentrates towards the more electronegative atom. The oxidation formalism for transition metal complexes is based on the left-hand side of the bond descriptions given in **1** and reflects the higher electronegativities of common ligands compared to the transition metals. There are situations, however, where the presence of strong π -acceptor spectator ligands may cause a reversal of the bond polarity. For example, for metal carbonyl hydride complexes, their acidic properties suggest that the protonic representation shown below may be an equally valid starting point for describing the bonding. The alternative representations are associated with the different formal oxidation states for the metals shown in **2**, i.e. Co(I) and Co(-I). This remains an artefact of the formalism and is the consequence of a very clumsy way of representing a redistribution of electron density. However, if the two alternative oxidation states (and their associated d electron counts) are accompanied by different geometries, the observed structure may give circumstantial evidence regarding the polarity of the metal-hydrogen bond.



2

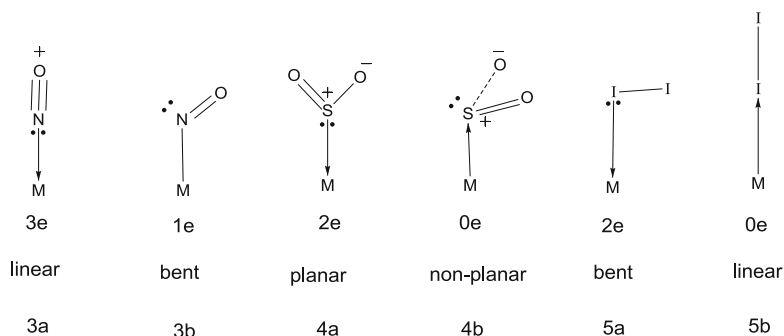
The other feature, which has become more apparent as the subject has developed, is that the metal-ligand bond may have multiple bond character resulting

from overlap between orbitals of π symmetry on the ligand with d orbitals with matching symmetries (usually d_{xz} and d_{yz}). Pauling [4–6] was the first to recognise that a ligand such as CO is able to function within its complexes simultaneously as a Lewis acid and Lewis base, by virtue of the synergic bonding interactions [5]. These synergic interactions involve complementary σ and π orbitals on the ligand and metal and the point group symmetry of the adduct remains unaffected by the relative contributions of the forward and back donation components, although the relative lengths of the M–C and C–O bonds do vary according to the relative contributions of the components. The relative contributions of forward and back donation components can change the partial charges on the metal and ligand and thereby influence the reactivities of the complexes. This flexibility has been used to tune the ability of complexes to function as Lewis acids or bases by changing the oxidation state, coordination number, steric effects and the donor/acceptor properties of the spectator ligands [7].

The earlier transition metals which have empty d orbitals of π symmetry are capable of accepting electron pairs from filled π orbitals of π -donor ligands, e.g. N^{3-} and O^{2-} [8–10]. Therefore, multiple bonding between ligand and metal is a general feature of complexes of transition metals with π -acid and π -donor ligands and has been supported by numerous structural and theoretical studies [7], although there have been differing views regarding the actual strength of multiple bonding and the assignment of formal oxidation states in the complexes.

The great majority of organometallic complexes of transition metals may be brought within the context of the effective atomic number rule (EAN), and this results from the consensus which has been achieved for defining the number of electrons donated by most ligands [7]. For simple innocent π -acid ligands, e.g. CO, the electron count is defined by the number of electrons in the σ -donor orbital (2), whereas for π -donor ligands, e.g. NR, the electron count needs to take into account the contribution from filled σ - and π -donor orbitals, and the EAN count depends in part on whether the metal has an empty orbital available to accept the electron pairs.

This discussion underlines the complexity of the bonding in metal complexes! In the 1960s, C K Jørgensen introduced the term *innocent and non-innocent ligands* to draw attention to these ambiguities [11–16]. A non-innocent ligand is one for which there is an ambiguity in its electron-donating properties. It may also have implications for assigning the formal oxidation state of the metal. Nitric oxide represents a pertinent example of a non-innocent ligand, and as the previous chapters have indicated, its coordination to metals results in different localised geometries and local point group symmetries, i.e. *linear*, *intermediate* and *bent*. The oxidation state ambiguities for NO as a non-innocent ligand led Feltham and Enemark [17] to propose a widely adopted and cited notation, which made no assumptions concerning the formal charge on the ligand or the metal. In Volume 154, I indicated the problems which have arisen from this notation and proposed an alternative formalism for describing the geometric complexities of nitrosyl complexes based on the EAN rule [18].



In this chapter I wish to draw attention to the fact that NO is not unique in this regard and it belongs to an important group of *ambivalent Lewis acid/bases with symmetry signatures* and this phenomenon is controlled in large measure by the symmetries and nodal characteristics of their frontier orbitals. These ligands are described as **ambivalent** because they are capable of formally donating alternative numbers of electrons to Lewis acids. **3–5** illustrate alternative geometries shown by NO, SO₂ and I₂ in transition metal complexes and as described below these differences may be related to the donor/acceptor properties of these molecules. Other ligands which may be described as **ambivalent** are illustrated in Fig. 1 [7–10]. All these ligands have two things in common – they adopt alternative metal–ligand geometries and have different electron-donating capabilities. The alternative geometries therefore represent **symmetry signatures** ($C_{\infty v}$ for linear MNO and C_s for bent MNO) for these ambivalent ligands.

The bonding in these complexes may be analysed using the Walsh diagram methodology described in the previous volume and the detailed geometries for complexes of these ligands may be accurately calculated using DFT procedures [19–28]. The purpose of this review is not to analyse the bonding in specific examples of these ligands and their complexes, but to draw together some general conclusions which bring together the common characteristics of ambivalent ligands and their geometric signatures.

The reader will now be familiar with the view that NO may behave as either as a three-electron donor (**3a**) in linear complexes or a one-electron donor in bent complexes (**3b**) [29]. Other ligands which exhibit related ambivalent symmetry signatures are summarised in Table 1. NR₂, N₂R and NCR₂ also are capable of behaving as three- or one-electron donors and exhibit symmetry signatures analogous to those described previously for NO. In N₂R complexes the R group does not lie on the MNN rotation axis and therefore the alternative geometries are commonly described as *bent* and *double bent*. The N₂R ligand is also capable of bonding in a π fashion (η^2) and this additional feature will be discussed in more detail below. A large number of ketimine, NCR₂, complexes have been structurally determined and the statistical pattern is very similar to that noted in the previous chapter for NO, i.e. the great majority are linear and the remainder have intermediate (140–160°) and bent (110–140°) geometries. For odd electron donors we shall avoid the

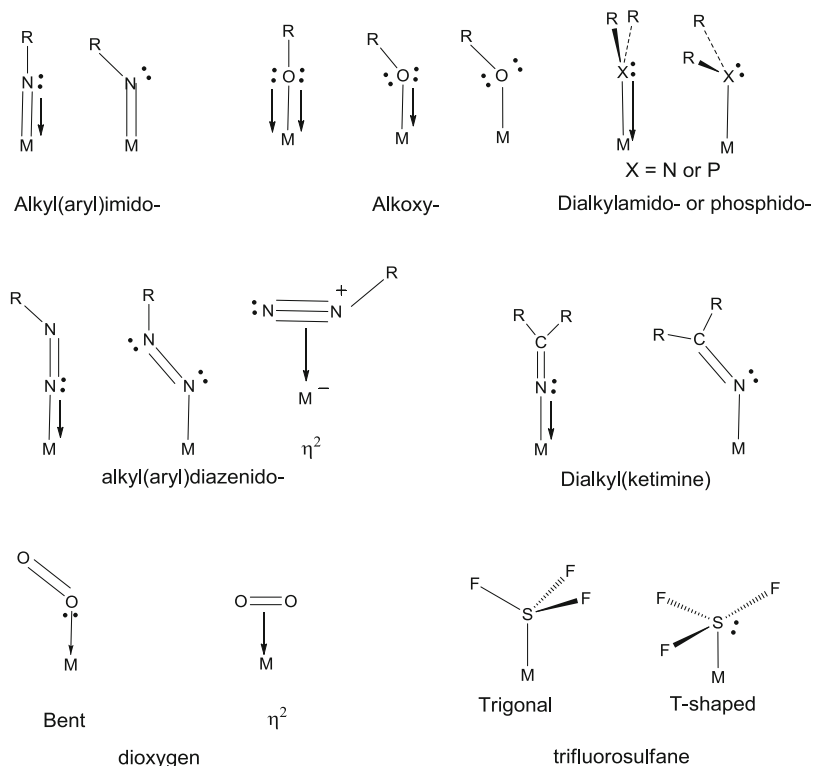


Fig. 1 Ligands with symmetry signatures (shown as neutral ligands)

complications which result from designating them as L^+ and L^- by formally and consistently using the neutral form of the ligand and no attempt is made to designate a formal oxidation state to the metal [7, 29]. Instead the new notation emphasises only the total electron count in the molecule. Numerous DFT calculations on complexes of the ligands given in Table 1 [19–28] have underlined the validity of the electroneutrality principle and therefore this seems the most reasonable approximate starting point for describing the bonding in classical Lewis electron pair bonding representations. The table also provides examples of ambivalent ligands which donate either four or two electrons. The alkoxy ligand, OR, is particularly flexible and is capable of donating five, three or one electron. O_2 and the isoelectronic RNO are not strictly ambivalent because in the bent and the η^2 geometries they donate the same number of electrons formally, although they certainly have different symmetry signatures. They have been added for completeness sake and will be discussed later. For NH_2 and NR_2 the planar geometry is invariably the geometry observed even for complexes of the later transition metals. Amido complexes of the later transition metals are highly nucleophilic and their interesting reactions with organic molecules have been studied by Bergman, Hartwig and

Table 1 Summary of the electron-donating capabilities of ambivalent ligands with symmetry signature

Ligand	M–L geometric description (<i>descriptor</i>)	Electron donation
NO	Linear (<i>l</i>) (180–160°)	Three electrons
NO	Bent (<i>b</i>) (100–140°)	One electron
NR ₂ (PR ₂)	Non-planar (<i>np</i>)	One electron
NR ₂ (PR ₂)	Planar (<i>p</i>)	Three electrons
NCR ₂	Linear (<i>l</i>)	Three electrons
NCR ₂	Bent (<i>b</i>)	One electron
N ₂ R	Singly bent (<i>sb</i>)	Three electrons
N ₂ R	Doubly bent (<i>db</i>)	One electron
N ₂ R	π bonded (η^2)	Three electrons
NR	Linear (<i>l</i>)	Four electrons
NR	Bent (<i>b</i>)	Two electrons
NOR	Linear (<i>l</i>)	Four electrons
NOR	Bent (<i>b</i>)	Two electrons
OR	Bent (<i>b</i>)	One or three electrons
OR	Linear (<i>l</i>)	Five electrons
SO ₂	Planar (<i>p</i>)	Two electrons
SO ₂	Non-planar (<i>np</i>)	Zero electron
I ₂	Bent (<i>b</i>)	Two electrons
I ₂	Linear (<i>l</i>)	Zero electron
O ₂	Bent (<i>b</i>)	Two electrons
O ₂	π bonded (η^2)	Two electrons
RNO	Bent	Two electrons
RNO	π bonded (η^2)	Two electrons

Gładysz [26, 30–33]. The related phosphido-arsenido ligands exhibit a wider range of geometries.

There is a smaller group of ambivalent ligands in Table 1 which are classified as two- or zero-electron donors. Of course a zero-electron donor is no longer a Lewis base, but a Lewis acid and therefore such ligands are ambiphilic. An ambiphilic molecule is one which is capable of forming adducts with either a Lewis base or a Lewis acid [4, 6]. The iodine molecule is not a very well-studied ligand, but it shows linear and bent geometries (see **5a** and **5b**), whereas SO₂ exhibits planar **4a** (point group C_{2v}) and non-planar **4b** (point group C_s) geometries. SO₂ and I₂ represent examples of ambiphilic molecules and in the Lewis notation this is represented by a reversal of the dative bond arrow in **4a** and **4b** and **5a** and **5b**. They have been included in the table because they show symmetry signatures closely related to those described for other ligands in the table and ambiphilicity and ambivalency are clearly closely interrelated. For example, if we had started our analysis based on NO⁺ rather than NO, then the linear and bent geometries could be described as manifestations of this ligand acting as a Lewis base or a Lewis acid, i.e. being ambiphilic. Indeed the first structurally characterised example of a bent nitrosyl ligand originated from the reaction of NO⁺ with a square-planar iridium (I) complex [29]. The ambivalent ligands in Table 1 which donate either three or

one electron may also be described as ambiphilic based on L^+ acting as a Lewis base or acid.

The long list of ligands summarised in Table 1 suggests that the ambivalency is quite an important characteristic of many small-molecule ligands. The ligands have the following features in common:

1. The donor atoms have elements from groups 15, 16 and 17 of the periodic table. The preponderance of these groups is closely related with electronegativity since the more electronegative atoms are more capable of stabilising the lone pair on the atom which bends [8–10].
2. The ambivalent characteristic involves a change of formal electron-donating ability of two electrons, i.e. one or three electrons and two or four electrons.
3. The ambivalence is often associated with the transfer of an electron pair from a lone pair localised on the ligand to the formation of a dative π bond from the ligand to the metal, i.e. electrons move in a way that is predictable from Lewis electron pair bond structures. Electronically this requires an empty orbital on the metal with π symmetry which accepts the lone pair from the ligand (see Fig. 1).

Interestingly carbene and carbyne complexes do not exhibit ambivalence because the multiply bonded structures are favoured by effective π -bonding from the carbon which has a lower electronegativity than nitrogen, oxygen and fluorine [8–10].

4. The geometries of the coordinated ligand may be understood in terms of the Valence Shell Electron Pair Theory (VSEPR). The alternative ambivalent geometries for SF_3 shown in Fig. 1 which have been proposed on the basis of DFT calculations by King et al. [34] demonstrate the validity of this approach for rationalising the structures of more complex ligands.

The preponderance of ligands with nitrogen donor atoms emphasises that this phenomenon is not only of importance for understanding the messenger role of nitric oxide but also of relevance for understanding the enzymatic conversion of dinitrogen to ammonia. The proposed intermediates in this process are shown in Fig. 2 [35–37] and many of them also appear in Fig. 1 and Table 1 as examples of ambivalent ligands albeit with R rather H substituents. Ambivalent ligands also participate in catalytic reactions involving organic molecules, and their flexible electron-donating abilities probably contribute to their high activities.

2 Ligands with Symmetry Signatures

2.1 *Ambivalent Ligands*

The ambivalent ligands listed in Table 1 share in common the ability to form complexes with a pair or triplet of structures. One of which has a lone pair localised on the donor atom and in accordance with VSEPR theory the stereochemical

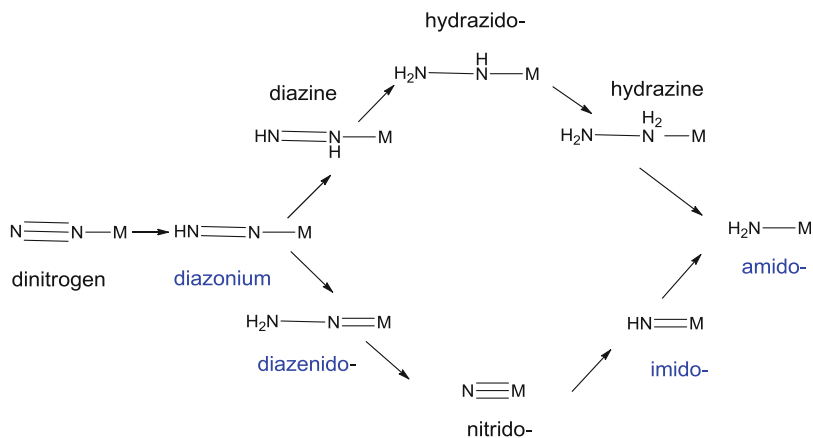


Fig. 2 Proposed intermediates in enzymatic nitrogen fixation [35–37]. Those shown in blue are potentially ambivalent ligands

activity of the lone pair leads to a less symmetrical structure, viz., *bent or non-planar* [8–10]. This less symmetrical structure is favoured if the metal has a filled d orbital of π symmetry which repels the lone pair on the ligand and prevents the formation of a dative $\text{L} \rightarrow \text{M} \pi$ bond. Figure 3 illustrates this four-electron destabilising interaction for an alkylimido complex. If the metal has an empty d orbital of π symmetry, then a dative $\text{L} \rightarrow \text{M} \pi$ bond is formed and is associated with the adoption of a more linear $\text{M}-\text{N}-\text{R}$ geometry. The resonance forms for the linear four-electron donor are illustrated on the right-hand side of Fig. 3. The figure also emphasises the close relationship between the ambivalent NR and NO ligands. Similar considerations apply to the other ambivalent ligands listed in Table 1 and illustrated in Fig. 1. The successful transfer of an electron pair suggested by Fig. 3 depends primarily on the electronegativity difference between the metal and the ligand noted in the previous section and the overlap integrals between the ligand and the metal orbitals. However, in contrast to the main group trio NO_2^+ (linear), NO_2 (intermediate) and NO_2^- (bent), the geometry depends on the electronic and steric characteristics of the spectator ligands on the metal and ligand, which are discussed in more detail below. For example, a strong π -donor *trans* to the imido or nitrosyl ligand will provide competition which will limit the extent of donation and favour a more bent geometry. There is some evidence that nitrosyl porphyrin complexes, which are expected to be linear, adopt nonlinear geometries when *trans* alkylthiolate or phenyl ligands are present [38–40]. In contrast strongly electron-withdrawing spectator ligands encourage linear geometries [18]. We have previously proposed a relationship between the ability of spectator ligands to conform to the EAN rule and the geometry of the nitrosyl ligand.

Figures 4 and 5 provide many specific examples of transition metal complexes of ambivalent ligands and underscore the widespread occurrence of the ambivalent signature phenomenon described above. Below each structure, the new notation,

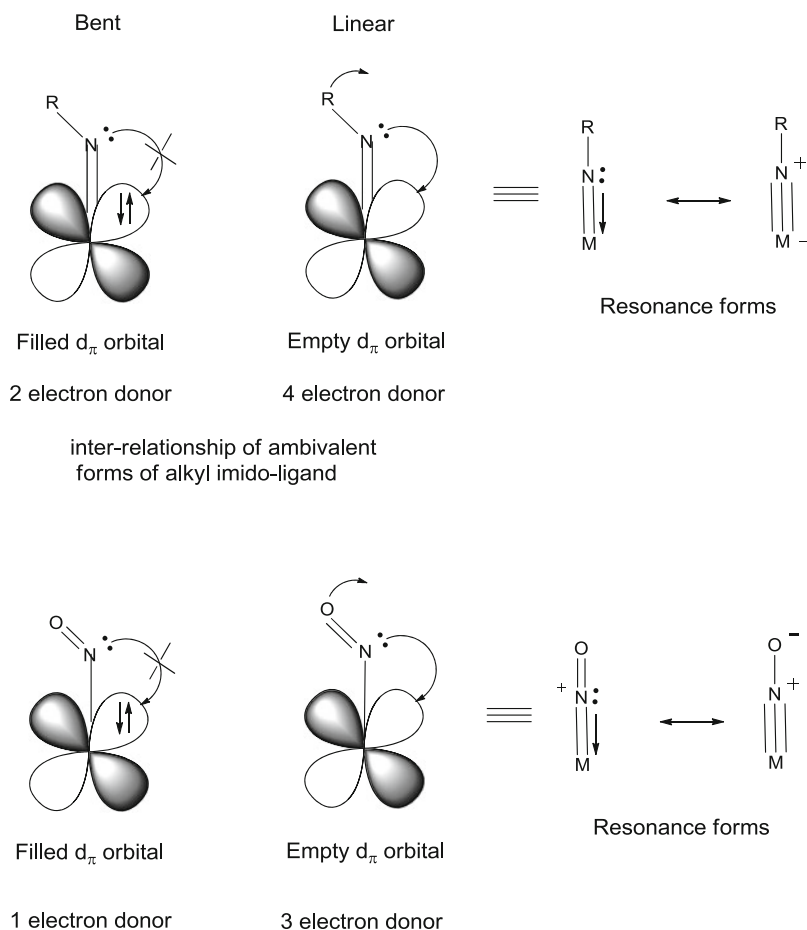
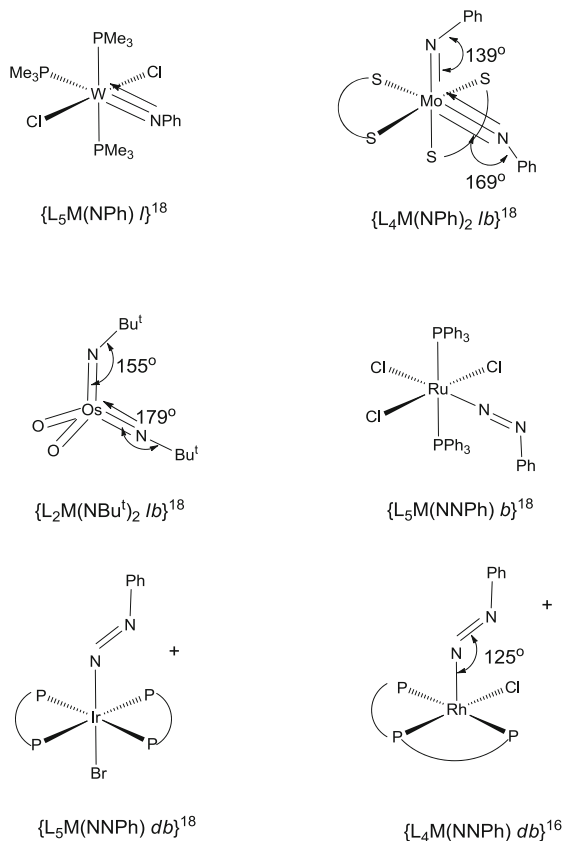


Fig. 3 Interrelationship between ambivalent forms of the alkylimido and NO ligands [8–10, 18]

introduced in volume 154 for nitric oxide [], has been extended to describe the geometries and electron counts in these ambivalent complexes [27, 41–53]. For nitric oxide, it was noted that the M–N–O geometries were not strictly limited to M–N–O = 180° or 120° and intermediate geometries are also observed. Therefore, for pragmatic reasons, the following classification was suggested M–N–O 180–160° (linear *l*), 160–140° (intermediate *i*) and 140–110° (bent *b*) and this has been extended to the other ambivalent ligands in Table 1 [18]. For triatomic ligands, the nomenclature planar and non-planar is proposed.

Figure 3 suggests that the donation of a lone pair from the ligand to the metal depends not only whether an empty orbital is available on the metal but also on the donor/acceptor properties of the spectator ligands, the hybridisation of the donor atom, the other substituents on the donor atoms and their steric requirements. In view of these competing electronic and steric effects, it will come as no surprise that

Fig. 4 Structures illustrating the ambivalency of nitrogen ligands



a wide range of bond angles are observed structurally. For example, alkyimido complexes provide numerous examples of linear, intermediate and bent geometries [23, 27, 46, 52, 53]. In contrast the corresponding dialkylamido complexes provide few examples of non-planar geometries even with metals of the later transition metals. The aryloxy structures (see Fig. 5) provide examples where the M–O–C angle falls in the intermediate category (between linear and bent) and this is indicated by *i* in the new notation. This intermediate angle is consistent with the aryloxy ligands behaving as either one- or three-electron donors – the notation in the figure is based on them acting as three-electron donors. The figure also provides an example of an alkoxy complex of zirconium with an almost linear geometry. The greater polarity of the metal–ligand bonds and the weaker π -bonding make the EAN rule less reliable. In addition the presence of several π -donors around the metal may lead to orbital combinations which do not match the symmetries of the metal orbitals and therefore remain non-bonding. Such complexes generally have electron counts which exceed the EAN rule.

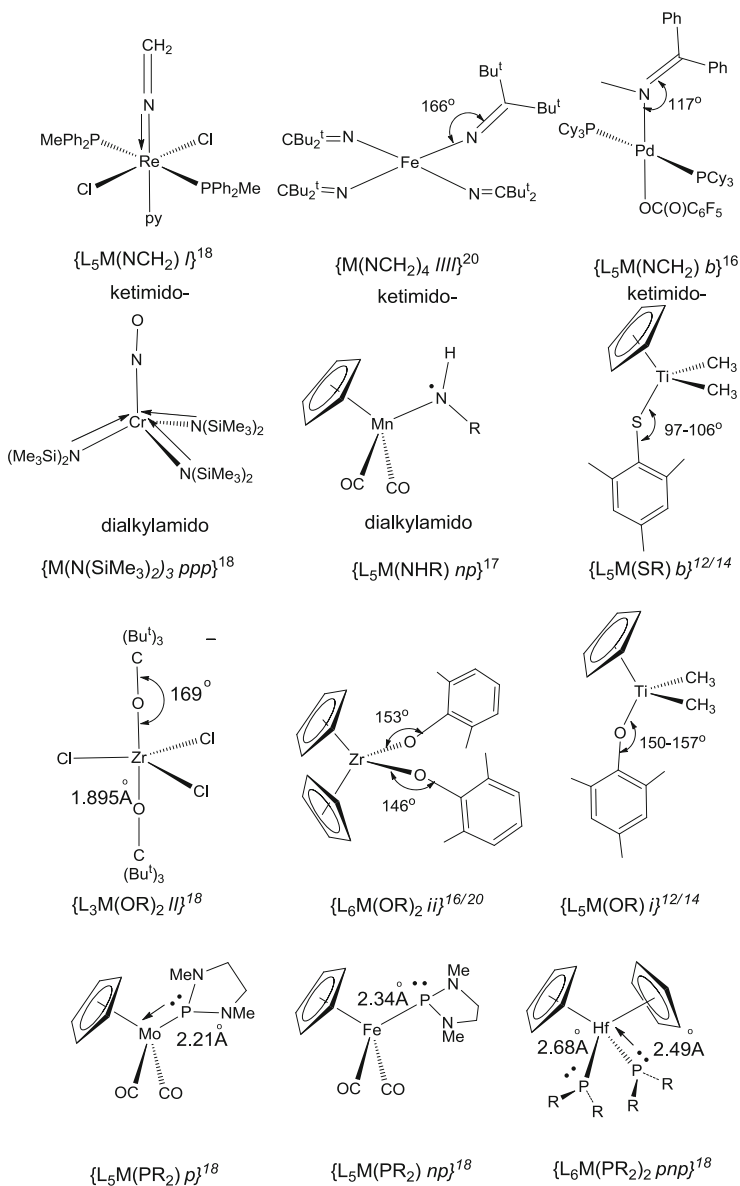


Fig. 5 Structures illustrating the ambivalence of nitrogen and oxygen ligands

Detailed statistical analyses of the structural metrics of ambivalent complexes have shown that linear complexes generally have shorter metal–ligand bonds than bent complexes, but the statistical significance of the correlations between M–O–R and M–N–R bond angles and the M–O and M–N bond lengths is not a strong one. This reinforces the proposal that there are significant ionic contribution to the

bonding for the more electronegative donors, and steric effects are important, especially when bulky substituents have been introduced [23, 27, 46, 52, 53]. Figure 5 illustrates some specific examples of complexes of these ligands and a summary of the geometries and electron counts using the newly proposed notation. For the aryl and alkyloxy and dialkylamido ligands (see Fig. 5), detailed calculations have confirmed that the ionic contributions to the bonding, which also favours a linear geometry, is important. Therefore many of the examples have either linear (*l*) or intermediate (*i*) geometries for alkoxy ligands and planar for dialkylamido ligands. The ketimine ligands provide examples of both linear (*l*), intermediate (*i*) and bent geometries (*b*) and Fig. 5 illustrates some linear and bent examples. Alkylimido complexes show a smaller range of M–N–R bond angles and the complexes may be classified as linear (*l*) or intermediate (*i*). Electronegative atoms adjacent to nitrogen and the ability to delocalise the electron pair to these atoms encourage the non-planar or bent geometries.

For the corresponding third-row donor atoms the π -bonding is weaker and the ionic contributions are smaller and therefore the balance between linear and bent or planar and non-planar geometries becomes more finely balanced. For example, in the arylthiolato complex shown in the middle of Fig. 5, the ionic contribution is smaller and a distinctly bent geometry is observed. Dialkyl and diarylphosphido ligands similarly show a much wider range of geometries than the corresponding amido compounds, and the bottom for Fig. 5 provides some specific examples of planar (*p*) and non-planar (*np*) geometries, which have been observed in molybdenum, iron and hafnium complexes. Not surprisingly the molybdenum and iron examples are 18-electron complexes, and the non-planar geometry results in significantly longer M–P bonds. This may be attributed to reduced metal–ligand π -bonding. The final example in the figure illustrates the occurrence of planar and non-planar dialkylphosphido ligands within one hafnium complex and the interchange of planar and non-planar is sufficiently fast on the NMR timescale to have been confirmed using ^{31}P NMR studies. This represents an example of ***valence tautomerism*** analogous to that observed in complexes with linear and bent nitrosyls in the previous volume.

The series of tetrahedral compounds $\text{OsO}_n(\text{NBu}')_{4-n}$ may be classified as follows in the new notation: $\{\text{L}_3\text{M}(\text{NBu}')\ l\}^{18}$, $\{\text{L}_2\text{M}(\text{NBu}')_2\ lb\}^{18}$, $\{\text{LM}(\text{NBu}')_3\ lbb\}^{20}$, $\{\text{M}(\text{NBu}')_4\ lbbb\}^{22}$. It is not uncommon for high symmetry oxo, nitrido and imido complexes to exceed the EAN rule when they have high symmetries. The additional electrons occupy non-bonding orbitals which are localised on the ligands [21, 22, 26, 28]. This aspect is discussed further in Sect. 3.7. There are also examples of alkylimido complexes where rather than showing a linear-bent duality both ligands adopt intermediate geometries [25]. It is also noteworthy that the amido complexes provide examples of radical species reminiscent of nitrosyl complexes with 17 and 19 electrons (see middle of Fig. 5 for a specific example).

The use of ***signature*** as a description is deliberate and attempts to convey that the phenomenon cannot be defined in a completely rigorous statistical manner, because of ambiguities associated with the subtle interplay of steric, π -bonding and ionic effects, but nonetheless represent a useful portmanteau addition to the

vocabulary of coordination chemistry. In our daily lives, we recognise that signatures are very variable in their legibilities, but they nonetheless provide a unique method of identifying an individual. So an *ambivalent signature* provides a unique description, but its detailed analysis depends as always in chemistry on a balance of competing effects. Also by bringing together a significant and important group of ligands with *ambivalent symmetry signatures*, it provides the opportunity for developing a deeper understanding of their biological and catalytic functions, which is based on a more detailed understanding of their chemical similarities and differences.

2.2 *Ambiphilic Ligands*

Molecules which are able to act as Lewis acids and Lewis bases are described as *ambiphilic*. Ligands exhibit ambiphilic properties when they have equally accessible HOMOs and LUMOs. Examples of ambiphilic ligands include SO_2 and I_2 . Ibers and Muir [54] and Ibers, Pearson and Hodgson [29] were the first to suggest that the geometries of SO_2 and NO^+ adducts of Vaska's compound, $[\text{IrCl}(\text{CO})(\text{PPh}_3)_2]$, could be rationalised if these ligands were viewed as Lewis acids which accepted an electron pair from the metal. Kubas, Moody Eller and Ryan [55] and Mingos [56] widened the scope of SO_2 complexes in the 1970s and more recently van Koten [57, 58] has studied the Lewis acid chemistry of SO_2 with platinum (II) square-planar complexes with pincer ligands. Hoffmann and Rogachev [59] have recently published a detailed bonding analysis of the alternative bonding modes of I_2 . They have described the I_2 molecule as a Janus-faced ligand which displays alternative coordination geometries [59]. I prefer to describe SO_2 and I_2 as ambiphilic or ambivalent ligands with symmetry signatures. Ligands, such as SO_2 and I_2 , share in common a donor orbital (D) which has a sufficiently low ionisation energy to enable them to donate to a Lewis acid and an acceptor orbital (A) which is accessible to an electron pair from a Lewis base [55, 56, 60]. According to frontier molecular orbital theory [61, 62], the nodal characteristics and localisation of the frontier orbitals determine the preferred donor and acceptor directions for SO_2 and I_2 . The donor and acceptor orbitals in these *ambiphilic ligands* are orthogonal to each other (see Fig. 6) and consequently if the approaching Lewis acid or Lewis base has only a single acceptor or donor orbital with σ pseudo-symmetry the shapes of the resultant adducts belong to different point groups. These preferred directions are indicated by the arrows in Fig. 6.

SO_2 functions as a donor using a lone pair-like orbital which is coincident with the rotation axis of the ligand, whereas I_2 has a donor orbital perpendicular to the rotation axis. When SO_2 functions as a donor it forms the higher symmetry planar adduct, whereas I_2 forms the lower symmetry T-shaped adduct (see Fig. 7). This geometry maximises the donation from the filled π^* orbitals of I_2 , which have their maximum electron density perpendicular to the molecular axis.

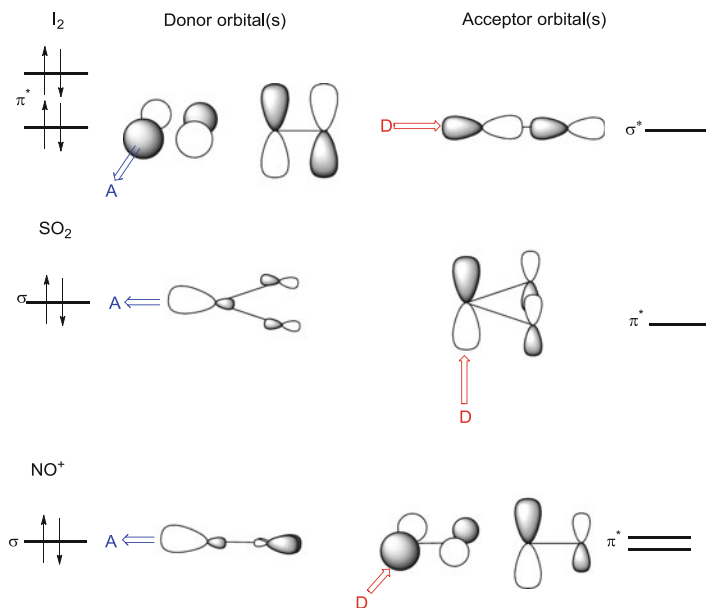


Fig. 6 Frontier orbitals of ambiphilic ligands. The HOMOs are shown on the *left* and the LUMOs on the *right*. Arrows indicate the preferred donor and acceptor directions for a simple Lewis acid (A) or base (D) based on frontier orbital considerations

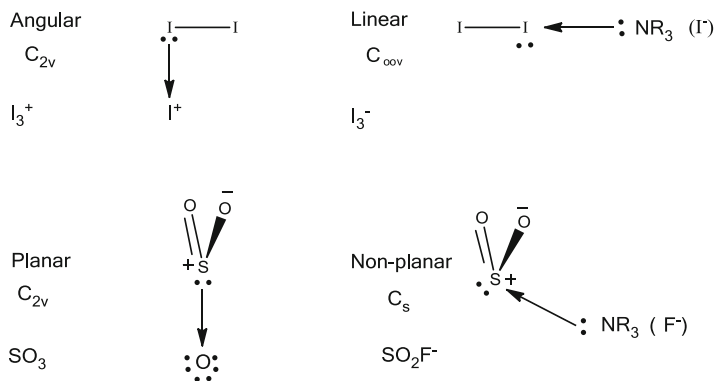


Fig. 7 Alternative geometries shown by ambiphilic ligands when they coordinate to an acceptor or donor with a single orbital of σ symmetry. The point group symmetries of the adducts are also indicated

In localised terms this corresponds to donation from one of the lone pairs of the I_2 molecule. They are illustrated in the Hoffmann and Rogachev paper [59]. When SO_2 functions as a Lewis acid, it forms a non-planar geometry. This geometry maximises the overlap between the lone pair of the Lewis base and the LUMO of SO_2 , which are more localised on S [55, 56, 63–65]. In contrast I_2 forms linear

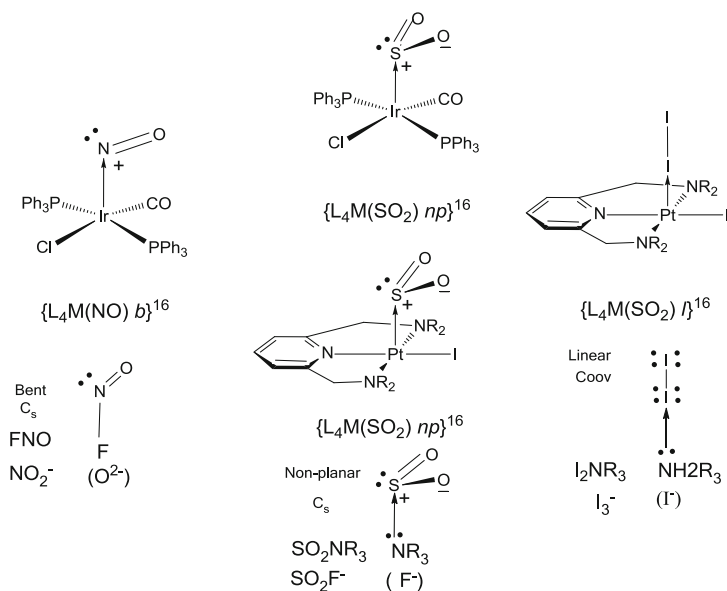


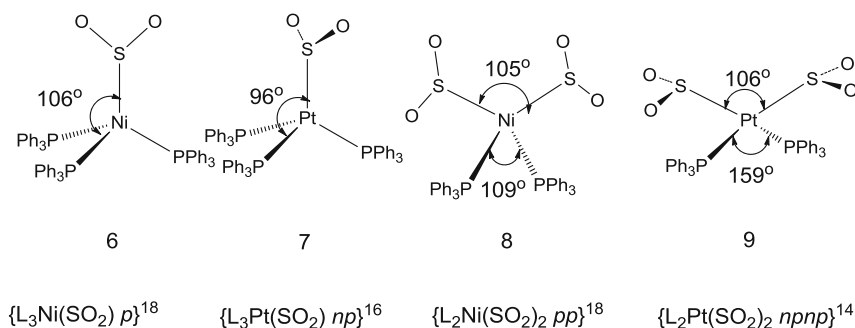
Fig. 9 Examples of square-planar d^8 complexes acting as Lewis bases towards NO^+ , SO_2 and I_2 . Main group analogues are shown below each example

geometry, the number of spectator ligands is indicated, and the total electron count is calculated using the data in Table 1. The cyclopentadienyl ligand is regarded for these purposes as occupying three coordination sites [7]. It is noteworthy that all the examples given for SO_2 and NO obey the 18-electron rule. Figure 3 illustrates specific examples of iodine acting as a ligand and the resultant bent geometry leads to a Ag^+ zigzag polymer with 14-electron counts at each metal centre [69]. Linear geometries are very common for Ag^+ . Hoffmann and Rogachev have discussed in detail examples of compounds where I_2 functions as a Lewis base to rhodium acetate metal–metal bonded dimers, where the ligand donates to the antibonding Rh–Rh antibonding σ^* orbital [59].

Figure 9 shows a series of related square-pyramidal NO^+ , SO_2 and I_2 adducts which have been derived from square-planar d^8 complexes, which function as Lewis bases through their filled d_{z^2} orbitals. The pincer ligands stabilise the square-planar Lewis base geometry relative to alternative trigonal-bipyramidal-based ML_4 geometries and this preference has been used to great effect by van Koten [57, 58]. All the examples in Fig. 9 have an EAN count of 16. The new proposed notation emphasises the changes in geometry for the NO (linear \rightarrow bent), SO_2 (planar \rightarrow non-planar) and I_2 (bent \rightarrow linear) and these geometric changes may be interpreted using simple extensions of the frontier orbital arguments summarised in Fig. 6.

The energy differences between the isomeric forms showing alternative symmetry signatures are calculated by DFT calculations to be small ($<5 \text{ kcal mol}^{-1}$) (see references [63–65] for specific DFT calculations on SO_2 complexes) but may be

greater in complexes with sterically rigid spectator ligands or where hydrogen bonding effects may stabilise one of the isomers, e.g. in a biological pocket. The subtlety of the electronic factors discriminating between two geometries is underlined by comparing the closely related complexes of nickel and platinum in **6–8**. The nickel complexes have planar (*p*) SO₂ geometries, whereas the platinum complexes have pyramidal (*np*) geometries [66–68]. The notations given under **6–8** emphasise the formal electronic relationships between the ambivalent ligands, since the planar SO₂ nickel complexes have 18-electron counts, whereas the non-planar SO₂ platinum compounds have 16 and 14 electron counts, respectively. The point group symmetries at the metals in the pairs of compounds are identical, but the P–M–P bond angles in **9** are larger than those in **8**. This distortion occurs towards the linear 14 electron geometries observed in R₃P–Pt–PR₃. Similarly **7** shows a distortion towards trigonal 16 electron (ideal angle S–Pt–P 90°) for Pt(PPh₃)₃.



A comparison of SO₂ (**7** and **9**) and related NO (**10** and **11**) complexes suggests that the barrier for converting SO₂ from planar to non-planar is smaller than that for converting linear to bent NO. The mononitrosyl has a symmetry imposed M–N–O bond angle of 180° and the dinitrosyl has Ir–N–O = 164° [70, 71], whereas the corresponding angle between the SO₂ plane and the Pt–S vector is approximately 120° in both complexes [55, 66–68]. This conclusion has been supported by calculations by Kubas, Moody and Ryan [55, 67] who have related the difference to the smaller HOMO–LUMO gap in SO₂.

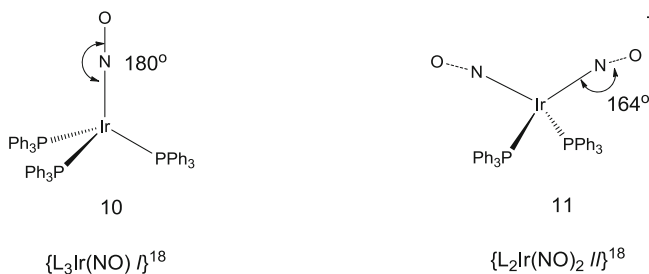
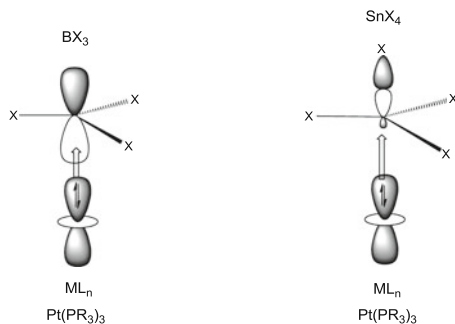


Fig. 10 Examples of σ -acceptor Z-type ligands with typical transition metal donor complexes



2.3 Ambiphilic and Ambivalent Metal Complexes

Recently great interest has been shown in the coordination of Lewis acid ligands such as AlCl_3 , BR_3 , and SnX_4 (and their organo-derivatives) to low oxidation state transition metal complexes of the later transition metals [72–75]. The majority of these Z-type ligands (Green/Parkin notation) [7, 76, 77] function exclusively as Lewis acids and as Parkin has pointed out do not display the geometric changes characteristic of SO_2 and NO^+ and I_2 [76, 77]. The complexes of these Lewis acids with platinum (0) and gold (I) accept an electron pair in an empty p_z orbital or a σ -bonding M–X orbital, e.g. SnX_4 [72]. In the latter example a three-centre four-electron bond results (see Fig. 10). These ligands function simply as Lewis acids and are not ambiphilic, because they do not also have a filled donor orbital localised on the central atom. Consequently, their point group symmetries do not show the symmetry signatures noted above for ambivalent and ambiphilic ligands [58, 59]. Interestingly, the transition metal centres are ambiphilic in these examples, but only in some examples do they show the symmetry signatures similar to those noted above for NO , SO_2 and I_2 .

The *Complementary Spherical Electron Density Model* (CSEDM) [78–81] provides an interesting insight into the origins of the symmetry signatures for ambiphilic molecules of both transition metal and main group donors and acceptors. This model has drawn attention to an important, but not widely appreciated, difference between main group and transition metal stereochemistries. For main group molecules the stereochemistries are controlled by the number of electron pairs provided by the ligands and the lone pairs on the central atom and this generalisation is enshrined in the VSEPR theory. For transition metal complexes which obey the EAN rule lone pairs associated with d shell electron pairs are *stereochemically non-active*, whereas electron pair holes in 16 and 14 complexes are stereochemically active. CSEDM has thereby provided some broad generalisations for rationalising the geometries of closed shell and coordinately unsaturated organometallic complexes [80] and the conclusions are relevant for understanding the symmetry signatures in ambiphilic metal complexes.

Specifically CSEDM makes an important distinction between d^{10} complexes and those with partially filled d shells. All the d^{10} examples shown in 6–11 are

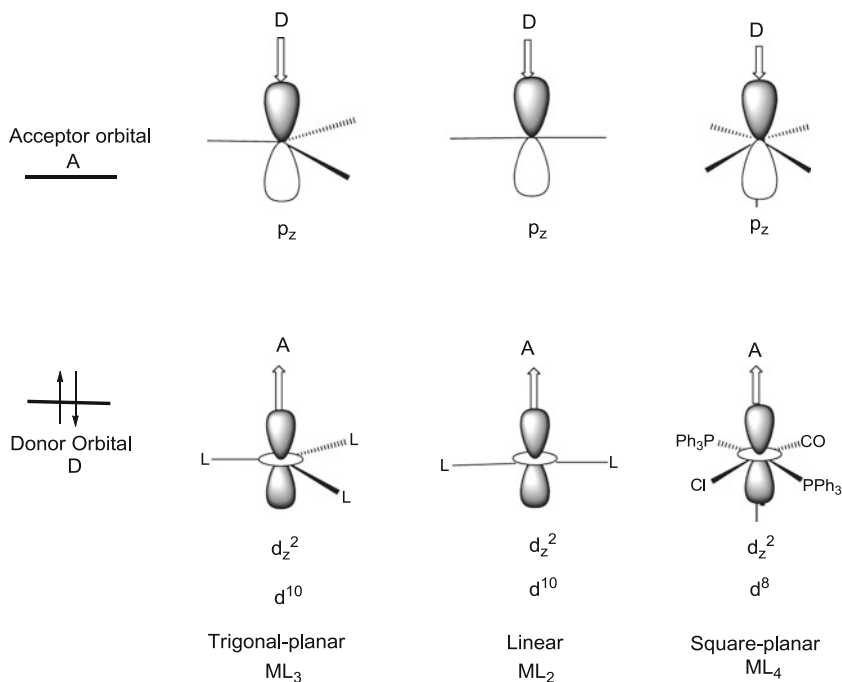
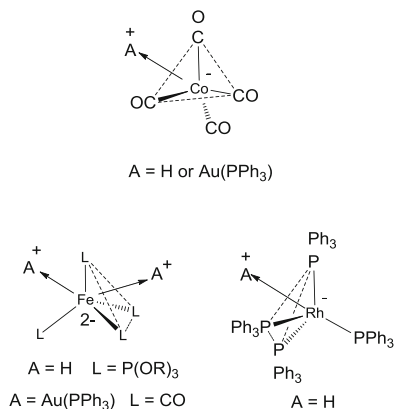


Fig. 11 Frontier orbitals of some d^8 and d^{10} ambiphilic metal fragments

ambiphilic at the metal centre, but do not display the symmetry signatures analogous to those discussed above for NO^+ , SO_2 and I_2 . In trigonal and linear d^{10} complexes, the pairs of donor and acceptor orbitals no longer have orthogonal symmetries (unlike SO_2 and I_2), but have the same symmetry properties with respect to the donor/acceptor direction (see Fig. 11). The Lewis basicity results from donation from a filled d_z^2 orbital and the acceptor orbital is the empty p_z orbital, i.e. both have pseudo- σ symmetry along the direction of the Lewis acid or base as shown in Fig. 11. Consequently the point group symmetries of these trigonal and linear complexes do not change when they switch their function from Lewis acids to Lewis bases, but they distort in a symmetrical fashion with the ligands moving symmetrically away from the incoming Lewis acid or base (see 6–11 for specific examples). The extent of distortion mirrors the strength of the Lewis acid/base interaction and in general when they function as Lewis acids the bonding is stronger and the distortions away from the parent geometries are larger.

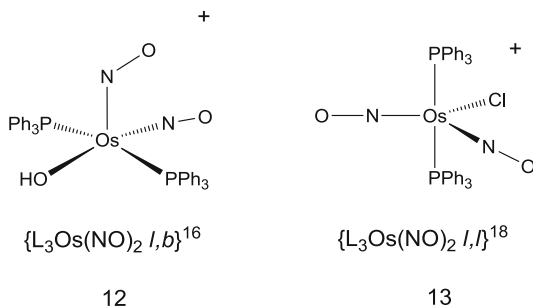
Low oxidation complexes of transition metals form complexes with H and $AuPPh_3$ which have structures which are difficult to classify unambiguously as to whether they are complexes of H^- or H^+ (or $AuPPh_3$). If the hydrogen ligand occupies a regular coordination site, then it may be classified as a complex of H^- , and it thereby follows the conventional Werner picture for a coordination complex, e.g. octahedral $(OC)_5Mn-H$ or $(OC)_5Mn-AuPPh_3$. However, other examples show

Fig. 12 Examples of ambiphilic metal complexes with other acceptors



distortion anion, which suggest that the bonding is more approximate to a protonated (or aurated) complex of metal carbonyl or phosphine. Figure 12 provides some specific examples of tetrahedral d^{10} complexes where the metals appear to be functioning as Lewis bases by donation from a donor orbital which points along the threefold axis of the tetrahedron [82–84].

For complexes with partially filled d shells, the geometry is sensitive to whether the incoming ligand is functioning primarily as a Lewis acid or a Lewis base. In d^8 complexes, the ML_4 fragment functions as a more effective donor if the geometry is square planar and the incoming Lewis acid approaches along the z -axis in order to maximise the overlap with this orbital. However, it functions more effectively as a Lewis acid if the ML_4 geometry is related to a trigonal bipyramid and has an unoccupied d_{z^2} orbital if the Lewis base approaches along the threefold axis and a mixture of d_{z^2} and $d_{x^2-y^2}$ if it approaches along the twofold axis [85–87]. Hoffmann, Mingos and their co-workers analysed these geometric preferences for d^8 five-coordinate nitrosyl complexes nearly 40 years ago [86, 87].



$[\text{Os}(\text{OH})(\text{NO})_2(\text{PPh}_3)_2]^+$ (**12**) and $[\text{OsCl}(\text{NO})_2(\text{PPh}_3)_2]^+$ (**13**) differ only in the replacement of OH by Cl, but they have dramatically different geometries. Crystallographic determinations have shown that **12** has a square-pyramidal geometry with an apical bent nitrosyl, whereas **13** has a trigonal-bipyramidal geometry with linear

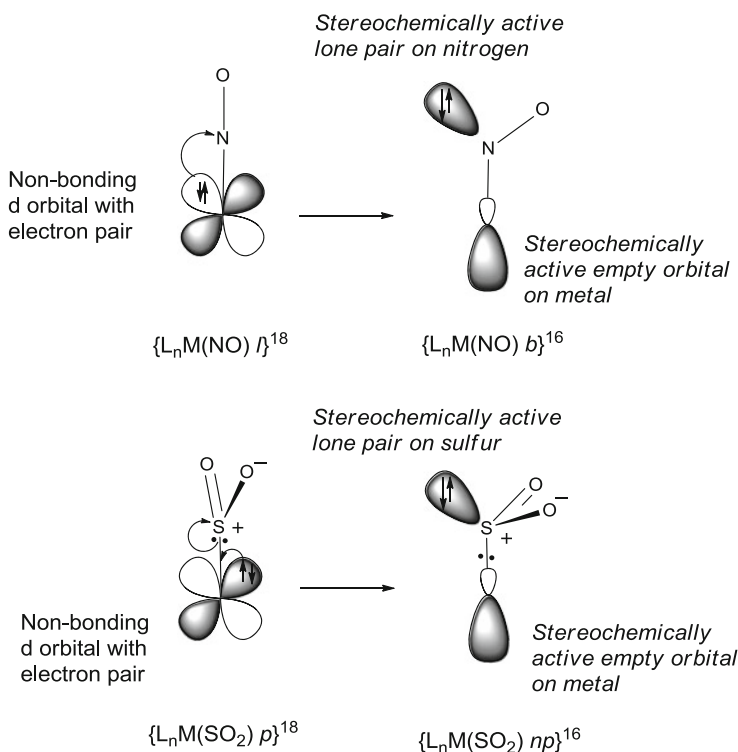


Fig. 13 Summary of stereochemical consequences of a switch of symmetry signatures for NO and SO₂

nitrosyls [87–89]. The comparison of **12** and **13** shows that both the nitrosyl and the ambiphilic metal centre are both showing distinctive *symmetry signatures*. The notation given below the structures confirms that **12** and **13** are formally associated with 16- and 18-electron counts and the empty orbital in the former is stereochemically active according to CSEDM. The transfer of an electron pair from the metal to nitrogen creates according to VSEPR a bent geometry at nitrogen to accommodate a lone pair and the hole which it leaves at the metal centre creates a square pyramid with a stereochemically active empty orbital at the metal.

This process is represented schematically in Fig. 13 for NO and SO₂. Therefore, complexes of this type provide examples of *double symmetry signatures*. Following the designations given in Table 1 for ligands the changes in metal geometry for the ambiphilic metal complex may also be indicated as follows: $\{spL_3M(NO)_2 lb\}^{16}$ (**12**) $\{tbpL_3M(NO)_2 ll\}^{18}$ (**13**), where sp and tbp represent the square pyramid and trigonal bipyramid geometries.

The different possible symmetry signatures for ligands and metal complexes results in the three possibilities summarised in Fig. 14. For the d⁸ iridium complexes the complexes undergo a double symmetry switch involving both the ligand and the metal-coordination sphere. In contrast the related d¹⁰ sulphur dioxide complexes

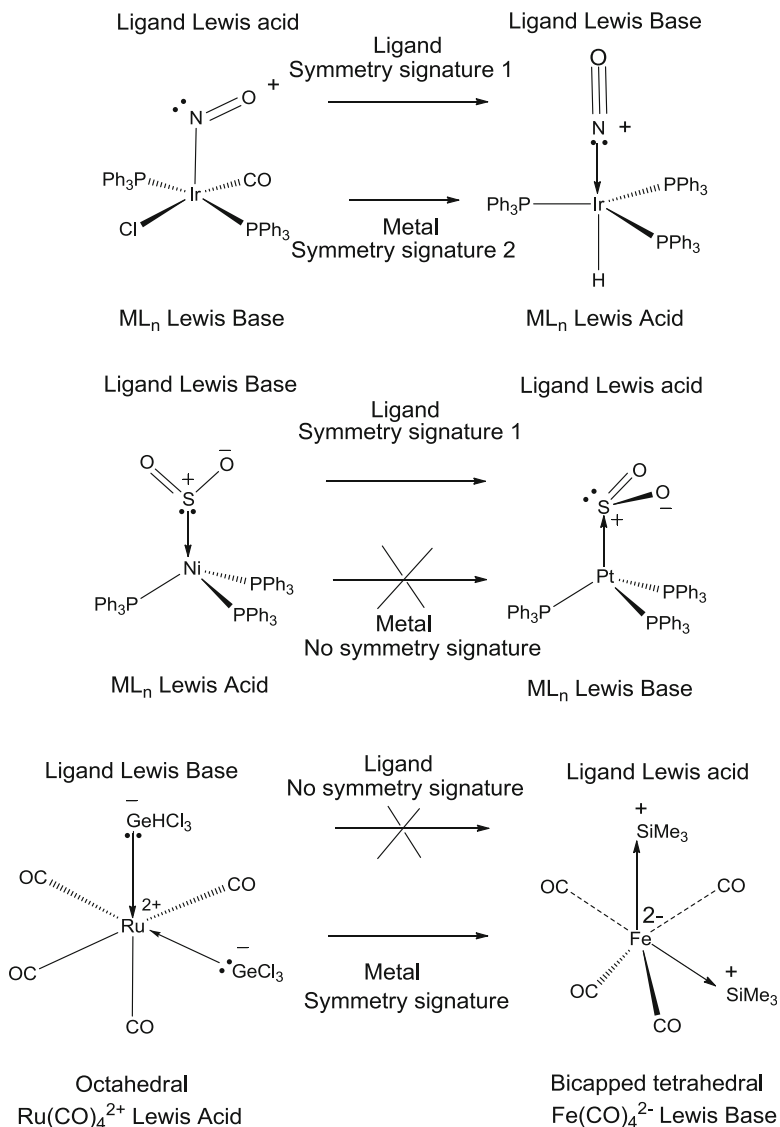


Fig. 14 Examples of double and single symmetry signatures in complexes where the metal and the ligand are both ambiphilic

involve only a ligand switch. The ruthenium and iron carbonyl complexes at the bottom of the figure provide an example where geometric changes are not observed at the group 14 centre, but a dramatic change in geometry from octahedral to bicapped tetrahedral is observed at the transition metal centre and would be characterised as a metal-based symmetry signature [84, 90].

Although the alternative structural formulae in Fig. 14 have been shown with dative bonds changing direction they may also be drawn with dative bonds pointing exclusively towards the metal in both examples if the charges on the ligands and the metal change by two units. Specifically, the NO^+ /dative bond formalism may be replaced by an NO^+/NO^- formalism with both alternatives forming a dative bond to the metal centre. In terms of formal oxidation states this switch results in a change in formal oxidation state of +2 at the metal centre, i.e. to compensate for the change from NO^+ to NO^- , SO_2 to SO_2^{2-} , H^+ to H^- , GeCl_3^+ to GeCl_3^- , etc. In the first example in Fig. 14 iridium(III) changes formally to iridium(I) as a consequence of the straightening of the nitrosyl ligand. In the second example, the group 10 metal changes formal oxidation state from 0 to +2. If several ligands are involved, e.g. the third example in Fig. 9, the change in oxidation state doubles for each successive ligand, and this results in a change of formal oxidation state from +2 to -2. It should be noted that in these circumstances this may lead to unusual and indeed in some cases unreasonable oxidation states, and for this reason we have consistently used only the dative bond notation. Hill and Parkin have discussed the complexities of these oxidation state formalism in some detail [58, 59]. The new notation introduced above removes the necessity of assigning formal oxidation states since it is based on the total number of electrons in the complex and a symmetry designator for the ligand. The Pauling electroneutrality principle [5] works well in these complexes, and none of these formal oxidation state formalisms approximate to the calculated charge distributions in these complexes, and therefore, we favour a notation which only specifies the total electron count in the molecule.

2.4 Valence Tautomerism

The symmetry signatures of ambidentate and ambiphilic ligands may lead to a *dynamic switching process* if the energy separation between two isomeric structures has similar energies. Solution and solid-state ^{15}N NMR in combination with infrared studies of ^{15}N -enriched isotopomers have proved particularly useful for studying dynamic processes involving linear and bent nitrosyls [87, 91–93]. Solid-state nmr studies have established that the linear and bent nitrosyls in molecules related to **12** do not exchange in the solid state. In solution it has been suggested that the square-pyramidal isomer with linear and bent nitrosyls is in equilibrium with a trigonal-bipyramidal isomer with essentially linear nitrosyls as shown in Fig. 15 [87, 91–93]. Both complexes occur in solution as a mixture of square-pyramidal and trigonal-bipyramidal forms (73% and 27% for ruthenium and <50% and >50% for osmium) and undergo a rapid fluxional process which makes the linear and bent forms equivalent on the nmr timescale (see Fig. 15). The interconversion does not occur through a Berry pseudo-rotation involving the intermediate trigonal-bipyramidal complex, but more likely via a turnstile mechanism involving the two nitrosyls and the chloride as shown in Fig. 15 [87–89].

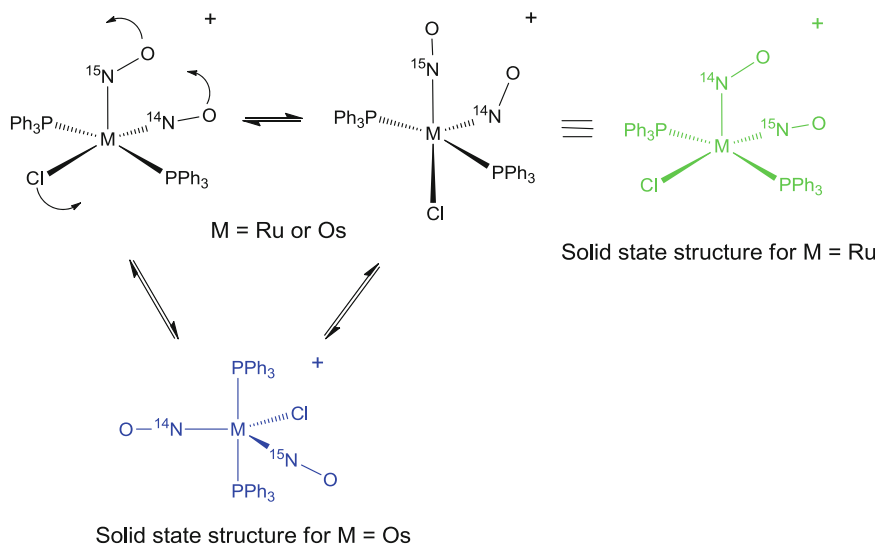


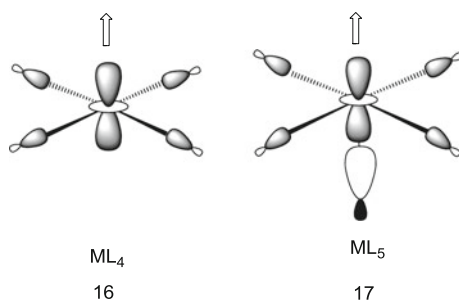
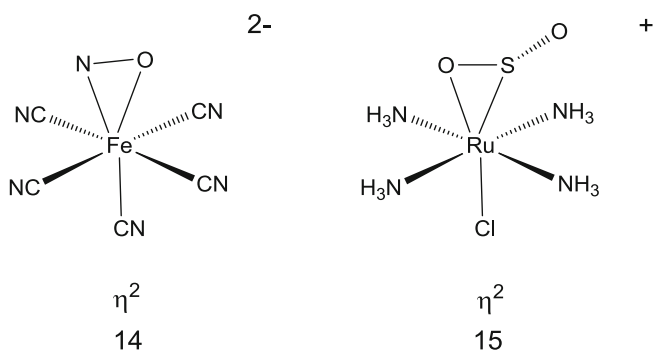
Fig. 15 The dynamic processes which have been proposed to account for the ^{15}N NMR spectra of $[\text{MCl}(\text{NO})_2(\text{PPh}_3)_2]^+$ M = Ru or Os

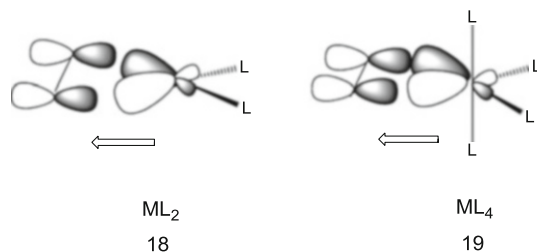
Valence tautomerism has also been observed in alkylimido complexes which have linear and bent geometries within the same molecule, e.g. $[\text{OsO}_2(\text{NBU}^t)_2]$, and the molecules are fluxional on the nmr timescale with an activation energy less than 5 kcal mol^{-1} . The diphosphido complexes of hafnium $[\text{Hf}(\eta\text{-C}_5\text{H}_5)_2(\text{PR}_2)_2]$ (see Fig. 5) have both planar and non-planar phosphido ligands (R = Et) in the solid state. For R = Cy two ^{31}P signals are observed at low temperatures, and they coalesce at higher temperatures indicating a valence tautomerism similar to that described above. The calculated activation energy is approximately 6 kcal mol^{-1} . Analogous arsenido complexes are known and a molybdenum complex undergoes a similar planar–non-planar valence tautomerism.

2.5 π -Bonded Alternative Geometries

In the foregoing discussion the emphasis has been placed on the two most characteristic geometries for complexes of the ambivalent ligands, but it is also necessary to draw attention to an additional possibility. Coppens [94, 95] has demonstrated that nitrosyl and sulphur dioxide complexes have metastable states which may be generated photochemically and structurally defined by X-ray crystallography. These studies have shown that η^2 geometries are only a few kcal mol^{-1} less stable than the linear and planar geometries for NO and SO_2 (14). And (15) provide specific examples of the compounds they structurally characterised. The general

point to make is that ambivalent ligands are not limited to only two symmetry signatures and alternative geometries may be favoured, particularly if the metal fragment functions effectively as a π -donor rather than as a σ -donor. Ambivalent metal centres which follow the frontier orbital analysis shown in Figs. 6, 10 and 11 require low oxidation states and high d electron counts which ensure that the filled d_{z^2} orbital is occupied and has a low ionisation energy. **16** and **17** illustrate this orbital for d^8 square-planar and square-pyramidal geometries and indicate that good σ -donors in the equatorial plane make the metal atom more basic and for the square pyramid a good σ -donor along the axis is particularly effective because it is strongly antibonding in this direction. However, other metal fragments are good π -donors and the frontier orbital analysis has to be modified. For example, angular $ML_2 d^{10}$ and $ML_4 d^8 C_{2v}$ fragments are particularly good π -donors (see **(18)** and **(19)**) and this favours a π interaction with the LUMO of the ligand acceptor orbital as shown in Fig. 6. Ryan and co-workers have reported a number of examples of η^2 complexes of SO_2 [60], but to date there are no examples of η^2 complexes of NO, but a structural determination of the native enzyme in *Alcaligenes faecalis* [96, 97] has suggested the presence of a side on nitrosyl.





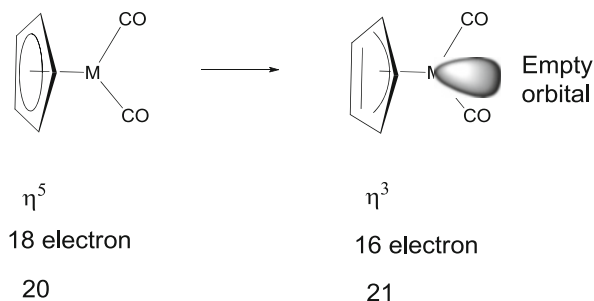
2.6 Summary

The discussion above has drawn together a wide range of ligands which are capable of coordinating to transition metals with alternative geometries. These geometries have been described as symmetry signatures and attributed primarily to the ambivalent and ambiphilic electronic properties of these ligands. A frontier molecular orbital analysis rationalises the geometric preferences, but it is noteworthy that ionic and steric effects also contribute to the observed solid-state geometries. The symmetry signatures may be observed only at the ligand, at the metal, or at both the ligand and the metal. The review has described specific examples of this behaviour and the general geometric principles are summarised in Fig. 14. Interestingly the diazenido and dioxygen complexes also show η^2 geometries, which have been discussed above in the context of η^2 SO_2 complexes. These are particularly favoured when the metal centre has filled π orbitals which may function as effective donors. It is noteworthy that King has recently reported DFT calculations on SF_3 complexes of transition metals where the SF_3 ligand displays symmetry signatures which resemble those described in this paper. The calculations suggest triplet states on the metal rather than the singlet states described in the complexes described herein [34].

There are of course chemical implications associated with the ambivalent/ambiphilic behaviour and we note that Berke [98, 99] has recently reviewed the catalytic implications of the linear-bent transformations in nitrosyl complexes. The occurrence of double signature processes described above involves the creation of a lone pair on the main group ligand, which is accompanied by the creation of a 16-electron centre at the metal, and this has chemical implications for reactivity, fluxionality and the catalytic behaviour of ambidentate and ambiphilic complexes. Since the symmetry signatures indicate the occurrence of a simultaneous creation of a lone pair on the ligand and a 16-electron metal centre, this suggests the internal creation of a frustrated Lewis acid/base pair [100–102]. The large *trans* influence differences associated with the ambidentate bonding modes of ligands such as NO also have significant biological and chemical implications.

Organometallic π -bonded ligands are capable of decreasing their hapticity and thereby creating an empty orbital on the metal centre. Therefore they are closely

related to the ambivalent ligands described above. The difference lies in the fact that for organic unsaturated ligands, double bonds rather than lone pairs are created in the lower symmetry geometry (see **20** and **21**). These changes may be controlled by the symmetries of the metal fragments and the substituents on the organic ligand. They have also been proposed as intermediates in ligand substitution reactions at the metal centre. In complexes which contain both ambivalent inorganic ligands and π -bonded ligands, there are opportunities for exploring their relative tendencies to adopt lower symmetry geometries and the possibility valence tautomerism involving both types of ligands [80].



3 Isolobal Analogies for Nitrosyl Complexes

3.1 Introduction

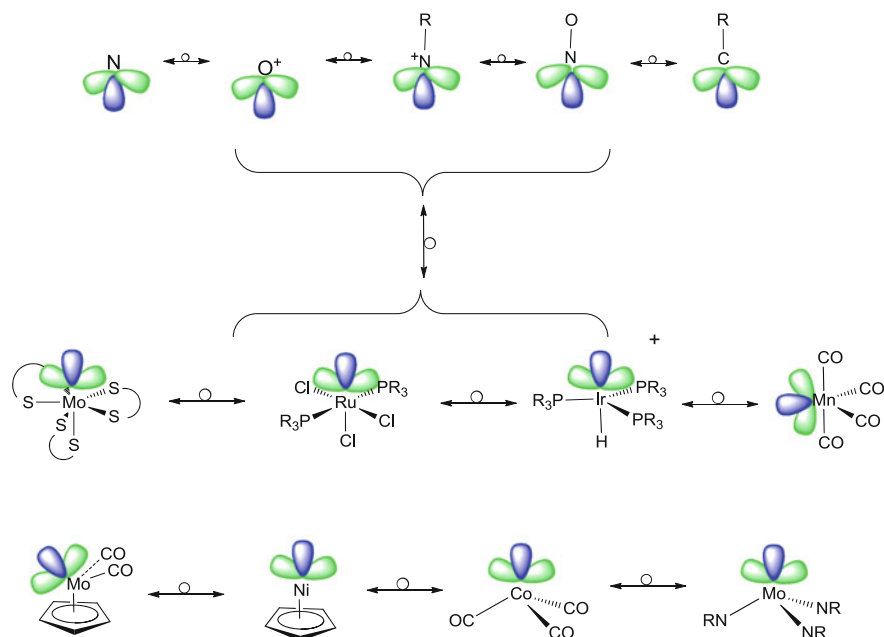
The synergic bonding interactions between CN^- , CO and NO^+ and transition metal fragments result in three bonding (σ and π) and three antibonding (σ^* and π^*) molecular orbitals and maximum stabilisation is achieved for six valence electrons. For such complexes the *isolobal* analogy [103–106] may be used to identify related groups of main group and transition fragments which have matching frontier orbitals. Some *isolobal* main group and metal fragments, which also have three outpointing orbitals occupied by three electrons, are summarised in Table 2 and illustrated in Fig. 16.

The *isolobal* analogy has proved to be a very useful concept for uniting large areas of inorganic and organometallic chemistry and highlighting important similarities between main group and transition metal chemistry and organic and inorganic chemistry [103–106]. Indeed the previous section on ambiphilic ligands has shown the close similarities in the structures of adducts of SO_2 and I_2 with main group and transition metal fragments, without explicitly stating that the *isolobal* analogy underpinned the similarities.

The left-hand side of Fig. 17 illustrates the frontier orbitals of metal fragments with 6–3 spectator ligands located along the equator or below the equator.

Table 2 Examples of isolobal main group and transition metal fragments

	Main group	Transition metal	Geometry
NO, NS	N, P, As	$M(S_2CNR_2)_3$	Pentagonal pyramid
PS, AsS	O^+	$[Fe(NH_3)_5]^{3+}$	C_{4v} octahedral
N_2R	$CR^- NR^+$	$[RuCl_5]^{2-}$	C_{4v} octahedral
		$Mn(CO)_4$	Trigonal bipyramid eq.
		$[IrH(PPh_3)_3]^+$	Trigonal bipyramid axial
		$Ni(\eta-C_5H_5)$	C_{5v} symmetry
		$[Co(CO)_3]$	C_{3v} pyramid
		$[Ir(PPh_3)_3]$	C_{3v} pyramid

**Fig. 16** *Isolobal analogies for nitrosyl, nitrido and related complexes*

The symmetrical partial coordination polyhedral may be described by analogy with cluster compounds as *nido*. Specifically they are based on pentagonal-bipyramidal, octahedral, trigonal-bipyramidal and tetrahedral polyhedral minus an axial vertex. They all share an empty frontier orbital pointing towards the missing vertex and a pair of d_{xz} , d_{yz} orbitals, occupied by three electrons, which symmetry match $\sigma(NO)$ and $\pi^*(NO)$ to form three stable molecular orbitals occupied by six electrons. For the three coordinate conical fragment the frontier orbitals are dp hybrids rather than pure d orbitals [103–106]. The frontier orbitals of the *isolobal* $M(\eta-C_5H_5)$ fragment are very similar to those of the conical $M(CO)_3$ fragment [104].

Figure 19 gives generalised molecular orbital interaction diagrams for comparable nitrido and nitrosyl transition metal complexes [107]. This emphasises the

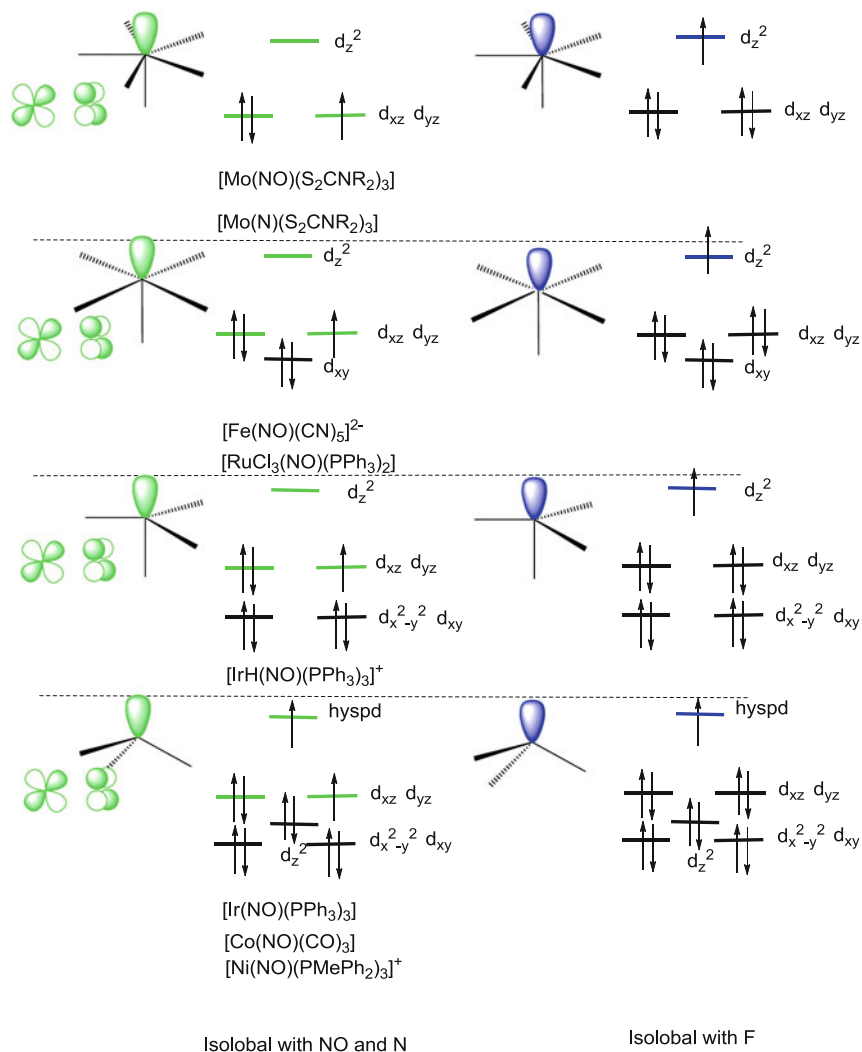


Fig. 17 Transition metal fragments which are *isolobal* with nitrosyl and nitrido on the *left-hand side* and F on the *right-hand side*. Specific examples of complexes derived from the *isolobal* analogy are given below the energy diagrams

similarity in the three bonding (σ and π) and three antibonding (σ^* and π^*) orbitals which are the major contributors to the bonding between the metal and the nitrido and nitrosyl ligands. They form the basis of the triple bond description favoured by Gray and Parkin if the bonding orbitals are occupied by six electrons [108–110]. The formation of multiple bonds by both ligands leads to their classification as strong field ligands and in general their coordination to transition metals

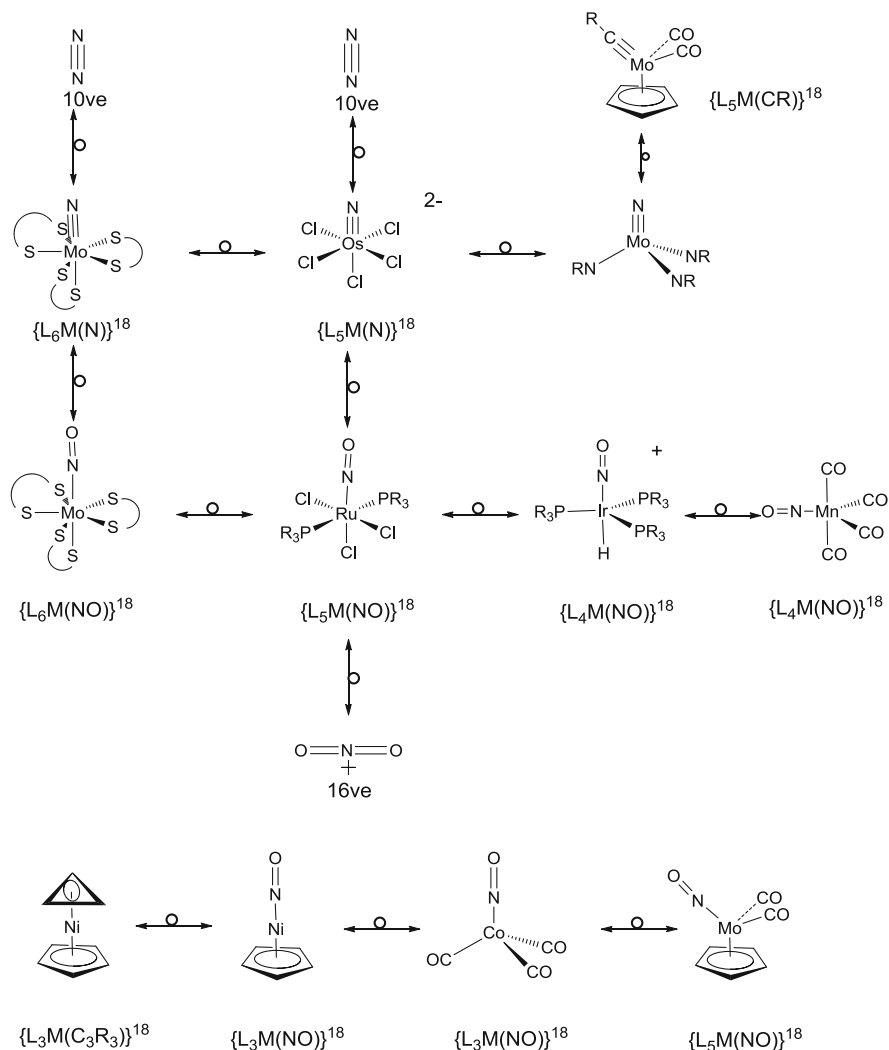


Fig. 18 Examples of *isolobal* nitrosyl, carbyne and nitrido complexes

leads to low-spin complexes. This property is particularly significant for understanding the changes in magnetic properties of biologically active metal complexes.

There are significant differences in the localisation of the bonding and antibonding orbitals which reflect the energies of the frontier orbitals of N and NO shown on the right-hand side of Fig. 19. For the nitrido complexes, the bonding molecular orbitals are localised more on the nitrogen which leads to a larger negative charge on the ligand in 18 electron nitrido complexes compared to nitrosyls (see Sect. 3.2 for more details). For nitrosyl complexes the bonding orbitals are localised more on the metal than the nitrosyl ligand (see bottom of Fig. 19). Differences in the

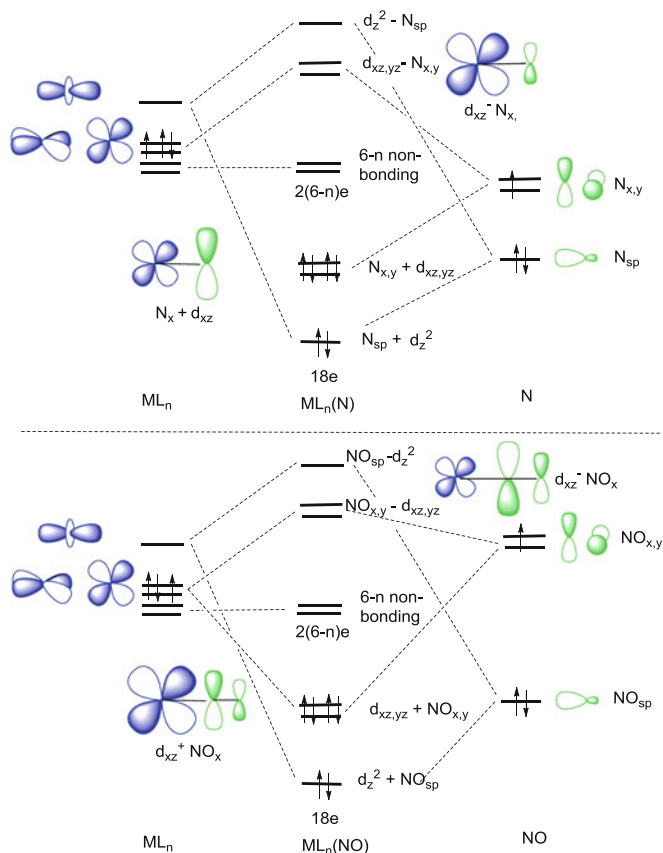


Fig. 19 Generalised molecular orbital diagrams for $ML_n(N)$ and $ML_n(NO)$

localisation of the electron density in the π -bonding orbitals are exaggerated in the designation of formal oxidation states in the two types of complex. Specifically assigning the four electrons in $N_{x,y} + d_{xz,yz}$ exclusively to nitrogen in the nitrido complex leads to N^{3-} and a formal metal oxidation state of 3+ in $ML_n(N)$, whereas if they are assigned to the metal in $d_{xz,yz} + NO_{x,y}$ in the nitrosyl, the formal oxidation state is -1 in $ML_n(NO)$. $\pi^*(NO)$ effectively donates an electron to $d_{xz,yz} + NO_{x,y}$, i.e. in the pre-Enemark–Feltham notation [17], it is an NO^+ complex. In the new notation introduced in these volumes of *Structure and Bonding* the large difference in oxidation states is not relevant since it depends only on the EAN count. The formal triple M–X bond described above is also applicable to oxo, linear carbyne, imido alkoxy and singly bent azenido complexes [8–10]. The EAN rule is satisfied for all these complexes if the $(6 - n)$ non-bonding orbitals shown in the figure are fully occupied.

One important difference between *isolobal* main group and transition metal fragments is the presence of non-bonding orbitals in the d orbital manifold.

These orbitals generally have nodes in the ligand directions. For ($n = 6$) there are no non-bonding orbitals, for ($n = 5$) the non-bonding orbital is d_{xy} , for ($n = 4$), d_{xy} and $d_{x^2-y^2}$; and for ($n = 3$), d_{xy} and $d_{x^2-y^2}$ and d_{z^2} (which is rendered non-bonding by the admixture of s orbital character). These orbitals may be depopulated without significantly affecting the M–X multiple bonding. Octahedral amine and cyano nitrosyl complexes provide examples of complexes with partially filled non-bonding orbitals.

The *isolobal* fragments have not been extended to $n = 7$ and $n = 8$ in Fig. 19 because according to the complementary nature of the ligand and metal orbitals, such coordination geometries no longer have d_{xz} or d_{yz} orbitals for interacting with $\pi^*(\text{NO})$. The π interactions between d_{xz} , d_{yz} and $\pi^*(\text{NO})$ are so important that eight (d^2) and nine (d^0) coordinate nitrosyl complexes are not stable.

The formal triple M–X bond in nitrido, alkylimido and oxo complexes is most commonly observed for metals on the left-hand side of the transition series. Electrons may occupy the ($6 - n$) non-bonding orbitals and thereby satisfy the EAN rule. Additional electrons then must occupy the antibonding metal–ligand orbitals $d_{xz,yz} - N_{x,y}$ in Fig. 19. Gray [110] has argued that in tetragonal complexes the importance of metal-oxo π -bonding leads to an “oxo wall” on the right-hand side of the transition series which makes the isolation of oxo (and nitrido) complexes a significant synthetic challenge. To find complexes beyond this wall reduced coordination numbers and geometries are required. Wilkinson’s $[\text{IrO}(\text{mesityl})_3]$ ($d^4 - 16$ electron) and Hillhouse’s two-coordinate imido complexes were cited as examples of complexes which overcome the wall by adopting lower coordination numbers [111, 112]. A corresponding wall exists for nitrosyl complexes on the left-hand side of the transition series as discussed above. In order to have six electrons occupying the three strongly bonding orbitals – $d_{z^2} + \text{NO}_{sp}$ and $d_{xz,yz} + \text{NO}_{x,y}$ – in Fig. 19 the metal must contribute at least three electrons. Therefore, metal nitrosyl complexes are very rare for the early transition metals. (In addition the strong electrophilicity of the early transition metals may result in the extraction of the oxygen atom from nitric oxide in the attempted synthesis of nitrosyl complexes of these metals.)

Nitrosyl complexes adhere more faithfully to the EAN rule than the corresponding nitrido complexes because the additional electrons contributed by metals in the middle and to the left in the transition series populate the ($6 - n$) orbitals shown in Fig. 19. For nitrido complexes additional electrons can only be accommodated if they occupy the antibonding orbitals and this results in a reduction of the M–X bond order [109].

In summary the molecular orbital descriptions of nitrido and nitrosyl complexes are more closely related than the formal oxidation state descriptions would suggest. In a later section of this review, detailed DFT calculations suggest very similar bond orders and charge distributions in both classes of complexes. However, there are also significant differences which lead to a preference for forming nitrido complexes for the early transition metals and nitrosyl complexes for the later transition metals. This complementarity suggests that the formation of mixed

Table 3 Summary of the electron populations (in electrons) of the d orbitals in $[\text{Ru}(\text{CN})_6]^{4-}$ and $[\text{Ru}(\text{NO})(\text{CN})_5]^{2-}$

d orbital populations	$[\text{Ru}(\text{CN})_6]^{4-}$	$[\text{Ru}(\text{NO})(\text{CN})_5]^{2-}$
$d_{x^2-y^2}$	1.16	1.33
d_{z^2}	1.16	1.25
d_{xy}	1.86	1.93
d_{xz}	1.86	1.47
d_{yz}	1.86	1.47

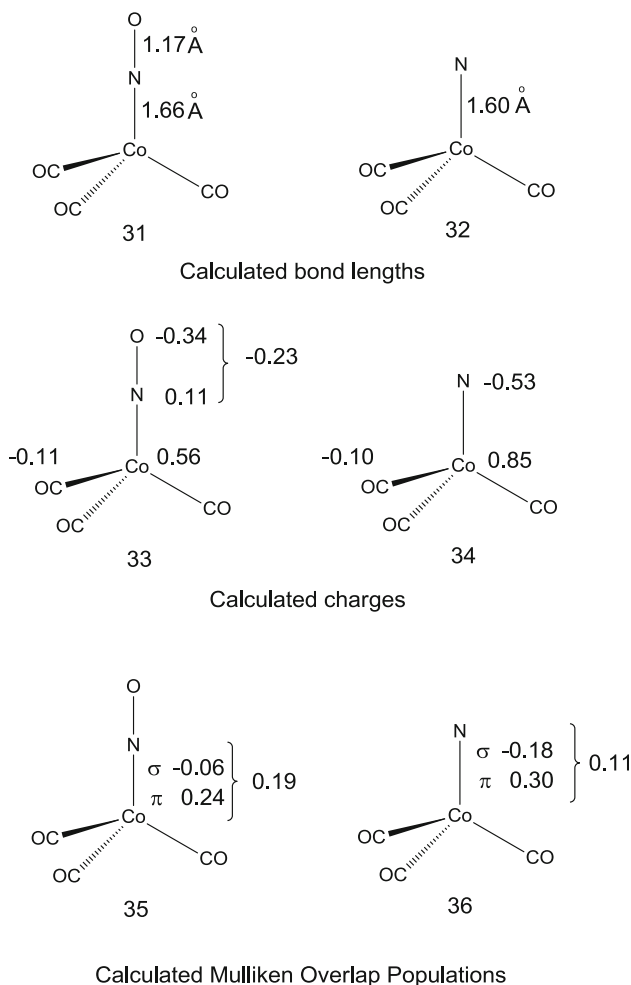
nitrido-nitrosyl complexes may not only lead to the annexation of a larger area of the transition series for both ligands, but also lead to interesting synergic interactions between the complementary ligands.

Examples of coordination and organometallic compounds, which illustrate the wide scope of the *isolobal* analogy, are shown in Fig. 18. All these examples are *isolobal* with NO_2^+ , N_2O and N_3^- (16 electron) and share in common with them linear X–N–O (X = M, O or N) geometries. The compounds in Fig. 18 span a range of coordination numbers (specifically 7–4) and a wide range of spectator ligands. They also share in common that they all obey the effective atomic number (EAN) (8 and 18 electron) rule if NO is categorised as a three-electron donor. To emphasise this the examples are accompanied by the notation $\{\text{L}_n\text{M}(\text{NO})\}^{18}$, which has been introduced for transition metal complexes of ambiphilic ligands. The examples shown also stress that the *isolobal* analogy also relates NO_2^+ , N_2O and N_3^- to a wide range of carbyne, nitrido, oxo and nitrosyl coordination and organometallic compounds.

3.2 Theoretical Underpinning of the Isolobal Analogy

The *isolobal* analogy does not however distinguish the relative importance of the σ and π M–X interactions in related compounds and how they vary across a series. Recent DFT molecular orbital calculations [24, 25, 113–116] for $[\text{Ru}(\text{CN})_6]^{4-}$ and $[\text{Ru}(\text{NO})(\text{CN})_5]^{2-}$, the ruthenium analogue of Prussian Blue, summarised in Table 3, provide a means of placing these bonding differences on a more quantitative basis. The e_g set of orbitals of $[\text{Ru}(\text{CN})_6]^{4-}$ has a slightly lower d orbital population than $[\text{Ru}(\text{NO})(\text{CN})_5]^{2-}$, suggesting more effective σ -donation from the lone pair orbital of CN^- into these orbitals, and the degeneracy of the t_{2g} set is removed and the reduced electron population of d_{xz} and d_{yz} in $[\text{Ru}(\text{NO})(\text{CN})_5]^{2-}$ emphasises more effective π -bonding between NO and Ru. The different population of d_{xy} which by symmetry cannot participate in the π -bonding to NO unlike d_{xz} and d_{yz} is particularly noteworthy (d_{xy} is the $(6 - n)$ non-bonding orbital in Fig. 19). The calculated Wiberg indices also confirm strong multiple bonding (see 22).

The *isolobal* analogy also depends on the formation of strong covalent bonds between the metal and the nitrosyl and the spectator ligands. For second- and third-row transition metal nitrosyl complexes, e.g. Ru, described above, this generalisation holds well.



3.3 Sixteen-Electron *Isolobal* Analogies

Figure 18 illustrates a wide range of examples of 18-electron complexes based on the *isolobal* analogy. There are a substantial number of transition metal complexes which follow a 16- rather than 18-electron rule and it is no longer appropriate to relate them directly to main group analogues (i.e. N_2O^{2+} and NO_2^{3+}), which are not stable ions. The partial occupation of the non-bonding orbitals shown in Fig. 19 leads to nitrosyl and nitrido complexes with fewer than 18 electrons, and analogies between *isolobal* transition metal complexes are instructive (see Fig. 20). Isoelectronic oxo, imido and carbyne complexes also exist. The 16-electron

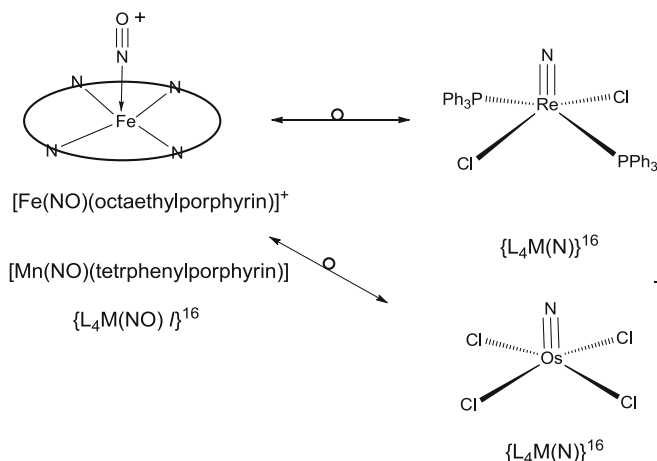


Fig. 20 Isolobal 16-electron nitrido and nitrosyl complexes

square-pyramidal iron porphyrin nitrosyl complexes have been extensively studied, particularly by Scheidt and Lehnert [38–40, 121–124], because of their relevance to the biological role of nitric oxide and their structures are discussed in detail [121–124]. There also exist a wide range of square-planar and trigonal complexes which are generally associated with 16 electrons, but they are not as relevant to understanding the structures of nitrosyl complexes.

3.4 Isolobal Analogies for Bent Nitrosyl Complexes

Bent nitrosyl complexes may also be interpreted using the *isolobal* analogy. Specifically, HNO, RNO and FNO with 18 valence electrons represent archetypical angular (bent) nitroso compounds and therefore transition metal fragments which reproduce this geometry are *isolobal* with H^- , R^- or F^- . The relevant transition metal fragments which are *isolobal* and pseudo-isoelectronic with H, R or F have a singly occupied d_{z^2} or spd hybrid orbital which points along the symmetry axis and is able to pair up with the single electron of $\pi^*(\text{NO})$ (see right-hand side of Fig. 17). The important point to note from Fig. 17 is that the same ML_n fragments may represent different *isolobal* analogues according to the population of the frontier orbitals. In each example, the *isolobal* analogue requires the addition of two electrons to the metal's manifold. The formation of a strong covalent bond is encouraged by good overlap between d_{z^2} and $\sigma(\text{NO})$ and $\pi^*(\text{NO})$ and is enhanced by strongly donating spectator ligands which lower its ionisation energy. The fragments shown in Fig. 17 are capable of being *isolobal* with X if the d_{xz} and d_{yz} orbital pair is completely occupied and a single electron resides in d_{z^2} . The fragments which are *isolobal* with F are associated with an additional electron pair which ends

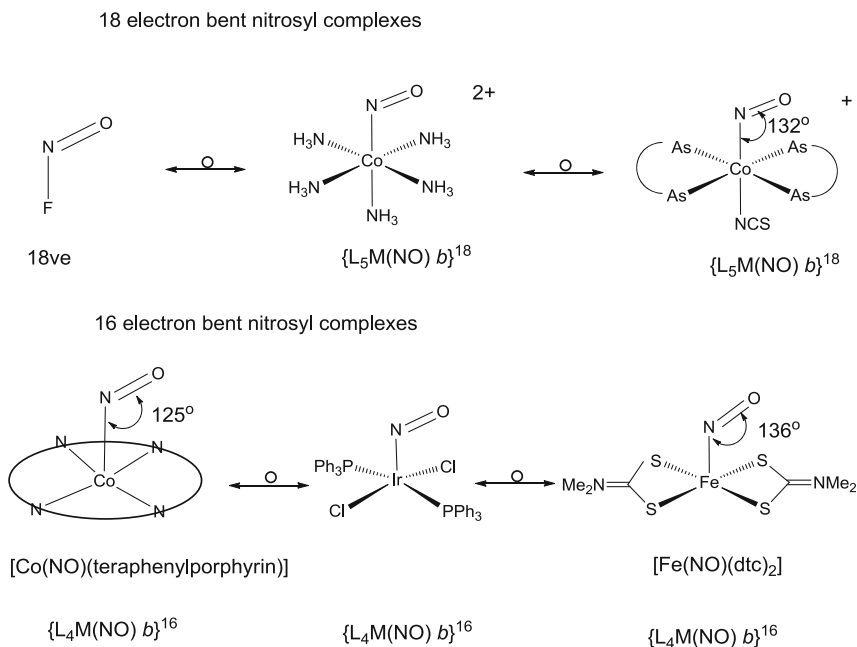


Fig. 21 Metal complexes isolobal with NOF

up in an orbital which resembles a lone pair in F–N–O, but which has significant contributions also from d_{z^2} and d_{xz} . One component of the π -bonding involving d_{yz} and $\pi^*(NO)$ is retained in the bent geometry and consequently bent M–N–O complexes retain some multiple bond character and this is reflected in the M–N bond lengths. The M–N(O) bond lengths in the following series of tetraphenylporphyrin complexes illustrate the loss of multiple bond character as the nitrosyl bends: $\{L_4Mn(NO) l\}^{18}$ Mn–N 1.644 Å (Mn–N–O 176°), $\{L_4Fe(NO) i\}^{19/17}$ Fe–N 1.717 Å (Fe–N–O 149°), $\{L_4Co(NO) b\}^{18}$ Co–N 1.837 Å (Mn–N–O 125°) [125].

Specific examples of $\{L_nM(NO) b\}^{18}$ bent nitrosyl complexes, which are *isolobal* with FNO, are illustrated in Fig. 21. Figure 21 also gives some examples of $\{L_nM(NO) b\}^{16}$ complexes which appear to conform to the 18-electron rule if NO acts as a 3-electron donor, but which have bent nitrosyls, suggesting that one of the electron pairs is localised mainly on nitrogen and thereby relating them to the $\{M(NO)\}^{16}$ complexes illustrated in Fig. 20. These complexes generally have tetragonal symmetries and consequently the isolation of these complexes is favoured by rigid porphyrin-like ligands [121–124] and pincer ligands [125] which encourage tetragonal-planar geometries.

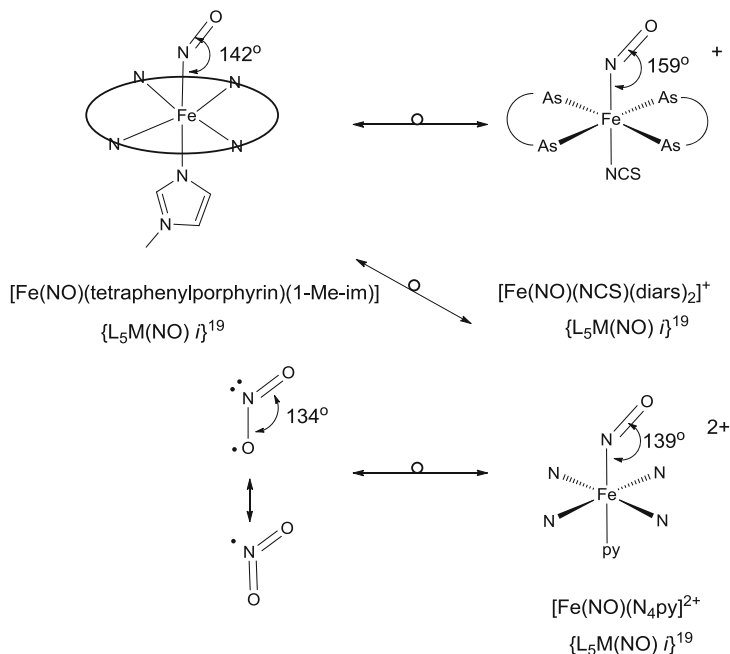


Fig. 22 19-Electron metal complexes which are isolobal with NO_2

3.5 Isolobal 19-Electron Complexes

The *isolobal* analogy has related NO_2^+ and NO_2^- to linear and bent transition metal nitrosyl complexes. The intermediate NO_2 , a radical with 17 valence electrons, is electronically related to these two charged species and has an intermediate bond angle (134°) and it is possible to identify a series of *isolobal* transition metal complexes. Examples of octahedral complexes are illustrated in Fig. 22 and in the new notation they are defined as $\{\text{L}_5\text{M}(\text{NO}) i\}^{17/19}$.

The compounds shown have intermediate M–N–O bond angles lying between 139 and 159° , i.e. neither linear nor bent and not dissimilar to that observed in NO_2 (134°). All these transition metal examples have one unpaired electron. A series of related five-coordinate square-pyramidal complexes is shown in Fig. 23. It is noteworthy that these $\{\text{L}_4\text{M}(\text{NO})\}^{17}$ complexes have M–N–O bond angles much closer to 180° than the related octahedral complexes and consequently are designated as *l* or *i*. They are also paramagnetic (single unpaired electron) and EPR studies on $[\text{Fe}(\text{NO})(\text{porphyrin})]$ confirm the lack of axial symmetry ($g_x \neq g_y \neq g_z$) and the spin density residing primarily in d_{z^2} , but the nitrogen hyperfine splitting confirms some localisation on N [123–127]. Comparison of the structures in Figs. 22 and 23 confirms that the presence of the *trans* ligand results in a more bent geometry. The bottom of Fig. 23 shows a simple orbital picture which rationalises this observation. In these complexes there is a three-electron

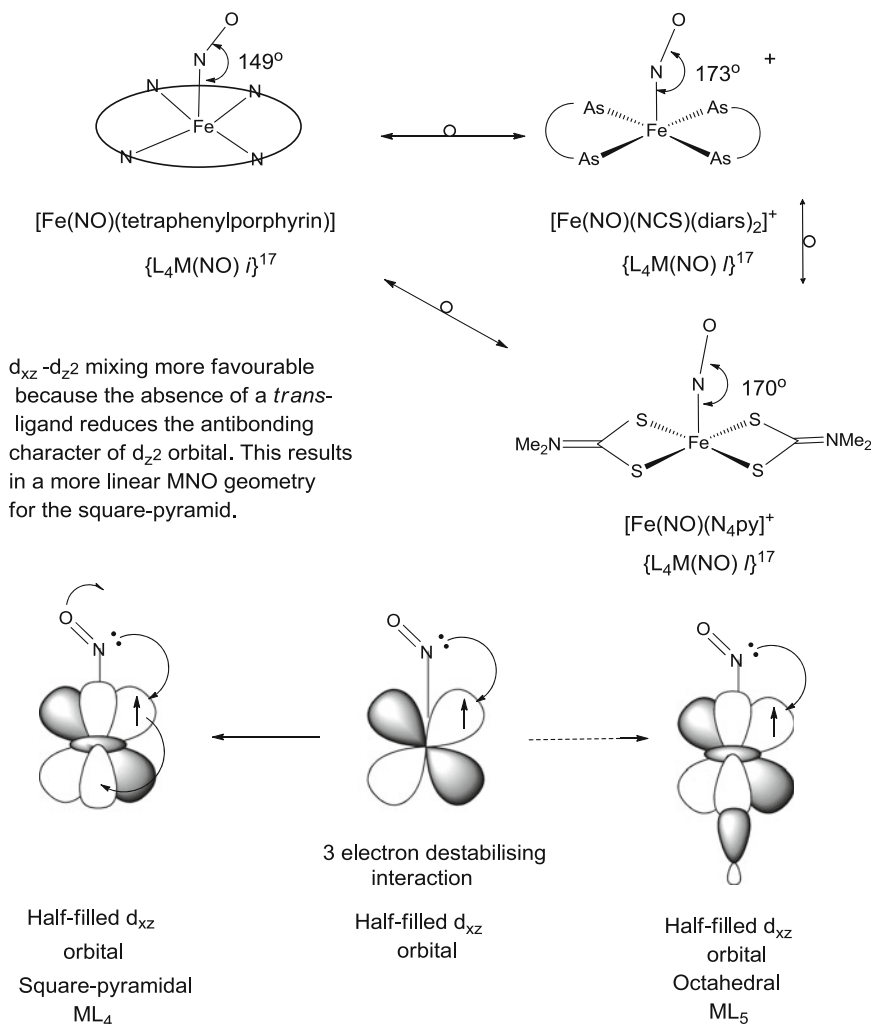


Fig. 23 17-Electron complexes isoelectronic with NO_2

two-centre interaction between the “lone pair orbital” on N and the d_{xz} orbital which hinders the adoption of a linear geometry. The antibonding character of this interaction is reduced by mixing with d_{z^2} because for the bent geometry these two metal orbitals have the same symmetry. For the square pyramid the absence of a *trans* ligand reduces the antibonding character of d_{z^2} and permits the M–N–O geometry to become more linear than in the corresponding octahedral complex.

3.6 *Trans-Influences in Isolobal Complexes*

The discussion above has emphasised important similarities between nitric oxide and other ligands capable of forming triple bonds to transition metals. These ligands, however, have very different *trans* influences and effects. *Trans* influence is a ground-state effect which is detected crystallographically or spectroscopically by bond lengthening or weakening effects on the ligand *trans* to the specified ligand. A *trans* effect is a kinetic phenomenon whereby the *trans* ligand is labilised differentially by the specified ligand. The *trans* influence and effect do not necessarily correlate, but if the nucleophilic substitution reaction is dissociative, then generally ligands which have a high *trans* influence also exert a strong *trans* effect, because the bond weakening effect reduces the activation energy for ligand dissociation [126, 127].

Coe and Glenwright [128] have proposed the following generalisations regarding *trans* influences for transition metal complexes:

Very large ($>0.2 \text{ \AA}$): SiR₃, NO (bent), N, O, S, RC

Large ($0.1\text{--}0.2 \text{ \AA}$) H, R, alkenyl, Ph, RCO, N₂R (double bent)

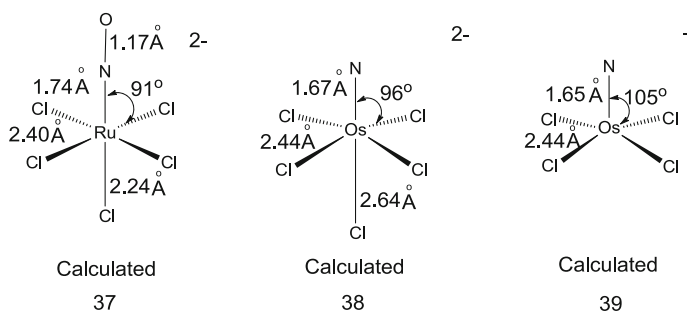
Moderate ($<0.1 \text{ \AA}$) CO, Cn, CNR, alkynyl, NO₂, NS and NO (linear)

The *isolobal* nitrido, oxo and alkyl (or aryl) imido ligands have a large *trans* influence, but linear nitrosyls do not. In contrast bent nitrosyls and double-bent diazenido ligands exert a large *trans* influence in octahedral complexes. The origins of the different *trans* influences for linear and bent nitrosyls were first interpreted within a framework of molecular orbital theory by Mingos in 1973 [85, 129–134]. Specifically it was shown that the bending of the nitrosyl ligand in [Co(NH₃)₅(NO)]²⁺ results in a lengthening of the Co–NH₃ bond *trans* to NO by 0.09 Å when compared to the *cis*-Co–NH₃ bonds [135]. The relevant Walsh diagrams and the importance of the metal d₂ orbital in creating the *trans* influence are discussed more fully in other chapters. The biological significance of the larger *trans* influence of NO compared to CO and NO was first recognised in 1976 by Perutz and co-workers [131] who interpreted differences in changes of the quaternary structures of haemoglobin adducts of carbonyl, nitrosyl and dioxygen ligands. In model octahedral tetraphenylporphyrin complexes of Mn and Fe with 4-methylpyridine *trans* to NO, the Mn–N bond length is 2.20 Å (Mn–N–O linear; {L₄M(NO) *l*}¹⁶), and this lengthens to 2.40 Å in the corresponding Fe complex (Fe–N–O = 142°; {L₄M(NO) *i*}¹⁷), underlining the fact that a significant *trans* influence also occurs for complexes with intermediate-bent geometries.

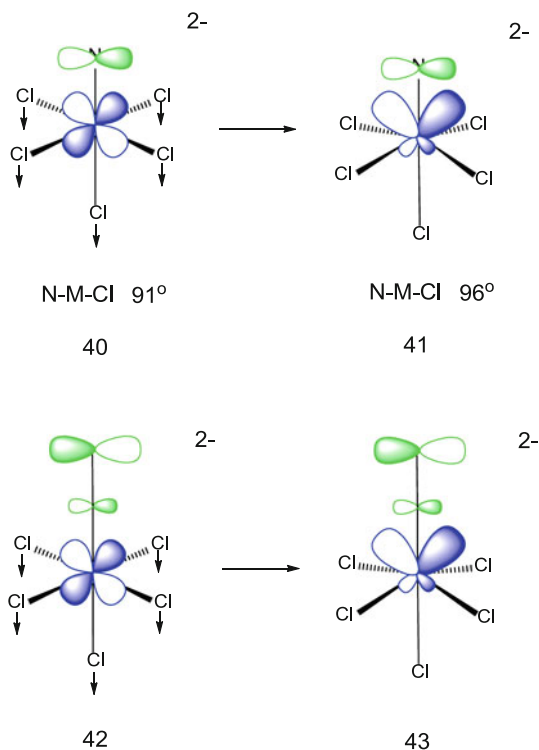
When the physiological and biological significance of NO as a signalling molecule was recognised in the 1980s, the reactions between NO and biological molecules with Fe(II) porphyrin cores took on a special importance. Specifically Traylor and Sharma [136] have proposed a mechanism for sGC (soluble guanylyl cyclase) activation by NO [137, 138]. Guanylyl cyclase is a heme enzyme with an

[Fe^{II}(protoporphyrin IX)] at its core with an open axial distal coordination site and a histidine nitrogen occupies the proximal site. Coordination of NO to the heme centre gives an {L₅M(NO)}¹⁹ complex that weakens the histidine–iron bond and results in changes in protein conformation that greatly activates the enzyme (see Figs. 22 and 23) [137, 138].

The electronic origins of the very different *trans* influences of nitrido and linear nitrosyl ligands were first examined using DFT molecular orbital calculations in 1995 by Lyne and Mingos [25, 115, 116, 118]. Specifically calculations were reported on [Ru(NO)Cl₅]²⁻, [Ru(N)Cl₅]²⁻ and [Os(N)Cl₄]⁻. These calculations explored the steric and electronic effects in these complexes and established that the electronic effects underlying the large *trans* influence in the nitrido complex were intimately connected with the bending of the *cis*-chloro ligands away from the nitrogen atom. It is apparent from 37 to 39 that in the nitrido complex 38, the lengthening of the *trans*-M–Cl is associated with the increase in the N–Os–Cl angle from 90° to 96° which strengthens the Os–N multiple bonding (see 40 and 41). This distortion does not occur in the corresponding nitrosyl complex 37, because the M–NO d_{z²} + N_{sp} and d_{xz,yz} + N_{x,y} molecular orbitals are less localised on N (see Fig. 16) and the back donation effects which strengthen the M–N bond simultaneously weaken the N–O bond (see 42 and 43).



Kaltsoyannis and Mountford [20, 26, 28] have reported DFT calculations on titanium imido complexes and have suggested that 25% of the *trans* influence in these complexes is related to bending distortion observed in osmium nitrido complexes and 75% to direct electronic effects involving antibonding interactions between the *trans* chloride and the titanium atom. Lyne and Mingos have reported the effect of d electron configurations on the *trans* influence in d⁰ and d² molybdenum and tungsten imido complexes, where the phosphine spectator ligands play an important role [25].

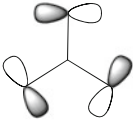
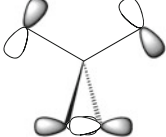
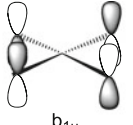
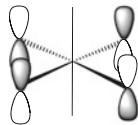


3.7 *Isolobal Poly(Nitrosyls) and Poly-Nitrido-Oxo and Imido Complexes*

The discussion above has focussed on *isolobal* complexes containing few nitrosyl and nitrido ligands, but it is also important to consider the bonding implications for complexes with several of these ligands. It is significant to note an important difference between complexes containing several nitrosyl or carbonyl ligands and complexes which contain several nitrido or oxo ligands. The former adhere to the EAN rule irrespective of the number of π -acceptor ligands, whereas the latter diverge increasingly from the EAN rule as the number of π -donor ligands increases. For example, the homoleptic complexes $\text{Cr}(\text{NO})_4$ and $\text{Cr}(\text{CO})_6$ both have 18 electrons, whereas OsO_4 and $[\text{OsO}_4(\text{OH})_2]^{2-}$ have 24 and 30 electrons, respectively. The generalised molecular orbital diagram in Fig. 19 emphasised the important role of the non-bonding metal d orbitals in metal nitrosyl and nitrido complexes. In homoleptic complexes with π -acid ligands the ligand π^* orbitals remain unoccupied, but in complexes with π -donor ligands, the ligand π orbitals are occupied, and when $n > 3$ then it is important to consider non-bonding LCAOs

Table 4 Symmetries of ligand-based orbitals in ML_n complexes

ML_n geometry	π -ligand LCAOs match d and p	π -ligand LCAOs do not match d and p ⁻	No of additional electrons
$n = 3$ D_{3h} symmetry	a_2'', e', e''	a_2''	4
$n = 4$ T_d symmetry	t_2, e	t_1	6
$n = 4$ D_{4h} symmetry	e_g, e_u, b_{2g}, a_{2u}	a_{2g}, b_{1u}	4
$n = 6$ O_h symmetry	t_{1u}, t_{2g}	t_{1g}, t_{2u}	12

			
a_2'	t_1	a_{2g}	t_{1g}
D_{3h}	T_d	D_{4h}	O_h

localised on the ligand. In ML_n where L is an axially symmetric π -donor ligand, there are $2n$ linear combinations generated from the $p_{x,y}$ orbitals of N, O, etc., and some of these do not have the nodal and symmetry properties to overlap with the metal nd , $(n + 1)s$ and $(n + 1)p$ orbitals. The Complementary Spherical Electron Density Model [78, 79, 81, 139, 140] has provided an analysis of the tensor surface harmonic functions generated in such ML_n complexes and the conclusions are summarised in Table 4. The number of non-matching LCAOs increases from 1 for trigonal ML_3 complexes to 6 for octahedral ML_6 complexes. Occupation of these orbitals leads to valence electron counts which exceed that required by the EAN rule. Figure 24 provides examples of complexes with π -donor ligands and contrasts them with complexes with π -acceptor ligands which generally obey the EAN rule [8–10, 19–23, 27, 48, 141–146].

3.8 Summary

The analysis presented above has indicated that it is possible to relate the geometries and electron counts of a large number of transition metal nitrosyl complexes to NO_2^+ , NO_2 and NO_2^- by utilising *isolobal* analogies. The definition of the frontier orbitals of the metal and ligand fragments provides a very flexible basis for relating a wide range of complexes. DFT calculations have provided a basis for confirming the basis of the *isolobal* analogies and have highlighted important differences between the ligands. Of particular note is the larger *trans*

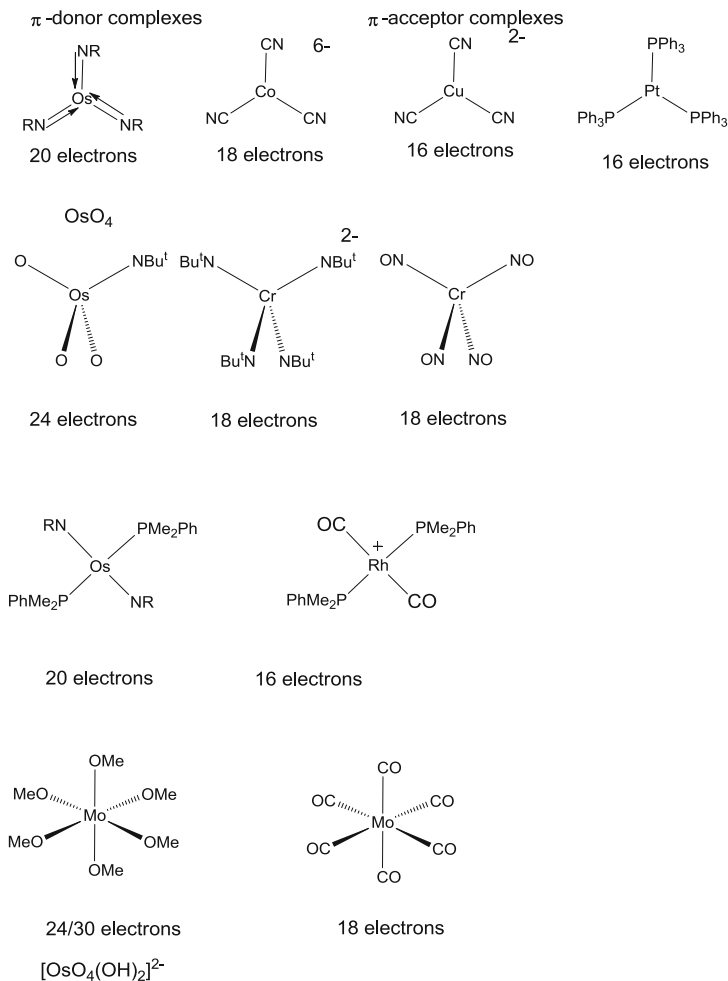


Fig. 24 Comparison of π -donor and π -acceptor complexes. The methoxy ligand may be viewed as a three- or five-electron donor

influence of nitrido and alkylimido ligands compared to linear nitrosyl. The high *trans* influence of intermediate and bent nitrosyls is significant not only from a chemical point of view, but appears to be essential for the biological function of NO.

Acknowledgements Professor Gerard Parkin and Professor Philip Mountford are thanked for their helpful comments and Professor Roald Hoffmann for providing a copy of his paper with Dr Rogachev who gives a theoretical analysis of iodine complexes of the transition metals. Professor John McGrady provided invaluable help with the DFT calculations quoted in the review.

References

1. Wang R (2004) Signal transduction and the gasotransmitters NO, CO and H₂S in biology and medicine. Humana Press, Totowa, NJ
2. Allan PK, Morris R (2013) *Struct Bond* 155
3. Huheey JE, Keiter EH, Keiter RL (1993) *Inorganic chemistry—principles, structure and reactivity*. HarperCollins, New York, p 197
4. Russell C (1971) A history of the concept of valency. Leicester University Press, Leicester, UK
5. Pauling L (1945) *Nature of the chemical bond*, 2nd edn. Cornell University Press, Cornell, p 251
6. Parkin G (2006) *J Chem Educ* 83:791
7. Parkin P (2006) Chapter 1. In: Crabtree RH, Mingos DMP (eds) *Comprehensive organometallic chemistry III*, vol. 1. Elsevier, Oxford, UK
8. Nugent WA, Mayer JM (1988) *Metal-ligand multiple bonds*. Wiley Interscience, New York
9. Bradley DC, Mehrotra IP, Rothwell DP, Singh A (2001) *Alkoxy and Aryoxy Derivatives of Metals* Academic Press. USA, New York
10. Collman JP, Hegedus LS, Norton JR, Finke RG (1987) *Principles and applications of organotransition metal chemistry*. University Science, Mill Valley, CA
11. Jørgenson CK (1962) *Coord Chem Rev* 1:164
12. Kaim W (2011) *Angew Chem Int Ed* 50:10498
13. Sproules S, Wieghardt K (2010) *Coord Chem Rev* 254:1358
14. Schonherr T (2004) *Struct Bond* 106:1
15. Kaim W (2011) *Inorg Chem* 50:9752
16. Sproules S, Weyhermueller T, De Beer S, Wieghardt K (2010) *Inorg Chem* 49:5241
17. Enemark JH, Feltham RD (1974) *Coord Chem Rev* 13:339
18. Mingos DMP (2013) *Struct Bond* 155
19. Cundari TR (2000) *Chem Rev* 100:807
20. Kaltsoyannis N, Mountford P (1999) *J Chem Soc Dalton Trans* 781
21. Ward BD, Orde G, Clot E, Cowley AR, Gade LH, Mountford P (2004) *Organometallics* 23:4444
22. Kahlal S, Saillard J-Y, Hamon J-R, Manzur C, Corillo D (2001) *New J Chem* 25:231
23. Benson MT, Bryan JC, Burrell AK, Cundari TR (1995) *Inorg Chem* 34:2348
24. Lyubinova C, Sizova OV, Losden C, Frenking G (2008) *J Mol Struct THEOCHEM* 865:28
25. Lyne PD, Mingos DMP (1994) *J Organomet Chem* 478:141
26. Schwarz AD, Nielson AJ, Kaltsoyanis N, Mountford P (2012) *Chem Sci* 3:819
27. Benson MT, Cundari TR, Moody EW (1995) *J Organomet Chem* 504:1
28. Stephan DW (2005) *Organometallics* 24:2548
29. Hodgson DJ, Payne NC, McGinnety JA, Pearson RG, Ibers JA (1968) *J Am Chem Soc* 90:4486
30. Rais D, Bergman RG (2004) *Chemistry* 10:3970
31. Tan Y, Hartwig JF (2010) *J CS Dalton Trans* 132:3676
32. Gladysz JA (1991) *J C S Chem Commun* 712
33. Fox DJ, Bergman RG (2004) *Organometallics* 23:1656
34. Schaeffer HF, Deng J, King RB (2011) *Inorg Chem* 50:2824
35. Hoffmann BM, Dean DR, Seefeldt LE (2009) *Acc Chem Res* 42:609
36. Schrock RR (1996) *Chem Rev* 6:3013
37. Pickett CJ (1996) *J Biol Inorg Chem* 1:601
38. Berto TC, Praneeth VKK, Goodrich IC, Lenhert N (2009) *J Am Chem Soc* 131:17116
39. Lenhert N, Sage JT, Silvermail NJ, Scheidt WR, Alp EE, Sturhahn W, Zhao J (2010) *Inorg Chem* 49:7197
40. Richter-Addo GB, Wheeler RA, Hixson CA, Chen L, Khan MA, Ellison MK, Schulz CE, Scheidt WR (2001) *J Am Chem Soc* 123:6314

41. Bradley DC, Hodge SR, Runnades JD, Hughes M, Mason J, Richards RL (1997) *J Chem Soc Dalton Trans* 1603
42. Haymore BL, Hughes M, Mason J, Richards RL (1988) *J C S Chem Commun* 2395
43. Greco GE, Schrock RR (2001) *Inorg Chem* 40:3861
44. De Crisci AG, Hamer GK, Fekl U (2010) *J Coord Chem* 63:2928
45. Bryndza HE, Futz WC, Tam W (1985) *Organometallics* 4:939
46. Steffey BC, Fenwick PE, Rothwell IP (1990) *Polyhedron* 9:963
47. Hoffmann R, DuBois DL (1977) *Nouveau J Chem* 1:479
48. Lin Z, Hall MB (1993) *Coord Chem Rev* 123:149
49. Howard DVA, Trnka TM, Parkin G (1995) *Inorg Chem* 34:3900
50. Selby JD, Manley CD, Schwarz AD, Clot E, Mountford P (2008) *Organometallics* 27:6479; 27:6096; 27:6111
51. Mountford P, Swallow D (1995) *J Chem Soc Chem Commun* 2357
52. Russo MR, Kaltsoyannis N, Sella A (2002) *Chem Commun* 2458
53. Manz TA, Fenwick AE, Phomberi K, Rothwell IP, Thompson KT (2005) *J Chem Soc Dalton Trans* 668
54. Ibers JA, Muir KW (1969) *Inorg Chem* 8:1921
55. Ryan RR, Kubas GT, Moody DC, Eller PG (1981) *Struct Bond* 46:47
56. Mingos DMP (1978) *Trans Met Chem* 3:1
57. Van Koten G (1990) *Pure Appl Chem* 62:1155
58. Bonnet S, van Lenthe JH, van Dam HJJ, Hubertus JJ, van Koten G, Klein G, Robertus JM (2011) *J Chem Soc Dalton Trans* 40:2542
59. Rogachev AY, Hoffmann R (2004) *J Am Chem Soc* 135:3762
60. Moody DC, Ryan RR (1976) *Inorg Chem* 15:1823
61. Salem L (1982) *Electrons in chemical reactions*. Wiley, New York
62. Fleming I (1977) *Frontier orbitals and organic chemical reactions*. Wiley, Chichester, UK
63. Petzer J, Gilbert TM (2003) *Inorg Chem* 42:7207
64. Brust DJ, Gilbert TM (2004) *Inorg Chem* 43:1116
65. Sasuku S, Sato H, Imai Y, Morokuma Y (1985) *Inorg Chem* 24:4538
66. Eller PG, Moody DC, Ryan RR (1976) *Inorg Chem* 15:2442
67. Eller PG, Moody DC, Ryan RR (1979) *Inorg Chem* 18:223
68. Ryan RR, Eller PG (1976) *Inorg Chem* 15:495
69. Cameron TS, Passmore J, Wang X (2004) *Angew Chem Int Ed* 43:1995
70. Ibers JA, Mingos DMP (1970) *Inorg Chem* 9:1105
71. Albano VG, Bellon PL, Sansoni M (1971) *J Chem Soc (A)* 2420
72. Amgoune A, Bourissou D (2011) *J Chem Soc Chem Commun* 47:859
73. Braunschweig H, Grass K, Radacki K (2005) *Angew Chem Int Ed* 46:7782
74. Crossley IRA, Hill AF, Willis AC (2006) *Organometallics* 25:289
75. Hill AF (2006) *Organometallics* 25:4741
76. Parkin G (2006) *Organometallics* 25:4744
77. Green MLH (1995) *J Organomet Chem* 500:127
78. Mingos DMP (1987) *Pure Appl Chem* 59:145
79. Mingos DMP (2006) *J Organomet Chem* 691:3165
80. Elschenbroich C (2006) *Organometallics*, 3rd edn. Wiley-VCH, Germany, p 238
81. Mingos DMP (2004) *J Organomet Chem* 689:4420
82. Bashkin J, Briant CE, Mingos DMP, Sherman DJ, Wardle RWM (1985) *Trans Met Chem* 10:113
83. Luke MA, Mingos DMP, Sherman DJ, Wardle RWM (1987) *Trans Met Chem* 12:37
84. Hoffmann R, Howell JM, Rossi AR (1976) *J Am Chem Soc* 98:2484
85. Mingos DMP (1973) *Inorg Chem* 10:1479
86. Hoffmann R, Chen MML, Rossi AR, Mingos DMP (1974) *Inorg Chem* 13:2666
87. Mingos DMP, Sherman DJ (1989) *Adv Inorg Radiochem* 34:293
88. Mingos DMP, Sherman DJ, Bott SG (1987) *Trans Met Chem* 12:471

89. Waters JH, Whittle KR (1971) *J Chem Soc Chem Commun* 518
90. Vancea L, Bennett MJ, Jones CE, Smith RA, Graham WAG (1977) *Inorg Chem* 16:897
91. Schonerer MW, Baker EC, Eisenberg R (1979) *J Am Chem Soc* 1880
92. Sherman DJ, Mason J, Mingos DMP (1987) *J Chem Soc Chem Commun* 1223
93. Mason J, Mingos DMP, Sherman DJ, Schaffer J, Stejskal EO (1985) *J Chem Soc Chem Commun* 444
94. Coppens P, Novozhilova I, Kovalovsky A (2002) *Chem Rev* 102:61
95. Lynch MS, Cheng M, van Kuikan BE, Khalil M (2011) *J Am Chem Soc* 133:5255
96. Tocheva EI, Rossell FI, Mauk AG, Murphy MP (2007) *Biochemistry* 46:12366
97. Tocheva EI, Rossell FI, Mauk AG, Murphy MP (2004) *Science* 304:867
98. Dudle B, Kanjenpillan R, Blaque O, Berke H (2011) *J Am Chem Soc* 133:8168
99. Berke H (2013) *Struct Bond* 155
100. Erker G (2012) *Pure Appl Chem* 84:2203
101. Stephan DW (2012) *Org Biomol Chem* 10:5740
102. Whitehed MT (2012) *Beilstein J Org Chem* 8:1554
103. Elian M, Hoffmann R (1975) *Inorg Chem* 14:1058
104. Elian M, Chen MML, Mingos DMP, Hoffmann R (1976) *Inorg Chem* 15:1148
105. Mingos DMP (1977) *Adv Organomet Chem* 15:1
106. Hoffmann R (1981) *Science* 211:995
107. Hayton TW, Legzdins P, Sharp WB (2002) *Chem Rev* 102:935
108. Landry VK, Pan K, Quan SM, Parkin G (2007) *J Chem Soc Dalton Trans* 820
109. Gray HB (2012) *Struct Bond* 142:17
110. Hummel P, Gray HB (2000) *Coord Chem Rev* 203:5
111. Hay-Motherwell RS, Wilkinson G, Hussain Bates B, Hursthouse MB (1993) *Polyhedron* 12:2009
112. Laskowski CA, Miller AJM, Hillhouse GL, Cundari TR (2011) *J Am Chem Soc* 133:791
113. Caramori GF, Kunitz AG, Andriaru KF, Doro FG, Frenking G, Thiouni E (2012) *J Chem Soc Dalton Trans* 41:7327
114. Siviva SV, Lyubimova OO, Sizov VV (2002) *Russ J Gen Chem* 74:317
115. Mingos DMP, McGrady JE (Unpublished results) The DFT calculations were performed using the ADF package and based on Becke Perdew functional (BP86) with triple zeta Slater basis functions
116. Lyne PD, Mingos DMP (1995) *J Chem Soc Dalton Trans* 1635
117. Ghosh A (2006) *Biol Inorg Chem* 11:671
118. Mingos DMP, Lyne PD, Pidun U (1994) *Pure Appl Chem* 67:2651
119. Rankin DJ, Robertson HE, Danapoulos AA, Lyne PD, Mingos DMP, Wilkinson G (1994) *J Chem Soc Dalton Trans* 1563
120. Conradie J, Hosh A, Ghosh A (2007) *J Phys Chem B* 111:12621
121. Lehnert N, Berto TC, Sage J, Silvernail N, Scheidt WR, Alp EE, Sherhan W, Zhao J (2013) *Coord Chem Rev* 257:244
122. Praneeth VKK, Nether C, Peters G, Lehnert N (2006) *Inorg Chem* 45:2795
123. Lehnert N, Scheidt WR, Wolf A (2013) *Struct Bond* 155
124. Scheidt WR, Barabanschikov A, Paolek JW, Silvernail NJ, Sage JT (2010) *Inorg Chem* 49:6240
125. Gaviglio C, Ben-David Y, Shimon LJW, Dotorovich F, Milstein D (2009) *Organometallics* 28:191
126. Tobe ML (1972) *Inorganic reaction mechanisms*. Thomas Nelson and Sons, Great Britain, p 42
127. Jordan RB (1991) *Reaction mechanisms of inorganic and organometallic systems*. Oxford University Press, Oxford, UK, p 57
128. Coe BJ, Glenwright SJ (2001) *Coord Chem Rev* 203:5
129. Mingos DMP (1971) *Nat Phys Sci* 229:193
130. Pandey KK (1990) *J Coord Chem* 22:307

131. Perutz MF, Kilmartin JV, Nagai K, Szabo A (1976) *Biochemistry* 15:378
132. Mingos DMP (1974) *Inorg Chem* 10:1479
133. Mingos DMP (1980) *Trans Am Crystallogr Assoc* 16:17
134. Jezowska-Trzbialowska B, Jezierski A (1978) *J Mol Struct* 46:197
135. Coyle B, Pratt CS, Ibers JA (1971) *J Chem Soc Dalton Trans* 2146
136. Traylor TG, Sharma VS (1992) *Biochemistry* 31:2847
137. Ford PC, Clayton J, Melo P, Miranda KM (2013) *Struct Bond* 155
138. Conradie J, Hopmann KH, Ghosh A (2010) *J Phys Chem B* 114:8517
139. Hawes JC, Mingos DMP (1985) *Struct Bond* 63:1
140. Hawes JC, Mingos DMP (1985) *J C S Chem Commun* 1811
141. Schofield MH, Kee TP, Anhaus JT, Schrock RR, Johnson KH, Davis WM (1991) *Inorg Chem* 30:3595
142. Benson MT, Cundari TR, Moody EW (1995) *J Organomet Chem* 564:1
143. Anhaus JT, Kee TP, Schofield MH, Schrock RR (1990) *J Am Chem Soc* 112:1642
144. Williams DS, Schofield MH, Anhaus JT, Schrock RR (1990) 112:6728
145. Williams DS, Schofield MH, Schrock RR (1993) *Organometallics* 12:4560
146. Morrison DL, Wigley DE (1995) *Inorg Chem* 34:2610

The Preparation, Structural Characteristics, and Physical Chemical Properties of Metal-Nitrosyl Complexes

Lauren R. Holloway and Lijuan Li

Abstract The preparation and characterization of a representative group of novel non-heme metal nitrosyl complexes that have been synthesized over the last decade are discussed here. Their structures are examined and classified based on metal type, the number of metal centers present, and the type of ligand that is coordinated with the metal. The ligands can be phosphorus, nitrogen, or sulfur based (with a few exceptions) and can vary depending on the presence of chelation, intermolecular forces, or the presence of other ligands. Structural and bonding characteristics are summarized and examples of reactivity regarding nitrosyl ligands are given. Some of the relevant physical chemical properties of these complexes, including IR, EPR, NMR, UV–vis, cyclic voltammetry, and X-ray crystallography are examined.

Keywords Dinitrosyl iron complex · Iron sulfur cluster · Metal nitrosyl · Nitric oxide

Contents

1	Introduction	54
2	Dinitrosyl Complexes Containing a Single Metal Center	55
2.1	Dicarbonyldinitrosyl Iron	55
2.2	Phosphorus Based Ligands	56
2.3	Nitrogen-Based Ligands	64
3	Nitrosyl Complexes Containing Two or More Metal Centers	70
3.1	Complexes Containing “M ₂ S ₂ ” Core	70
3.2	Iron–Sulfur and Iron–Selenium Nitrosyl Clusters	80
3.3	Multinuclear Metal Nitrosyl Complexes	85

4	Mononitrosyl and Trinitrosyl Complexes	87
4.1	Mononitrosyl Complexes:	87
4.2	Trinitrosyl Complexes	92
5	Organometallic Metal Nitrosyl Complexes	92
6	Conclusion	93
	References	95

1 Introduction

Metal nitrosyl complexes are classified as having at least one nitric oxide group attached to a transition metal atom. The synthesis and study of these molecules began in the mid-1960s and have increased exponentially since the 1990s because of the discovery that nitric oxide can be used within the body for smooth muscle relaxation, tumor regulation, and long-term memory formation [1–3].

There are many different types of metal nitrosyl complexes. Homoleptic nitrosyl complexes containing only a metal atom and nitric oxide groups are very rare [4]. The majority of metal nitrosyl complexes contain two nitric oxide groups and are known as dinitrosyl complexes. However, mononitrosyl complexes are numerous and sometimes represent the products of nitric oxide transfer reactions of their precursor, dinitrosyl complexes. Examples of trinitrosyl complexes are very rare, but do exist. The majority of known nitrosyl complexes have simple structures consisting of a single metal core, but some have several metal atoms in a cluster arrangement. Nearly all metal nitrosyl complexes also have one or more organic ligand molecules of varying size, shape, and donor/acceptor properties. The type of ligand present and the coordination of the ligand to the metal center ultimately define the overall characteristics of the complex.

It has been reported that these complexes exhibit properties that make them useful for pharmaceutical and biological applications; the most useful of these is the storage and transport of nitric oxide [5, 6]. Many recently synthesized complexes demonstrate the ability to deliver NO and a few are currently being used to treat common ailments such as high blood pressure. It is predicted that these nitrosyl complexes can have more complex biological implications, including aiding in long-term memory formation, fighting infection, and treating cancer.

Although this subject has been frequently and comprehensively reviewed [7–11], this review describes a selection of representative metal nitrosyl complexes synthesized during the last decade or so. The representative compounds are chosen in order to give a wide array of structures, including different metal center type, different ligand type and structure, and better synthetic procedures. The synthetic methods, structural characteristics, and spectroscopic properties of those selected complexes are described in detail, while structures similar to those mentioned here are cited but not necessarily discussed. Organometallic metal nitrosyl complexes are minimally discussed with a few examples relating to the reactivity of nitric oxide at transition-metal centers. Work on heme nitrosyls is not discussed, as this subject is the focus of another chapter.

2 Dinitrosyl Complexes Containing a Single Metal Center

Dinitrosyl complexes with single transition metal center are commonly represented with a general formula of $M(\text{NO})_2(\text{L})_2$ and are known to possess tetrahedral geometry. Recently, these dinitrosyl units have been detected within living tissues under a wide range of conditions, including inflammatory responses [12]. The $[\text{M}(\text{NO})_2]$ unit has also been shown to bind to proteins containing cysteine residues and can be formed when a protein with a coordinated iron atom reacts with gaseous nitric oxide [13–15]. These dinitrosyl iron complexes have a nickname of “ $g = 2.03$ species” and are also referred to as non-heme iron nitrosyls in biological systems. Thus, nowadays, dinitrosyl metal complexes are often synthesized with ligands containing sulfur, nitrogen, phosphorus, or oxygen atoms with an ultimate goal of mimicking biological non-heme iron nitrosyls.

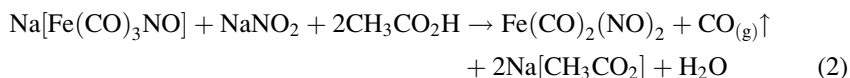
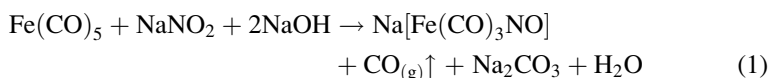
2.1 Dicarbonyldinitrosyl Iron

The most common starting material used to synthesize dinitrosyl metal complexes is dicarbonyldinitrosyl iron (DDI). This useful starting material has been synthesized through several different procedures starting in the early 1930s. Some of the different methods included a simple acidification of nitrate ion and $\text{Fe}(\text{CO})_5$, or pyrolysis of $\text{Hg}[\text{Fe}(\text{CO})_3\text{NO}]_2$, the second of which is only suitable for small amounts of material [16]. Another method involves reacting $\text{Fe}_3(\text{CO})_{12}$ or $\text{Fe}_2(\text{CO})_9$ with nitric oxide [17].

One of the more common procedures for making DDI involves placing a stoichiometric ratio of iron pentacarbonyl and nitrosyl chloride in a stainless steel bomb. This container is sealed and allowed to sit at room temperature for approximately 24 h before cooling to -196°C . Carbon monoxide, the ubiquitous by-product of these reactions, is then pumped off. The contents of the container are distilled under reduced vacuum pressure into a trap cooled to a temperature of -78°C . Analysis by vapor phase chromatography shows that the red liquid collected in the trap is approximately 65% dicarbonyldinitrosyl iron and 35% iron pentacarbonyl [18]. It was found that when the ratio of iron pentacarbonyl to nitrosyl chloride exceeded 1:2, no appreciable amount of dicarbonyldinitrosyl iron is produced.

The most recent method for synthesizing and collecting dicarbonyldinitrosyl iron involves a reaction between iron pentacarbonyl and sodium nitrite and is a slightly modified version of a previously published procedure [19]. The reactions, shown in Eqs. (1) and (2), illustrate the two-step process that occurs. A three-necked round bottom flask is equipped with a condenser column, a nitrogen inlet, and a pressure equalized dropping funnel. The flask is filled with 50 ml of degassed water, 6.0 g sodium nitrite, and 10.0 g sodium hydroxide. Once all of the reactants are dissolved, 5.0 ml of iron pentacarbonyl is injected into the flask. The reaction mixture is refluxed for 3 h with stirring under a gentle nitrogen flow. After the reaction is complete, the temperature is reduced to $30\text{--}40^\circ\text{C}$ and a stream of

nitrogen is passed through the system, into two traps containing approximately 20 g of calcium chloride, and another two traps cooled to -78°C using an acetone/dry ice bath. A 75% solution of glacial acetic acid and water is added dropwise from the dropping funnel. Brown fumes of DDI begin to form and are collected in the cold trap. A reaction of this scale can be expected to afford up to 60% yield. It is noted that any reaction involving ironpentacarbonyl as a reactant may have trace amounts of the material as a contaminant after the reaction has completed.



2.2 Phosphorus Based Ligands

One of the first DNIC structures synthesized with phosphine ligands was reported in the early 1960s. Since then, many new structures have been synthesized that range from simple derivatives of triphenyl phosphine [20, 21] to more complicated structures that make use of different metal centers [22–24]. We choose to use the following examples to illustrate the structures, spectroscopic properties, and mechanisms of reactions.

$\text{Fe}(\text{NO})_2(\text{CO})(\text{PR}_3)$: Several different nitrosyl complexes were synthesized using phosphine-type ligands PR_3 , where $\text{R} = \text{PPh}_3, \text{OCH}_3, \text{P}(n\text{-Bu})_3, \text{PMe}_2\text{Ph}, \text{PEt}_2\text{Ph}$. These compounds are synthesized by reacting a 1:1 ratio of $\text{Fe}(\text{NO})_2(\text{CO})_2$ with the appropriate phosphine ligand at room temperature for approximately 12–15 h [25, 26]. These carbonyl substitution reactions are slow, requiring a longer reaction time for the replacement of the first carbonyl and requiring heating at 85°C for 1–2 days to replace the second carbonyl [27], and is believed to proceed via a conventional associative mechanism. The FT-IR data of these complexes are listed in Table 1. The spectrum of the starting material, $\text{Fe}(\text{NO})_2(\text{CO})_2$, exhibits two nitrosyl stretches and two carbonyl stretches. Upon replacement of a single carbonyl moiety by a phosphite or phosphine group, the remaining CO absorbs in the lower frequency range $1995\text{--}2018\text{ cm}^{-1}$. The two nitrosyl IR stretches in these complexes also shift to lower wavenumbers. The shifting can be explained by the fact that phosphorus donor increases the electron density at the iron center, which in turn enhances the back-bonding from the filled d -orbitals on the metal to the vacant anti-bonding orbitals of the carbonyl and the nitrosyls, with concomitant weakening of the $\text{C}=\text{O}$ bond as well as the $\text{N}\equiv\text{O}$ bond. This results in shift of both carbonyl and the nitrosyl stretches towards lower wavenumbers, in the regions of $\sim 1995\text{--}2018$ and $1700\text{--}1770\text{ cm}^{-1}$, respectively. The cyclic voltammogram data for these complexes are listed in Table 2. The family of $\text{Fe}(\text{NO})_2(\text{PR}_3)(\text{CO})$

Table 1 A list of IR stretching frequencies for the Fe(NO)₂(PR₃)(CO) family and Fe(NO)₂(PR₃)(TCNE) family

Complex	CN stretch (cm ⁻¹)	CO stretch (cm ⁻¹)	NO stretch(es) (cm ⁻¹)	Average NO stretch (cm ⁻¹)
Fe(NO) ₂ (CO) ₂	–	2090, 2040	1817, 1766	
Fe(NO) ₂ (PPh ₃)(CO)	–	2007	1766, 1718	
Fe(NO) ₂ (PPh ₃)(η ² -TCNE), 1	2224	–	1834, 1790	
Fe(NO) ₂ [P(OMe ₃)](CO)	–	2018	1770, 1722	1770, 1722
Fe(NO) ₂ [P(OMe ₃)](η ² -TCNE), 2	2230 (2233)	–	1843, 1790 (1843, 1797)	1843, 1797
Fe(NO) ₂ [P(<i>n</i> -Bu) ₃](CO)	–	(1995) ^a	(1752, 1704)	1752, 1704
Fe(NO) ₂ [P(<i>n</i> -Bu) ₃](η ² -TCNE), 3	2229 (2230)	–	1828, 1778 (1824, 1785)	1824, 1785
Fe(NO) ₂ [PMe ₂ Ph](CO)	–	(2004)	(1754, 1708)	1754, 1708
Fe(NO) ₂ [PMe ₂ Ph](η ² -TCNE), 4	2219 (2226)	–	1839, 1792 (1830, 1786)	1830, 1786
Fe(NO) ₂ [PEt ₂ Ph](CO)	–	(2004)	(1755, 1706)	1755, 1706
Fe(NO) ₂ [PEt ₂ Ph](η ² -TCNE), 5	2225 (2231)	–	1812, 1755 (1827, 1790)	1827, 1790

^aValues shown in parentheses were measured in CH₂Cl₂ solution

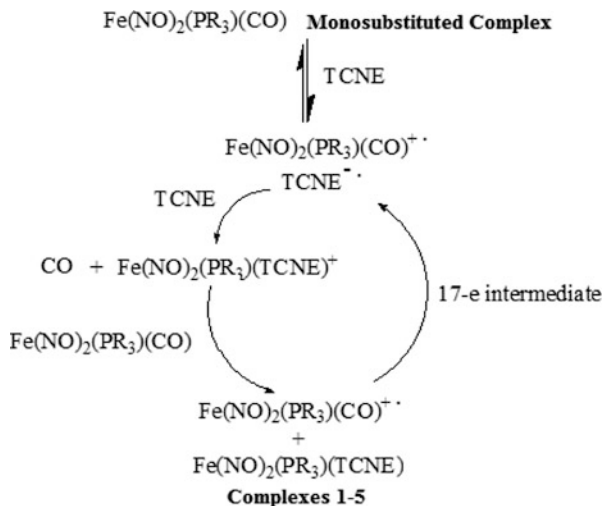
Table 2 Electrochemical potentials for the family of Fe(NO)₂(PR₃)(TCNE) species vs FeCp₂^{+/}FeCp₂ at scan rate of 100 mV/s and the pK_a values for the phosphines and phosphite

Complexes	E _{pc} (V)	E _{pa} (P) (V)	E° (ΔE) (V)	pK _a (Phosphine)
Fe(NO) ₂ [P(OMe ₃)](η ² -TCNE), 2	–0.990	–0.398		2.6
Fe(NO) ₂ [PEt ₂ Ph](η ² -TCNE), 5	–1.120	–0.604		6.25
Fe(NO) ₂ [PMe ₂ Ph](η ² -TCNE), 4	–1.123	–0.607		6.5
Fe(NO) ₂ [P(<i>n</i> -Bu) ₃](η ² -TCNE), 3	–1.146	–0.652		8.43
Fe(NO) ₂ [P(OMe ₃)](CO),			–1.96 (125 mV)	2.6
Fe(NO) ₂ [PEt ₂ Ph](CO)			–2.108 (131 mV)	6.25
Fe(NO) ₂ [PMe ₂ Ph](CO)			–2.101 (268 mV)	6.5
Fe(NO) ₂ [P(<i>n</i> -Bu) ₃](CO)			–2.150 (130 mV)	8.43

compounds shows a quasi-reversible reduction potential E° from –1.96 V to –2.15 V with large peak-to-peak separations. A correlation between the pK_a values and reduction potentials has been observed. This observation can be qualitatively rationalized in that with increasing electron density being donated to the iron center, it is rendered less prone to reduction. A comparison can be made between the decreasing average IR stretching frequencies for the nitrosyls in Table 1 and the increasing pK_a values in Table 2.

Fe(NO)₂[PR₃](η²-TCNE): The substitution of the CO group by TCNE is further accomplished by treating a 1:1 molar ratio of Fe(NO)₂(CO)(PR₃) with TCNE, which afforded complexes of Fe(NO)₂[PR₃](η²-TCNE) (where PR₃ = PPh₃, **1**, P(OCH₃)₃, **2**, P(*n*-Bu)₃, **3**, PMe₂Ph, **4**, and PEt₂Ph, **5**) [20]. These reactions typically

Scheme 1 Mechanism of the reactions of $\text{Fe}(\text{NO})_2(\text{CO})(\text{PPR}_3)$ with TCNE showing the electron transfer autocatalytic pathway through a 17-electron intermediate



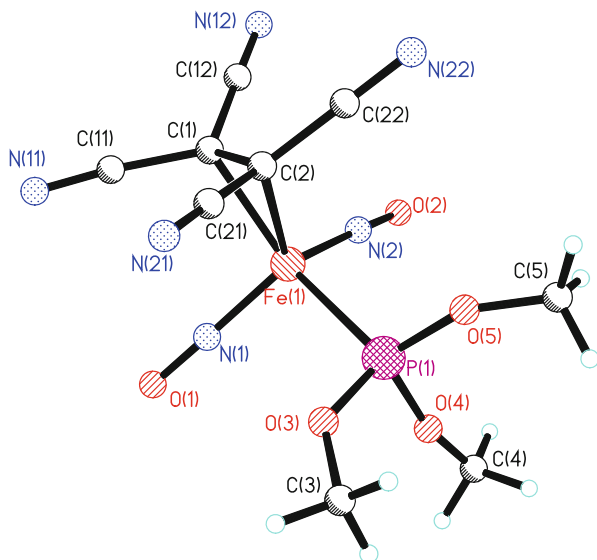
occur over 1–2 h at room temperature with yields over 80%. These complexes are soluble in polar solvents such as CH_2Cl_2 , THF, $(\text{CH}_3)_2\text{CO}$, CH_3CN , and MeOH. However, decomposition occurs after a few hours. They are relatively stable when stored in the solid state under a nitrogen atmosphere and at low temperatures.

The rapidity of such a substitution reaction is due to the participation of free radicals, as evidenced by the observation of the intermediates of $\text{TCNE}^{\bullet-}$ and $\text{Fe}(\text{NO})_2(\text{PPh}_3)\text{L}^{\bullet+}$ (where L may be CO or a coordinated solvent molecule) radicals using EPR upon mixing of the starting materials. We proposed that the reaction proceeds *via* an electron transfer autocatalysis mechanism, through a 17-electron paramagnetic intermediate as shown in Scheme 1.

The FT-IR data for **1–5** and other related complexes are listed in Table 1. The IR spectrum shows that the carbonyl stretching band of the CO group disappears during replacement of the carbonyl group by TCNE. Only one broad cyano stretching frequency at 2225 cm^{-1} in both solid state and in solution is visible in the IR spectra. This gives evidence that the TCNE moiety is in fact π -bonded to the iron. The cyano stretching frequency is shifted to a lower wavenumber in comparison with the corresponding stretching frequencies for free TCNE, which can be interpreted in terms of the efficient back-donation from the filled metal *d*-orbitals on iron into the vacant π^* -orbital of TCNE. This back-donation results in a weakening of the $\text{C}\equiv\text{N}$ bond. X-ray crystal structures for compounds **1** and **2** were obtained, and a representative ball-and-stick model of structure **2** is shown in Fig. 1. From the crystal data, the dihedral angle between the plane containing $\text{C}(1)=\text{C}(2)$, that is perpendicular to the $\text{Fe}-\text{C}(1)-\text{C}(2)$ plane and the plane containing $\text{C}(1)-\text{C}(12)-\text{N}(12)$, and $\text{C}(11)-\text{N}(11)$ is 15.6° . This loss of planarity presumably results from the back-donation of electron density from the metal to the alkene π^* manifold.

The ^{13}C -NMR spectrum of **2** at room temperature showed pairs of cyano peaks at 113.1 ppm ($J_{\text{C-P}} = 4.0\text{ Hz}$) and 113.3 ppm ($J_{\text{C-P}} = 5.6\text{ Hz}$), in addition to the

Fig. 1 A ball-and-stick representation of the X-ray crystal structure of compound **2**

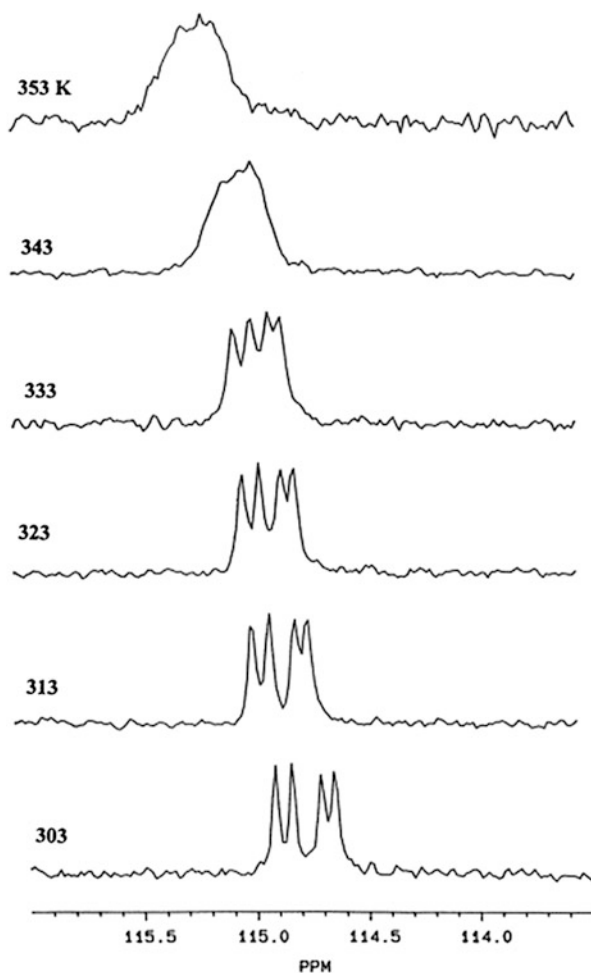


expected methoxy carbon at 55.3 ppm ($J_{C-P} = 6.5$ Hz). A very weak peak, due to relatively long relaxation time, at 29.0 ppm was also observed and was assigned to the ethylene carbons. Because of coordination to the iron center, the ethylene carbons are significantly shielded compared to those of free TCNE (112.6 ppm). This phenomenon was also observed in the ^{13}C NMR spectrum of **1**. The crystallographic data support these observations, especially the lengthening of the C(1)–C(2) distance in the π -bonded TCNE moiety relative to free TCNE. These chemical shifts are indicative of significant sp^3 -character at the olefinic carbons of the tetracyanoethylene moiety.

A shift of the two nitrosyl peaks to higher frequencies (1750 cm^{-1} and 1850 cm^{-1}) is also observed. This is explained by the electron-withdrawing effect of TCNE, which reduces back-bonding, which in turn strengthens the nitrosyl bond. The magnitude of this high frequency shift completely compensates for the bond weakening observed on initial incorporation of the phosphine or phosphite moiety. The average N–O distance in **2** (1.158 Å) is similar to the corresponding values found in **1** (1.169 Å) and $\text{Fe}(\text{NO})_2(\text{CO})_2$ (1.171 Å) [28]. This confirms that the electron-withdrawing effect of the TCNE moiety is sufficient to counteract the corresponding electron-donating strength of the phosphorus ligand, as compared to the $\text{Fe}(\text{NO})_2(\text{CO})_2$ reference.

Upon replacement of the carbonyl by TCNE, the reduction becomes irreversible. Table 2 lists the reduction potentials, E_{pc} , of complexes **2–5** at a scan rate of 100 mV/s. This reduction has no corresponding oxidation peak, even at a scan rate of 1 V/s, which indicates that the reduction is chemically irreversible at room temperature. Thus, the radical anion, $[\text{Fe}(\text{NO})_2\text{PR}_3(\eta^2\text{-TCNE})]^-$, decomposes rapidly to yield a decomposition product. The complexes **2–5** ($E_{pc} = -0.990\text{ V} \sim -1.146\text{ V}$) are harder to reduce than the free TCNE ligand ($E_{1/2} = -0.207\text{ V}$) but are easier to reduce than the

Fig. 2 Variable-temperature ^{13}C -NMR spectra of structure **1** in CD_3CN . Reprinted from Journal of Organometallic Chemistry Volume 550, A. Horsken, G. Zheng, M. Stradiotto, C. T.C. McCrory, L. Li "Iron Dinitrosyl Complexes of TCNE: A Synthetic, X-Ray Crystallographic High Field NMR and electrochemical Study." p 1–9, 1998, with permission from Elsevier



corresponding carbonyl compound, $\text{Fe}(\text{NO})_2(\text{PR}_3)(\text{CO})$ ($E^\circ = -1.96 \sim -2.15 \text{ V}$) [20]. The coordination of TCNE leads to a shift in the reduction potentials to a more negative value compared to free TCNE and to a more positive value in comparison with $\text{Fe}(\text{NO})_2(\text{PR}_3)(\text{CO})$. This indicates that the back-bonding from the iron center to the TCNE ligand is stronger than the characteristic covalent bonding arising from σ -donation by the TCNE ligand. This back-donation to the TCNE ligand renders the iron atom partially positive, and thereby easier to reduce. The reduction is presumed to occur at the iron center rather than on the TCNE ligand since the basicity of the phosphorus moiety has an impact on the electrochemical behavior of these compounds.

It is interesting to note that rotation along Fe-TCNE π -bond is restricted on the NMR time-scale. Variable-temperature ^{13}C NMR spectra were recorded as shown in Fig. 2. The peaks coalesce at about 70°C and is consistent with an activation

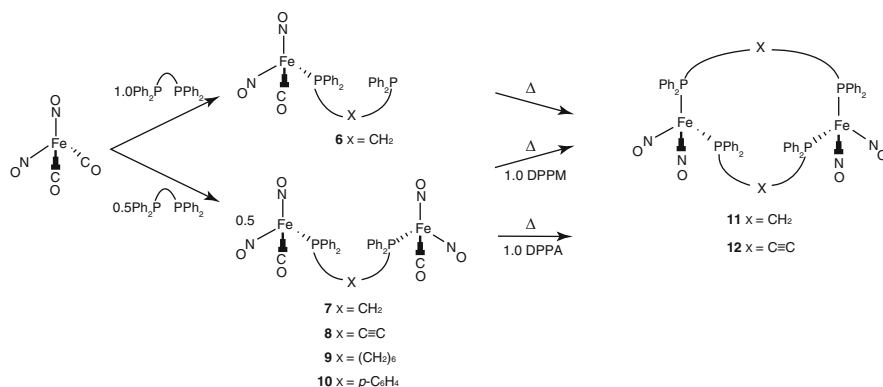
energy barrier of 18.1 kcal/mol. This is rather high compared to the published barriers for the rotation of coordinated olefins, which are typically between 12 and 15 kcal/mol. Clearly, the increased barrier to TCNE rotation is a reflection of the enhanced back-donation from metal *d*-orbitals into π^* of the alkene.

One crystallographic feature worthy of noting is that the two nitrosyl groups in **2** are nearly linear with angles of $175.1(7)^\circ$ and $172.6(6)^\circ$, while for **1**, angles of $178.0(5)^\circ$ and $165.8(5)^\circ$ were observed. The $\text{Fe}(\text{NO})_2$ unit is in an “*attracto*” conformation in **2** with O–Fe–O and N–Fe–N angles of 116.2° and 120.9° , respectively. “*Attracto*” conformations generally favor first row transition-metal dinitrosyls containing ligands that are good π -acceptors. The reverse conformation (O–M–O > N–M–N) is called “*repulso*” and is more common for the second-row and third-row transition metals [29]. For example, the N–M–N and O–M–O bond angles reported for $\text{M}(\text{NO})_2(\text{PPh}_3)_2$ complex are 139.2° and 142.7° when $\text{M} = \text{Ru}$ [30, 31] and 139.1° and 140.6° when $\text{M} = \text{Os}$ [32]. This is also true for the cationic species, $[\text{M}(\text{NO})_2(\text{PPh}_3)_2]^+$, where the reported N–M–N and O–M–O bond angles are 157.5° and 173.7° for Rh [33] and 154.2° and 167.5° for Ir [21], respectively. Five coordinated dinitrosyls also fit this correlation, indicating the conformation is an electronic rather than steric effect [34].

$(\text{NO})_2\text{FeP}\sim\text{PFe}(\text{NO})_2$: Despite the well-established history of dinuclear bis(phosphine) complexes in the field of inorganic chemistry, bis(dinitrosyliron) derivatives of this class are still rare and their properties remain essentially unexplored with the exception of a few select structures [35, 36]. Depending on the reaction conditions employed, either linear diiron constructs connected by one bis(phosphine) linker, $(\text{NO})_2\text{FeP}\sim\text{PFe}(\text{NO})_2$, or macrocyclic species spanned by two bridging ligands, $[(\text{NO})_2\text{Fe}]_2(\text{P}\sim\text{P})_2$, can be obtained [35].

Several different compounds including a mononuclear complex, $(\text{NO})_2\text{FeP}\text{--}\text{X}\text{--}\text{P}$ ($\text{X} = \text{CH}_2$, **6**), and several linear diiron species, $(\text{NO})_2\text{FeP}\text{--}\text{X}\text{--}\text{PFe}(\text{NO})_2$ ($\text{X} = \text{CH}_2$, **7**, $\text{C}\equiv\text{C}$, **8**, $(\text{CH}_2)_6$, **9**, and *p*- C_6H_4 , **10**), could be easily synthesized from $\text{Fe}(\text{NO})_2(\text{CO})_2$ via addition of the desired ligand (Scheme 2). From those compounds, the cyclic structures **11** and **12** can be synthesized. All of these species are air sensitive and will completely decompose after several hours. Decomposition occurs at a slower rate and is minimized when the compounds are stored in a proper degassed solvent or as a pure solid under a nitrogen atmosphere at ambient temperature.

The conversion of $\text{Fe}(\text{NO})_2(\text{CO})_2$ into compounds **6–10** and subsequently into **11** or **12** is readily monitored by the use of infrared spectroscopy; selected FT-IR data are listed in Table 3. The decrease in stretching frequencies observed for the carbonyl and the two nitrosyl ligands in **6–10**, relative to $\text{Fe}(\text{NO})_2(\text{CO})_2$, is characteristic of phosphine substituted dinitrosyl iron complexes. In turn, the nitrosyl stretching frequencies observed for both **11** and **12** appear at even lower wavenumbers. The macrocyclic DPPM-supported complex, **11**, exhibits four distinct IR absorptions (1733 , 1721 , 1687 , and 1668 cm^{-1}) in the solid state and in solution, possibly arising from the interaction of the $\text{Fe}(\text{NO})_2$ centers, as has been observed in other cyclic systems [37, 38]. This phenomenon appears to depend on ring size, as the related ten-membered ring compound, **12**, displays only two nitrosyl stretching signals



Scheme 2 Generalized synthetic pathway to compounds **6–12**

Table 3 Nitrosyl and carbonyl IR stretching frequencies for species **6–12** (KBr pellet)

Compound	ν_{CO} (cm^{-1})	ν_{NO} (cm^{-1})
[Fe(DPPM)(NO) ₂ (CO)], 6	2014, 1994, 2005 ^a	1763, 1720 (s), 1700, 1761, ^a 1718 ^a
[Fe ₂ (μ -DPPM)(NO) ₄ (CO) ₂], 7	2005, 2004 ^a	1760, 1719 (s), 1702, 1764, ^a 1718 ^a
[Fe ₂ (μ -DPPA)(NO) ₄ (CO) ₂], 8	2020, 2005	1767, 1716
[Fe ₂ (μ -DPPH)(NO) ₄ (CO) ₂], 9	1999	1755, 1701
[Fe ₂ (μ -DPPB)(NO) ₄ (CO) ₂], 10	2009, 1999	1760, 1707
[Fe ₂ (μ -DPPM) ₂ (NO) ₄], 11	–	1733, 1721, 1687, 1668
[Fe ₂ (μ -DPPA) ₂ (NO) ₄], 12	–	1723, 1679

^aMeasured in THF solution

(1723 and 1679 cm^{-1}) in both the solid and liquid states. Based on the observed IR frequencies, the nitrosyl groups are best described as linear donating NO^+ fragments (vide infra). The formation of **6–12** was also followed by the use of NMR spectroscopy, and each of the dinuclear compounds **7–12** exhibits a single ^{31}P NMR resonance in the range of 33–57 ppm, consistent with a disubstituted bis(phosphine) complex.

X-ray crystallographic studies of compounds **7**, **8**, **11**, and **12** were conducted and the thermal ellipsoid plots of the refined molecular structures of the DPPM compounds **7** and **11** appear in Figs. 3 and 4, respectively. The iron centers in all four of the crystallographically characterized compounds possess distorted tetrahedral geometries, a structural feature that is common to dinitrosyliron complexes. The iron–iron distances in both the linear (**7**, ~ 5.2 Å; **8**, ~ 7.6 Å) and macrocyclic (**11**, ~ 4.4 Å; **12**, ~ 7.0 Å) compounds are all significantly longer than the related distances found in other structurally characterized species that are described as possessing a metal–metal bond. The crystallographically determined structures of the linear species, **7** and **8**, can be compared with that of [Fe(NO)₂Cl]₂(μ -DPPE) (DPPE = 1,2-bis(diphenylphosphino)ethane), where DPPE stands as a single bridge joining the two metal centers [35].

Fig. 3 An X-ray crystallographic representation of species **7** with thermal ellipsoids drawn at 50%. Hydrogen atoms are eliminated for clarity

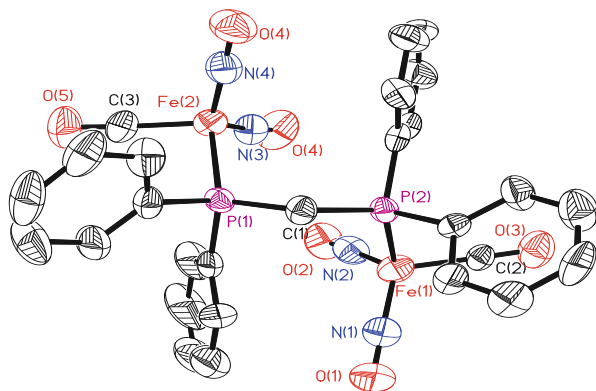
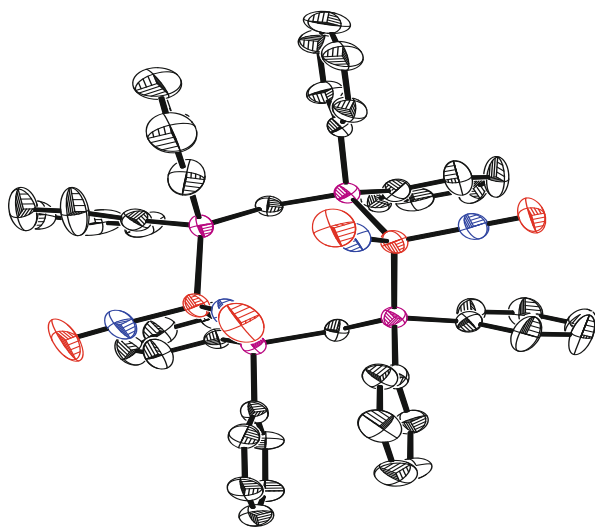
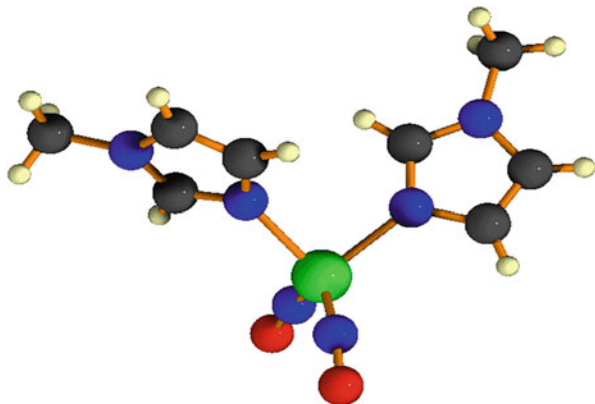


Fig. 4 An X-ray crystallographic representation of species **11** with thermal ellipsoids drawn at 50%. Hydrogen atoms are eliminated for clarity



Despite the range in N–Fe–N angles (115.6° to 126.5°), all eight of the $\text{Fe}(\text{NO})_2$ units in compounds **7**, **8**, **11**, and **12** exhibit “attracto” conformations where the N–Fe–N angle is greater than the $> \text{O–Fe–O}$ angle. The observation of contracted Fe–N distances (~ 1.64 to ~ 1.73 Å) and lengthened N–O bonds (~ 1.16 to ~ 1.20 Å) in these complexes indicates significant iron-nitrosyl multiple bond character, arising due to appreciable back-donation from the iron fragment into the π^* -orbital on the nitrosyl ligand. By comparison, Ray et al. reported crystallographic data for a series of trigonal bipyramidal, iron nitrosyl complexes, in which the Fe–N(O) and N–O distances are in the range of ~ 1.73 – 1.75 Å and ~ 1.12 – 1.15 Å, respectively [39]. These X-ray structural data and the IR results suggest that the NO units in **7**, **8**, **11**, and **12** function as three-electron donors. Compounds **8** and **12** represent the first examples of crystallographically characterized species containing the $\text{Fe}(\text{NO})_2(\mu\text{-DPPA})$.

Fig. 5 A ball-and-stick representation of the X-ray crystal structure of complex **13**



2.3 Nitrogen-Based Ligands

Dinitrosyl iron complexes in biological systems have been investigated intensively by EPR techniques and usually exhibit a characteristic isotropic g -factor of 2.03 [21, 31–43]. Three types of EPR-active “ $g = 2.03$ ” complexes have been identified in mammalian ferritins, which have been attributed to iron-nitrosyl complexes with imidazole groups of histidine, thiol groups of cysteine, and carboxylate groups of aspartate and glutamate [44]. While there are plenty of examples of in situ characterization by IR or EPR spectroscopy, the isolation and structural determination of these compounds are both extremely tedious and difficult. It was not until 1994 that the first “ $g = 2.03$ ” species, $\text{Fe}(\text{NO})_2(1\text{-MeIm})_2$, **13**, was isolated [45]. Since then, other structures utilizing ligands pertaining to the imidazole family [46, 47] or containing metals other than iron [48] have been reported. In this section, the physical and chemical properties of several well-studied structures are thoroughly examined. General synthesis steps and some spectroscopic data are given for other representative compounds in order to demonstrate the array of structures that have been synthesized so far.

$\text{Fe}(\text{NO})_2(1\text{-MeIm})_2$: Single crystals of structure **13** suitable for X-ray analysis were obtained from diethyl ether by mixing a 1:1 ratio of DDI with 1-methylimidazole. The X-ray crystal structure is shown in Fig. 5. The complex is pseudo-tetrahedral with a d^{10} iron center. The nitrosyl groups are linear with Fe-N-O angles of 167.5° and 170.1° and are displaced at the $\text{N}(\text{NO})\text{-Fe-N}(\text{Im})$ angles of 111.3° and 107.8° away from the imidazole ligands. The $\text{Fe-N}(\text{NO})$ bond distances are 1.648 and 1.650 Å. The Fe-N-O groups are bent symmetrically, with a O-Fe-O angle of 107.3° as compared to the $\text{N}(\text{NO})\text{-Fe-N}(\text{NO})$ angle of 116.6° . This is considered an “attracto” conformation because the N-M-N bond angle is less than 130° and the two oxygen atoms bend towards each other. The $\text{Fe-N}(\text{Im})$ bond distances are 2.048 and 2.044 Å. The horizontal plane through each 1-methylimidazole ligand is skewed 106.7° away from the other [45].

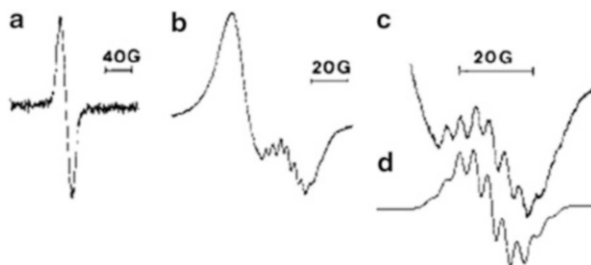


Fig. 6 The evolution of $\text{Fe}(\text{NO})_2(\text{Me-Im})_2^+$ upon addition of Me-Im to a solution of $\text{Fe}(\text{CO})_2(\text{NO})_2$. Reprinted with permission from N. Reginato, C.T.C. McCrory, D. Pervitsky and L. Li. 1999. *J. Am. Chem. Soc.* 121, pp. 10217-10218. Copyright 1999 American Chemical Society

Table 4 A list of EPR parameters measured at 240 K and IR stretching frequencies of the isolated product

Compound	g -value	a_{N} (G)	ν_{NO} (cm^{-1})
$\text{Fe}(\text{NO})_2(\text{1-MeIm})_2^+$	2.0151	$a_{\text{N}1} = 3.60, a_{\text{N}2} = 3.90$	1673, 1616
$\text{Fe}(\text{NO})_2(\text{4-MeIm})_2^+$	2.0338	$a_{\text{N}1} = 2.33, a_{\text{N}2} = 2.64$	1677, 1620
$\text{Fe}(\text{NO})_2(\text{Im})_2^+$	2.0337	$a_{\text{N}1} = 2.28, a_{\text{N}2} = 2.44$	1680, 1622
$\text{Fe}(\text{NO})_2(\text{BenzIm})_2^+$	2.0341	$a_{\text{N}1} = 1.97, a_{\text{N}2} = 2.12$	1682, 1625
$\text{Fe}(\text{NO})_2(\text{5,6-dimethylBenzIm})_2^+$	2.0352	$a_{\text{N}1} = 1.88, a_{\text{N}2} = 2.04$	1683, 1625
$\text{Fe}(\text{NO})_2(\text{L-Histidine})_2^+$	2.0222	$a_{\text{N}1} = 2.66, a_{\text{N}2} = 3.01$	–

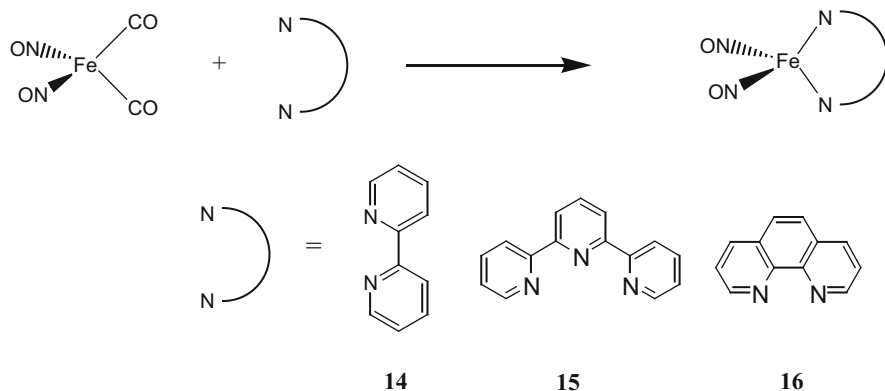
The reaction of $\text{Fe}(\text{NO})_2(\text{CO})_2$ with L-histidine and a series of substituted imidazoles, such as 1-methylimidazole, 4-methylimidazole (4-MeIm), imidazole (Im), benzimidazole (BenzIm), and 5,6-dimethylbenzimidazole (Me_2BenzIm) were also investigated by EPR spectroscopy in order to establish the validity of using this ligand as the biomimetic model. Figure 6 shows a typical reaction monitored by EPR spectroscopy. The starting material, $\text{Fe}(\text{NO})_2(\text{CO})_2$, underwent an auto-oxidation in the solution and produced a broad singlet with $g = 2.0275$ and $\Delta H_{\text{pp}} = 18.5$ G corresponding to $[\text{Fe}(\text{NO})_2(\text{CO})_2]^+$. Upon the addition of one of the ligands, a new set of signals, corresponds to the 17e species, overlapping with the broad singlet was observed after approximately 15 min. A list of the EPR parameters measured at 240 K in solution and some of the IR stretching frequencies of the isolated product are shown in Table 4. The g -values for the imidazole and substituted imidazole radicals fall in the range of 2.0151–2.0338. Computer simulations gave rise to two sets of equivalent nitrogens (^{14}N , $I = 1$) and a_{N} in the range of 2.28–3.90 G. The hyperfine structure is due to coupling of two equivalent ^{14}N nuclei from the nitrosyls and two equivalent ^{14}N nuclei from the 1-MeIm, yielding a structure of $\text{Fe}(\text{NO})_2(\text{1-MeIm})_2^+$. For benzimidazole and substituted benzimidazole, the g -values are slightly higher (2.0341–2.0352) while the a_{N} values are smaller (1.88 G–2.12 G). For L-histidine, both g -value (2.0222) and hyperfine couplings (2.66 G and 3.01 G) fall in the range of substituted imidazoles.

FT-IR investigations showed that upon addition of the imidazole ligands to $\text{Fe}(\text{NO})_2(\text{CO})_2$, the ν_{NO} 's were lowered by approximately 140 wavenumbers and no carbonyl stretching frequencies were observed. This indicates that two Im ligands had replaced the two CO ligands. The nitrosyls fall into the region of $1650\text{--}1940\text{ cm}^{-1}$, indicating they are linear. Table 4 lists the NO stretching frequencies observed for these complexes. Addition of 1-MeIm shifted the IR stretching frequencies of the nitrosyl groups from 1810 and 1767 cm^{-1} [ν_{NO} for $\text{Fe}(\text{NO})_2(\text{CO})_2$] to 1673 and 1616 cm^{-1} , suggesting that 1-MeIm acts as a strong σ -donor. To explain the trend in the IR stretching frequencies, EHMO calculations were made. The results show that the LUMO of the $\text{Fe}(\text{NO})_2$ unit has more contribution to the overall molecular orbitals. Thus, effectively, imidazole units act as electron donors to the LUMO of $\text{Fe}(\text{NO})_2$ fragment.

$\text{Fe}(\text{NO})_2(\text{N},\text{N}'\text{-chelate})$: Despite the fact that coordination of N,N' -chelating ligands to transition metals is very common, only a limited number of examples on isolated iron-nitrosyl with nitrogen donor ligands involving N,N' -chelation could be found. Earlier work includes: a reaction of $[\text{Fe}(\text{NO})_2\text{Cl}]_2$ with 1,4,-diaz-1,3-butadiene, which yielded a DNIC with N,N' -chelation [49], a salt $[\text{Fe}(\text{bipy})_3][\text{Fe}(\text{NO})_2\text{Cl}_2]_2$, which was isolated by using large excess of bipy vs. $[\text{Fe}(\text{NO})_2\text{Cl}]_2$ (10:0.75) [50], and $[(\text{sparteine})\text{Fe}(\text{NO})_2]$ was prepared by reacting sparteine with $\text{Fe}(\text{CO})_2(\text{NO})_2$ [51].

Recently, we reported the synthesis, structures, and spectroscopic and electrochemical properties of three new dinitrosyl iron complexes with bidentate $[\text{N},\text{N}]$ chelating ligands; 2,2'-bipyridine, **14**, 2,2',2''-terpyridine, **15**, and 1,10-phenanthroline, **16** [52]. Complexes **14–16** were prepared by mixing 1:1 ratio of $\text{Fe}(\text{NO})_2(\text{CO})_2$ and the proper chelating ligands, bipy, terpy, and phen in THF and was stirred 48 h at room temperature under nitrogen atmosphere as shown in Scheme 3 (yields between 82 and 88%). X-ray quality single crystals of **14** and **15** were obtained by slow evaporation of either THF or methanol. Complexes **14–16** are stable in the solid state under nitrogen, and all three complexes are relatively soluble in most polar organic solvents including dichloromethane, methanol, and THF but are insoluble in diethyl ether and hexane.

Similar to the imidazole-based ligands, upon reacting, the typical carbonyl stretching frequencies from $\text{Fe}(\text{NO})_2(\text{CO})_2$ disappeared, indicating that both carbonyl groups are replaced by the bidentate ligands 2,2'-bipyridine, 2,2',2''-terpyridine, or 1,10-phenanthroline as observed in the crystal structures. In the meantime, the characteristic IR absorptions of nitrosyl groups (ν_{NO} , $1807, 1760\text{ cm}^{-1}$) shifted $\sim 120\text{--}146\text{ cm}^{-1}$. These values are located in the range of NO^+ , suggesting again that these nitrogen-containing ligands act as strong σ donors rather than π -acceptors. The peaks close to 1619 cm^{-1} , 1621 cm^{-1} , and 1614 cm^{-1} in complexes **14–16** are assigned to the coordinated bidentate ligands by comparing them with the IR spectra of the free ligands. The characteristic nitrosyl stretching frequencies are similar to the reported values for the mononuclear metal complex $\text{Fe}(\text{NO})_2(\text{sparteine})$ [44] and for $\text{Fe}(\text{NO})_2(1\text{-MeIm})_2$ [38]. However, they are clearly lower than the values 1774 cm^{-1} , 1712 cm^{-1} for the anionic complex $[\text{Fe}(\text{NO})_2(\text{Im-H})_2]^-$ [53], and 1796 cm^{-1} , 1726 cm^{-1} for the tetranuclear iron complex $[\text{Fe}(\text{NO})_2(\text{Im-H})]_4$ (Im-H = imidazolate). The results show that the NO stretching frequencies are related to the



Scheme 3 Synthesis scheme for compounds **14–16**

oxidation levels of dinitrosyl iron complexes and the observed ν_{NOs} in complexes **14–16** make them $\{\text{Fe}(\text{NO})_2\}^{10}$ according to the Enemark-Feltham notation [54].

These complexes are diamagnetic thus, well-resolved $^1\text{H-NMR}$ and $^{13}\text{C-NMR}$ spectra were recorded in DMSO. The NMR results indicate that both complexes **14** and **16** possess high symmetry. Four sets of resonances between 7.54 and 8.66 ppm were observed in the $^1\text{H-NMR}$ of complex **14**, and five distinct peaks in the aromatic carbon region for the $^{13}\text{C-NMR}$, which corresponds to the coordinated bipy ligand. Complex **16** exhibits four sets of resonances between 7.74 and 8.86 ppm with two of them very close to each other and the $^{13}\text{C-NMR}$ shows six distinct carbons which correspond to the protons and carbons in the coordinated phen ligands, respectively. On the contrary, complex **15** displays seven sets of resonances between 7.07 and 9.21 ppm, which are attributed to the magnetic inequivalence of the three pyridyl rings in the terpy ligand, meaning this compound bears low symmetry. These observations are consistent with the results found in the crystal structures of complexes **14** and **15**. These show that the two NOs are symmetrically located on two sides of $\text{Fe}(\text{bipy})$ plane in complex **14**, while in complex **15**, the two NOs are distributed in two sides of plane consisted of Fe and two coordinated pyridyl rings but almost parallel to the uncoordinated pyridyl ring.

As shown in the X-ray crystal structures (Fig. 7), complex **14** crystallizes in triclinic $P-1$ space group and the asymmetric unit consists of one $\text{Fe}(\text{NO})_2(\text{bipy})$ molecule with NO groups in the two sides of $\text{Fe}(\text{bipy})$ plane, while complex **15** crystallizes in monoclinic $P21/n$ space group. In both cases, the iron center is connected to four nitrogen atoms, which include two from the nitrosyls and two nitrogen atoms from the ligands, with a pseudo-tetrahedral geometry. In complex **15**, the uncoordinated pyridyl is perpendicular to the plane consisted of iron atom and two coordinated pyridyl rings, but almost parallel to the $\text{Fe}(\text{NO})_2$ plane.

The average $\text{Fe-N}_{(\text{NO})}$ and $\text{Fe-N}_{(\text{N,N-L})}$ bond lengths are 1.650 Å and 2.046 Å for complex **14** and 1.648 Å and 2.048 Å for **15**, respectively. The average $\text{Fe-N}_{(\text{NO})}$ bond distance of 1.649 Å is similar to those reported in other mononuclear

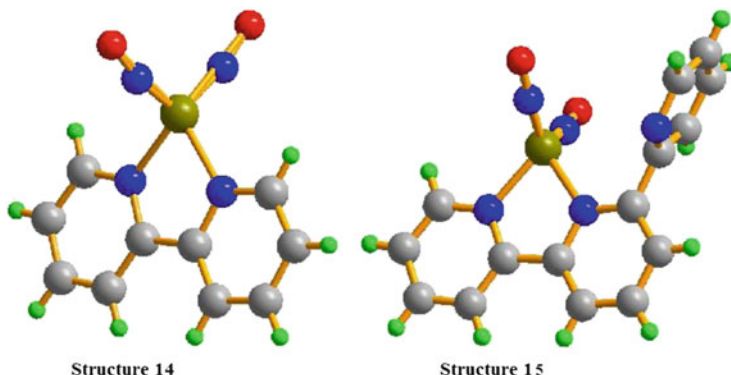


Fig. 7 Ball-and-stick representations of the X-ray crystal structures of complexes **14** and **15**. Reprinted with permission from R. Wang, X. Wang, E. B. Sundberg, P. Nguyen, G. Paola, G. Grant, C. Sheth, Q. Zhao, S. Herron, K. A. Kantardjieff, and L. Li. 2009. *Inorg. Chem.* 48, pp 9779–9785. Copyright 2009 American Chemical Society

complexes but is clearly shorter than those found in the tetranuclear $[\text{Fe}(\text{NO})_2(\text{Im-H})_4]$ (Im-H = imidazolate) and the dinuclear complexes, $[(\text{N}_2\text{C}_5\text{H}_7)\text{Fe}(\text{NO})_2]_2$ ($\text{N}_2\text{C}_5\text{H}_7 = 3,5\text{-dimethylpyrazolyl}$). The average Fe–N–O bond angle of 167.9° is thought to be close to linear formation, indicating that the nitrosyl moieties exhibit *sp* hybridized NO^+ character in complex **14**, while the $\text{N}_{(\text{N},\text{N-L})}\text{--Fe1--N}_{(\text{N},\text{N-L})}$ bond angle of 78.4° shows that the Fe(N4) possesses severe distorted tetrahedral environment.

Complexes **14** and **15** also exhibit “attracto” conformations with the Fe–N–O groups symmetrically bent with the average $\text{O}_{(\text{NO})}\text{--Fe--O}_{(\text{NO})}$ and $\text{N}_{(\text{NO})}\text{--Fe--N}_{(\text{NO})}$ angles of 104.1° and 114.6° , respectively. In both complexes **14** and **15**, Fe–N_(NO) bond distances are all clearly shorter than Fe–N_(N,N-L) distances, indicating the NO groups are much better π -acceptors than either 2,2'-bipyridine or 2,2',2''-terpyridine.

Both complexes **14** and **15** reveal a layering effect on the crystal packing diagrams, in which different layers interact by the π - π stacking and H-bonding effects (Fig. 8). Both molecules of different layers are staggered with the iron nitrosyls in the opposite sides. The uncoordinated pyridyl groups are clearly oriented away from each other in **15**. Interestingly, in both complexes, the aromatic rings almost completely overlap, which is expected because the space hindrance is compensated by the H-bonding interactions of nitrogen and oxygen atoms of nitrosyls with the hydrogen atoms from the adjacent bipyridine or pyridyl ligands. The distances between the planes are 3.5880 \AA and 3.4254 \AA for **14** and **15**, respectively. This indicates that there are quite strong π - π stacking interactions between the two bipyridine ligands and the two coordinated pyridyl rings of terpyridine ligands. However, almost no interactions are observed between the adjacent uncoordinated pyridyls.

The electronic absorption spectra of complexes **14–16** are recorded and the data are shown in Table 5 together with cyclic voltammetry (CV) results. The relative

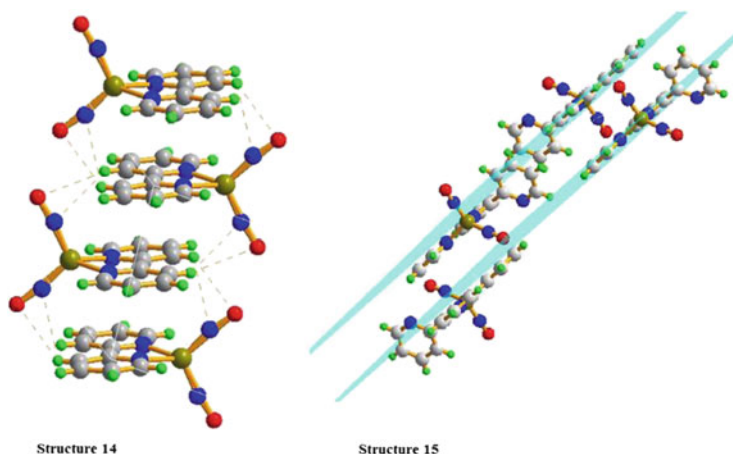


Fig. 8 Ball-and-stick representations of the molecular packing in the crystal structures of **14** and **15**. Reprinted with permission from R. Wang, X. Wang, E. B. Sundberg, P. Nguyen, G. Paola, G. Grant, C. Sheth, Q. Zhao, S. Herron, K. A. Kantardjieff, and L. Li. 2009. *Inorg. Chem.* 48, pp 9779–9785. Copyright 2009 American Chemical Society

Table 5 List of electrochemical redox potentials and the UV–vis absorptions of complexes **14–16**

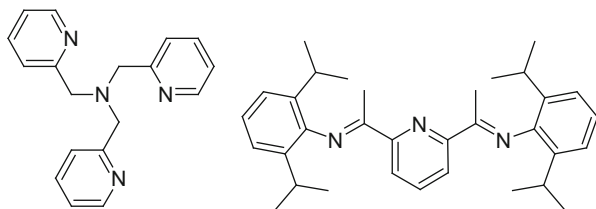
Complex	$E^{\circ}_{1/2, \text{expt}}$ (V) (vs. Fc^+/Fc)		Absorptions
$\text{Fe}(\text{NO})_2(\text{N}_2\text{C}_{10}\text{H}_8)$, 14	−0.48	−2.07	221(s), 245(m), 294(m), 390(w), 471(w)
$\text{Fe}(\text{NO})_2(\text{N}_3\text{C}_{15}\text{H}_{11})$, 15	−1.09	−1.85 ^a	211(s), 272(m), 304(m), 374(w) 470(w)
$\text{Fe}(\text{NO})_2(\text{N}_2\text{C}_{12}\text{H}_8)$, 16	−0.50	−1.80 ^a	212(s), 224(s), 271(m), 389(w), 470(w)

^aIrreversible redox of a solvated species

low-energy absorption bands at 374–471 nm can be assigned mainly to the MLCT ($d_{\text{Fe}}-\pi^*_{\text{NO}}$, $d_{\text{Fe}}-\pi^*_{\text{N,N-L}}$), while the absorptions at higher energy are attributed to combined contributions from LMCT ($\pi^*_{\text{NO}}-d_{\text{Fe}}$, $\pi^*_{\text{N,N-L}}-d_{\text{Fe}}$), π_{NO} ($\pi_{\text{N,N-L}}$) $\rightarrow d_{\text{Fe}}$, $\pi_{\text{NO}} \rightarrow \pi^*_{\text{NO}}$, and ligand-localized transitions of the coordinated [N,N] ligands, $\pi_{\text{N,N-L}} \rightarrow \pi^*_{\text{N,N-L}}$.

As shown in Table 5, complex **14** exhibits two quasi-reversible one-electron reductions at −0.48 V and −2.07 V [versus $E_{1/2}^{\circ}(\text{Cp}2\text{Fe}/\text{Cp}2\text{Fe}^+)$], while complexes **15** and **16** show two quasi-reversible one-electron reductions at −1.09 V, −2.07 V and −0.50 V, −2.05 V, and one irreversible reduction at −1.85 V and −1.80 V, respectively. The first reductions of all complexes are assigned to the $[\text{LFe}(\text{NO})_2]/[\text{LFe}(\text{NO})_2]^-$ couple, while the reductions close to −2.07 V are believed to be the usual ligand-based reductions. The half-wave potential of the first reduction peak for complex **15** is clearly more negative than the corresponding values for complexes **14** and **16**, showing that complex **15** is more difficult to reduce. It is consistent with the greater electron donor effect of the uncoordinated pyridyl ring in complex **15**. The results indicate that the electronic property of the ligands has important influence on the electrochemical properties of the relevant complexes.

Fig. 9 Structures for TPA and PDI ligands



[(TPA)Fe(NO)₂][BF₄] and [(PDI)Fe(NO)₂][BF₄]: Several new structures have been synthesized that result in 5 and 6 coordinate compounds [55]. These structures make use of a single ligand, which contains three or four nitrogen atoms that all coordinate with the metal center. The structures of these ligands are shown in Fig. 9. The first compound was synthesized by 1:1 ratio of tris(2-methylpyridine)amine (TPA) ligand and [Fe(CO)₂(NO)₂][BF₄] in THF at 0°C. This reaction led to a product containing two IR ν_{NO} stretching frequencies at 1720 and 1619 cm^{-1} . This cationic six-coordinate [(NO)₂Fe(TPA)][BF₄] molecule was characterized using several different methods. In a similar fashion as above, a five-coordinate DNIC was also be synthesized by 1:1 ratio of Fe(CO)₂(NO)₂ with 2,6-bis[1-(2,6-diisopropylphenylimino)ethyl]pyridine (PDI). This reaction generated a cationic five-coordinate [(NO)₂Fe(PDI)][BF₄] molecule. The IR stretching frequencies (ν_{NO} 1794 s, 1721 s cm^{-1}) imply the formation of the five-coordinate DNIC, coordinated by the tridentate PDI ligand. It was noticed that the IR spectra of the six-coordinate, five-coordinate, and four-coordinate DNICs ([Fe(NO)₂L₂] (L=thiolate, imidazolate)) all had the same peak patterns but differed in the position of ν_{NO} and the separation of q_{NO} in the NO stretching frequencies (q_{NO} , ~101 cm^{-1} for six-coordinate vs. ~73 cm^{-1} for five-coordinate vs. ~60–45 cm^{-1} for four-coordinate DNICs). Interestingly, several other 4 and 5 coordinate nitrosyl complexes have also been synthesized using cobalt instead of iron [56].

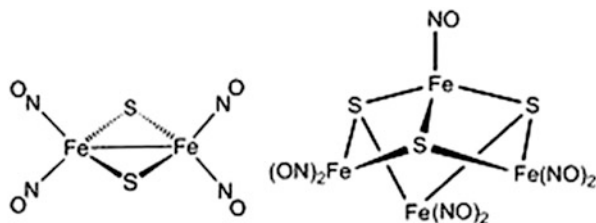
While the majority of metal dinitrosyl complexes have ligands containing phosphorus, nitrogen, or sulfur atoms, coordination of other ligands such as oxygen or arsenic has become more common [44, 57]. Recent work is also focusing on compounds that are harder to synthesize, like those involving rare or radioactive metals [58, 59], or the isolation of unstable products with metals that usually do not form nitrosyls such as copper [60] while other molecules are synthesized for their specific abilities, such as hydrogen bonding [61].

3 Nitrosyl Complexes Containing Two or More Metal Centers

3.1 Complexes Containing “M₂S₂” Core

Sulfur-containing ligands have been known to coordinate with the [M(NO)₂] unit for some time. These complexes were discovered as being bound to the cysteine

Fig. 10 Roussin's Red and Black Salt Structures

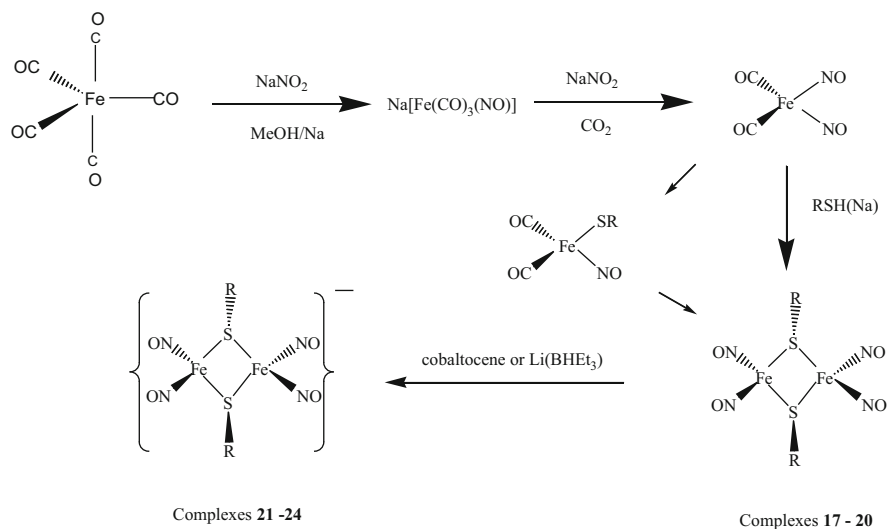


residues of proteins within body tissues. It was also found that proteins containing [Fe–S] clusters, such as rubredoxin and ferredoxin, can react with nitric oxide to form protein-bound DNICs and Roussin's Red Ester types of complexes [62]. The dinitrosyl iron complexes and RREs were found to be interchangeable when binding to proteins. These molecules were tested for their effects on tumor cell growth and were found to be efficient NO donors that lead to eventual cell death [63].

RREs and RBEs are a class of compounds frequently used as a starting material in the synthesis of novel metal nitrosyl complexes (Fig. 10). Many structures resembling Roussin's Red and Black Esters have been prepared [64–70]. RREs may be synthesized through the alkylation of Roussin's Red Salt (RRS) with an alkyl halide or treatment of $\text{Fe}_2(\mu\text{-I})_2(\text{NO})_4$ with an organic thiol compound in the presence of a proton acceptor [71]. Many substituted complexes are also generated by reacting DDI with the proper ligand under an inert atmosphere [72, 73] or by reacting a protein containing a biological Rieske center with nitric oxide [74]. A wide variety of structures mimicking Rieske centers have also been reported [73, 75–80]. Ford and others studied the photochemical NO release of RREs and found that the photochemical response and the light harvesting ability improved when the R groups were changed [70, 81, 82]. Here, several structures are discussed in depth to illustrate the chemical and physical characteristics. General synthesis steps for several other compounds are also given in order to display the wide variety of structures discovered in the past decade.

[Fe₂(μ-RS)₂(NO)₄]: The Roussin's Red Salt Esters [Fe₂(μ-RS)₂(NO)₄] (R = *n*-Pr, **17**, *t*-Bu, **18**, 6-methyl-2-pyridyl, **19**, and 4,6-dimethyl-2-pyrimidyl, **20**), were prepared by mixing Fe(NO)₂(CO)₂ with equal molar of the corresponding ligands, 1-propanethiol, 2-methyl-2-propanethiol, 4,6-dimethyl-2-mercaptopyrimidine, or 6-methyl-2-mercaptopyridine in CH₂Cl₂ in the presence of potassium carbonate and was stirred 72 h at ambient temperature under nitrogen atmosphere (Scheme 4) [72]. The reaction solution was filtered to remove undissolved potassium carbonate, and methanol was slowly added to the filtrate, then the mixed solution was kept at –35°C overnight to crystallize. Black crystals suitable for X-ray crystallography were collected by filtration and washed with methanol. The solids were dried under vacuum for several hours and yields ranging from 49% to 69% were obtained [72].

Another method of preparing **18** was also reported, in which Fe(NO)₂(CO)₂ and sodium 2-methyl-2-propanethiolate were dissolved in methanol and stirred 48 h at room temperature under nitrogen atmosphere. The solution turned from green to dark brown. The reaction solution was filtered and recrystallized from a mixture of CH₂Cl₂ and methanol.



Scheme 4 A general synthesis method for complexes **17–24**

These complexes are soluble in common organic solvents such as CH_2Cl_2 , THF, and acetone. The infrared spectra of **17–20** were studied in both KBr pellets and in THF solution, as shown in Fig. 11. The characteristic carbonyl stretching frequencies disappeared, indicating that both carbonyl groups were replaced by the sulfur-containing ligands, while the typical IR absorptions of nitrosyl groups (ν_{NO}) shift from 1807, 1760 cm^{-1} to 1805–1823, 1770–1793, and 1743–1759 cm^{-1} , suggesting that these sulfur-containing ligands only act as weak electron donors.

In solution, complexes **17–20** display one weak and two strong NO stretching frequencies. However, in the solid state, only two strong NO stretching frequencies were observed. It was proposed that in solution, the *cis*- and *trans*-isomers coexist, while in the solid state, only *trans*-isomers are present. To explain the vibrational modes, frequency calculations using density functional theory (DFT) were carried out for *cis*- and *trans*-isomers using complex **17** as a model. The calculated results for the *cis*-isomer show four different vibrational modes, which correspond to the two symmetric and two anti-symmetric vibration modes, whereas the *trans*-isomer results in only two vibrational modes derived from two anti-symmetric vibrational modes. The bands at 1775 and 1748 cm^{-1} are the result of the overlap of those bands derived from symmetric and anti-symmetric vibration modes of the *cis*- and *trans*-isomers, but the band at 1810 cm^{-1} is only derived from one of symmetric vibration modes of *cis*-isomer. Hence, these complexes actually show only three vibrational bands for the NO moieties in the experimental solution IR spectra, as shown in the theoretical simulation in Fig. 12.

Geometry optimizations using density functional theory (DFT) were also performed on the *cis*- and *trans*-isomers of complex **17** and the results showed that the energy difference is only about 3 kcal/mol, as shown in Fig. 13. Such a

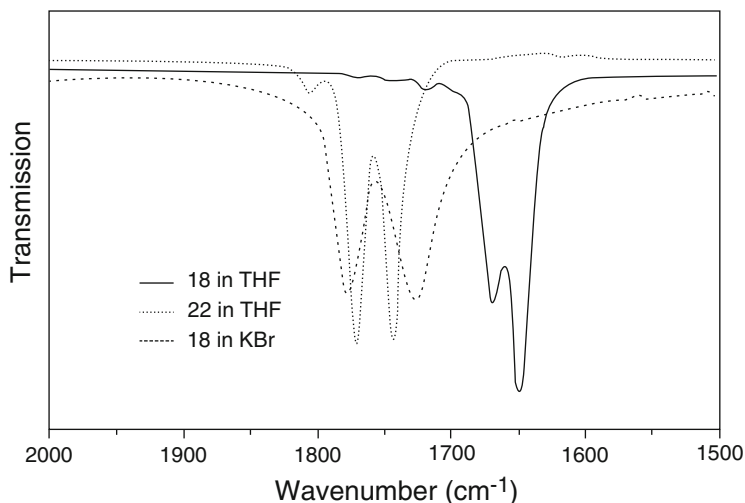


Fig. 11 Infrared spectra of the nitrosyl stretching region of complexes **18** and **22**

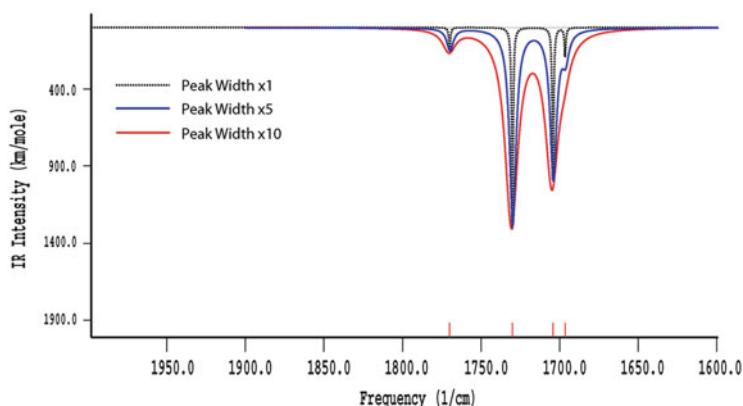


Fig. 12 Theoretical IR simulation of NO stretching frequencies

small energy difference of two spatial isomers could easily be supplied by the solvent in solution, which allows both isomers to coexist. Indeed, experimentally, with the increase of spatial hindrance of the R group from complex **17** to **20**, the intensity of the weak absorption band at $\sim 1810\text{ cm}^{-1}$ derived from the *cis*-isomer gradually decreases in comparison with two strong ones in both THF and CH_2Cl_2 solution. In solid state, complexes **17–20** only contain the *trans*-isomer as shown by the X-ray crystal structures; hence, their IR spectra only display two strong NO stretching frequencies (Fig. 14).

The redox behavior of complexes **17–20** was studied by cyclic voltammetry (CV) in CH_2Cl_2 . All of the complexes exhibited irreversible oxidations, which is consistent with the fact that these complexes are very unstable in air. As shown in

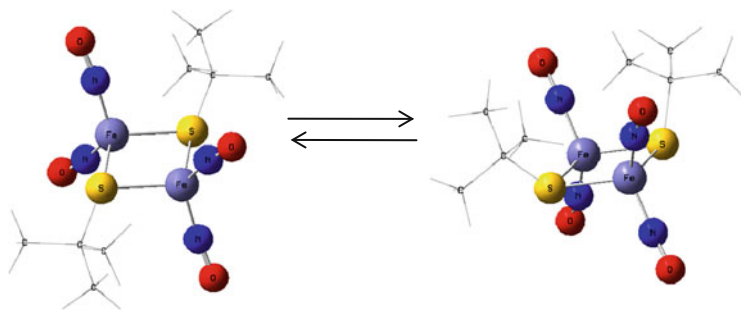


Fig. 13 Geometry optimizations using DFT showing conversion of the *cis*- and *trans*-isomers of complex **17**

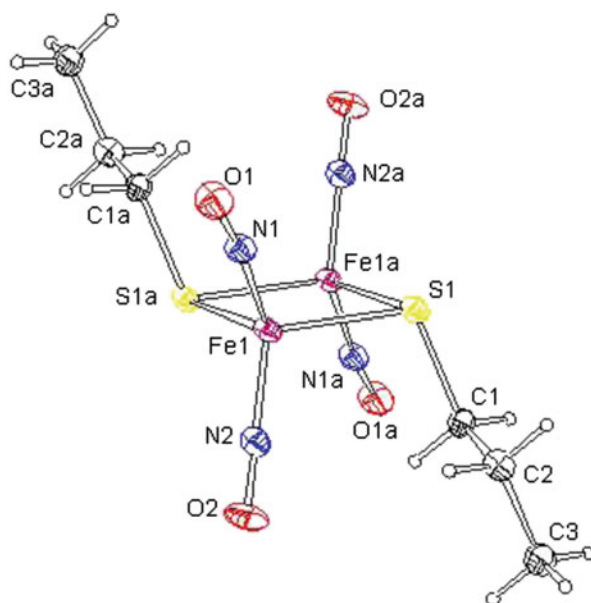
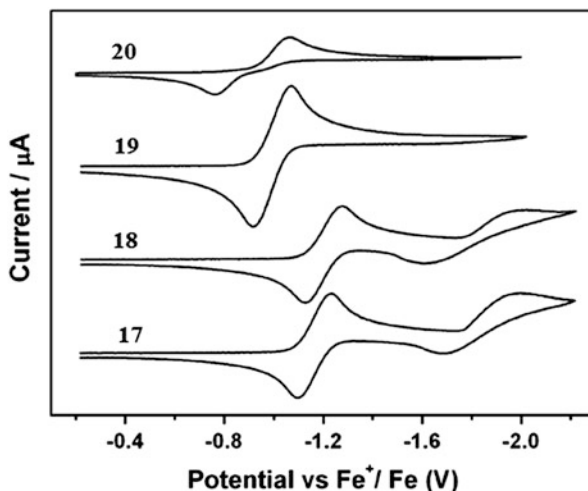


Fig. 14 The molecular structure of complex **17** with thermal ellipsoids drawn at the 30% probability displaying the chair shape and the *trans*-isomer found in the solid state

Fig. 15, complexes **17** and **18** exhibit two quasi-reversible one-electron reductions at -1.16 , -1.84 V and -1.20 , -1.81 V, respectively, but complexes **19** and **20** only show one quasi-reversible one-electron reduction at -0.99 and -0.91 V, respectively. All of these reductions can be attributed to iron–sulfur-based redox processes. The half-wave potentials for the first reduction peak clearly turn to more positive values in the order of complex **18**, **17**, **19**, and **20**, showing these complexes are easier to reduce along the sequence. This is consistent with the less electron donor effect of the R group in this order. These results indicate that the electronic properties of the R group of the RREs significantly influence the electrochemical properties of the relevant complexes.

Fig. 15 Cyclic voltammograms of a 2 mM solution of complexes **17–20** in 0.1 M $[\text{NBu}_4][\text{PF}_6]/\text{CH}_2\text{Cl}_2$



The molecular structures of complexes **17–20** were determined by X-ray diffraction analysis, and it showed that all these complexes possess a “chair-shape” structure with the two R groups are almost parallel to each other along opposite direction and form an angle of $\sim 110^\circ$ with the $2\text{Fe}-2\text{S}$ plane as shown in Fig. 14. The $\text{Fe}(1)-\text{Fe}(1a)$ distance of 2.70 \AA suggests that there is fairly strong interaction between the two iron centers. The $\text{Fe}-\text{Fe}$ distance and the average $\text{Fe}-\text{S}$ bond length for complex **20** are 2.741 and 2.278 \AA , respectively, which are longer than the corresponding values ($2.698, 2.708, 2.708$ and $2.257, 2.257, 2.270 \text{ \AA}$) for complexes **17–19**, indicating that complex **20** is essentially more unstable. The observations are consistent with the electrochemical studies where complex **20** possesses the most positive reduction potential amongst the four complexes.

The average $\text{Fe}-\text{N}(\text{NO})$ bond distance for complex **17–20** is $\sim 1.670 \text{ \AA}$, which is slightly shorter than the reported value in the complex $\text{Fe}(\text{NO})_2[(\text{SC}_6\text{H}_4\text{-}o\text{-NHC}(\text{O})\text{CH}_3)_2]^-$ (average value: 1.681 \AA), the dinuclear complex $[(\text{N}_2\text{C}_5\text{H}_7)\text{Fe}(\text{NO})_2]_2$ ($\text{N}_2\text{C}_5\text{H}_7 = 3,5\text{-dimethylpyrazolyl}$) (average value: 1.696 \AA), and the tetramer $[\text{Fe}(\text{NO})_2(\text{Im-H})]_4$ ($\text{Im-H} = \text{imidazolate}$) (average value: 1.694 \AA), but significantly longer than the found value in the dinuclear complex $\text{Fe}_2(\mu\text{-L})_2(\text{NO})_4$ ($\text{L} = \text{Ph}_2\text{PCH}_2\text{PPh}_2$ and $\text{Ph}_2\text{PC}\equiv\text{CPh}_2$) (average value: 1.644 and 1.656 \AA).

$[\text{Fe}_2(\mu\text{-RS})_2(\text{NO})_4]^-$ anionic form: The corresponding family of reduced species, $[\text{Fe}_2(\mu\text{-RS})_2(\text{NO})_4]^-$, was prepared by the reaction of neutral $[\text{Fe}_2(\mu\text{-RS})_2(\text{NO})_4]$ with a slight excess of cobaltocene or $\text{Li}(\text{BHEt}_3)$ in THF. The dark brown solution turned to dark green after the reduction. Complex **20** slowly decomposes during the course of the reduction reaction.

IR spectra of the monoanionic complexes $[\text{Fe}_2(\mu\text{-RS})_2(\text{NO})_4]^-$ (**21–24**) were collected and exhibit the characteristic ν_{NO} stretching frequencies at $1673, 1655$ (**21**); $1670, 1650$ (**22**); $1690, 1670$ (**23**) and $1693, 1674 \text{ cm}^{-1}$ (**24**) in THF. The corresponding ν_{NO} bands are shifted by 100 cm^{-1} to a lower energy in comparison with neutral species due to their negative charge. Roussin’s Red Salt Esters are

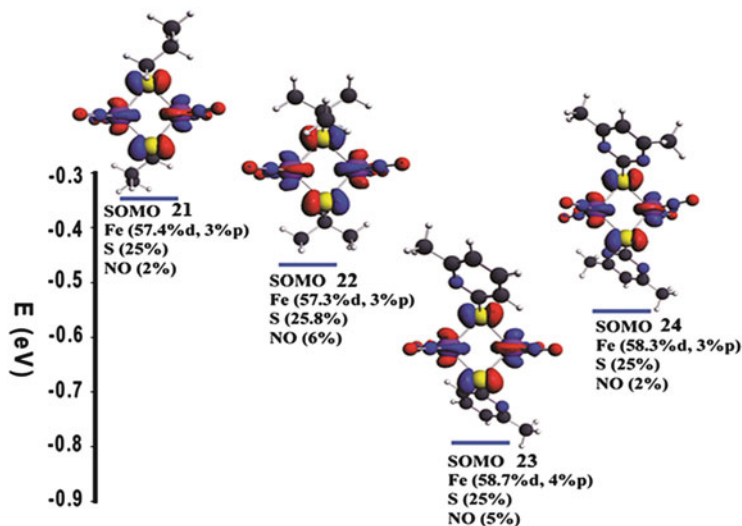


Fig. 16 Spin density distribution of the SOMO for the complexes **21–24** and the calculated composition (in percent) of the SOMO in terms of Fe, S, and NO fragments

diamagnetic and EPR-silent. The reduced species, $[\text{Fe}_2(\mu\text{-RS})_2(\text{NO})_4]^-$, are EPR active and exhibit an isotropic signal at $g = 1.998\text{--}2.004$ without hyperfine splitting in the temperature range from 180 K to 298 K. This is quite different from the typical DNICs, where the g -values are close to 2.03 and the hyperfine structures arising from the coupling between the unpaired electron and the nitrogen of the NO.

In order to interpret the difference, optimizations were first performed on neutral and negatively charged complexes with the spin-unrestricted method. The optimized structures were all obtained at minimum energy as proved by no negative frequencies evident in frequency calculations. The spin density distributions of the singly occupied molecular orbit (SOMO) for the complexes **21–24** were obtained by single point calculations on the four optimized structures of the anionic complexes by including all electrons (Fig. 16). The results show that there are 60–63% of the electron delocalized on two irons, 25.0–25.8% of the electron delocalized on two sulfurs, and only 2–6% of the electron delocalized on four NOs. Since most of the unpaired electron is delocalized over the Fe and S atoms and the most natural abundance of isotopes of these are ^{56}Fe and ^{32}S , whose nuclear spins (I) are zero, the lack of hyperfine splitting in the EPR spectra of these complexes is expected.

In order to understand the differences between the g -values for **21–24** (~ 2.000) and the typical DNICs (2.03), the distribution of electron density on the SOMO of complex $[\text{Fe}(\text{NO})_2(\text{CO})_2]^+$ was also calculated by using DFT as shown in Fig. 17.

The results showed that Fe and NO moiety possessed 54.4% and 41.8% of the electron density of the SOMO, respectively. It should be pointed out that the

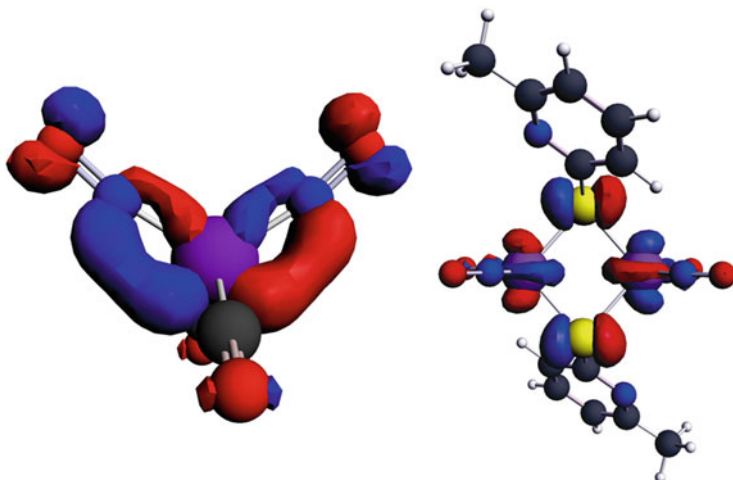


Fig. 17 Comparison of the distribution of electron density on the SOMO of complex $[\text{Fe}(\text{NO})_2(\text{CO})_2]^+$ and RRE calculated by DFT

calculated distribution of electrons on the iron in DNICs (54%) is lower than the values obtained by ^{57}Fe -enriched EPR experiments on other $g = 2.03$ species [83]. However, it is well known that DFT calculations often produce an over-delocalized distribution. Nonetheless, for complexes **21–24**, the amount of electron density on each iron is in the range of 30–32%, and the total percentage of the electrons on the NO moieties is only 2–6%. Therefore, the difference between the EPR g -values for **21–24** (~ 2.000) and the typical DNICs (2.03), and the lack of hyperfine couplings from the NO group in complexes **21–24**, can be well explained by the percentage of the electrons on the metal and NO moiety.

In order to validate the above-mentioned results, additional calculations were carried out to obtain the g -values by using complex **22** as an example. The calculated isotropic g -value is 1.995, which is very close to the experimental data of 1.999. The calculated anisotropic parameters, $g_{\perp} = 2.014$ and $g_{\parallel} = 1.958$ are in agreement with the experimental data $g_{\perp} = 2.009$ and $g_{\parallel} = 1.965$, for this complex. These theoretical results explain clearly why hyperfine structures were not observed and corroborate that the electron density of the SOMO is mostly delocalized on the Fe and S atoms. In fact, the single point calculations show that the extra electron goes mainly on the Fe atoms, which further explains why adding electrons causes weakening the bond between two irons. The molecular orbital characters of the SOMOs shown in Fig. 17 are clearly anti-bonding: thus adding electrons into the SOMO actually increases electron–electron repulsion between iron atoms and contributes to the weakening of the Fe–Fe bond. The composition of the SOMO mainly comes from the d orbital of the metal but also has some $3p$ character, although in a very small amount for all four complexes, while the sulfur contribution is solely from its p orbital.

[PPN]₂[Fe₂(μ-StBu)₂(NO)₂]: Several other RRE-like structures have been synthesized. One of these was formed by dissolving a precursor complex containing an iron atom bound to several chelating oxygen atoms in an appropriate amount of CH₃CN solvent. To this mixture, 2 molar equivalents of [StBu][−] was added [55] and the product was easily isolated and is surprisingly stable. This product was characterized by IR, UV–vis, and other methods. The FT-IR ν_{NO} bands of this product [1637 m, 1613 s, 1578 s, 1567 s cm^{−1} (KBr)] shifted by ~30 cm^{−1} from those of the precursor molecule, indicating a complete reaction. The UV–vis spectrum of the product displays absorptions 270 and 396 nm (CH₃CN). This is in direct contrast to that of the reduced RRE [(NO)₂Fe(μ-StBu)]^{2−} which displays an intense transition absorption around 982 nm. It is thought that the conversion of the precursor molecule into the product is due to the capability of the thiolate ligand to bridge two {Fe(NO)₂}¹⁰ fragments. This is also attributed to the preference of {Fe(NO)₂}¹⁰ motifs which are connected by the electron-donating thiolate group.

Another branch of nitrosyl complex exists containing sulfur ligands that do not resemble Roussin's Red or Black Esters. These complexes frequently seek to mimic amino acids such as cysteine [84]. Several different structures have been discussed pertaining to the dinuclear {Fe(NO)₂}¹⁰–{Fe(NO)₂}¹⁰ and mononuclear {Fe(NO)₂}¹⁰ constructs. These complexes rapidly convert between the DNIC and RRE forms [85] or into the RBE forms [86, 87]. Recently, Lippard's group reported reactions of NO with synthetic [2Fe–2S] and [4Fe–4S], yielded the DNIC, [Fe(NO)₂(SR)₂][−], (R = Ph, p-tolyl, 4-MeC₆H₄) [88]. Other work focuses on the effects that thiolate ligands play on the conversion between DNICs and RREs [89] or the means by which nitric oxide is delivered [90]. Reaction pathways of iron nitrosyls in sulfur-rich biological coordination environments are also a well-studied area [91, 92].

[Fe₂(μ-SCys)₂(NO)₄]: It has been proven that DNICs as well as other metal nitrosyl complexes can form upon reacting with biological Rieske centers. In order to determine this, the Rieske protein, toluene/o-xylene monooxygenase component C (ToMOC) from *Pseudomonas* was exposed to several different components [74]. The Rieske center of this protein was slowly exposed to Na₂S₂O₄. As the reaction took place, three new maxima characteristic of reduced ToMOC began appear at 380, 420, and 520 nm and steadily increased. Once Na₂S₂O₄ was added to the protein, the spectra ceased to change. This lack of further changes indicated a complete reduction of the iron–sulfur cluster. The optical features of ToMOCox and ToMOCred were used as standards to determine whether the various redox states of the Rieske cluster will undergo reaction with NO(g) and NO donors such as DEANO and SNAP under anaerobic conditions. The charge-transfer bands of ToMOCox were bleached which is consistent with cluster disassembly, upon addition of a large excess (~20 equivalents) of DEANO or SNAP under anaerobic conditions. When the reaction was complete, a new optical feature indicative of an iron dinitrosyl species was evident at 367 nm. This is indicative of the ability of DNICs and/or other nitrosyl complexes to form at Rieske centers of certain proteins.

[Fe₂(μ-SEt)₂(NO)₄]²⁺ (cationic form): A separate body of work has studied the effects of sulfur ligands on the ability of an Fe–S cluster to convert into DNICs [89]. This work began with the synthesis of DNIC cations, which is a reactive species that can undergo further transformations under proper condition. A precursor complex, [Fe(μ-SEt)(NO)₂]₂ coordinated with the anion of choice, was dissolved in an appropriate amount of THF and stirred at ambient temperature for approximately 20 min. During this time, a reduction reaction occurred to yield complexes of [Fe(μ-SEt)(NO)₂]²⁺ (cation) coordinated with PPN⁺, Na⁺-18-crown-6-ether or, Me₄N⁺. These complexes were identified by IR, UV–vis, EPR, and single-crystal X-ray diffraction. The complex coordinated with the PPN ligand exhibits diagnostic IR ν_{NO} stretching frequencies at 1673 s, 1655 s cm⁻¹ (THF). In contrast to Roussin's red esters with {Fe(NO)₂}⁹–{Fe(NO)₂}⁹ coupling, rationalizing the absence of paramagnetism and the EPR signal, the anionic Roussin's red ester using PPN is best described as a fully delocalized [{Fe(NO)₂}⁹–{Fe(NO)₂}¹⁰] complex.

[Fe₂(SC₆H₄-o-NHC(O)Ph)₂(NO)₄]: Another metal nitrosyl complex that falls into this category is a mixed ligand structure. In this case, the DNIC contains sulfur, nitrogen, and oxygen coordinated ligands. Several different complexes were obtained by varying the ligand structure slightly [93]. In order to synthesize this particular compound freshly prepared Fe(CO)₂(NO)₂ liquid was dissolved in degassed THF solvent. Separately bis(o-benzamidophenyl) disulfide was dissolved in THF solvent. The second solution was added to the first by cannula under a positive N₂ pressure at 0°C. The resulting solution was allowed to stir at ambient temperature overnight. The solution was filtered through Celite to remove solid contaminants. An appropriate amount of hexane was then added to the filtrate to precipitate the brown-green solid [Fe(SC₆H₄-o-NHC(O)Ph)(NO)₂]₂ (Yield 90%). This product was characterized by ¹H NMR, IR, and UV–vis spectra.

[(ON)Ni(S(CH₂)₂S(CH₂)₂S)Fe(NO)₂]: This interesting compound makes use of two different metals to form the nitrosyl complex [94]. It was prepared by mixing the starting materials: [PPN][Fe(NO)₂(SePh)₂], NaNO₂, and [Ni(S(CH₂)₂S(CH₂)₂S)] into a Schlenk flask and CH₂Cl₂ was added and stirred at 50°C overnight. A dark green solid was isolated by recrystallization from CH₂Cl₂ and hexane. IR (ν_{NO}): 1805 m, 1767 s, 1725 s cm⁻¹ (CH₂Cl₂); 1798, 1763 s, 1723 s cm⁻¹ (THF).

(μ-depdt)[Fe(NO)₂PMe₃]₂PF₆: Here, a rather complicated, mixed-valent molecule is shown with two iron centers and several different ligand groups [95]. This species was synthesized through addition of a cold (–78°C) CH₂Cl₂ solution of a precursor molecule to a dry ice cooled solution of Fe[PF₆]₂. This resulted in an immediate color change from red to purple red. The reaction was stirred for 10 min and then warmed to –42°C. Addition of precooled hexane formed purple/red precipitates. X-ray quality crystals were obtained by mixture of CH₂Cl₂ with pentane/diethyl ether solution. IR (cm⁻¹, in CH₂Cl₂): ν_{CO} 2041 (s), 2005 (s) 1993 (sh), 1874 (w).

[Fe₂(C₁₄H₁₂N₃S)₂(NO)₄]: A dinuclear iron nitrosyl complex was also prepared [Fe₂(C₁₄H₁₂N₃S)₂(NO)₄], **25**, (C₁₄H₁₂N₃S = 2-mercapto-1-[2-(4-pyridyl)-ethyl]-benzimidazolyl) by stirring Fe(NO)₂(CO)₂ with 2-mercapto-1-[2-(4-pyridyl)-ethyl]-benzimidazole in 1:1 ratio in CH₃OH (30 ml) at ambient temperature

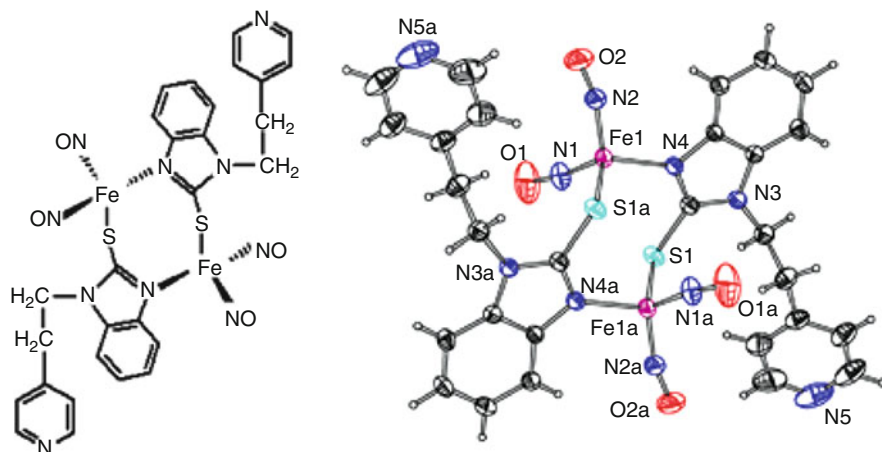


Fig. 18 A molecular drawing and X-ray crystal structure of complex **25**

under nitrogen atmosphere for 96 h [66]. The reaction solution was filtered to remove any dissolved impurities. The residue was redissolved in CH_2Cl_2 and methanol was slowly added to the solution. The solution was then left at -35°C in a glove box overnight to crystallize. Black crystals suitable for X-ray crystallography were collected by filtration, washed with methanol, and dried under vacuum for several hours. Yield: 40%.

The complex shown in Fig. 18 is soluble in common organic solvents such as CH_2Cl_2 , THF, and acetone and is characterized by IR, UV-vis, electrochemistry, and single-crystal X-ray diffraction. IR spectrum displays two strong characteristic NO stretching frequencies (ν_{NO}) in solution and in solid state. Cyclic voltammetry shows one irreversible, two quasi-reversible, and two reversible one-electron reductions and irreversible oxidizations. This result is consistent with the fact that complex **25** is very unstable and ready to lose NO in the air. The single-crystal X-ray diffraction of complex **25** shows a “chair-shape” structure by the connections of two iron centers and S–C–N frames of benzimidazole. The dihedral angle of benzimidazole ring and $2\text{Fe}-2\text{S}$ plane is 73.6° (Fig. 18).

3.2 Iron–Sulfur and Iron–Selenium Nitrosyl Clusters

As the only structurally authenticated example iron–sulfur nitrosyl cluster of $[\text{Fe}_4\text{S}_3]$ was foremost found in the Roussin’s Black Salt anion $[\text{Fe}_4\text{S}_3(\text{NO})_7]^-$, several iron–sulfur nitrosyl clusters, such as $[\text{Fe}_4\text{S}_3(\text{NO})_7]^{n-}$, ($n = 1-3$), $[\text{Fe}_4\text{S}_4(\text{NO})_4]^0, 1^-$ and $[\text{Fe}_6\text{S}_6(\text{NO})_6]^{2-}$ were also obtained [96–99]. However, some clusters such as $[\text{Fe}_6\text{S}_6(\text{NO})_6]^{2-}$ were obtained only by complicated multistep procedures [98]. Subsequently, a new $[\text{Fe}_8\text{S}_6(\text{NO})_8]^{2-}$ cluster [100] was synthesized with improved

one-step synthetic method, in which $[\text{Fe}_4\text{S}_3(\text{NO})_7]^-$ was used as one of the starting materials. Yet, despite many known examples of iron–sulfur nitrosyl clusters, iron–selenium nitrosyl clusters are extremely rare. Prior to our recent work on $[(n\text{-Bu})_4\text{N}]_2[\text{Fe}_6\text{Se}_6(\text{NO})_6]$, which will be described in more detail below, only one iron–selenium nitrosyl cluster, $(\text{Ph}_4\text{As})[\text{Fe}_4\text{Se}_3(\text{NO})_7]$, has been reported, with no characterization other than its structure [101].

$[(n\text{-Bu})_4\text{N}]_2[\text{Fe}_6\text{Se}_6(\text{NO})_6]$: Recently, a new complex $[(n\text{-Bu})_4\text{N}]_2[\text{Fe}_6\text{Se}_6(\text{NO})_6]$, **26**, was synthesized by mixing $[(n\text{-Bu})_4\text{N}][\text{Fe}(\text{CO})_3\text{NO}]$, selenium, and methanol in a vial under a nitrogen atmosphere [102]. The vessel was then sealed and heated at 85°C for 48 h in an autoclave, which was subsequently allowed to cool to room temperature. After the reaction solution was filtered and washed using methanol, black solids were obtained, which was then redissolved in acetonitrile, and diethyl ether was slowly added to the solution. The mixed solution was placed in a glove box at –35°C overnight and yielded black crystals, which were collected by filtration, washed with methanol, and dried under vacuum for several hours. Yield: 52 mg (85%, based on $[(n\text{-Bu})_4\text{N}][\text{Fe}(\text{CO})_3\text{NO}]$). This complex is soluble in most polar organic solvents including acetonitrile, dichloromethane, and THF but is insoluble in methanol, ethyl ether, and hexane.

The IR spectrum of **26** displays one strong characteristic NO stretching frequency at 1694 cm^{-1} (ν_{NO}) in solution with the characteristic of NO^+ . The X-ray crystallographic study shows two parallel “chair-shape” structures, consisting of three iron and three selenium atoms, and are connected by Fe–Se (Fig. 19). The Fe–Se bonds have an average distance of 2.341 Å, and each iron center is bonded to three selenium atoms and a nitrogen atom from nitrosyl ligand with pseudo-tetrahedral center geometry. The average Fe–Fe distance of 2.730 Å suggests that there is a fairly strong interaction between the two iron centers. The Fe–N bond distances range from 1.661 to 1.665 Å with an average of 1.663 Å. The N–O bond lengths range from 1.172 to 1.186 Å with an average of 1.180 Å. The Fe–N–O bond angles range from 174.5° to 178.9° with an average of 176.5°, which is close to linear. These nitrosyl moieties exhibit *sp* hybridized NO^+ character, which indicates a considerable amount of charge transfer between the NO and the metal took place.

The electrochemistry of this complex was studied by cyclic voltammetry and showed two cathodic current peaks at $E_{\text{pc}} = -0.42$ and -1.36 V and three anodic peaks at $E_{\text{pa}} = -0.04$, -0.38 and -1.30 V. The peak at $E_{\text{pc}} = -0.42$ V is unusually strong. Detailed electrochemical studies indicate that it consists of a minimum of three processes as shown in Fig. 20. One is the quasi-reversible reduction at $E_{1/2}^\circ = -0.41$ V and the other two are from an irreversible electrochemical process that occurred at $E_{\text{pc}} = -0.42$ V, in which the compound went through a typical electron transfer and chemical reaction (ECE) mechanism of which its product is easier to reduce than the original one, resulting in an overlap of the reduction potentials and subsequently, a very strong peak (Table 6). The peak at $E_{\text{pa}} = -0.04$ V is the product from such a chemical reaction. The electronic absorption spectra of the complex show bands in the range of 259–562 nm (Fig. 21), which are assigned to the

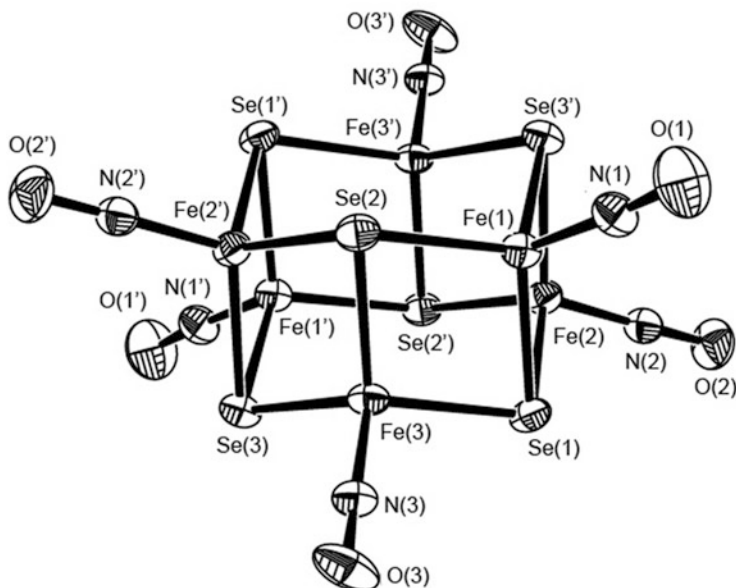


Fig. 19 The X-ray crystal structure of complex **26** with thermal ellipsoids drawn at 50% probability. Reprinted with permission from R. Wang, W. Xu, J. Zhang, and L. Li. *Inorg. Chem.* 49, pp 4814–4819. Copyright 2010 American Chemical Society

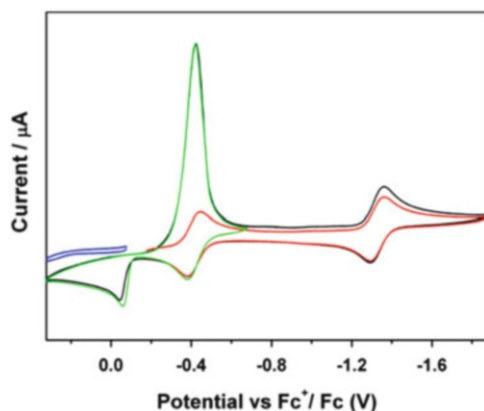


Fig. 20 Cyclic voltammograms of a 1 mM solution of compound **26** in 0.1 M (NBu₄)(PF₆)/CH₃CN at scan rate of 100 mV/S. Reprinted with permission from R. Wang, W. Xu, J. Zhang, and L. Li. *Inorg. Chem.* 49, pp 4814–4819. Copyright 2010 American Chemical Society

transitions between orbitals delocalized over the Fe–S cluster, the ligand to metal charge transfer (LMCT), $\pi^*_{\text{NO}}-d_{\text{Fe}}$, and the metal to ligand charge transfer (MLCT), $d_{\text{Fe}}-\pi^*_{\text{NO}}$.

Table 6 List of redox potentials and IR frequencies for complexes **26–28**

Compounds	Redox potentials vs. Fc^+/Fc (V)			IR frequencies	
	Epa	$E^\circ_{1/2}$		(ν_{NO}) (cm^{-1})	
$[(n\text{-Bu})_4\text{N}]_2[\text{Fe}_6\text{Se}_6(\text{NO})_6]$, 26	-0.04	-0.41	-1.33	1694	
$[(n\text{-Bu})_4\text{N}]_2[\text{Fe}_6\text{S}_6(\text{NO})_6]$, 27	0.07	-0.33	-1.32	1698	
$(\text{Me}_4\text{N})[\text{Fe}_4\text{S}_3(\text{NO})_7]$, 28		-1.09	-1.71	-2.21	1799, 1744, 1710

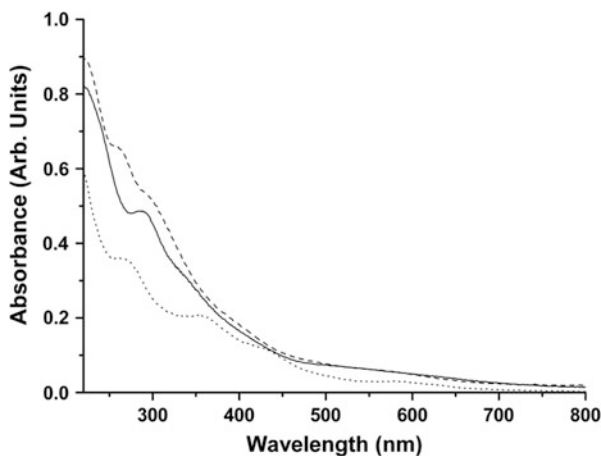


Fig. 21 The UV-vis spectra of complexes **26** (solid line), **27** (dashed line) and **28** (dotted line). Reprinted with permission from R. Wang, W. Xu, J. Zhang, and L. Li. *Inorg.* 2010. *Chem.* 49, pp 4814–4819. Copyright 2010 American Chemical Society

$[(n\text{-Bu})_4\text{N}]_2[\text{Fe}_6\text{S}_6(\text{NO})_6]$: A hexanuclear iron-sulfur nitrosyl cluster, $[(n\text{-Bu})_4\text{N}]_2[\text{Fe}_6\text{S}_6(\text{NO})_6]$, **27**, was synthesized using similar solvent-thermal reactions described in **26**, at 120°C using sulfur (32 mg, 1 mmol) and the product was obtained in high yield of 92% based on $[(n\text{-Bu})_4\text{N}][\text{Fe}(\text{CO})_3\text{NO}]$ [102]. Complex **27** is also soluble in most polar organic solvents including acetonitrile, dichloromethane, and THF. However, it is insoluble in methanol, ethyl ether, and hexanes. The IR spectrum of complexes **27** is similar to **26** and displays one strong characteristic NO stretching frequency at 1698 cm^{-1} (ν_{NO}) in solution with the characteristic of NO^+ .

The X-ray crystal structure of complex **27** was determined and it was found to be consistent with the reported one [99]. The average Fe-Fe distance is 2.644 \AA , which is shorter than that of **26** (2.730 \AA), which is understandable as the radius of selenium atom is larger than that of sulfur. The Fe-N bond distances for compound **27** range from 1.659 to 1.672 \AA with an average of 1.667 \AA , which is similar to **26**. Accordingly, the N-O bond lengths in compound **27** range from 1.168 to 1.197 \AA with an average of 1.182 \AA , which is also similar to compound **26**. The average Fe-N-O bond angle of 174.4° is similar to the average value of 176.5° found in complex **26**, 176.9° in $[\text{Fe}_8\text{S}_6(\text{NO})_8]^{2-}$, 177.6° in $[\text{Fe}_4\text{S}_4(\text{NO})_4]$, 177.5° in $[\text{Fe}_4\text{S}_4(\text{NO})_4]^-$, and the Fe-N-O bond angles of 177.6° arising from the apical Fe(NO) in $[\text{Fe}_4\text{S}_3(\text{NO})_7]^{2-}$.

The redox behavior of compound **27** was also studied by CV and showed two cathodic current peaks at $E_{pc} = -0.30$ and -1.29 V and three anodic peaks at $E_{pa} = 0.08$, -0.23 , and -1.19 V at scan rate of 100 mV/s (Table 6). It is similar to compound **26** in that the first reduction peak is much stronger than the second one. Various scan rates from 0.1 to 1.0 V/s were recorded. When faster scan rates were applied, the first reduction peak was separated to two reductions, and the faster the scan rate, the clearer the separation between the two reduction peaks. In addition, the peaks correspond to the ECE process did not disappear even at the scan rate of 1 V/s, which indicates that the chemical step is quite fast.

The electronic absorption spectra of complexes **27** show bands in the range of 259–562 nm (Fig. 21), which are assigned to the transitions between orbitals delocalized over the Fe–S cluster, the ligand to metal charge transfer (LMCT), $\pi^*_{NO-d_{Fe}}$, and the metal to ligand charge transfer (MLCT), $d_{Fe}-\pi^*_{NO}$.

(Me₄N)[Fe₄S₃(NO)₇]: A tetranuclear cluster, **(Me₄N)[Fe₄S₃(NO)₇]**, **28**, was also prepared through a solvent-thermal reaction by mixing FeCl₂·4H₂O, thiourea, (CH₃)₄NCl, NaNO₂ in methanol in a vial under nitrogen atmosphere. The vessel was sealed and heated at 85°C for 48 h [102]. The autoclave was then allowed to cool to room temperature. The solution was filtered and washed using methanol and the solid mixture was dissolved in the acetonitrile and filtered to remove the undissolved white solid. Subsequently, diethyl ether was slowly added to the solution, and the mixed solution was placed in a glove box at -35°C overnight to crystallize. The black crystals were collected by filtration, washed with methanol, and dried under vacuum for several hours. Yield: 88%, based on FeCl₂·4H₂O. Complex **28** is more or less soluble in all organic solvents and is fairly stable in the solid state and in solution under air. IR spectrum of complex **28** shows three stretching frequencies at 1799, 1744, and 1710 cm⁻¹. The UV–vis spectrum for **28** was also recorded and is shown in Fig. 21.

X-ray crystal structure of complex **28** was determined. The average Fe–Fe distance is 2.705 Å, which is similar to [Fe₆S₆(NO)₆]²⁻ (2.644 Å), [Fe₆Se₆(NO)₆]²⁻ (2.730 Å), but is clearly shorter than the relevant value of 2.764 Å for dianion [Fe₄S₃(NO)₇]²⁻. This difference was explained by the HOMO of [Fe₄S₃(NO)₇]²⁻, which contains an unpaired electron, and has anti-bonding character involving all pairs of iron atoms of the Fe₄S₃ core. This leads to the increase of Fe–Fe bond lengths. When comparing [Fe₄S₃(NO)₇]²⁻ and [Fe₄S₃(NO)₇]⁻ (**28**), the Fe–N interactions are evidently strengthened in the dianion (average value: 1.646 Å vs. 1.671 Å in the monoanion) owing to more back-donation from d_{Fe} to π^*_{NO} . On the other hand, the average N–O bond lengths are 1.176 Å for [Fe₄S₃(NO)₇]²⁻ and 1.166 Å for **28** – an opposite trend. These observations are consistent with the results of IR spectra, which display that the absorptions of nitrosyl groups (ν_{NO}) appear at higher frequencies for complex **28**.

The Fe–N–O bond angles is 178.3°, which is clearly larger than the average Fe–N–O bond angles of 167.9° and 166.6° arising from the three sets of Fe(NO)₂ of [Fe₄S₃(NO)₇]²⁻ and complex **27**, respectively. When comparing complex **28** with other Roussin's Black Salt, no differences could be attributed to effects of the counter ion besides the packing effects. These results show that the Fe–N–O bond

angles of iron–sulfur (selenium) clusters are irrelevant to their dimension and charge, but relevant to the number of nitrosyls attached to the iron atoms and the localized symmetry of the iron atoms. This also means that the variance of NO^+ (linear, sp hybridized) and NO^- (bent, sp^2 hybridized) may be brought out because of the greater deviations of the Fe–N–O bond angles from 180° in the iron dinitrosyl units for complex **28** and $[\text{Fe}_4\text{S}_3(\text{NO})_7]^{2-}$.

Compound **28** has three quasi-reversible reductions with half-wave potentials of -1.09 , -1.71 , and -2.21 V (Table 6). The electronic absorption spectra of complexes **28** show bands in the range of 259–562 nm (Fig. 21), which are assigned to the transitions between orbitals delocalized over the Fe–S cluster, the ligand to metal charge transfer (LMCT), $\pi^*_{\text{NO}}-d_{\text{Fe}}$, and the metal to ligand charge transfer (MLCT), $d_{\text{Fe}}-\pi^*_{\text{NO}}$.

3.3 *Multinuclear Metal Nitrosyl Complexes*

In addition to the iron–sulfur or iron–selenium nitrosyl clusters, a few multinuclear metal nitrosyl clusters have been synthesized. Here a well-documented structure is examined and its physical and chemical characteristics are explained in thorough detail.

$\text{Fe}_4(\text{NO})_8(\text{Im-H})_4$: One example of a tetra-nuclear DNIC was synthesized when one equivalent of $\text{Fe}(\text{NO})_2(\text{CO})_2$ was reacted with two equivalents of imidazole, Im, in methylene chloride at room temperature in a glove box under nitrogen atmosphere [103]. After stirring for 24 h, a dark reddish brown precipitate was obtained and collected by filtration with 50% yield. Single crystals suitable for X-ray diffraction were isolated by recrystallization of **29** from acetone at -38°C under nitrogen atmosphere.

The structure shows four iron centers that are linked together through four deprotonated imidazole bridging ligands forming a neutral 16-membered rhombic macrocycle with alternating imidazolates and irons as shown in Fig. 22. Each iron center possesses a pseudo-tetrahedral geometry and is coordinated with four nitrogen atoms, two from the nitrosyl ligands and two from the imidazolate ligands (Im-H). The molecule has dimensions of $8.18 \times 8.70 \text{ \AA}$ ($\text{Fe1} \cdots \text{Fe1} \times \text{Fe2} \cdots \text{Fe2}$). A solvent molecule, acetone, is crystallized inside the cavity. Upon detailed examination of the crystal structure, it is found that the two C–N bond lengths are approximately equal to the mean value of 1.336 \AA , while the crystal structure of imidazole free ligand shows two different C–N bond lengths of 1.349 \AA and 1.326 \AA . This is due to the deprotonation of the bridging ligand, which created a six-electron aromatic ring with expected delocalization. The deprotonation also created a negative charge on the imidazolate ligand, which has to be balanced by one positive charge on each iron center, since the whole molecule is neutral. This is reflected by both the nitrosyl IR stretching frequencies of the complex, the relatively longer Fe–NO bond distances, and shorter N–O bond distances.

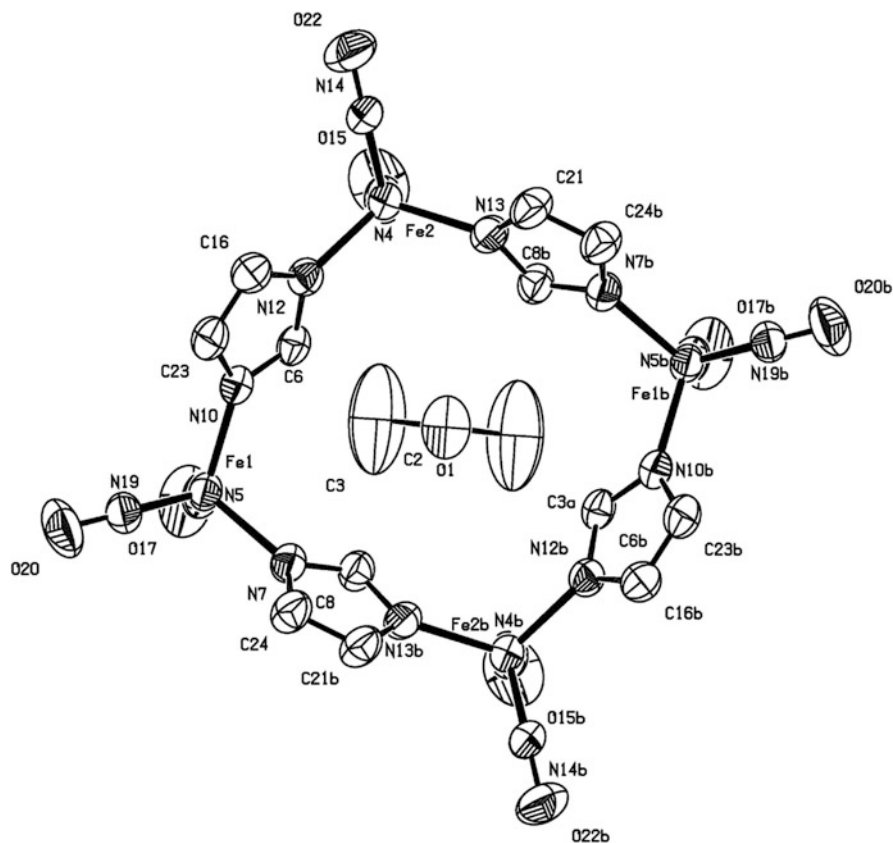
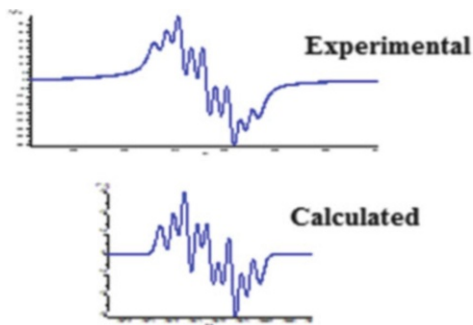


Fig. 22 X-ray crystal structure of complex **29** with anisotropic thermal displacement ellipsoids drawn at 50%. An acetone molecule is crystallized inside of the cavity

The average Fe–N (Im-H) bond distances is 2.005 Å, which is shorter than the values reported for $\text{Fe}(\text{NO})_2(1\text{-MeIm})_2$ (average value of 2.046 Å). The average N–O bond length is 1.166 Å, which is also shorter than the N–O distance of 1.189 Å in $\text{Fe}(\text{NO})_2(1\text{-MeIm})_2$. This is because the positive iron atom in complex **29** donates less electron density to the π^* orbitals of the nitrosyl ligands than the neutral iron of $\text{Fe}(\text{NO})_2(1\text{-MeIm})_2$. This is also reflected in the average Fe–N (NO) bonds length (1.694 Å), which is longer than those in $\text{Fe}(\text{NO})_2(1\text{-MeIm})_2$ due to the less extensive π back-bonding.

The ν_{NO} values for $\text{Fe}(\text{NO})_2(\text{CO})(\text{Im})$, **30**, (1731 cm^{-1} and 1687 cm^{-1}) appear at lower frequencies than those of $\text{Fe}(\text{CO})_2(\text{NO})_2$, consistent with electron-donating property of the imidazole ligand. Since both carbonyls have been replaced by a donor ligand on each metal, one would expect the nitrosyl stretching frequencies of complex **29** to shift to even lower wavenumbers. However, the nitrosyl stretching frequencies ν_{NO} occur at 1796 cm^{-1} and 1726 cm^{-1} for **29**, which is even higher than that of **30**, suggesting that the oxidation of the $\text{Fe}(\text{NO})_2$ units took place to

Fig. 23 Comparison of the experimental and simulated EPR spectra of the 17-electron solvated species derived from complex **29**



balance deprotonation of the bridging ligands. The observed ν_{NO} in **29** makes it $\{\text{Fe}(\text{NO})_2\}^9$, according to the Enemark-Feltham notation.

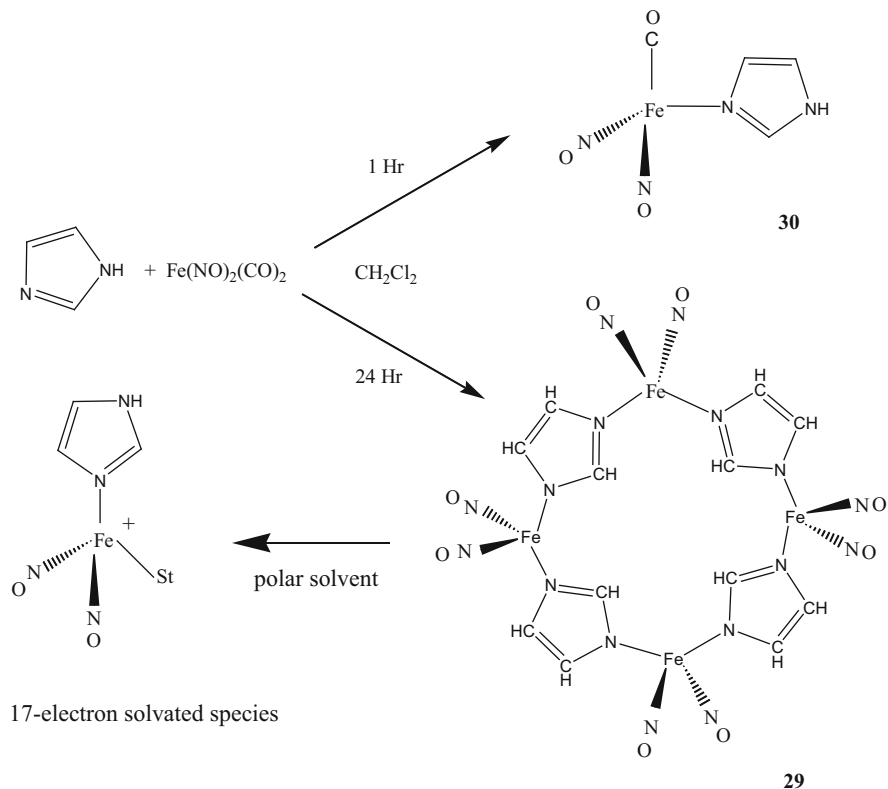
EPR studies of complex **29** in the solid-state at room temperature showed a very broad peak at $g = 2.023$ with a peak-to-peak width of 250 G, indicating that the metal centers are weakly coupled to each other. In THF solution, a signal at $g = 2.031$ with $\Delta H_{\text{pp}} = 13.2$ G was observed at room temperature and it becomes a well-resolved 9-line spectrum at 170 K as shown in Fig. 23. The computer simulation of the low temperature spectrum indicates that the hyperfine structure is a result of the coupling of two equivalent ^{14}N nuclei from the nitrosyls and one ^{14}N from the imidazolate, with hyperfine coupling constants of 2.54 G and 4.50 G, respectively. From this observation, one concludes that the tetrameric molecule has fragmented and most likely solvated to give the seventeen electron species $\text{Fe}(\text{NO})_2(\text{Im-H})(\text{THF})$ or its protonated analog $[\text{Fe}(\text{NO})_2(\text{Im-H})(\text{THF})]^+$ as shown in Scheme 5. The presence of the solvated species, $[\text{Fe}(\text{NO})_2(\text{Im-H})(\text{THF})]$, was further investigated using FT-IR spectroscopy and the results showed that the more polar the solvent, the more solvated products were observed. The characteristic g -value close to 2.03 and the small hyperfine coupling constants (2–3 G) indicate that the unpaired electrons are localized on the Fe center.

Nitric oxide release from complex **29** was also studied by photolytic and thermo methods. It showed four steps of weight losses at different temperature ranges determined by TGA attributed to stepwise loss of imidazole and NO and a slow decomposition under photolytic conditions. Other tetranuclear compounds that are very similar to **29** have also been isolated [104, 105].

4 Mononitrosyl and Trinitrosyl Complexes

4.1 Mononitrosyl Complexes:

Majority of the mononitrosyl complexes are existed as pentacoordinated. Earlier work pioneered by Mingos [106–108] laid out the foundations for these complexes and a few representative work will be discussed in more detail in the following.



Scheme 5 Preparation of compounds **29** and **30** and the formation of the 17-electron solvated species in polar solvents

Nowadays, many mononitrosyl complexes are often synthesized with a purpose of comparing their structures and properties with the products of nitric oxide transfers in order to confirm a successful reaction. For instance, using sterically hindered β -Diketimate ligand, a new complex $[\text{Fe}(\text{NO})(\text{Ar-nacnac})]$, Ar-nacnac = anion of $[(2,6\text{-diisopropylphenyl})\text{NC}(\text{Me})_2\text{CH}]$, was isolated and studied by Lippard recently [109]. Some mononitrosyl complexes are stabilized by highly coordinated metal centers [110], while others contain metal centers besides iron, such as $(\text{OEP})\text{Ru}(\text{NO})(p\text{-C}_6\text{H}_4\text{F})$ (where OEP = octaethylporphyrinato dianion) [111], $[\text{Mn}(\text{PaPy}_3)(\text{NO})]\text{ClO}_4$ [112], and $[\text{NBu}_4][\text{cis-RuCl}_4(4\text{-pyha})\text{NO}]$ (4-pyha=4-pyridinehydroxamic acid) [113] giving a wide variety of mononitrosyl complexes. Some of these structures have demonstrated the ability to release nitric oxide under visible light, making them possibly useful candidates for nitric oxide transfer reactions [114–117]. Other structures make use of porphyrins as a bulky ligand in order to stabilize the nitric oxide group, and an axially bound NO on cobalt porphyrins with the formula $(\text{T}(p/m\text{-X})\text{PP})\text{Co}(\text{NO})$ ($p/m\text{-X} = p\text{-OCH}_3, p\text{-CH}_3, m\text{-CH}_3, p\text{-H}, m\text{-OCH}_3, p\text{-OCF}_3, p\text{-CF}_3, p\text{-CN}$) [118, 119], and with a ruthenium

metal [120, 121]. Photolability studies on mixed-type structures with both S and N ligands were also examined [122, 123]. X-ray absorption spectroscopic study of nitric oxide binding to iron in active sites was also reported [124]. Here, several different compounds are summarized along with some relevant spectroscopic data.

[Ir(NO)(PPh₃)₂L₁L₂] and [IrH(NO)(PPh₃)₃][ClO₄]: The structures of the complexes with formula [Ir(NO)(PPh₃)₂L₁L₂], (L₁ = I, L₂ = Me and L₁ = L₂ = Cl) have been determined [106, 107] and showed that they form a square-pyramidal geometries with the nitrogen atom of the nitrosyl group occupying the apical position and the other ligands lying in the basal plane. The nitrosyl ligand is coordinated with iridium in a nonlinear fashion, with an iridium–nitrogen–oxygen bond angle between 120 and 123°, which is described formally as an NO⁻ to a transition metal. To the contrary, the structure [IrH(NO)(PPh₃)₃][ClO₄] is described as distorted trigonal bipyramidal with the hydrido and nitrosyl ligands occupying the axial positions and the triphenylphosphine ligands the equatorial positions [108]. The nitrosyl ligand is linear (Ir–N–O bond angle of 175°) and best described as an NO⁺. A general bonding model for linear and bent transition metal nitrosyl complexes was also reported and it was concluded that nitric oxide, unlike carbon monoxide and dinitrogen, forms linear and bent complexes primarily because it has a low-lying π* orbital [125]. Further investigations on molecular orbital model of pentacoordinate nitrosyls indicate that the σ- or π-donating capability of the basal ligands in a square pyramid affects the degree of bending of the nitrosyl ligand [126].

Mingo also pioneered the use of ¹⁵N NMR to differentiate linear and bent nitrosyls in transition metal complexes, including nitro and nitrito ligands in 4-, 5-, and 6-coordinate transition metal complexes [127, 128]. Nitrogen-15 solid-state NMR of [RuCl(NO)₂(PPh₃)₂](BF₄) using high-resolution cross-polarization magic-angle spinning (CP/MAS) also showed a large chemical shift anisotropy for the bent as compared with the linear nitrosyl ligand [129].

[TcCl(NO)(DPPE)₂]: Several other noteworthy structures include a novel technetium complex with phosphine ligands [130]. To synthesize this particular compound, a sample of (NH₄)[TcO₄] was evaporated to dryness and added to a fivefold excess amount hydroxylamine hydrochloride in dry methanol. The reaction mixture was heated to the reflux temperature and allowed to react for approximately 45 min. This reaction yielded a red solution. Six equivalents of diphenylphosphinoethane (DPPE) were added to the refluxed solution. This mixture was then heated and refluxed for an additional 45 min. One equivalent of ammonium hexafluorophosphate was then added to the reaction mixture. The solvent was evaporated from the reaction mixture yielding a red oily liquid. This product was dissolved in methylene chloride and then layered with methanol and diethyl ether. After being allowed to sit at room temperature for approximately 24 h, the solution yielded red-brown crystals. Yield: 373 mg (93%). Analytical results IR (KBr): m (Tc=N), 1098 cm⁻¹, m (N=O), 1723 cm⁻¹.

[Ni(NO)(nP₃)]X: Several different compounds of nickel have been synthesized that also make use of phosphine ligands. The basic formula of these compounds is [Ni(NO)(nP₃)]⁺ where nP₃ is tris(2-diphenylphosphinoethyl)amine and X is the coordinating anion. Four structures are given that utilize four different anions [22].

X = BF₄: A solution was made up of np₃ ligand dissolved in acetone. A mixture containing [NiBF₄]·6H₂O dissolved in ethanol was added to the previous solution. The resulting mixture was concentrated by evaporation. Crystals were obtained from this solution. The formula of these crystals was [NiH_x(nP₃)]BF₄ where (x = 0.06–0.26). In order to form the final product, the purified crystals were dissolved in dichloromethane. Nitrogen oxide was bubbled through the solution for approximately 20 min until the color changed to a deep violet purple (this solution is further reacted with later mentioned reagents to form new products). The solution was diluted with ethanol and then concentrated again. This yielded dark black–violet crystals with the formula [Ni(NO)(nP₃)]BF₄.

X = BPh: Another member of this family of compounds makes use of a different coordinated ligand. This product was formed by dissolving NaBPh₄ in ethanol to the earlier mentioned violet solution. The solution was concentrated and recrystallized from a THF-ethanol mixture.

X = I: This alternate product was prepared using the same procedure as the tetrafluoroborate derivative. The starting reagents used were NiI dissolved in dichloromethane. This mixture was added to the solution containing nP₃ ligand in acetone and reacted in the same manner.

X = NO₃: In order to synthesize this compound, a suspension of Ni(NO₃)₂ was dissolved in THF. The solution was stirred and NO was bubbled through it. The solution turned black–violet and was concentrated to yield the solid product.

[(N-N)Ru(NO)Cl₃]: A family of complexes has been made that makes use of diimine ligands [131]. The members of this family, *fac*-[(N-N)Ru(NO)Cl₃], (N-N = R'N=CR-CR=NR'), differ in size, shape, and formula of the R groups present on the diimine ligands. The synthetic procedures for the family Ru(II) nitrosyl complexes [(N-N)Ru(NO)Cl₃] were obtained through the single step reactions between Ru(NO)Cl₃·5H₂O dissolved in an appropriate solvent. To this mixture, 1 molar equivalent of the appropriate ligand molecule was added. The products of these reactions were collected and purified. Interestingly, a novel unexpected by-product, which was classified by the rearrangement of one of the NO ligands, was also isolated (very low yield of 5%) from the reaction mixture.

Monoanionic [(NO)Mn(S,S-C₆H₃-R)₂]⁻ and dianionic [(NO)Mn(S,S-C₆H₃-R)₂]²⁻: An interesting family of new structures based on sulfur ligand is discussed here. These structures make use of manganese as the coordinated metal center instead of the usual iron atom. Several compounds within this family were obtained by changing the substituents on the ring of the benzenedithiolate ligand. Two different complexes were formed here with the ligands bound to manganese in a bidentate and a monodentate manner [132]. These structures were synthesized by dissolving the proper precursor molecule in THF solvent. An NO(g) mixture (10% NO + 90% N₂) was then bubbled through the solution. This reaction leads to the formation of the final product, which was isolated and characterized. IR and UV–vis spectra implied the formation of the anionic {Mn(NO)}⁵ complex [(NO)Mn(S,S-C₆H₃-R)₂]⁻ (R = H or Me). The simple H containing complex was isolated in solid form and characterized by single-crystal X-ray analysis. Several structures have been synthesized that are very similar to these, but make use of different metal centers [133, 134].

[Ru(L)(PPh₃)₂(NO)](ClO₄) (L = pyridine 2,6-dicarboxylic acid): Another example of a mixed ligand molecule is discussed here. This molecule makes use of a ruthenium atom as its metal center [135]. A precursor complex [Ru(L₁)(PPh₃)₂(Cl)] was reacted with NO that was generated in situ by an acidified NaNO₂ solution. The brownish-red color of the initial solution changed to yellow after approximately 1 h of stirring. The resultant yellow compound was isolated as a perchlorate salt. The precursor complex possesses a band near 400 nm in UV-Vis spectrum. This band was not present in the final product spectrum, where a peak near 320 nm was observed. The IR spectrum of the final product provided ν_{NO} at $\sim 1890\text{ cm}^{-1}$ and the presence of perchlorate ion was confirmed by peaks near 1090 and 623 cm^{-1} .

(OEP)Os(NO)(OiPr): One of the interesting structures using porphyrin as a ligand makes use of osmium as the metal center [136]. To form this product (OEP)Os(NO)-(OEt) was dissolved in 2-propanol. To this solution, HBF₄·Et₂O was added in the absence of light. The resulting dark red solution was brought to the reflux temperature and allowed to react for 2 h. The solvent was then removed using a vacuum; the resulting residue was redissolved in a solvent mixture made up of CH₂Cl₂ and pyridine. This mixture was stirred at room temperature for 5 min to completely dissolve the residue. The volatile solvents were removed from the solution again using a vacuum. The red residue was dissolved again in a minimum amount of CH₂Cl₂ and purified by being quickly chromatographed on a short silica gel column by using an eluent solution of CH₂Cl₂/THF (5:1). The bright red band was collected and evaporated to dryness, and the alkoxide compound (OEP)Os(NO)(OiPr) was obtained as a red solid (65% yield).

[Fe(NO)(cyclam-ac)](ClO₄)Cl·H₂O: A molecule similar to that of the aforementioned porphyrin structure is an octahedral pentadentate molecule described here [93]. This compound has a mixed chelated structure, having both nitrogen and oxygen coordinating atoms that are part of the same ligand molecule. In order to synthesize this molecule the precursor molecule was dissolved in degassed acetonitrile solvent at ambient temperature with stirring. To this solution (tris(4-bromophenyl)ammoniumyl) hexachloroantimonate was carefully added in a 1:1 molar ratio. The mixture was allowed to stir for 5 min. This yielded a light yellow solution and upon sitting undisturbed, colorless tris(4-bromophenyl)amine precipitated. This solid was filtered off. Following this, a threefold excess of tetra-*n*-butyl ammonium perchlorate was dissolved in degassed CH₃CN and added to the previous yellow solution. A slow flow of Ar gas was passed through the solution in order to slowly evaporate off the solvent. After $\sim 12\text{ h}$ a yellow solid had precipitated and was collected by filtration. The solid was recrystallized in water and yellow crystals were obtained with a 72% yield.

4.2 Trinitrosyl Complexes

Trinitrosyl metal complexes are rarely isolated due to their relative instability. However, a few structures have been reported which make use of large bulky ligands that stabilize the three nitrosyl groups.

[(IMes)Fe(NO)₃][BF₄]: One form of trinitrosyl iron complex (TNIC) was synthesized by the Darensbourg group [137]. This new compound was only made possible with the use of a bulky carbene ligand that stabilizes the three NO groups on the iron center. This was synthesized by reacting an appropriate amount of Fe(NO)₂(CO)₂, with 1 molar equivalent of the carbene ligand (abbreviated here as IMes) to form the precursor DNIC molecule (IMes)Fe(CO)(NO)₂. This precursor molecule was then reacted with NOBF₄ and left to stir overnight. Purification using hexane yielded the final product [(IMes)Fe(NO)₃][BF₄]. Green crystals of X-ray quality were obtained that are air and moisture stable, as well as being thermally stable in THF with a very slow decomposition rate. This molecule was qualitatively tested using IR spectroscopy and a nitric oxide trapping agent. The results showed that this new structure was able to transfer nitric oxide under these conditions.

5 Organometallic Metal Nitrosyl Complexes

Organometallic metal nitrosyl complexes represent a large portion of the subject and the methods of preparing these complexes have been published in several helpful texts [7, 28, 138, 139]; therefore, it is minimally discussed here. Instead we picked a few recent examples that deal with controlling the reactivity of nitric oxide at transition-metal centers, because of their fundamental significance and possible biological relevance.

Legzdins' group recently reported an intramolecular insertion of bound NO into an adjacent metal–ligand bond in the presence of an oxygen-atom transfer reagent [140]. Treatment of the dialkyl compounds Cp^{*}M(NO)(CH₂CMe₃)₂ (where Cp^{*} = η⁵-C₅Me₅, M = Mo or W) with cumene hydroperoxide induced the insertion of NO into one of their metal–carbon bonds and resulted in the formation of the η²-nitrosoalkane oxo complexes Cp^{*}M(O)(η²-ONCH₂CMe₃)(CH₂CMe₃). Further treatment of Cp^{*}M(O)(η²-ONCH₂CMe₃)(CH₂CMe₃) with excess O₂ yielded the dioxo alkyl complexes Cp^{*}M(O)₂(CH₂CMe₃).

Recently, Bergman et al. reported several examples of double additions of C–N bond-forming reactions of metal nitrosyls, some of which are shown in Fig. 24 [141, 142]. For instance, the dinitrosyl complex [RuCl₂(NO)₂(THF)], in the presence of an additional neutral chelating ligand, binds alkenes to the nitrosyl nitrogen atoms at room temperature [142]. This was achieved by the reaction of [(cymene)RuCl₂]₂ with 10 equiv of norbornadiene in the presence of NO in THF, which yielded a six-coordinate ruthenium dinitro-soalkane adduct [(THF)₂RuCl₂{(μ-NO)₂(C₇H₈)}] in high yield.

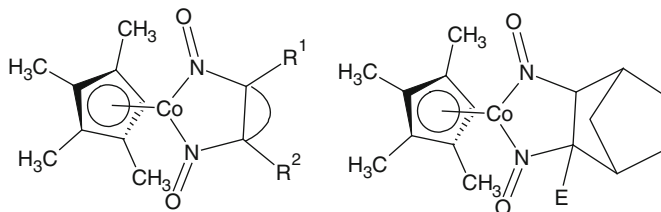


Fig. 24 Examples of double additions of C–N bond-forming reactions of metal nitrosyls

Using a combination of experimental techniques (XRD, EPR, UV–vis, NIR, and X-ray absorption spectroscopies) and computational studies (DFT, time-dependent DFT, complete active space self-consistent field (CASSCF), and multireference configuration interaction (MRCI) calculations), the ground-state electronic structure of a four-coordinate Co nitrosyl complex: $\text{Tp}^*\text{Co}(\text{NO})$ ($\text{Tp}^* =$ hydro-tris (3,5-dimethylpyrazolyl)borate) was well described. A detailed understanding of the interaction between the metal center and the nitrosyl ligand was obtained from correlating between experiment and theory [143].

6 Conclusion

In summary, the preparation of some novel metal nitrosyl complexes, which have been synthesized over the last decade, has been summarized and several selected examples have been discussed in detail. From those examples, one can see that dinitrosyl complexes are typically prepared by using $\text{Fe}(\text{NO})_2(\text{CO})_2$ as the starting material, which is then reacted with appropriate ligands. Final products are formed as a result of simple substitution reactions. These processes can easily be followed through the use of FT-IR spectroscopy, as the remaining carbonyl group(s) can help to differentiate between single or double substituted complexes. Depending on the donating/accepting properties of the ligands, the IR stretching frequencies of the nitrosyl group will shift into different directions, as well as the electrochemical reduction potentials. As shown in the X-ray crystallographic studies, all of these complexes possess tetrahedral geometry at their metal centers with the exception of a very few. NMR is also useful in studying the geometry changes of the ligands and in some cases, a restricted rotation of the ligand has been observed. The 17-electron paramagnetic form of these complexes is EPR active and shows exclusively well-resolved spectra with g -factors close to 2.03. This high g -value is related to the high electron density on the metal center, and the hyperfine couplings are attributed to the nitrogens of the nitrosyl ligands (though the coordinated ligands also contribute). These complexes are closely related to the biological non-heme iron nitrosyl complexes, the so-called $g = 2.03$ species.

Nitrosyl complexes containing two or more metal centers have also been summarized. The complexes containing Fe_2S_2 cores are closely related to the

RRE structures and are often used as biomimics of NO bound to the cysteine residues of proteins. Formation of DINCs at Rieske centers of certain proteins has been achieved. These complexes are typically synthesized through the reaction of $\text{Fe}(\text{NO})_2(\text{CO})_2$ with the appropriate thiol or thiolating ligands. A few mixed metal complexes have also been prepared. Characterizations of these complexes are usually done through a combination of X-ray crystallographic methods and FT-IR spectroscopy. The structures in their solid state are almost exclusively *trans*-isomers, while in solution, *cis*- and *trans*-isomers coexist. DFT calculations show that the two isomers can interchange and the activation energy barrier is only ~ 3 kcal/mol. The electrochemical studies show ligand-based redox behavior with SR group influence of the reduction potentials. These complexes are diamagnetic and EPR silent. The reduced form of the complexes are EPR active and show a single line at $g = 1.99$ without any hyperfine coupling. The electron distribution calculated by DFT methods shows that the unpaired electron is delocalized between the iron and sulfur atoms with $\sim 60\%$ and 25% , respectively, and very small amount ($\sim 2\%$) on the nitrosyl groups. In contrast, the unpaired electron in DNICs is mostly on the iron atom and there are significantly larger spin densities on the nitrogens of the nitrosyl ligands. These results explain the lack of hyperfine coupling in the reduced RREs and the g -value difference between the RREs ($g = 1.99$) and the DNICs ($g = 2.03$).

The method of using simple one-step solvent-thermal reactions to prepare iron–sulfur and iron–selenium nitrosyl clusters is also discussed in detail. The results show that the solvent-thermal reaction is a more effective and simple procedure for the synthesis of polynuclear iron nitrosyl compounds than traditional methods, in which other iron–sulfur nitrosyl clusters are used as starting materials. The structural analysis done by single-crystal X-ray diffraction shows that each iron center is bonded to three selenium (sulfur) atoms and a nitrogen atom from the nitrosyl ligand with pseudo-tetrahedral geometry. The UV–vis spectra are also presented along with the electrochemical study, in which an ECE mechanism is identified. The formation and structural characteristics of multinuclear metal nitrosyl complexes containing four iron and four imidazole or four substituted imidazoles have also been presented.

Mononitrosyl complexes are usually prepared through the treatment of a precursor molecule with source of NO. Many mononitrosyl complexes are often synthesized with the intention of comparing their structures and properties with the products of nitric oxide transfer reactions. Trinitrosyl metal complexes are harder to prepare due to their relative instability and the example presented shows that it is made possible only with the use of a bulky ligand that stabilizes the three NO groups on the iron center. The subject of organometallic metal nitrosyl complexes is minimally discussed here with a few recent examples related to the reactivity of nitric oxide at transition-metal centers.

Many of the aforementioned structures show promising properties including the ability to bind to proteins, transfer nitric oxide, and reversibly convert into Roussin's Red or Black Esters. Despite this intensive study, further work is needed in order to completely understand the chemical properties of these compounds.

Quantitative studies of the NO transfer and delivery have yet to be accomplished on many of these complexes. The full potential of these complexes can be unlocked once these properties are quantified and fully understood.

Acknowledgment We wish to thank the National Institute of Health (NIH) MBRS Score program (Grant # 5 SC3 GM 092301) for their continued financial support.

References

1. Koshland DE (1992) *Science* 258:1861–1902
2. Feldman PL, Griffith OW, Stuehr DJ (1993) *Chem Eng News* 71:26–38
3. de Mel A, Murad F, Seifalian AM (2011) *Chem Rev* 111:5742–5767
4. Lin Z, Chiou T, Liu K, Hsieh C, Yu JK, Liaw WF (2012) *Inorg Chem* 51:10092–10094
5. Vanin FA, Serezhnikov VA, Mikoyan VD, Genkin MV (1998) *Nitric Oxide* 2:224–234
6. Muller B, Kleschyov AL, Stoclet JC (1996) *Br J Pharmacol* 119:1281–1285
7. Richter-Addo GB, Legzdins P (1988) *Chem Rev* 88:991–1010
8. Saraiva J, Oliveira SS, Cicillini SA, Eloy JO, Marchetti JM (2011) *J Drug Deliv* 1–16
9. Reglinski J, Butler AR, Glidewell C (1994) *Appl Organomet Chem* 8:25–31
10. Mingos DMP, Sherman DJ (1989) *Adv Inorg Chem* 34:293–393
11. Ford PC, Laverman LE (2005) *Coord Chem Rev* 249:391–403
12. King SB (2004) *Free Radical Biol Med* 37:735–737
13. Lancaster JR, Hibbs JB Jr (1990) *Proc Natl Acad Sci USA* 87:1223–1227
14. Wang PG, Xian M, Tang X, Wu X, Wen Z, Cai T, Janczuk AJ (2002) *Chem Rev* 102:1191–1200
15. Vanin AF (1991) *FEBS Lett* 289:1–3
16. Hieber W, Klingshirn W (1963) *Z Anorg Allgem Chem* 323:292
17. King B (1965) *Organometallic synthesis*, 1st edn. Academic, New York, pp 167–168
18. McBride DW, Stafford SL, Stone FGA (1962) *Inorg Chem* 1:386–388
19. Klein A, Mering Y, Uthe A, Butsch K, Schaniel D, Mockus N, Woike T (2012) *Polyhedron* 29:2553–2559
20. Li L (2002) *Commun Inorg Chem* 23:335–353
21. Mingos DMP, Ibers JA (1970) *Inorg Chem* 9:1105–1111
22. Divara M, Ghilardi CA, Sacconi L (1976) *Inorg Chem* 15:1555–1561
23. Darensbourg DJ, Decuir TJ, Stafford NW, Robertson JB, Draper JD, Reibenspies JH, Kathó A, Joó F (1997) *Inorg Chem* 36:4218–4226
24. Matsukawa S, Kuwata S, Hidai M (2000) *Inorg Chem* 39:791–798
25. Li L, Enright GD, Preston KF (1994) *Organometallics* 13:4686–4688
26. Horsken A, Zheng G, Stradiotto M, McCrory CTC, Li L (1998) *J Organomet Chem* 558:1–9
27. Allano VG, Araneo A, Bellon PL, Ciani G, Manassero M (1974) *J Organomet Chem* 67:413
28. Richter-Addo GB, Legzdins P (1992) *Metal nitrosyls*. Oxford University Press, New York, 81
29. Martin RL, Taylor D (1976) *Inorg Chem* 15:2970–2976
30. Gaughan AP, Corden BJ, Eisenberg R, Ibers JA (1974) *Inorg Chem* 13:786–791
31. Bhaduri S, Sheldrick GM (1975) *Acta Crystallogr Sect E* 31:897
32. Haymore BL, Ibers JA (1975) *Inorg Chem* 14:2610–2617
33. Kaduk JA, Ibers JA (1975) *Inorg Chem* 14:3070–3073
34. Laing M, Reimann RH, Singleton E (1970) *Inorg Chem* 18:2666–2670
35. Guillaume P, Wah HLK, Postel M (1991) *Inorg Chem* 30:1828–1831
36. Li L, Reginato N, Urschey M, Stradiotto M, Liarakos DJ (2003) *Can J Chem* 81:468–475

37. Atkinson FL, Blackwell HE, Brown NC, Connelly NG, Crossley JG, Orpen AG, Rieger AL, Rieger PH (1996) *J Chem Soc Dalton Trans* 3491–3502
38. Bryar TR, Eaton DR (1992) *Can J Chem* 70:1917–1926
39. Ray M, Bolombek AP, Hendrich MP, Yap GPA, Liable-Sands LM, Rheingold AL, Borovik AS (1999) *Inorg Chem* 38:3110–3115
40. Vanin AF, Van Faassen E (2007) *Radicals for life, the various forms of nitric oxide*. Elsevier, Oxford, pp 19–74
41. Foster MW, Cowan JA (1999) *J Am Chem Soc* 121:4093–4100
42. Heo J, Campbell SL (2004) *Biochemistry* 43:2314–2322
43. Sanina NA, Aldoshin SM (2004) *Russ Chem Bull Int Ed* 53:2428–2448
44. Lee M, Arosio P, Cozzi A, Chasteen ND (1994) *Biochemistry* 33:3679–3687
45. Reginato N, McCrory CTC, Pervitsky D, Li L (1999) *J Am Chem Soc* 121:10217–10218
46. Tsai FT, Kuo TS, Liaw WF (2009) *J Am Chem Soc* 131:3426–3427
47. Tsai ML, Liaw WF (2006) *Inorg Chem* 45:6583–6585
48. Puiu SC, Warren TH (2003) *Organometallics* 22:3974–3976
49. Dieck HT, Bruder H, Kuhl E, Junghans D, Hellfeldt K (1989) *New J Chem* 13:259–268
50. Wah HLK, Postel M, Tomi F, Mordenti L (1991) *New J Chem* 15:629–633
51. Hung MC, Tsai MC, Lee GH, Liaw WF (2006) *Inorg Chem* 45:6041–6047
52. Wang R, Wang X, Sundberg EB, Nguyen P, Grant GPG, Sheth C, Zhao Q, Herron S, Kantardjiev KA, Li L (2009) *Inorg Chem* 48:9779–9785
53. Huang HW, Tsou CC, Kuo TS, Liaw WF (2008) *Inorg Chem* 47:2196–2204
54. Enemark JH, Feltham RD (1974) *Coord Chem Rev* 13:339–406
55. Shih WC, Lu TT, Yang LB, Tsai FT, Chiang MH, Lee JF, Chiang YW, Liaw WF (2012) *J Inorg Biochem* 113:3–93
56. Crimmin MR, Rosebrugh LE, Tomson NC, Weyhermüller T, Bergman RG, Toste FD, Wieghardt K (2011) *J Organomet Chem* 696:3974–3981
57. Yeh SW, Lin CW, Li YW, Hsu IJ, Chen CH, Jang LY, Lee JF, Liaw WF (2012) *Inorg Chem* 51:4076–4087
58. Siladke NA, Meihaus KR, Ziller JW, Fang M, Furche F, Long JR, Evans WJ (2012) *J Am Chem Soc* 134:1243–1249
59. Kozhukh J, Lippard SJ (2012) *J Am Chem Soc* 134:11120–11123
60. Wright AM, Wu G, Hayton TW (2010) *J Am Chem Soc* 132:14336–14337
61. Chiou SJ, Wang CC, Chang CM (2008) *J Organomet Chem* 693:3582–3586
62. Chiang CY, Miller ML, Reibenspies JH, Darensbourg MY (2004) *J Am Chem Soc* 126:10867–10874
63. Lin Z, Lo F, Li C, Chen C, Huang W, Hsu I, Lee J, Horng J, Liaw WF (2011) *Inorg Chem* 50:10417–10431
64. Chang HH, Huang HJ, Ho YL, Wen YD, Huang WN, Chiou SJ (2009) *Dalton Trans* 6396–6402
65. Baltusis LM, Karlin KD, Rabinowitz HN, Dewan JC, Lippard SJ (1980) *Inorg Chem* 19:2627–2632
66. Wang R, Xu W, Zhang J, Li L (2009) *J Mol Struct* 923:110–113
67. Lee CM, Chen CH, Chen HW, Hsu JL, Lee GH, Liaw WF (2005) *Inorg Chem* 44:6670–6679
68. Harrop TC, Song D, Lippard SJ (2007) *J Inorg Biochem* 101:1730–1738
69. Conradie J, Quarless DA Jr, Hsu HF, Harrop TC, Lippard SJ, Koch SA, Ghosh A (2007) *J Am Chem Soc* 129:10446–10456
70. Weckler SR, Hutchinson J, Ford PC (2006) *Inorg Chem* 45:1192–1200
71. Rauchfuss TB, Weatherill TD (1982) *Inorg Chem* 21:827–830
72. Wang R, Camacho-Fernandez MA, Xu W, Zhang J, Li L (2009) *Dalton Trans* 777–786
73. Tsou CC, Lu TT, Liaw WF (2007) *J Am Chem Soc* 129:12626–12627
74. Tinberg CE, Tonzetich ZJ, Wang H, Do LH, Yoda Y, Cramer SP, Lippard SJ (2011) *J Am Chem Soc* 132:18168–18176
75. Tsou CC, Lin ZS, Lu TT, Liaw WF (2008) *J Am Chem Soc* 130:17154–17160

76. Tonzetich ZJ, Do LH, Lippard SJ (2009) *J Am Chem Soc* 131:7964–7965
77. Hsu IJ, Hsieh CH, Ke SC, Chiang KA, Lee JM, Chen JM, Jang LY, Lee GH, Wang Y, Liaw WF (2007) *J Am Chem Soc* 129:1151–1159
78. Tsai ML, Chen CC, Hsu IJ, Ke SC, Hsieh CH, Chiang KA, Lee GH, Wang Y, Liaw WF (2004) *Inorg Chem* 43:5159–5167
79. Tsai FT, Chiou SJ, Tsai MC, Tsai ML, Huang HW, Chiang MH, Liaw WF (2005) *Inorg Chem* 44:5872–5881
80. Lu TT, Chiou SJ, Chen CY, Liaw WF (2006) *Inorg Chem* 45:8799–8806
81. King SB (2004) *Free Radical Biol Med* 37:737–738
82. Ford PC (2001) *Int J Photoenergy* 3:161–169
83. Li L, Morton JR, Preston KF (1995) *Magn Reson Chem* 31:s14–s19
84. Roncaroli F, Olabe JA (2005) *Inorg Chem* 44:4719–4727
85. Lu TT, Huang WH, Liaw WF (2009) *Inorg Chem* 48:9027–9035
86. Wecksler SR, Mikhailovsky A, Korystov D, Buller F, Kannan R, Tan LS, Ford PC (2007) *Inorg Chem* 46:395–402
87. Chen TN, Lo FC, Tsai ML, Shih KN, Chiang MH, Lee GH, Liaw WF (2006) *Inorg Chim Acta* 359:2525–2533
88. Harrop TC, Tonzetich ZJ, Reisner E, Lippard SJ (2008) *J Am Chem Soc* 130:15602–15610
89. Lu TT, Tsou CC, Huang HW, Hsu IJ, Chen JM, Kuo TS, Wang Y, Liaw WF (2008) *Inorg Chem* 47:6040–6050
90. Chen YJ, Ku WC, Feng LT, Tsai ML, Hsieh CH, Hsu WH, Liaw WF, Hung CH, Chen YJ (2008) *J Am Chem Soc* 130:10929–10938
91. Harrop TC, Song D, Lippard SJ (2006) *J Am Chem Soc* 128:3528–3529
92. Sellmann D, Blum N, Heinemann FW, Hess BA (2007) *Chem Eur J* 7(9):1
93. Serres RG, Grapperhaus CA, Bothe E, Bill E, Weyhermuller T, Neese F, Wieghardt K (2004) *J Am Chem Soc* 126:5138–5153
94. Liaw WF, Chiang CY, Lee GH, Peng SM, Lai CH, Darensbourg MY (2000) *Inorg Chem* 39:480–484
95. Hsieh CH, Erdem OF, Harman SD, Singleton ML, Reijerse E, Lubitz W, Popescu CV, Reibenspies JH, Brothers SM, Hall MB, Darensbourg MY (2012) *J Am Chem Soc* 134:13089–13102
96. D'Addario S, Demartin F, Grossi L, Iapalucci MC, Laschi F, Longoni G, Zanello P (1993) *Inorg Chem* 32:1153–1160
97. Chu CTW, Lo FYK, Dahl LF (1982) *J Am Chem Soc* 104:3409–3422
98. Scott MJ, Holm RH (1993) *Angew Chem Int Ed Engl* 32:564–566
99. Geiser U, Williams JM (1998) *Acta Crystallogr C* 54:292–293
100. Kalyvas H, Coucouvanis D (2006) *Inorg Chem* 45:8462–8464
101. Barnes JC, Glidewell C, Lees A, Howie R (1990) *Acta Crystallogr C* 46:2051–2053
102. Wang R, Xu W, Zhang J, Li L (2010) *Inorg Chem* 49:4814–4819
103. Wang X, Sundberg EB, Li L, Kantardjieff KA, Herron SR, Lim M, Ford PC (2005) *Chem Commun* 477–479
104. Hess JL, Hsieh CH, Reibenspies JH, Darensbourg MY (2011) *Inorg Chem* 50:8541–8552
105. Hess JL, Hsieh CH, Brothers SM, Hall MB, Darensbourg MY (2011) *J Am Chem Soc* 133:20426–20434
106. Mingos DMP, Ibers JA (1971) *Inorg Chem* 10:1035–1042
107. Mingos DMP, Robinson WT, Ibers JA (1971) *Inorg Chem* 10:1043–1048
108. Mingos DMP, Ibers JA (1971) *Inorg Chem* 10:1479–1486
109. Tonzetich ZJ, Heroguef F, Do LH, Lippard SJ (2011) *Inorg Chem* 50:1570–1579
110. Lehnert N, Galinato MGI, Paulat F, Richter-Addo GB, Sturhahn W, Xu N, Zhao J (2010) *Inorg Chem* 49:4133–4148
111. Fry NL, Mascharak PK (2011) *Acc Chem Res* 44:289–298
112. Richter-Addo GB, Wheeler RA, Hixson CA, Chen L, Khan MA, Ellison MK, Schulz CE, Scheidt WR (2001) *J Am Chem Soc* 123:6314–6326

113. Schweitzer D, Ellison JL, Shoner SC, Lovell S, Kovacs JA (1998) *J Am Chem Soc* 120:10966–10977
114. Eroy-Reveles AA, Leung Y, Mascharak PK (2006) *J Am Chem Soc* 128:7166–7167
115. Rose MJ, Olmstead MM, Mascharak PK (2007) *J Am Chem Soc* 129:5342–5343
116. Eroy-Reveles AA, Leung Y, Beavers CM, Olmstead MM, Mascharak PK (2008) *J Am Chem Soc* 130:4447–4458
117. Rose MJ, Fry NL, Marlow R, Hinck L, Mascharak PK (2008) *J Am Chem Soc* 130:8834–8846
118. Lee J, Kovalevsky AY, Novozhilova IV, Bagley KA, Coppens P, Richter-Addo GB (2004) *J Am Chem Soc* 126:7180–7181
119. Cheng L, Chen L, Chung HS, Khan MA, Richter-Addo GB, Young VG Jr (1998) *Organometallics* 17:3853–3864
120. Richter-Addo GB, Hodge SJ, Yi GB, Khan MA, Ma T, Van Caemelbecke E, Guo N, Kadish KM (1996) *Inorg Chem* 35:6530–6538
121. Kadish KM, Adamian VA, Van Caemelbecke E, Tan Z, Tagliatesta P, Bianco P, Boschi T, Yi GB, Khan MA, Richter-Addo GB (1996) *Inorg Chem* 35:1343–1348
122. Rose MJ, Betterley NB, Mascharak PK (2009) *J Am Chem Soc* 131:8340–8341
123. Madhani A, Patra AK, Miller TW, Eroy-Reveles AA, Hobbs AJ, Fukuto JM, Mascharak PK (2006) *J Med Chem* 49:7325–7330
124. Schweitzer D, Ellison JL, Shoner SC, Lovell S, Kovacs JA (1998) *J Am Chem Soc* 120:9237–9245
125. Mingos DMP (1973) *Inorg Chem Corres* 12:1209–1211
126. Hoffmann R, Chen MML, Elian M, Rossi AR, Mingos DMP (1974) *Inorg Chem* 13:2666–2675
127. Bell LK, Mason J, Mingos DMP, Tew DG (1983) *Inorg Chem* 22:3497–3502
128. Mason J, Mingos DMP, Sherman D, Wardleb RWM (1984) *J Chem Soc Chem Commun* 1223–1227
129. Mason J, Mingos DMP, Schaefer J, Sherman D, Stejskal EO (1985) *J Chem Soc Chem Commun* 444–446
130. Nicholson T, Muller P, Davison A, Jones AG (2006) *Inorg Chim Acta* 359:1296–1298
131. Xu HJ, Lu XY, Cheng Y, Sun JF, Chen XT, Xue ZL (2009) *Organometallics* 28:6687–6694
132. Lin CH, Chen CG, Tsai ML, Lee GH, Liaw WF (2008) *Inorg Chem* 47:11435–11443
133. Chen HW, Lin CW, Chen CC, Yang LB, Chiang MH, Liaw WF (2005) *Inorg Chem* 44:3226–3232
134. Tennyson AG, Dhar S, Lippard SJ (2008) *J Am Chem Soc* 130:15087–15098
135. Tsai ML, Hsieh CH, Liaw WF (2007) *Inorg Chem* 46:5110–5117
136. Cheng L, Powell DR, Khan MA, Richter-Addo GB (2001) *Inorg Chem* 40:125–133
137. Hsieh CH, Darensbourg MY (2010) *J Am Chem Soc* 132:14118–14125
138. Hayton TW, Legedins P, Sharp WB (2002) *Chem Rev* 102:935–991
139. Bitterwolf TE (2006) *Coord Chem Rev* 250:388–413
140. Graham PM, Buschhaus MSA, Baillie RA, Semproni SP, Legzdins P (2010) *Organometallics* 29:5068–5072
141. Schomaker JM, Boyd WC, Stewart IC, Toste FD, Bergman RG (2008) *J Am Chem Soc* 130:3777–3779
142. Crimmin MR, Bergman RG, Toste FD (2011) *Angew Chem Int* 50:4484–4487
143. Tomson NC, Crimmin MR, Petrenko T, Rosebrugh LE, Sproules S, Boyd WC, Bergman RG, DeBeer S, Toste FD, Wieghardt K (2011) *J Am Chem Soc* 133:18785–18801

Mechanisms of Nitric Oxide Reactions Mediated by Biologically Relevant Metal Centers

Peter C. Ford, Jose Clayston Melo Pereira, and Katrina M. Miranda

Abstract Here, we present an overview of mechanisms relevant to the formation and several key reactions of nitric oxide (nitrogen monoxide) complexes with biologically relevant metal centers. The focus will be largely on iron and copper complexes. We will discuss the applications of both thermal and photochemical methodologies for investigating such reactions quantitatively.

Keywords Copper · Heme models · Hemes · Iron · Metalloproteins · Nitric oxide

Contents

1	Introduction	101
2	Metal-Nitrosyl Bonding	101
3	How Does the Coordinated Nitrosyl Affect the Metal Center?	104
4	The Formation and Decay of Metal Nitrosyls	107
4.1	Some General Considerations	107
4.2	Rates of NO Reactions with Hemes and Heme Models	110
4.3	Mechanistic Studies of NO “On” and “Off” Reactions with Hemes and Heme Models	115
4.4	Non-Heme Iron Complexes	116
4.5	Other Metal Centers of Biological Interest	118
5	Reductive Nitrosylation and Other Reactions of Coordinated NO	120
5.1	Reactions of Iron(III) Nitrosyls with Nucleophiles	121
5.2	Reduction of Copper(II) Complexes by NO	122
5.3	Protonation of Metal Nitrosyls	127
5.4	Reactions with Dioxygen	128
6	Summary	130
	References	131

P.C. Ford (✉) and J.C.M. Pereira
Department of Chemistry and Biochemistry, University of California, Santa Barbara,
CA 93106-9510, USA
e-mail: ford@chem.ucsb.edu

K.M. Miranda
Department of Chemistry and Biochemistry, University of Arizona, Tucson, AZ, USA
e-mail: kmiranda@email.arizona.edu

Abbreviations

AN	Acetonitrile
aq	Aqueous
Cbl	Cobalamin
cGMP	Cyclic guanylyl monophosphate
CysSH	Cysteine
Cyt ^{II}	Ferrous cytochrome <i>c</i>
DAC	Bis(9-Anthracylmethyl)cyclam
DFT	Density functional theory
dmp	2,9-Dimethyl-1,10-phenanthroline
DNIC	Dinitrosyl iron complexes
dpp	2,9-Diphenyl-1,10-phenanthroline
EDTA ⁴⁻	Ethylenediaminetetraacetate
EPR	Electron paramagnetic resonance
F ₈ Por	Tetrakis(2,6-difluorophenyl)-porphyrinato
GSH	Glutathione
GSNO	<i>S</i> -Nitrosoglutathione
GTP	Guanylyl triphosphate
Hb	Hemoglobin
Mb	Myoglobin
metMb	Metmyoglobin
MLCT	Metal-to-ligand charge transfer
MNIC	Mononitrosyl iron complexes
NiR	Nitrite reductase
NOS	Nitric oxide synthase
Por	Porphyrinato
PPIX	Protoporphyrin IX
RBS	Roussin's black salt
RRE	Roussin's red esters
RRS	Roussin's red salt
sGC	Soluble guanylyl cyclase
THF	Tetrahydrofuran
TMPS	Tetra(sulfonato-mesityl)porphyrinato
TPP	Tetraphenylporphyrinato
TPPS	Tetra(4-sulfonatophenyl)porphyrin
tren	Bis-(2-aminoethyl)amine
UV	Ultraviolet

1 Introduction

From the early studies leading to the discovery that nitric oxide (nitrogen monoxide) plays important regulatory roles in mammalian physiology, it has been clear that this bioactivity is closely connected to the interactions of NO with metal centers [1–3]. A key target is the ferroheme enzyme soluble guanylyl cyclase (sGC), which catalyzes the transformation of guanylyl triphosphate (GTP) to give the secondary messenger cyclic guanylyl monophosphate (cGMP), and the interactions of NO with this and with other metalloproteins and model compounds have been widely studied [4]. A critical feature of sGC activation is that it is triggered by very low concentrations of NO (as low as 1 nM) in aerobic media [5], and this sensitivity requires a remarkable selectivity of this enzyme for NO [6]. Furthermore, while NO may be generated by acid-catalyzed nitrite disproportionation, the principal biosynthetic pathways endogenous to mammals involve constitutive and inducible forms of the enzyme nitric oxide synthase (NOS), which are also heme proteins [7]. So, heme centers are involved both in the endogenous formation of NO and as one of the primary targets.

Thus, to understand the physiological mechanisms of NO, we need to define its direct interactions with metal centers. This includes visualizing the products formed and elucidating the dynamics and thermodynamics of these reactions. Furthermore, one needs to understand the effect of NO coordination both on the properties of the resulting metal complexes and on the reactivity of coordinated NO itself. Such effects may involve structural and reactivity changes at protein sites remote from the metal center, in analogy to the cooperative effects seen when dioxygen binds to hemoglobin. Similarly, one needs to consider the interactions of other NO_x derivatives with metals, given extensive biomedical interest in the therapeutic, signaling, and/or deleterious effects of nitroxyl (HNO), nitrite ion (NO_2^-), nitrogen dioxide, and peroxynitrite (OONO^-) and more complex species such as *S*-nitrosothiols (RSNO) and *N*-nitrosoamines (RR'NNO).

The goal of this article is to outline fundamental chemical processes that may be relevant to the mammalian chemical biology of NO and other key species. The focus will be on the dynamics, thermodynamics, and mechanisms of the formation and subsequent reactions of various metal-NO complexes. This will not be a comprehensive review of the huge body of work reported over the past several decades, but a selective overview of these topics.

2 Metal-Nitrosyl Bonding

NO coordinates to numerous transition metals, but we will largely focus on metal centers having biological relevance, principally iron (both heme and non-heme systems) and copper. NO typically coordinates to a metal center via the nitrogen atom, and in such M–NO complexes the character of this ligand can range from a

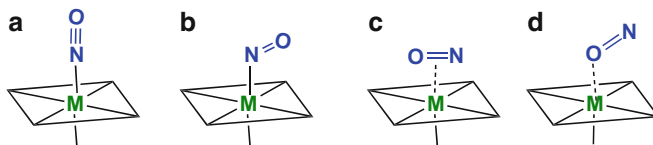
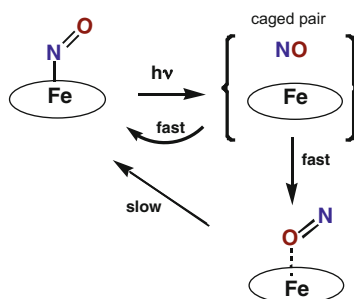


Fig. 1 Linear, bent, side-on bonding, and isonitrosyl forms of metal-NO complexes



Scheme 1 Likely pathway for forming the isonitrosyl complex $\text{Fe}^{\text{II}}(\text{Por})(\text{ON})$ by visible range photolysis of low-temperature solids (25 K KBr) containing $\text{Fe}^{\text{II}}(\text{Por})(\underline{\text{NO}})$ (circles represent a porphyrato ligand, Por^{2-})

nitrosonium cation (NO^+) to a nitroxyl anion (NO^-) or somewhere in between [8]. The nitrosonium cation would be the case when considerable charge transfer from the NO to an oxidizing metal center (such as an Fe(III) heme) has occurred, leaving NO^+ , which is isoelectronic to CO. Correspondingly, the $\text{M}-\text{NO}^+$ bond angle is roughly linear ($\sim 180^\circ$, Fig. 1a). A coordinated nitroxyl might be seen for the interaction of NO with a reducing metal, where charge transfer has occurred in the opposite direction. In that case, a more acute $\text{M}-\text{NO}$ bond angle of $\sim 120^\circ$ (Fig. 1b) would be anticipated. Numerous metal-NO complexes fall between these extremes, as do the corresponding bond angles (see below).

There are limited examples of other types of coordination involving side-on bonding or O-coordination (Fig. 1c, d). These have largely been seen for metastable complexes generated in low-temperature solids by photochemical excitation of stable nitrosyl complex, and both types rearrange to the more stable N-coordinated form upon warming as illustrated in Scheme 1 [9, 10]. A side-on bonding mode with the NO bond perpendicular to the metal-ligand axis has also been demonstrated in the crystal structure of a copper nitrite reductase (NiR) prepared by infusing crystals of the wild-type protein with NO [11, 12]. Computational studies using density functional theory (DFT) showed the end-on $\text{Cu}-\text{NO}$ structure to be ~ 40 kJ more stable than the side-on isomer for model complexes, although the difference was smaller for the protein [13, 14].

Qualitative theoretical discussions of metal-NO complexes $\text{L}_x\text{M}(\text{NO})$, published sometime ago used Walsh orbital energy diagrams to predict the $\text{M}-\text{NO}$ bond angles [15, 16]. The metal-nitrosyl unit was further described in terms of the

formulation $\{MNO\}^n$, where n is the sum of the metal d -electrons and the nitrosyl π^* electrons [16]. Other ligands influence the structure and the nature of the $M-NO$ bonding. For example, when there is a strong axial perturbation, as is the case with the metalloproteins, the $M-N-O$ angle is predicted to be linear for $n \leq 6$ but bent for $n > 6$. This treatment is generally considered a good place to start discussing metal nitrosyls.

The ability to form a stable nitrosyl complex and the resulting structure of that species depend strongly on the oxidation state of the metal center. However, assigning an oxidation state to the metal of a $M-NO$ complex is subject to considerable ambiguity, since NO is by no means an innocent ligand. It might minimize confusion to begin by treating NO as a neutral ligand and then examining the system carefully to see if it is likely that charge transfer has occurred to or from the nitrosyl ligand from or to the metal center. For example, let us compare the NO adducts $Mn^{II}(TPP)(NO)$, $Fe^{II}(TPP)(NO)$, and $Co^{II}(TPP)(NO)$ (TPP^{2-} = the tetraphenylporphyrinato dianion), which can be prepared in each case by the reaction of the $M^{II}(TPP)$ complex with free NO . These nitrosyl adducts display the respective $M-N-O$ bond angles 176.2° , 149.2° , and 124.8° (180 K) [17]. The first is consistent with the bond angle predicted above for the $\{MnNO\}^6$ formulation as well as with assigning the charge distribution as $Mn^I(TPP)(NO^+)$, since NO^+ is isoelectronic with CO and the latter ligand generally coordinates linearly. The structure of the cobalt product would be consistent with that predicted for the $\{CoNO\}^8$ formulation or with assigning the charge distribution as a $Co(III)$ nitroxyl complex $Co^{III}(TPP)(NO^-)$. Notably, the $M-N-O$ angle seen for the $Fe^{II}(TPP)(NO)$ adduct is intermediate between these extremes, and this is generally considered a ferrous complex $Fe^{II}(TPP)(NO)$. Oxidation gives the $\{FeNO\}^6$ system $Fe^{III}(TPP)(NO)$, which is isoelectronic to $Mn^{II}(TPP)(NO)$ and is predicted (and found) to be nearly linear.

The metal- N_{NO} bond lengths for the above $M^{II}(TPP)(NO)$ complexes follow the order 1.644, 1.717, and 1.837 Å for $M = Mn, Fe, \text{ or } Co$, respectively [17]. In addition, structural studies also show that the $Fe-N_{NO}$ bond is tilted a few degrees from perpendicular to the porphyrin plane in $Fe^{II}(TPP)(NO)$, and this is common for ferrous heme nitrosyls [18].

Non-heme iron nitrosyl complexes include the sodium salt of the nitroprusside ion $Fe(CN)_5(NO)^{2-}$, which has long been used as a vasodilator in hypertensive emergencies [19]. Chemical mechanisms potentially relevant to its bioactivity are discussed later in this review. Figure 2 illustrates some other non-heme nitrosyl complexes. Roussin's red salt (RRS) and Roussin's black salt (RBS) anions are iron/sulfur/nitrosyl clusters that have been known since the mid-nineteenth century [20, 21]. These salts and certain Roussin's red esters (RREs) have been studied as potential sources of therapeutic NO either thermally [22] or photochemically activated [23–29]. In addition, both mononitrosyl iron complexes (MNICs) and dinitrosyl iron complexes (DNICs) are drawing increasing attention with regard to their potential roles in mammalian physiology [30–34]. The structures drawn in Fig. 2 are qualitative representations of structures that have been determined using X-ray crystallography [35–38].

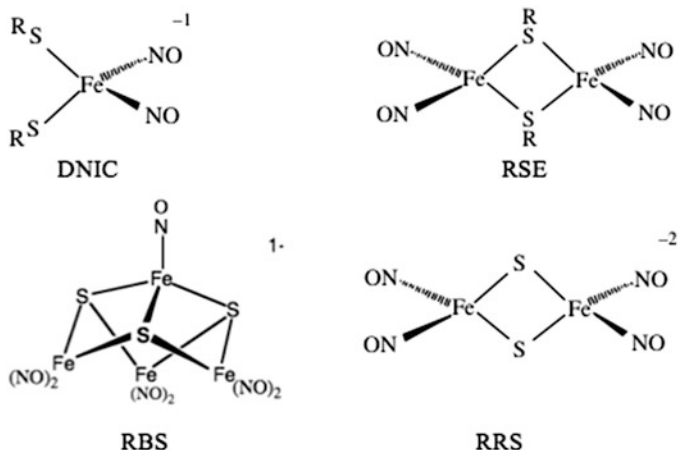


Fig. 2 Several representative non-heme iron complexes. *DNIC* dinitrosyl iron complex, *RBS* Roussin's black salt anion, *RRS* Roussin's red salt anion, *RSE* Roussin's red salt ester

Although quite a few iron complexes of NO have been isolated and characterized structurally, the list of such copper compounds is considerably shorter. In addition to the copper-NO structure described above for a NiR protein [12], the X-ray structures of a small number of model compounds have been described [13, 39, 40]. In contrast to the side-on bonded structure in the protein, the $\{\text{CuNO}\}^{11}$ complexes formed from the reaction of Cu(I) species and free NO have linear structures. Surprisingly, the structurally characterized $\{\text{CuNO}\}^{10}$ species, which is formed from the reaction of $[\text{NO}][\text{PF}_6]$ with copper in nitromethane solution, has a strongly bent structure (Cu-N-O angle of 121°) [41]. While this suggests a $\text{Cu}^{\text{III}}(\text{NO}^-)$ formulation, the NO stretching frequencies ($\nu_{\text{NO}} = 1,933 \text{ cm}^{-1}$) are much higher than expected for a nitroxy anion, leading to the suggestion that this complex should be formulated as $\text{Cu}^{\text{II}}(\text{NO})$. Notably, the complex is not very stable, and NO readily dissociates from the Cu coordination site.

Table 1 summarizes some structural and IR spectral data for examples of heme and non-heme iron nitrosyls and of copper nitrosyls [17, 18, 36–46].

3 How Does the Coordinated Nitrosyl Affect the Metal Center?

Electron paramagnetic resonance (EPR) spectroscopy provides insight into the electronic structure of metal nitrosyls. For example, the high-spin manganese(III) tetraphenylporphyrinato complex, $\text{Mn}^{\text{III}}(\text{TPP})(\text{CN})$ ($3d^4$, $S = 2$), reacts with the free radical NO to give $\text{Mn}(\text{TPP})(\text{CN})(\text{NO})$ for which the EPR spectrum indicates an $S = 1/2$ spin state [47]. Similarly, the NO adduct of the chromium(II)

Table 1 M–NO and N–O bond lengths, M–N–O angles and IR NO stretching frequencies (ν_{NO}) for selected iron and copper nitrosyl complexes

Metal complex ^a	{MNO} ⁿ ^b	M–NO (Å) ^c	N–O (Å) ^c	Fe–N–O angle (°) ^c	ν_{NO} (cm ⁻¹)	References
<i>Heme models and proteins</i>						
Fe ^{II} (TPP)(NO)	{FeNO} ⁷	1.717	1.122	149.2	1,670	[42]
Fe ^{II} (T _{piV} PP)(NO)	{FeNO} ⁷	1.716	1.197	143.8	1,665	[43]
Fe ^{II} (TPP)(NO)(MeIm)	{FeNO} ⁷	1.743	1.121	142.1	1,625	[44]
hh-Mb(NO)	{FeNO} ⁷	1.87	1.20	144		[18]
		2.13	1.17	120		
sw-Mb(NO)	{FeNO} ⁷	1.87	1.15	112		[46]
T-state-h-Hb(NO)						
α-heme	{FeNO} ⁷	1.74	1.13	150		[47]
β-heme		1.75	1.15			
[Fe ^{III} (OEP)(NO)] ⁺	{FeNO} ⁶	1.644	1.112	176.9	1,868	[17]
[Fe ^{III} (TPP)(H ₂ O)(NO)] ⁺	{FeNO} ⁶	1.652	1.150	174.4	1,937	[17]
[Fe ^{III} (OEP)(NO)(MeIm)] ⁺	{FeNO} ⁶	1.647	1.135	177.3	1,921	[17]
<i>Non-heme iron complexes</i>						
Na ₂ [Fe(CN) ₅ (NO)]	{FeNO} ⁶	1.63	1.13	178.3	1,945	[35]
Fe ₂ [(μ-SC ₂ H ₅) ₂ (NO) ₄]	{Fe(NO) ₂ } ⁹	1.675 (ave.)	1.171 (ave.)	168.5 (ave.)	1,774 s, 1,749 s, 1,819 w	[36]
[N(PPh ₃) ₂][Fe(NO) ₂ I ₂]	{Fe(NO) ₂ } ⁹	1.68	1.145 (ave.)	166 (ave.)	1,775 1,719	[37]
<i>Copper complexes</i>						
Cu(TpRR')(NO)	{CuNO} ¹¹	1.759	1.108	163.4	1,712	[42]
Cu(L3')(NO)	{CuNO} ¹¹	1.786	1.035	176.4	1,742	[43]
[Cu(NM) ₅ (NO)][PF ₆] ₂	{CuNO} ¹⁰	1.955	1.109	121.0	1,933	[41]

^aTpRR' tris(3-R,5-R'-pyrazolyl)hydroborate, L3' HC(3-tBu-5-iPrpz)₃, 4-Me-pip 4-methyl-piperidine, MeIm 1-methyl imidazole, NM nitromethane. See Sect. 6 for other abbreviations

^bFeltham/Enemark parameter *n* for the notation {MNO}^{*n*}, where *n* is the total number of d-electrons from the metal and π* electrons from NO [16]

^cAs determined by X-ray crystallography

porphyrin Cr^{II}(TPP) ($3d^4$, $S = 2$) exhibits an EPR spectrum consistent with an $S = 1/2$ spin state, while the reaction of NO with Mn^{II}(TPP) or Fe^{III}(Por) ($S = 5/2$) gives adducts with $S = 0$ [47, 48]. Thus, NO coordination usually gives strong field, low-spin complexes with such metal centers.

Similarly, the high-spin-state $3d^6$ ferrous analogs Fe^{II}(Por) ($S = 2$) coordinate NO to give low-spin ($S = 1/2$) Fe^{II}(Por)(NO) complexes. The EPR spectra of these complexes show super hyperfine splitting due to the nitrogen atom of the axial NO, indicating the unpaired electron density to be largely in the d_{z^2} orbital of the iron [47]. The spectra display three unique *g* values consistent with the non-axial symmetry and the bent form of the Fe–N=O moiety, in accordance with the X-ray structure (Table 1). Nitrosyl adducts of ferroheme proteins with a histidine residue in the *trans* (proximal) axial site display N hyperfine splitting of both NO and the histidine imidazole [49].

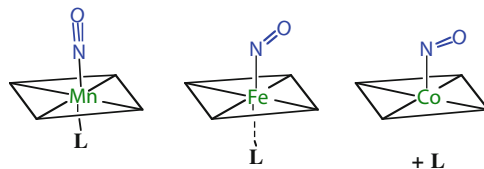


Fig. 3 Illustrated is the effect of electronic configuration on the bonding between NO and a divalent metal tetraphenylporphyrinato complex and the effect of NO coordination on the proximal ligand. Mn(II) gives a $\{\text{MnNO}\}^6$ species with a linear Mn–NO bond angle and a stable 6-coordinate complex. Fe(II) gives a $\{\text{FeNO}\}^7$ species with a bent Fe–NO bond angle and a weaker and more labile proximal ligand. Co(II) gives a $\{\text{CoNO}\}^8$ species that has a more acute M–NO bond angle and is five-coordinate. In all cases, coordination of NO switches the high spin $\text{M}^{\text{II}}(\text{TPP})$ complexes from high spin to low spin

The optical spectra of metalloporphyrins are dominated by characteristic π – π^* porphyrin ligand bands in the near UV and visible regions [50]. The spectral shifts induced by NO coordination can be diagnostic, especially in solution studies [47, 51].

For a six-coordinate $\text{L}_5\text{M}(\text{NO})$ complex, the model described above for $\{\text{MNO}\}^n$ complexes also predicts that going from $n = 6$ to $n = 7$ will weaken the proximal M–L bond *trans* to the NO owing to the axial σ -antibonding nature of the iron d_{z^2} orbital where much of the added electron density localizes [16]. This effect is demonstrated by structural studies of the porphyrin complex $\text{M}^{\text{II}}(\text{TPP})(\text{L})(\text{NO})$ ($\text{L} = 4$ -methylpiperidine) [52]. For $\text{M} = \text{Mn}^{\text{II}}$ ($n = 6$), not only is the Mn–NO angle nearly linear (176°); the Mn– N_{pip} bond length is relatively short (2.20 Å). For $\text{M} = \text{Fe}^{\text{II}}$ ($n = 7$), the Fe–NO angle is bent to 142° , and the bond to the methylpiperidine is considerably weakened (Fe– $\text{N}_{\text{pip}} = 2.46$ Å). For $\text{M} = \text{Co}^{\text{II}}$ ($n = 8$), the Co–NO angle is even sharper, and a stable complex with methylpiperidine could not be isolated. As we will see below, such a perturbation, which is illustrated in Fig. 3, can have a profound impact on the activity of metalloproteins.

It was on the basis of this *trans* labilizing effect for the $n = 7$ case that Traylor and Sharma proposed a mechanism for sGC activation by NO [53]. Soluble guanylyl cyclase is a heme enzyme with a $\text{Fe}^{\text{II}}(\text{PPIX})$ (“hemin,” PPIX = protoporphyrin IX) as the metal center with an open axial coordination site (the distal site). The *trans*, or proximal site, is occupied by a histidine nitrogen. Coordination of NO to the heme center gives the $\{\text{FeNO}\}^7$ complex, and the associated *trans*-influence on the metal-ligand bonding weakens the proximal histidine-iron bond. The result is a change in the protein conformation that activates the enzyme by several orders of magnitude. This model follows an earlier discussion of the electronic origins of the NO induced *trans*-effect in Fe^{II} nitrosyl complexes introduced by Mingos in 1973 [16]. It also follows the application of this concept by Perutz and coworkers [54] to explain different quaternary structural changes induced by the addition of inositol hexaphosphate to the O_2 , CO, and NO adducts of hemoglobin.

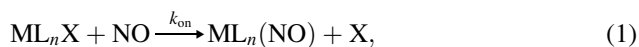
An impressive test of the Traylor/Sharma model for sGC activation by NO was offered by Burstyn and coworkers [55], who investigated the activities of non-native sGC prepared by substituting Mn^{II}(PPIX) and Co^{II}(PPIX) for the heme of the native enzyme. Addition of NO failed to activate sGC(Mn) above basal activity, presumably because the proximal histidine was not labilized in this {MnNO}⁶ complex. In contrast, NO addition to sGC(Co) giving a {CoNO}⁸ complex resulted in even greater activity than with sGC that had been reconstituted with heme. The overall trend sGC(Co)(NO) > sGC(Fe)(NO) >> sGC(Mn)(NO) substantiates the Traylor/Sharma hypothesis [53] that the *trans*-effect of NO on proximal ligand lability is responsible for the activation of wt-sGC by NO. (It should be noted, however, that subsequent studies of sGC activation have proposed additional subtleties, including possible involvement of a second NO [56].)

The effect of NO coordination on the ligands *trans* to the M–NO bond has also been addressed computationally for several {MNO}⁶ and {MNO}⁷ systems [57–62]. For the latter complexes the interaction between the axial *d*_{z²} orbital of the metal and the half-filled π* orbital of the bent nitrosyl ligand leads to weakening of the bond to the ligand *trans* to the nitrosyl as suggested by the Traylor/Sharma hypothesis. Correspondingly, a strongly bonding proximal ligand can weaken the M–NO bond in heme nitrosyl complexes, and this property may play an important role in labilizing NO from the ferroheme center in certain complexes (see below).

4 The Formation and Decay of Metal Nitrosyls

4.1 Some General Considerations

In this section we will be concerned with the reaction of a metal center with NO to form a metal-nitrosyl complex ((1), L and X are other ligands) as well as the reverse, the dissociation, or displacement of a coordinated NO (2). Although M–NO species can be formed by various pathways including the reduction of nitrite ion, the direct reaction is especially relevant to potential roles of the free NO generated by nitric oxide synthase in tissue or various biological fluids. Thus, it is necessary to have a sound understanding of the rate laws and dynamics of such reactions and of the mechanisms by which they proceed. The reverse reaction is equally of interest, given that this step may be a key determinant in the formation of NO from NOS among various biological roles. In general, the mechanisms for the forward and back reactions will occur along analogous reaction coordinate(s) as dictated by the “principle of microscopic reversibility.” Much of our focus here will be on reactions involving either heme iron or non-heme iron.





Scheme 2 Formation of a geminate pair of a diatomic molecule AB and the metal complex L_nM prepared either by flash photolysis of the AB complex or by diffusion of AB to L_nM



Since NO is a free radical, a key question is whether its ligand substitutions on metal centers occur by mechanisms analogous to those of other small ligands such as CO that are not free radicals. Various studies have shown a substitution reactivity pattern for NO similar to that seen for other Lewis bases; however, there clearly are differences. Since the odd electron of NO resides in the π^* orbital, it very likely does not become involved in the overall bonding until the metal-NO bond is largely formed, so in this regard, a key question might be whether the transition state lies early or late along the reaction coordinate.

One example where the reactivity difference between NO and CO is quite apparent concerns the back reaction of the geminate pairs $\{L_nM, AB\}$ formed by flash photolysis¹ of a L_nM-AB complex (Scheme 2, AB = NO, CO, or similar small molecule). An analogous encounter pair would also be expected to form by the diffusion of L_nM and AB together. For cases where L_nM is incorporated into a protein, such as the heme centers in myoglobin (Mb) or hemoglobin, ultrafast laser flash photolysis has been used to probe the dynamics of such geminate pairs. Typically the kinetics display significant differences between NO and CO, the recombination of the metal center with NO being much faster. In this context, Fig. 4 illustrates the different ΔG^\ddagger barriers for geminate recombination of ferrous Mb with NO, O₂, and CO [63]. The barrier for the recombination with NO is so small that very little NO escapes from the protein pocket upon flash photolysis of the Mb(NO) adduct owing to efficient recombination. In contrast, the barrier is much larger for the recombination with CO, so the quantum yields for photo-induced release of CO from Mb(CO) are much greater. These differences have been attributed in part to the required spin-state changes undertaken by the Mb upon coordination of these ligands [64, 65]. Interpreting these kinetics data required proposing a distribution of geminate pair configurations and protein conformations, each characterized by its own recombination rate [66, 67]. A similar behavior has been noted for other heme proteins [68].

¹The flash photolysis kinetics studies generally employ a pump-probe approach. Typically, the pump pulse is delivered from a laser. The time frame of the experiment will depend in part upon the length of the laser pulse, which in some systems can be as short as a few fs. The probe can be a continuous or pulsed source at wavelengths ranging from the ultraviolet into the infrared depending upon the detection system, the time constant of which is typically matched to that of the pump system.

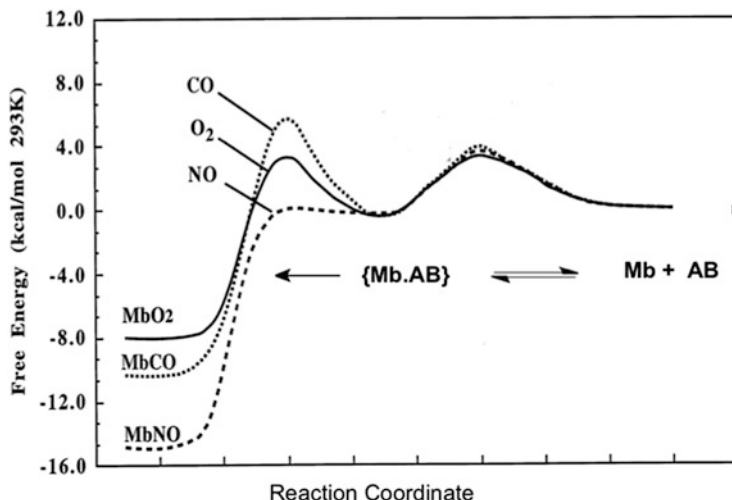
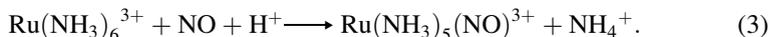
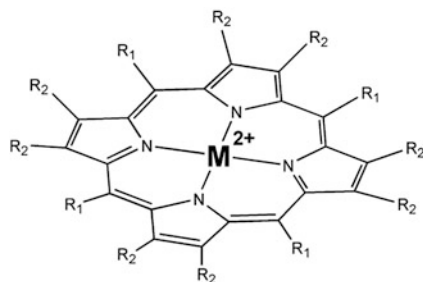


Fig. 4 Illustration of the different barriers defining the kinetics of the geminate recombination of Mb with CO, O₂, or NO (adapted from [63])

Another example where ligand free radical character apparently plays a role is the slow reaction of NO with the d^5 ruthenium(III) complex ion $\text{Ru}(\text{NH}_3)_6^{3+}$ (3). Taube and coworkers [69] studied the aqueous solution kinetics of this process and found the second-order rate constant to be much larger ($k_{\text{NO}} = 0.2 \text{ M}^{-1} \text{ s}^{-1}$ at 298 K) than the replacement of NH_3 by typical Lewis bases such as water. As a result these workers concluded that the reaction proceeds by an associative pathway, whereby the paramagnetic Ru(III) center engages the NO radical to give a seven-coordinate intermediate $[\text{Ru}(\text{NH}_3)_6(\text{NO})]^{3+}$, which then loses NH_3 . This mechanism gains further support from subsequent studies of the temperature [70] and hydrostatic pressure effects [71] on the kinetics that determined the activation enthalpy ΔH^\ddagger to be small (36 kJ mol^{-1}), the activation entropy ΔS^\ddagger to be large and negative ($-138 \text{ J K}^{-1} \text{ mol}^{-1}$), and the activation volume ΔV^\ddagger also to be large and negative ($-13.6 \text{ cm}^{-3} \text{ mol}^{-1}$).



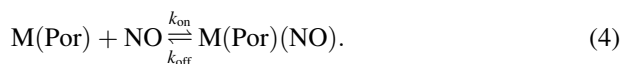
Interestingly, Armor and Pell [70] found entirely different products when the reaction of $\text{Ru}(\text{NH}_3)_6^{3+}$ with NO was carried out in alkaline solution. Above pH 8.3, the sole ruthenium product was the Ru(II) dinitrogen complex $\text{Ru}(\text{NH}_3)_5(\text{N}_2)^{2+}$. Under these conditions the dominant reaction is not ligand substitution but instead appears to be NO attack on a coordinated amide ligand ($-\text{NH}_2^-$) coupled with reduction of the ruthenium [72]. Although this is an unusual mechanism, we will see below that a similar pathway can be invoked to describe the reactivity of certain copper(II) complexes used as NO sensors.



Scheme 3 Illustration of some M(Por) complexes are discussed here. TPP has $R_1 = \text{Ph}$ and $R_2 = \text{H}$. TPPS is the same except that the phenyl groups are sulfonated to provide water solubility, and OEP has $R_1 = \text{H}$ and $R_2 = \text{Et}$. Porphinato, which is often used in computational modeling, has $R_1 = \text{H}$ and $R_2 = \text{H}$

4.2 Rates of NO Reactions with Hemes and Heme Models

Given their importance to the chemical biology of NO, it is not surprising that the formation and decay of nitrosyl complexes of heme proteins and of ferrous and ferric porphyrins heme models (Scheme 3) have been subject to considerable scrutiny. The very strong UV/visible absorptions of the metalloporphyrins and the sensitivity of these bands to the nature of the axial ligands make these systems ideal for using optical spectroscopy to follow the reaction dynamics with experimental time constants ranging from hours to less than a picosecond. The biological relevance of the “on” and “off” reactions (4) is emphasized by noting that the activation of sGC involves such an “on” reaction where the acceptor site of sGC is a Fe^{II} (PPIX) moiety. Nitric oxide effects such as cytochrome oxidase inhibition also involve coordination at heme iron, so delineating the “on” reaction dynamics is crucial to understanding NO biochemistry. Similarly, processes such as sGC deactivation and NO generation by NOS must involve Fe–NO bond labilization, so the “off” reaction dynamics are equally important.



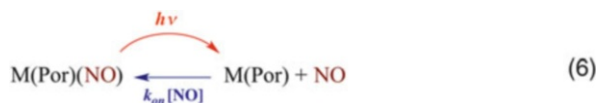
Early flash photolysis studies of nitrosyl heme protein and heme model complexes [73–77] actually preceded recognition of NO’s importance as a bioregulator. For example, flash lamp photolysis techniques were used to determine quantum yields (Φ_{dis})² for CO, O₂, and NO release from the respective myoglobin complexes as ~ 1.0 , $< 10^{-2}$ and $< 10^{-3}$, while photo-induced NO loss from the ferric

²The quantum yield Φ is a quantitative measure of the photoreaction efficiency and can be defined as the number of moles of the photoproduct formed (either transiently or permanently) per Einstein of light absorbed by the system.

metmyoglobin analog metMb(NO) gave a Φ_{dis} of ~ 1.0 [75]. Subsequent studies using faster ns laser flash photolysis techniques [76] reported a Φ_{dis} of 0.1 for NO loss from the ferrous model heme complex $\text{Fe}^{\text{II}}(\text{PPIX})(1\text{-MeIm})(\text{NO})$, much larger than for Mb(NO) but still significantly less than unity. The larger Φ_{dis} for $\text{Fe}^{\text{II}}(\text{PPIX})(1\text{-MeIm})(\text{NO})$ relative to Mb(NO) was interpreted in terms of a mechanism in which NO photolabilization first gives a {heme:NO} “encounter pair” surrounded by a solvent cage or embedded in a protein pocket as illustrated above in Scheme 2. Separation of this geminate pair was presumed to be much more facile for the solvated heme model than from the protein pocket. The result is that the NO undergoes recombination with the metal in the latter case more readily than it does diffusion away to give net ligand labilization. This scheme has been confirmed by a number of ultrafast flash photolysis studies that observed the geminate pair directly and have probed the influence of protein structure (as modified by site-directed mutagenesis) on the efficiency and dynamics of the ligand escape relative to recapture [63, 66, 68, 78, 79].



The much higher net photolability of nitrosyl metalloporphyrins in the absence of the protein was further demonstrated by ns laser flash photolysis (355 nm) studies of the ferrous complexes $\text{Fe}^{\text{II}}(\text{TPP})(\text{NO})$ in benzene solution [80] and $\text{Fe}^{\text{II}}(\text{TPPS})(\text{NO})$ (TPPS = tetra(4-sulfonatophenyl)porphyrin) in aqueous solution [81]. In these cases, Φ_{dis} values for NO photolabilization were 0.5 and 0.16, respectively. However, for such measurements, the measured value Φ_{dis} may be dependent upon the time interval of observation. If the back reaction to re-form the original complex is facile (6), products initially formed by the photochemical step may have low steady-state concentrations; thus, the apparent Φ_{dis} values measured under low-intensity continuous photolysis would be small. However, the products would be directly observable using flash photolysis techniques with the appropriate time resolution.



NO photodissociation from nitrosyl metalloporphyrins is commonly reversible, so pulsed laser techniques are well suited for investigating the kinetics of the nitrosylation reaction. In such studies, flash photoexcitation using a pulsed laser is used to labilize NO from the $\text{M}(\text{Por})(\text{NO})$ precursor, and subsequent relaxation of the non-steady-state system back to equilibrium (4) is monitored spectroscopically, usually in the presence of excess NO (Fig. 5) [82]. Under these conditions, the transient spectra would decay exponentially to give the observed rate constant k_{obs} for the return of the system to equilibrium. For the simple model photoreaction indicated by (4), a plot of k_{obs} vs. NO concentration should be linear according to (7), where the slope k_{on} equals the rate constant for the second-order thermal back

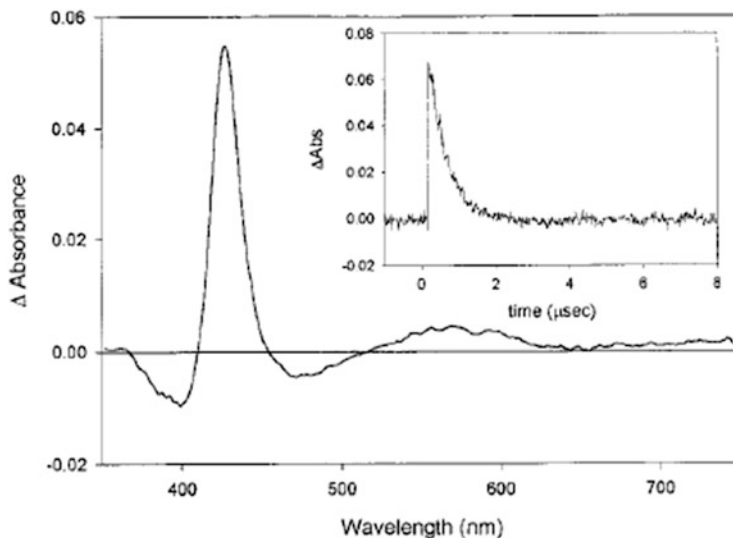


Fig. 5 Transient difference spectrum 50 ns after 355 nm flash photolysis of $\text{Fe}^{\text{II}}(\text{TMPS})(\text{NO})$. *Inset:* Relaxation to equilibrium at 426 nm (Adapted with permission from [82]. Copyright 2001 American Chemical Society)

reaction and the intercept k_{off} is the overall rate constant for spontaneous (thermal) NO release from the complex.

$$k_{\text{obs}} = k_{\text{on}}[\text{NO}] + k_{\text{off}} \quad (7)$$

The equilibrium constant K_{NO} for the formation of $\text{M}(\text{Por})(\text{NO})$ from $\text{M}(\text{Por})$ and NO under those conditions can be calculated from the ratio $k_{\text{on}}/k_{\text{off}}$. For example, k_{on} and k_{off} values have been determined using the flash photolysis kinetics technique for the nitrosyl complexes of metMb, ferri cytochrome *c* and catalase, and the K_{NO} 's so measured agreed well with values measured by static spectroscopic methods. However, when K_{NO} is very large, this is not a reliable method for measuring k_{off} , since the intercept in that case is often of the same magnitude as the experimental error. This is a common problem with ferrous heme protein and model nitrosyls, since they typically display very high K_{NO} values and very small k_{off} values. To address this, k_{off} can be sometimes determined by following the thermal disappearance of the $\text{M}(\text{Por})(\text{NO})$ by trapping any NO released by using another compound with a very high affinity for NO, therefore serving as a NO sink. One trapping agent that has proved useful in this regard is the Ru(III) complex Ru(EDTA) [83]. However, this method is only accurate if the spontaneous NO release rate is not perturbed by the presence of the trapping agent.

Time-resolved spectroscopy has been used to define the kinetics of numerous nitrosyl metalloproteins and models under ambient conditions. Table 2 provides some examples of rate constants measured for various ferrous and ferric heme

Table 2 Representative k_{on} and k_{off} (298 K) values for Fe(II) and Fe(III) heme models and proteins in near neutral aqueous solutions unless noted (Adapted from Table 1 of [84], Copyright: American Chemical Society)

	k_{on} ($\text{M}^{-1} \text{s}^{-1}$)	k_{off} (s^{-1})	Reference
<i>Fe^{III} models/proteins^a</i>			
Fe ^{III} (TPPS) ^b	4.5×10^5	500	[82]
Fe ^{III} (TMPS) ^c	9.6×10^5	51	[82]
Fe ^{III} (TMPS)(OH) ^d	7.4×10^3	1.5	[85]
metMb ^e	1.9×10^5	13.6	[81]
metMb ^f	4.8×10^4	43	[83]
Cyt ^{III} g	7.2×10^2	4.4×10^{-2}	[81]
Cat ^h	3.0×10^7	1.7×10^2	[82]
	1.3×10^7	1.6	[79]
eNOS ⁱ	8.2×10^5	70	[86]
nNOS ^j	2.1×10^7	40	[87]
NPn ^k	$1.5\text{--}5.5 \times 10^6$	0.006–12.7	[88]
P450 CYP125 ^l	17.1×10^6	11.2	[89]
P450 _{cam} CYP101 ^m	0.32×10^6 (34.5×10^6)	0.35 (1.93)	[90]
<i>Fe^{II} models/proteins</i>			
Fe ^{II} (TPPS) ^b	1.5×10^9	6.4×10^{-4}	[82]
Hb ₄ ^{T n}	2.6×10^7	3.0×10^{-3}	[63]
Hb ₄ ^{R n}	2.6×10^7	1.5×10^{-4}	[63]
sGC ^o	1.4×10^8	$6\text{--}8 \times 10^{-4}$	[91]
sGC ^p	–	5.0×10^{-2}	[91]
Mb ^q	1.7×10^7	1.2×10^{-4}	[63]
Cyt ^{II r}	8.3	2.9×10^{-5}	[81]
eNOS ^s	1.1×10^6	70	[86]
nNOS ^t	1.1×10^7	~0	[87]
P450 BM3 ^u	4.7×10^6	13.8	[92]
<i>P. aeruginosa</i> cd ₁ NiR ^v	3.9×10^8	~27.5, 3.8	[93]

^aeNOS endothelial nitric oxide synthase, nNOS neuronal nitric oxide synthase, NPn nitrophorin^b298 K, pH 3^c282 K, pH 3^d283 K, pH 11^e298 K, sperm whale skeletal metMb^f298 K, horse heart metMb^g293 K^h293 Kⁱ283 K, 1 mM arginine^jpH 7.8, 293 K, heme domain^kRange of 298 K rate constants for NPn1, NPn2, NPn3, and NPn4, pH 5.0 and pH 8.0; the k_{off} displays two phases^l10°C^m25°C, pH 7.4; values in parentheses are rate constants for camphor-bound proteinⁿ293 K; two phases are observed for NO binding^opH 7.4, 293 K, 3 mM Mg²⁺, 0.5 mM GTP^pPhosphate buffer pH 7.0, 293 K^qH₂O, pH 6.5^r283 K, 1 mM arginine^spH 7.8, 293 K, heme domain^tpH 7.0, 283 K^u30°C, pH 7.0^v20°C, pH 7

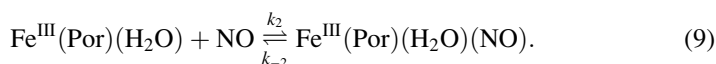
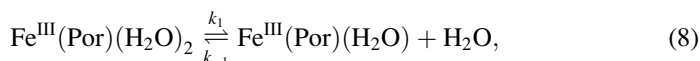
proteins and models [63, 81–93] and illustrates the range of k_{on} and k_{off} values found for ferriheme and ferroheme proteins. As noted above, the small values of k_{off} for the latter lead to very large K_{NO} 's, although ferrous cytochrome *c* (Cyt^{II}) is an exception. The latter also displays a very small k_{on} , presumably owing to the six-coordinate nature of Cyt^{II} for which the axial sites are occupied by an imidazole nitrogen and a methionine sulfur of the protein, so that forming a nitrosyl complex requires both ligand displacement and protein conformational changes. There are other ferrous heme proteins such as neuroglobin and the nonsymbiotic hemoglobin from *Arabidopsis thaliana* (AHb1) that exist in equilibrium between a six-coordinate form with histidines occupying both axial sites and a five-coordinate form [94, 95]. Understandably, the six-coordinate form is considerably less reactive with NO than is the five-coordinate analog. The ferric forms of catalase and nNOS are both more reactive than the model complex Fe^{III}(TPPS). Thus, it appears that in these cases, the protein structure accelerates nitrosyl formation; in contrast, the k_{off} values for metMb, Cyt^{III}, and cat are all smaller than for Fe^{III}(TPPS), consistent with retardation of NO dissociation by those proteins.

The usually small k_{off} values for the ferroheme proteins are relevant to the question of how soluble guanylyl cyclase, once activated by forming an NO complex, is turned off. Stopped-flow kinetics techniques were used by Koesling and coworkers to study loss of NO from sGC-NO [91], and these workers reported a first-order rate constant of $\sim 7 \times 10^{-4} \text{ s}^{-1}$ in 293 K, pH 7.4 buffered solution. This is a k_{off} value typical of ferroheme globins (Table 2). When excess substrate guanylyl triphosphate (GTP, 5 mM) and the cofactor Mg²⁺ (3 mM) were present, the rate was significantly faster ($k_{\text{off}} \sim 5 \times 10^{-2} \text{ s}^{-1}$), and a subsequent study suggested that the *in vivo* rate of sGC deactivation may be several orders of magnitude higher [96].

Although ferrous nitrosyl porphyrinato complexes and ferrous nitrosyl heme proteins are commonly assumed to be unreactive toward NO dissociation, it is clear from the k_{off} values listed in Table 2 that there is a wide range of NO dissociation rates. Several of the proteins listed are as much as five orders of magnitude more reactive than Mb(NO), for example, a notable feature being that the more labile species have thiolates as proximal ligands. In this context, computational studies on the simple system Fe^{II}(P)(L)(NO) (where P²⁻ is the dianion of porphine) have shown that the Fe–NO bond length is predicted to be longer (and weaker) when the proximal ligand L is a thiol or thiolate than when L is H₂O or an imidazole [59, 61]. While it is not surprising that the proximal ligand may have a major effect on the lability of a ferroheme coordinated NO, this topic remains to be explored systematically.

4.3 Mechanistic Studies of NO “On” and “Off” Reactions with Hemes and Heme Models

While it is clear from the experiments cited above that formation of nitrosyl heme complexes are generally much faster if the distal and proximal coordination sites are not both occupied by a strongly bonding ligand, this observation does not define whether the mechanism of NO attachment is associative or dissociative. To address this issue, Laverman and coworkers [82, 83] used laser flash photolysis kinetics to probe temperature and hydrostatic pressure effects on the rates of NO reactions with the water-soluble complexes $\text{Fe}^{\text{III}}(\text{Por})$ (Por = TPPS or TMPS) and for metMb. In each case, the iron(III) centers are six-coordinate, but unlike the ruthenium(III) example discussed above, the axial H_2O ligands are quite labile. These kinetics data were then used to calculate the enthalpies, entropies, and volumes of activation (ΔH^\ddagger , ΔS^\ddagger and ΔV^\ddagger) for the “on” and “off” reactions. The large and positive activation entropies and volumes for both k_{on} and k_{off} are strong indications of substitutions dominated by ligand dissociation ((8) and (9)).



This mechanism implies that H_2O exchange with $\text{Fe}^{\text{III}}(\text{Por})(\text{H}_2\text{O})_2$ should be much faster than the reaction with NO, and this was indeed previously been reported by Hunt et al. for $\text{Fe}^{\text{III}}(\text{TPPS})(\text{H}_2\text{O})_2$ ($k_{\text{ex}} = 1.4 \times 10^7 \text{ s}^{-1}$ in 298 K water) [97]. Furthermore, these workers reported $\Delta H_{\text{ex}}^\ddagger$ (57 kJ mol^{-1}) and $\Delta S_{\text{ex}}^\ddagger$ (+84 $\text{J K}^{-1} \text{ mol}^{-1}$) values similar to the respective k_{on} activation parameters for the NO reaction with $\text{Fe}^{\text{III}}(\text{TPPS})(\text{H}_2\text{O})_2$ (69 kJ mol^{-1} and 95 $\text{J K}^{-1} \text{ mol}^{-1}$). A subsequent study by van Eldik et al. using NMR techniques [98] reported $\Delta H_{\text{ex}}^\ddagger = 67 \text{ kJ mol}^{-1}$, $\Delta S_{\text{ex}}^\ddagger = +99 \text{ J mol}^{-1} \text{ K}^{-1}$, and $\Delta V_{\text{ex}}^\ddagger = +7.9 \text{ cm}^3 \text{ mol}^{-1}$ for $\text{Fe}^{\text{III}}(\text{TPPS})(\text{H}_2\text{O})_2$ in even better agreement with the k_{on} activation parameters for the reaction of NO with this heme model ($\Delta V_{\text{on}}^\ddagger = 9 \pm 1 \text{ cm}^3 \text{ mol}^{-1}$) [82]. Thus, the solvent exchange kinetics for $\text{Fe}^{\text{III}}(\text{TPPS})(\text{H}_2\text{O})_2$ confirm that the k_{on} activation parameters are largely defined by ligand dissociation, the limiting step being (8). Notably, the k_{on} activation parameters for metMb are similar ($\Delta H_{\text{on}}^\ddagger = 63 \text{ kJ mol}^{-1}$) with large and positive values of $\Delta S_{\text{on}}^\ddagger$ (+55 $\text{J mol}^{-1} \text{ K}^{-1}$) and $\Delta V_{\text{on}}^\ddagger$ (+20 $\pm 6 \text{ cm}^3 \text{ mol}^{-1}$), so the protein apparently does not change the mechanism [83].

Coordination of NO to the high-spin iron of $\text{Fe}^{\text{III}}(\text{Por})$ is accompanied by considerable charge transfer to give a linearly bonded, diamagnetic complex that can be formally represented as $\text{Fe}^{\text{II}}(\text{Por})(\text{NO}^+)$. Thus, the activation parameters for k_{off} should also reflect the intrinsic entropy and volume changes associated with the spin change and solvent reorganization as the charge relocates on the metal.

This argument is consistent with the large and positive $\Delta V_{\text{off}}^{\ddagger}$ values for $\text{Fe}^{\text{III}}(\text{Por})(\text{H}_2\text{O})(\text{NO})$ ($\Delta V_{\text{off}}^{\ddagger} = +18$ and $+17 \text{ cm}^{-3} \text{ mol}^{-1}$ for Por = TPPS and TMPS, respectively) [82]. The principle of microscopic reversibility tells us that the lowest-energy pathway of the “off” reaction should involve the same reactive intermediates as the “on” reaction ((8) and (9)).

Laverman also investigated the flash photolysis kinetics of the water-soluble ferrous complexes $\text{Fe}^{\text{II}}(\text{TPPS})$ and $\text{Fe}^{\text{II}}(\text{TMPS})$ in the presence of excess NO [82]. As is common for ferrous heme globins and models, the “on” rates are ~ 3 orders of magnitude faster than for the ferric analogs (Table 2). Correspondingly, the activation parameters for k_{on} are consistent with processes largely defined by diffusion, even though the rate constants are about an order of magnitude less than diffusion limits in water. Since the ferroheme center may be five-coordinate in such cases, formation of the metal-NO bond would not be rate-limited by ligand labilization, but instead would reflect the formation of an encounter complex such as illustrated in Scheme 2.

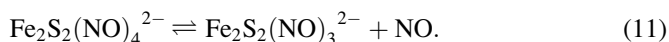
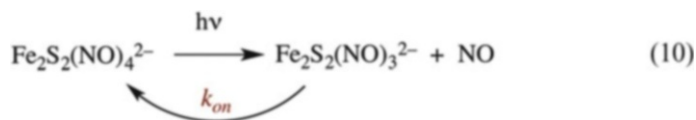
The “off” reactions for ferrous models such as $\text{Fe}^{\text{II}}(\text{TPPS})(\text{NO})$ are too slow to measure by the flash photolysis technique. When trapping methods were used in an attempt to evaluate loss of NO from $\text{Fe}^{\text{II}}(\text{TPPS})(\text{NO})$, k_{off} values were found to be quite small but were sensitive to the nature of the trapping agents used, since Lewis bases that could coordinate at the proximal site appeared to accelerate NO loss [82]. More reliable estimates for the uncatalyzed “off” reaction were obtained by using $\text{Ru}(\text{EDTA})^-$ as a NO scavenger, and the k_{off} values listed for $\text{Fe}^{\text{II}}(\text{TPPS})(\text{NO})$ in Table 2 was obtained in this manner.

4.4 Non-Heme Iron Complexes

Given the growing interest in the biological chemistry of the nitrosyl complexes of non-heme iron, especially the DNICs [31–34, 99–103], there is a need to have a better understanding of the rates and mechanisms of the reactions leading to the formation and decay of such species. It has been shown that dinitrosyl iron species (DNICs) are rapidly formed in cells from the chelatable iron pool (CIP) by the reaction with NO donors [32]. Notably, such reactions have not been studied as extensively or quantitatively as those of the metalloporphyrin complexes, although some information is available through a combination of techniques.

For example, when a neutral aqueous solution of Roussin’s red salt anion $\text{Fe}_2(\mu\text{-S})_2(\text{NO})_4^{2-}$ (RRS^{2-} , Na^+ salt) was subjected to flash photolysis, the spectral changes and kinetics behavior indicate one NO is labilized to give the $\text{Fe}_2(\mu\text{-S})_2(\text{NO})_3^{2-}$ anion (10) [104]. The back reaction is quite fast with a second-order rate constant of $k_{\text{on}} = 9.1 \times 10^8 \text{ M}^{-1} \text{ s}^{-1}$. In aerated solution, this intermediate is competitively trapped by the more plentiful O_2 ($k_{\text{ox}} = 5.6 \times 10^7 \text{ M}^{-1} \text{ s}^{-1}$) to give (eventually) the stable Roussin’s black salt anion $\text{Fe}_4\text{S}_3(\text{NO})_7^-$ (RBS^-). In a separate study by Samina et al. [105], the rates of spontaneous NO release from several dinuclear DNICs including RRS (11) were investigated by following

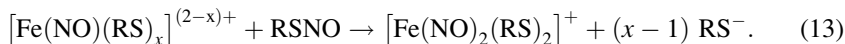
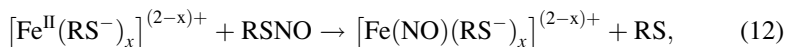
changes in the optical spectrum of hemoglobin, which traps the NO as it is released to give Hb(NO). For RRS^{2-} , the first-order rate constant k_{off} measured in this way was $0.061 \times 10^{-3} \text{ s}^{-1}$. Accordingly, we can estimate the equilibrium constant for NO dissociation from RRS^{2-} (11) from the ratio $k_{\text{off}}/k_{\text{on}}$ as $K_{11} = \sim 10^{-13} \text{ M}$.



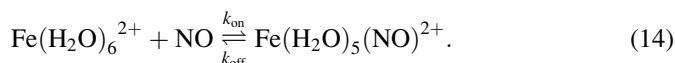
Analogous flash photolysis studies were carried out on the anionic Roussin's red ester $\text{Fe}_2(\mu\text{-SCH}_2\text{CH}_2\text{SO}_3)_2(\text{NO})_4^{2-}$ in aqueous solution. These gave a k_{on} value of $1.1 \times 10^9 \text{ M}^{-1} \text{ s}^{-1}$ for the reaction equivalent to that described by (10) [26]. Although k_{on} has not been measured for this compound, it has been determined for several similar esters, and k_{off} values of $(1\text{--}9) \times 10^{-3} \text{ s}^{-1}$ were found [105]. Thus, the equilibrium constant for NO dissociation from such RSEs would appear to be about 10^{-12} M .

Flash photolysis studies of Roussin's black salt anion $\text{Fe}_4\text{S}_3(\text{NO})_7^-$ displayed similar reversible NO photodissociation in aqueous solutions [106]. In this case, two back reaction pathways with k_{on} values of 1.3×10^7 and $7.0 \times 10^5 \text{ M}^{-1} \text{ s}^{-1}$ were observed. A time-resolved optical and infrared spectroscopic study revealed two separate intermediates, both of which react with NO to re-form the parent complex. The identities of the intermediates are interpreted in terms of photolytic loss of chemically distinct nitrosyls found on the $\text{Fe}_4\text{S}_3(\text{NO})_7^-$ anion. The "off" reaction rates have not been reported, but must be slow.

Despite reports that dinitrosyl-iron complexes are the most abundant nitric oxide-derived cellular adducts [34], quantitative investigations of DNIC formation are quite limited. Vanin and coworkers [107] studied the reaction between Fe^{2+} , nitrosothiol (RSNO), and thiol (RSH = cysteine or glutathione) and demonstrated that first a mononitrosyl iron complex $\text{Fe}(\text{NO})(\text{RS})_n$ is formed followed by formation of the DNIC $[\text{Fe}(\text{NO})_2(\text{RS})_2]^n$ ((12) and (13)). MNIC formation apparently occurs by a direct reaction between *S*-nitrosothiols and Fe^{2+} ions with rate constants of 3.0 and $30 \text{ M}^{-1} \text{ s}^{-1}$ for *S*-nitrosglutathione and *S*-nitrosocysteine, respectively (100 mM Hepes buffer, pH 7.4). Since deoxyhemoglobin does not inhibit subsequent formation of DNIC, the reaction apparently does not require the release of free NO from the RSNO.



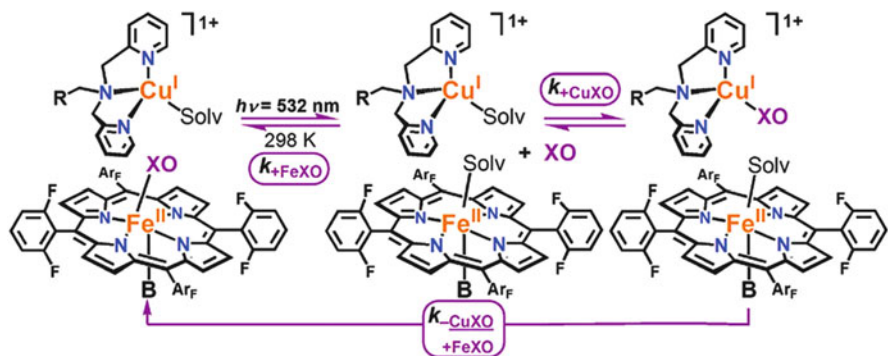
The reaction of NO with the simple aqueous complex $\text{Fe}(\text{H}_2\text{O})_6^{2+}$ may be an important first step in the formation of DNICs from iron in the chelatable iron pool, and the kinetics of this reaction has been studied by Wanat et al. using stopped-flow and flash photolysis kinetics techniques [108]. The k_{on} and k_{off} values determined were, respectively, $1.42 \times 10^6 \text{ M}^{-1} \text{ s}^{-1}$ and $3.2 \times 10^3 \text{ s}^{-1}$ (25°C). On the basis of the activation parameters, it was argued that this reaction follows an interchange dissociative mechanism, similar to that for the water exchange reaction with $\text{Fe}(\text{H}_2\text{O})_6^{2+}$. Given that the DNICs are very stable toward NO dissociation, the relatively small equilibrium constant for (14) ($K_{12} = k_{\text{on}}/k_{\text{off}} \sim 4 \times 10^2 \text{ M}^{-1}$) is noteworthy.



Schnepensieper et al. [109] have determined the rates and activation parameters for NO reactions with different ferrous aminocarboxylato complexes in aqueous solution. The k_{on} values ranged from 10^5 to $10^8 \text{ M}^{-1} \text{ s}^{-1}$ ($2.4 \times 10^8 \text{ M}^{-1} \text{ s}^{-1}$ for $\text{Fe}^{\text{II}}(\text{EDTA})$), while k_{off} values were in the range 4 to 91 s^{-1} (91 s^{-1} for $\text{Fe}^{\text{II}}(\text{EDTA})$). The reaction of NO with $\text{Fe}^{\text{II}}(\text{EDTA})$ gave a $\Delta V_{\text{on}}^\ddagger$ of $+4.1 \text{ cm}^{-3} \text{ mol}^{-1}$, and a dissociative interchange mechanism was proposed.

4.5 Other Metal Centers of Biological Interest

The mammalian chemical biology of NO includes interactions with Cu centers. However, although a limited number of copper(I) and copper(II) nitrosyl complexes have been prepared, there have been few kinetics studies probing the formation and dissociation of such species. The ligand substitution reactions of both Cu(II) and Cu(I) are generally very fast owing to the high lability of their coordination spheres. So, in this context, one might expect the NO “on” reactions to be similarly fast. However, given that Cu–NO complexes tend to be unstable, the “off” reactions are also likely to be relatively fast. One study of Cu–NO ligand substitution reactions involved the flash photolysis of a model system consisting of a heme model complex and a second copper complex in solution (at varying ratios) under an inert atmosphere as a model for heme–copper oxidases [110]. The two components were the six-coordinate ferrous species, $\text{Fe}^{\text{II}}(\text{F}_8\text{Por})(\text{NO})(\text{THF})$ [F_8Por = tetrakis(2,6-difluorophenyl)porphyrinate $^{2-}$], while the other was a $\text{Cu}^{\text{I}}\text{L}$ unit (L = the tridentate ligand bis-(2-pyridylmethyl)(benzyl)amine or the tetradentate ligand tris(2-pyridylmethyl)-amine). Flash photolysis led to NO labilization from

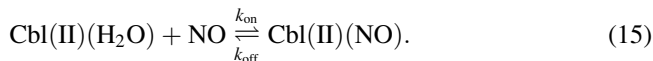


Scheme 4 Illustration showing the flash photolysis of a mixture of a Cu^{I} complex ($\text{R} = \text{phenyl}$ or 2-pyridyl) with a NO or CO (XO) complex of $\text{Fe}^{\text{II}}(\text{F}_8\text{Por})$ ($\text{B} = \text{THF}$ when $\text{XO} = \text{NO}$) in THF solution. Photolysis-induced XO labilization is followed by trapping by the Cu^{I} , followed by slower transfer of XO back to the Fe^{II} center (Reprinted with permission from [110]. Copyright 2009 American Chemical Society)

$\text{Fe}^{\text{II}}(\text{F}_8\text{Por})(\text{NO})(\text{THF})$ followed by competitive NO trapping by the Fe^{II} and Cu^{I} centers. Subsequently, a slower, first-order process was observed, indicating that the NO trapped by the cuprous center was being released then recaptured by the Fe^{II} (Scheme 4).

Given that trapping of NO by the ferrous complex would be expected to occur with near diffusion-limited second-order rate constants ($\sim 10^9 \text{ M}^{-1} \text{ s}^{-1}$), the competitive trapping by Cu^{I} suggests that the rate constants for the NO reaction of these Cu^{I} centers are comparable. If the subsequent slower process is rate-limited by dissociation of NO from the $\text{Cu}^{\text{I}}\text{-NO}$ center, the apparent rate constant (64 s^{-1} at 298 K) implies that the first-order NO dissociation rate constant is $\sim 10^2 \text{ s}^{-1}$. These values give $k_{\text{on}}/k_{\text{off}} = \sim 10^7 \text{ M}^{-1}$ as an estimate overall equilibrium constant for $\text{Cu}^{\text{I}}\text{-NO}$ bonding, which is substantial, but less than that typical for ferrous heme proteins and models.

Another metal- NO interaction of potential biological interest is the cobalt of vitamin B_{12} . The reduced (Co^{II}) form of aquacobalamin binds nitric oxide to yield the adduct $\text{Cbl}(\text{II})(\text{NO})$ with an equilibrium constant of $\sim 10^8 \text{ M}^{-1}$ (25°C) [111]. Flash photolysis led to the transient disruption of this equilibrium followed by relaxation back to the equilibrium state. Varying the NO concentration allowed Wolak et al. [112] to determine the k_{on} for reforming the $\text{Co}\text{-NO}$ bond as $7.4 \times 10^8 \text{ M}^{-1} \text{ s}^{-1}$, a value that is comparable to the second-order rate constants reported for reactions of free radicals with reduced cobalamin. The k_{off} value was determined by using $\text{Fe}(\text{EDTA})$ trapping of NO , and the resulting $k_{\text{on}}/k_{\text{off}}$ ratio is, as it should be, in good agreement with the K_{14} value reported previously. Notably, while the cobalamin- NO interaction has drawn some interest, it is not clear what physiological role this might play.



A recent publication by Bakac et al. [113] has reported the results of flash photolysis and NO scavenger kinetics studies to determine the NO k_{on} and k_{off} values, respectively, for several other cobalt(II) macrocycle complexes and their rhodium(II) analogs as well as for the Cr(II) nitrosyl complex $\text{Cr(H}_2\text{O)}_5\text{(NO)}^{2+}$. These rate constants as well as literature values were then used to calculate the K_{NO} values for nitrosyl complex formation in solution, which were compared to K_{O_2} values for formation of the analogous dioxygen complexes. The plot of $\log K_{\text{NO}}$ vs. $\log K_{\text{O}_2}$ in 298 K aqueous solution proved to be linear with a unitary slope, indicating a direct correlation between the intrinsic bonding affinities of NO and O₂ for these metal centers. However, such a correlation would not carry over to the heme proteins given the huge differences in the affinities of O₂ and NO for soluble guanylyl cyclase and for myoglobin that can be attributed to the different interactions of the coordinated diatomic ligands with the protein amino acid residues [6].

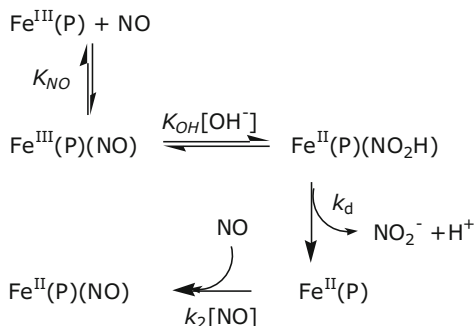
In this section we have focused on the reactions of NO with Cu and Fe systems primarily by the reaction of these metal complexes with NO itself. However, there are other pathways to nitrosyl complexes. For example, nitrite reduction concomitant with (formal) oxidation of the metal can lead to a metal-nitrosyl complex illustrated in (16) [114–117].



5 Reductive Nitrosylation and Other Reactions of Coordinated NO

Ligand-metal bonding generally involves electronic redistribution owing to the balance between ligand-to-metal σ - and π - donation and metal-to-ligand-backbonding. NO is especially versatile in this regard, as we have described above in Sect. 2. If there is charge transfer to the metal center resulting (formally) in a coordinated nitrosonium cation (NO^+), that species might have enhanced susceptibility to reactions with nucleophiles. On the other hand, if such charge transfer is in the opposite direction, the resulting coordinated nitroxyl anion NO^- may be susceptible to electrophilic attack. However, it is worth remembering that the nitrosyl typically undergoes reverse dissociation as a neutral NO, so assigning the oxidation states in this manner is rather arbitrary.

Scheme 5 Mechanism proposed by Hoshino et al. [122] for the reductive nitrosylation of selected ferriheme proteins (P = porphyrin ligand)

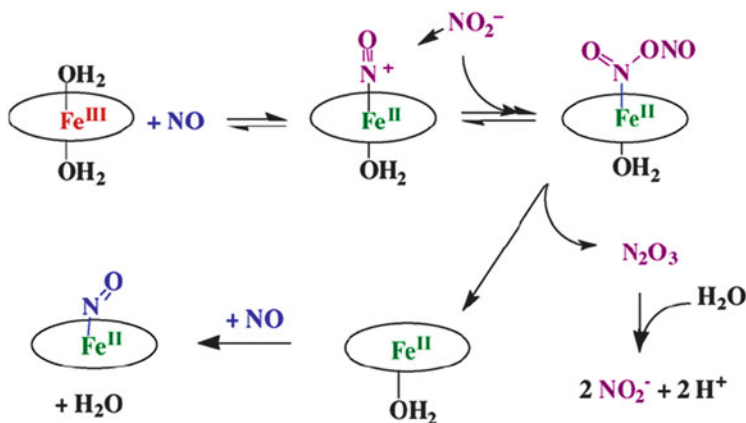


5.1 Reactions of Iron(III) Nitrosyls with Nucleophiles

Nucleophilic reactions with coordinated NO can be illustrated by the long-known reversible reaction of hydroxide with the nitrosyl ligand of the nitroprusside ion (NP) (17). The reaction rate is first order each in $[\text{OH}^-]$ and in $[\text{Fe}(\text{CN})_5(\text{NO})^{2-}]$ [118], so the likely reactive intermediate is the hydroxide adduct $\text{Fe}(\text{CN})_5(\text{N}(\text{O})\text{OH})^{3-}$. The reaction is reversed in acidic solution. NP reacts with other nucleophiles such as mercaptans (RSH) and mercaptides (RS^-) to form deeply colored metal nitroso–thiolato intermediates [118]. These are unstable and decay via formation of disulfides and reduced NP, which subsequently decomposes by cyanide loss. Such reactions have physiological significance given that sodium nitroprusside has long been used as an intravenously administered vasodilator for hypertensive emergencies [119, 120].



Facile nucleophilic attack at a coordinated nitrosyl is the likely mechanism for the NO reduction of metal centers. Ferric porphyrins have long been known to undergo such “reductive nitrosylation” in the presence of excess NO [47, 72, 121]. For example, when aqueous metHb is exposed to excess NO, the product is the ferroheme globin NO adduct, Hb(NO) (Scheme 5) [122]. Other ferriheme proteins such as cytochrome *c* (Cyt^{III}) and metMb are reduced by excess NO in aqueous solutions at pH values >7 , but metHb is susceptible even at lower pH. The kinetics behavior for Cyt^{III} and metMb with regard to the NO concentration and the pH is consistent with the proposed base catalyzed mechanism shown in Scheme 5. However, it is important to recognize that the driving force of the reductive nitrosylation of the heme proteins and models at near neutral pH is the very great stability of the ferrous nitrosyl complexes formed under excess NO. In the absence of excess NO, the reverse reaction, namely, nitrite reduction by the ferrous complexes, is thermodynamically favored [117, 123].



Scheme 6 Proposed mechanism for the nitrite catalysis of the reductive nitrosylation of Fe^{III}(TPPS), metHb, and metMb [127]

The nitrosyl complex of metMb has also been reported to react with the biological antioxidant glutathione GSH (in the presence of excess NO) to give Mb(NO) and *S*-nitrosoglutathione (GSNO) [124]. The GSH reaction with metMb(NO) is surprisingly facile, given that the smaller and more basic hydroxide ion is only an order of magnitude more reactive [122]. Nonetheless, this result points to the potential role of ferriheme nitrosyls acting as nitrosating agents toward biologically relevant nucleophiles [125, 126].

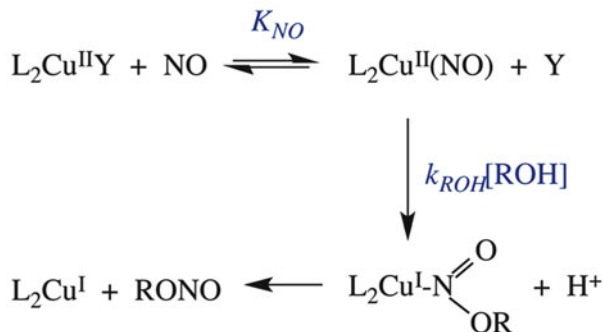
More recent studies by Fernandez et al. demonstrated that the reductive nitrosylations of Fe^{III}(TPPS) [127] and of metHb and metMb [128] are promoted by general base catalysis and by other nucleophiles, including nitrite ion (Scheme 6). In the case of the latter, the catalytic role of nitrite in promoting reductive nitrosylation of these ferric heme models and proteins was first discovered in an attempt to pin down experimental anomalies that were eventually attributed to the ubiquitous NO₂⁻ impurities in aqueous NO solutions.

The observation of nitrite catalysis of ferriheme nitrosyl reactions has generated considerable interest in the potential formation of N₂O₃ as an intermediate that might assume key biological roles [129, 130]. Receiving particular attention is the possibility that this reaction might explain the vasodilatory and other protective effects of nitrite ion in mammalian physiology [131, 132].

5.2 Reduction of Copper(II) Complexes by NO

The Cu(II) complex Cu(dmp)₂(H₂O)²⁺ (dmp = 2,9-dimethyl-1,10-phenanthroline) is a stronger oxidant than most Cu(II) complexes (reduction potential = 0.58 V vs. NHE) [133]. Since the Cu(phen)₂(H₂O)²⁺ analog (phen = 1,10-phenanthroline) is a much weaker oxidant (0.18 V), this property can be attributed to the steric

Scheme 7 Proposed mechanism for NO reduction of $\text{Cu}(\text{dmp})_2(\text{H}_2\text{O})^{2+}$ in buffer solution



Y = solvent, ROH or X⁻

repulsion between the methyl groups of the respective dmp ligands that favors the tetrahedral coordination of Cu(I) over the tetragonal pyramidal structure of Cu(II).

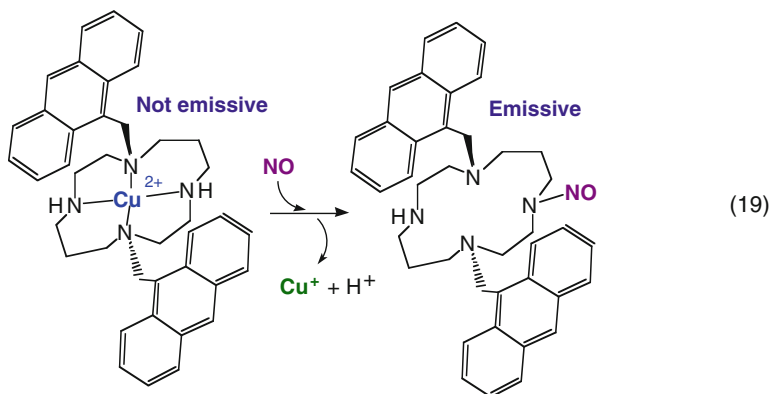
In methanol, $\text{Cu}(\text{dmp})_2(\text{H}_2\text{O})^{2+}$ reacts with NO to give $\text{Cu}(\text{dmp})_2^+$ and methyl nitrite (18); in water, the second product is NO_2^- [134]. In CH_2Cl_2 , the reaction does not occur unless methanol is added. At a fixed pH, the kinetics in aqueous solution proved to be first order in [NO] and in $[\text{Cu}(\text{dmp})_2(\text{H}_2\text{O})^{2+}]$. Addition of a small concentration of NaNO_2 (5×10^{-5} M) had no effect, although at higher concentrations, various anions, including the conjugate bases of the buffers, inhibited the reaction. This inhibition was attributed to competition for the labile fifth coordination site of the Cu(II).



One prospective mechanism discussed for this reaction would be simple outer sphere electron transfer from NO to Cu(II) followed by hydrolysis of the resulting NO^+ . Alternatively, a mechanism that is more consistent with the inhibition noted above and closer to those discussed above for NO reductions of the ferriheme proteins and models would be an inner sphere pathway such as illustrated in Scheme 7. The latter alternative gains credence from studies showing that NO reduction of the more sterically crowded, but stronger, oxidant $\text{Cu}(\text{dpp})_2^{2+}$ (dpp = 2,9-diphenyl-1,10-phenanthroline) is slower under comparable conditions than the reduction of $\text{Cu}(\text{dmp})_2(\text{H}_2\text{O})^{2+}$ [135].

A somewhat different mechanism has prove necessary to interpret the reaction of NO with the Cu(II) complex $\text{Cu}(\text{DAC})^{2+}$ (DAC = 1,8-bis(9-anthracylmethyl)(1,4,8,11-tetraaza-cyclotetradecane or bis(9-anthracylmethyl)-cyclam) [136, 137]. Although free DAC is fluorescent, analogous solutions of $[\text{Cu}(\text{DAC})]^{2+}$ are not, owing to intramolecular quenching by the Cu(II) center. Introduction of NO to a methanolic solution of $\text{Cu}(\text{DAC})^{2+}$ led to the disappearance of the characteristic weak *d-d* absorption band at 566 nm and to the appearance of

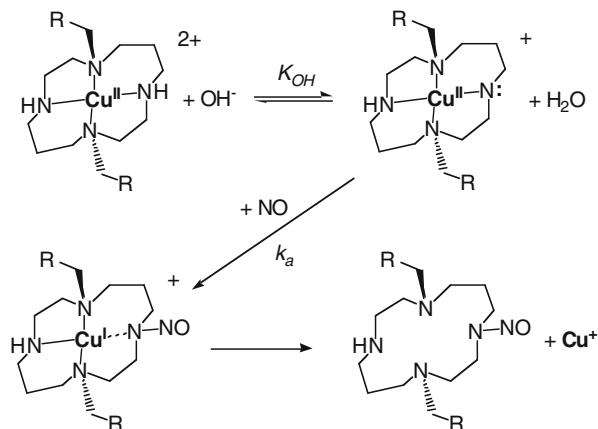
anthracene-type fluorescence. Cu(I) was detected electrochemically; however, in marked contrast to (18), the reduction of Cu(II) was accompanied by the *N*-nitrosation and release of the DAC ligand (19) as evidenced by ESI-mass spectral and $^1\text{H-NMR}$ analysis. It is this *N*-nitrosated DAC that is responsible for the strong luminescence.



The rate of the reaction depicted in (19) is relatively slow in neutral aqueous media but is accelerated by base. Kinetic studies show it to be first order in the concentrations of $\text{Cu}(\text{DAC})^{2+}$, NO, and OH^- [137]. Based on these observations, two mechanisms have been discussed. The first is analogous to Scheme 7 with the NO initially reacting at the Cu(II) site to form a $\text{Cu}^{\text{II}}\text{-NO}$ (or $\text{Cu}^{\text{I}}\text{-NO}^+$) complex. This would be followed by deprotonation of one of the amines and NO^+ migration to the resulting coordinated amide. Given that the DAC type ligand is well suited for square planar coordination to Cu(II) but is not well suited for tetrahedral coordination to Cu(I), the nitrosated ligand is then released. The other proposed mechanism involves NO attack at a coordinated amine that has been deprotonated. This step would lead directly to amine nitrosation and concomitant reduction of Cu(II) to Cu(I) (Scheme 8). This latter pathway is analogous to electron transfer between metal centers involving a bridging ligand, and DFT calculations suggest that this is the more favorable pathway [137].

Since reductions of metal centers by NO are generally thought to occur via nucleophilic attack at an activated $\text{M}^{n+}\text{-NO}$ ($\text{M}^{(n-1)+}(\text{NO}^+)$) species to give the nitroso-nucleophile product and the reduced metal center [72], there was little precedent for Scheme 8. An exception was the reaction of NO with $\text{Ru}(\text{NH}_3)_6^{3+}$ in alkaline media, which is reported to give the Ru(II) dinitrogen complex $\text{Ru}(\text{NH}_3)_5(\text{N}_2)^{2+}$ [70]. Given that the latter reaction leads to the formation of an N–N bond, it is likely that it is proceeding by NO attack on a coordinated amide ligand [72] with concomitant reduction of the metal center. Such a mechanism for the nitrosation of coordinated ligands may have broader implications. For example, it was reported by Montfort et al. [138] that reaction of excess NO with bedbug nitrophenorin leads to nitrosylation and reduction of the heme iron as well as to

Scheme 8 Prospective inner sphere electron transfer mechanism for the NO reduction of $\text{Cu}(\text{DAC})^{2+}$

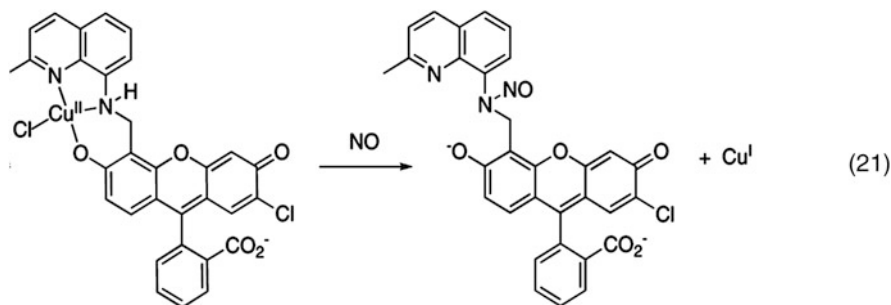


nitrosation of the proximal cysteinate ligand (cys-60). Similarly, van Eldik et al. [139] described the reaction of a nitrosyl ferriheme thiolate complex with NO to form $\text{Fe}^{\text{II}}(\text{Por})(\text{NO})$ and RS-NO (20). While these reactions could occur via homolytic Fe-SR cleavage followed by trapping of $\text{RS}\cdot$ by NO, an alternative could be NO attack at the coordinated thiolate ligand in analogy to the NO reduction of $\text{Cu}(\text{DAC})^{2+}$. Furthermore, it is notable that the NO reaction with a coordinated thiolate is the microscopic reverse of the decomposition of *S*-nitrosothiols catalyzed by copper(I) [140], a reaction that is likely to proceed via the initial coordination of Cu(I) at the RSNO sulfur followed by homolytic dissociation of the RS-NO bond [141].



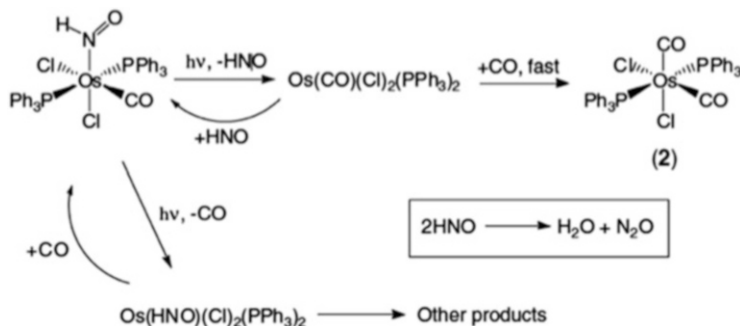
For some time, there has been an interest in possible utilization of the NO reduction of coordinated metal complexes of luminescent ligands as turn-on sensors for NO detection [142, 143]. In this context, it is of interest that in weakly coordinating solvents, the cuprous complex $\text{Cu}(\text{dmp})_2^+$ is strongly luminescent from its metal-to-ligand charge transfer (MLCT) state(s), while the Cu(II) analog is not [144]. However, since the MLCT emission from $\text{Cu}(\text{dmp})_2^+$ is strongly quenched by nucleophiles, including H_2O and CH_3OH , the reaction depicted by (18) would not be an effective NO sensor, so another approach was needed. This was a stimulus for exploring the reactions of $\text{Cu}(\text{DAC})^{2+}$, since free ligand DAC is luminescent from its anthracene chromophores, but its emission is nearly completely quenched in $\text{Cu}(\text{DAC})^{2+}$. The reaction of NO with $\text{Cu}(\text{DAC})^{2+}$ did lead to strongly enhanced luminescence, the emissive luminophore being the nitrosated DAC; however, the reaction was considered to be too slow at physiological pH to be of practical application. Lim et al., however, saw greater potential in analogous systems and were able to build sensitive NO sensors using Cu(II) complexes such as CuL_2^{2+} , where L is a bidentate ligand such as dansyl ethylenediamine or dansyl aminomethylpyridine [145], or $\text{Cu}^{\text{II}}(\text{Cl})(\text{FL})$, where FL is a tridentate metal chelating ligand

modified with a pendant fluorescein [146]. In each case NO reduction of the Cu(II) center leads to strongly enhanced (“turned on”) emission from the ligands. In the case of FL the luminophore product is the *N*-nitrosated FL–NO (21), which is actually more fluorescent ($\Phi_F = 0.58$) than FL itself ($\Phi_F = 0.08$) owing to suppression of electron transfer fluorescence quenching involving the free amine functionality [147]. Cu^{II}(Cl)(FL) has been utilized as a NO sensor in cell cultures and tissue. Notably, a quantitative study of the NO reduction of Cu^{II}(Cl)(FL) found the rate to be first order in [Cu^{II}(Cl)(FL)], [OH⁻], and [NO] as seen for Cu(DAC)²⁺ [137], and an inner sphere mechanism in analogy to Scheme 8 was proposed [147].



Mondal and coworkers have also prepared similar sensors with copper(II) coordinated by tridentate ligands with pendant dansyl groups that become much more fluorescent when the Cu(II) is reduced by NO in methanol [148]. In this case, however, the ligand was not nitrosated, so a mechanism along the lines of Scheme 7 is likely, although there was no direct evidence for the formation of a Cu^{II}NO intermediate. Previous studies by this research group with other ligands did observe ligand nitrosation occurring concomitant with NO reductions of Cu(II) complexes [149]. In another interesting study [150], these researchers prepared the cupric complexes Cu(2-aminomethylpyridine)₂²⁺ and Cu(tren)(AN)²⁺ (tren = bis-(2-aminoethyl)amine, AN = acetonitrile). When an acetonitrile solution of the former complex was purged with NO, immediate changes in the absorption spectra (shifts in the LF band from 582 to 660 nm) were apparent, and the solution became EPR silent. A similar pattern was seen with Cu(tren)(AN)²⁺. This was followed by a slow reaction to form the final products, which were Cu(I) plus species apparently formed by the diazotization of the ligand primary amines. The FTIR spectrum of the transient species showed a strong new band at 1,642 cm⁻¹ that was attributed to the ν_{NO} of a transient Cu^{II}L₂(NO)²⁺ complex. However, this ν_{NO} occurred nearly 300 cm⁻¹ lower frequency than that of the structurally characterized Cu^{II}(NO) complex reported by Hayton and coworkers [41], so the difference is puzzling.

The redox chemistry between NO and Cu²⁺ has also been invoked as being important to the biological function of the multi-copper blood protein ceruloplasmin, which has been termed a “nitric oxide oxidase” [151]. It was proposed that ceruloplasmin is an NO oxidase that helps to maintain the homeostasis between nitrite and NO in mammalian blood by converting NO to NO₂⁻.



Scheme 9 Competitive CO and HNO photodissociation from $\text{Os}(\text{CO})\text{Cl}_2(\text{PPh}_3)_2(\text{HNO})$ [154]

5.3 Protonation of Metal Nitrosyls

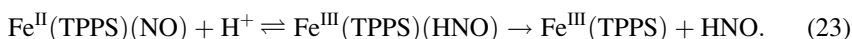
An important form of electrophilic attack on metal nitrosyls is protonation. An early example of which is the reversible reaction of HCl with the osmium compound $\text{Os}(\text{CO})\text{Cl}(\text{PPh}_3)_2(\text{NO})$ to give the first structurally characterized N-coordinated HNO complex $\text{Os}(\text{CO})\text{Cl}_2(\text{PPh}_3)_2(\text{HNO})$ (Scheme 9) [152, 153]. Subsequent studies by Marhenke et al. [154] demonstrated that photolysis of the latter compound led competitive reversible dissociation of CO and of HNO (Scheme 9).

A more biologically relevant example of M–NO protonation is the electrochemical reduction/protonation of $\text{Mb}(\text{NO})$ demonstrated by Farmer and coworkers [155]. Surfactant $\text{Mb}(\text{NO})$ films deposited on the graphite electrodes were shown to undergo reduction to $\text{Mb}(\text{NO}^-)_{\text{surface}}$ ($E_{1/2} = -0.63$ V vs. NHE) accompanied by protonation to give $\text{Mb}(\text{HNO})_{\text{surface}}$. At more negative potentials, the latter was reported to undergo catalytic reaction with excess NO in solution to give N_2O . When $\text{Mb}(\text{HNO})$ was subsequently prepared in solution by reducing $\text{Mb}(\text{NO})$ with Cr^{2+} , the nitroxyl proton was observable by ^1H NMR as a singlet at 14.8 ppm [155].

Olabe and coworkers [156] have shown that the nitroprusside ion $\text{Fe}(\text{CN})_5(\text{NO})^{2-}$ can be sequentially reduced by two electrons in aqueous solution. The product of the second reduction $\text{Fe}(\text{CN})_5(\text{NO})^{4-}$ undergoes protonation (pK_a 7.7) to give an N-coordinated HNO complex (22) that is remarkably stable. The stability of $\text{Fe}(\text{CN})_5(\text{NO})^{4-}$ clearly points to the NO functionality as being the site of the second reduction, and this complex can be considered to be a low-spin d^6 Fe(II) complex of the nitroxyl anion, that is, a $\text{Fe}^{\text{II}}(\text{NO}^-)$ species. If instead the second electron was localized on the metal, the resulting low-spin d^7 complex should be very labile toward ligand substitution. The proton NMR spectrum shows a proton resonance at 20.02 ppm that splits into a doublet when ^{15}NO -labeled nitroprusside was used.



The osmium, reduced myoglobin, and reduced nitroprusside cases described above each involve protonation of a $\{\text{MNO}\}^8$ complex. A different example has recently been reported where a $\{\text{MNO}\}^7$ complex displays a tendency to decompose slowly in aqueous solution presumably via protonation of the nitrosyl followed by dissociation of HNO. In this case, the complex was the water-soluble heme model $\text{Fe}^{\text{II}}(\text{TPPS})(\text{NO})$ that had been prepared in slightly acidic (pH 5.8) aqueous buffer [149]. Although, such ferrous porphyrinato nitrosyls are often considered to be quite unreactive, this solution slowly underwent spontaneous decay to give the ferric species $\text{Fe}^{\text{III}}(\text{TPPS})$ (23). The possible formation of HNO was first suggested by the observation of N_2O as a reaction product [157] (free HNO readily dimerizes to nitrous oxide) [158, 159] and was later demonstrated by direct observation using an HNO-specific electrochemical technique [61]. The proposal that this occurs via protonation (effectively an oxidative addition of H^+) followed by dissociation of HNO was based on the pH-dependence of the reaction.



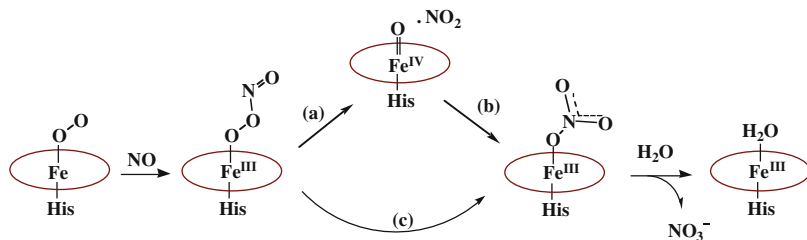
The chemistry of HNO and the formation and reactions of HNO metal complexes have been extensively reviewed [158–161].

5.4 Reactions with Dioxygen

Reactions with O_2 represent some of the most important processes involving NO under physiological conditions. Nitric oxide autoxidation that is not mediated by metal centers has been shown to display third-order kinetics (24) whether in the gas phase, in aprotic solvents or in aqueous media [162]. The fact that this reaction rate is second order in $[\text{NO}]$ is particularly significant in the biological context. Under the very low concentrations (nanomolar) where NO is an important signaling agent, such as in blood pressure control, the reaction with oxygen is very slow. In contrast, at the higher concentrations that are typical of induced NO production during immune response to pathogens, the autoxidation process may play important physiological roles, such as the generation of cytotoxic nitrogen oxides like N_2O_3 .

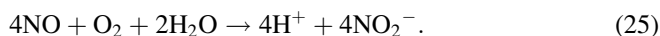
$$-d[\text{NO}]/dt = k_{\text{aut}}[\text{NO}]^2[\text{O}_2]. \quad (24)$$

Notably, there are differences in the products observed in aqueous vs. non-aqueous media and this may also have biological relevance. NO autoxidation in aqueous solution leads to the formation of nitrous acid according to the stoichiometry shown in (25) [163]. In contrast, the autoxidation product in aprotic media is nitrogen dioxide, which is a much stronger oxidant toward cellular components [164, 165]. Aprotic autoxidation may have particular relevance biologically owing to the higher solubility of both NO and O_2 in hydrophobic media. As a consequence

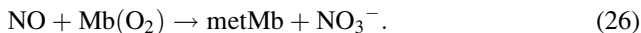


Scheme 10 Hypothetical pathways leading to the dioxygenation of NO by Mb(O₂) or Hb(O₂) [171]

of reactant partitioning between cellular hydrophobic and hydrophilic regions and the third-order kinetics, a disproportionate fraction of autoxidation may occur in hydrophobic regions to give NO₂ as a key intermediate at these locations [166].



The reactivity of NO with O₂ is dramatically affected by coordination of one or the other of these reactants to a metal center. For example, dioxygenation of NO by oxymyoglobin (e.g. (26)) or by oxyhemoglobin is quite fast and occurs by a rate law that is first order in NO concentration (e.g., $-d[\text{NO}]/dt = k_2[\text{NO}][\text{Mb}(\text{O}_2)]$, $k_2 = >10^7 \text{ M}^{-1} \text{ s}^{-1}$ at pH 7) [167, 168]. Furthermore, the NO_x product is nitrate (NO₃⁻), not nitrite or nitrogen dioxide, and the other product is metMb. Such reactions are generally considered to be important sinks that scavenge NO in the cardiovascular system [169].



Mechanistically, given that the O₂ bound to the iron of myoglobin or hemoglobin is considered to have superoxide character, the rapid reaction with the free radical NO is not surprising. Since the product of solution phase reaction of free O₂⁻ with NO is the peroxynitrite ion OONO⁻, one might expect that the first species formed in the NO reaction with oxymyoglobin would be the corresponding peroxynitrite complex (Scheme 10). This reaction has been the subject of several fast-flow spectroscopic studies, and while earlier studies claimed to have observed this intermediate, later ones concluded that the first species observable is the nitrate complex Fe^{III}(NO₃⁻) [170]. In this context, Kurtikyan et al. [171] used low-temperature matrix spectroscopy to probe the reaction of the heme model Fe^{II}(TPP)(O₂) (TPP²⁻ = tetraphenylporphyrinato dianion) with NO. Even at 100 K, the purported peroxynitrite intermediate Fe^{III}(TPP)(OONO⁻) was not observable, so it was concluded that once this species is formed, it must decay very rapidly to the more stable nitrate complex Fe^{III}(TPP)(NO₃⁻). Notably, different computational approaches also disagree on the potential stability of that intermediate [172, 173].

Superficially, the reaction of O₂ with nitrosyl myoglobin Mb(NO) (27) appears similar to that of NO with Mb(O₂). This reaction has been studied in detail by Skibsted and coworkers [174], owing in part to its importance to the stability of cured meat. The same products, metMb and NO₃⁻, are formed; however, the oxygenation of Mb(NO) is very much slower and follows a different rate law. Indeed several kinetics studies [174, 175] indicated the operation of two slow (pseudo) first-order processes under an oxygen atmosphere with different activation parameters, one of the two being modestly dependent on the O₂ concentration. However, under one atm of O₂ at 30°C, the two rate constants were nearly the same, $\sim 6 \times 10^{-4} \text{ s}^{-1}$. Notably, these values are close to the rate of spontaneous NO dissociation from Mb(NO), and one of these was indeed attributed to NO dissociation followed by O₂ trapping of the resulting Mb to give Mb(O₂), which then reacts rapidly with NO according to (27) [174]. The efficiency of this step would be enhanced by containment of NO in the hydrophobic pockets of the protein. For the second kinetically detected process, it was suggested that O₂ plays a role in labilizing the NO, although it is still dominated by dissociation. The reaction is also markedly accelerated by light [176], consistent with the thermal autoxidation of Mb(NO) being dominated by NO dissociation.



6 Summary

This chapter has provided a brief review of NO reactions with metal centers and our principal focus has been on studies where quantitative photochemical and thermal kinetics techniques have been used to probe reactions that may play key roles in the biological activity of NO. As a consequence, we have concentrated principally on reactivity involving iron and copper metal centers, but even with this approach, it was necessary to leave out numerous topics relevant to chemists and chemical biologists owing to the volume of information regarding the chemistry, biochemistry, and pathobiology of NO. For example, NO is a reversible inhibitor of the critical redox protein cytochrome *c* oxidase, which contains both hemes and a redox-active copper site [177]. Furthermore, other closely related species such as HNO and nitrite are drawing considerable attention as being key components of the larger picture. Nonetheless, we can reemphasize certain important general patterns. The first is that NO is a stable free radical that reacts readily with other free radicals and redox-active metal centers, especially if the latter are substitution labile. For example, mammalian blood pressure regulation by NO centers on the rapid reaction with the ferroheme site of sGC, and this process must be fast with a large formation constant if the low NO concentrations generated are to be effective. Key biological roles not only involve formation and decay of nitrosyl complexes but also how NO coordination affects the reactivities of the metal and other ligands and how the

metal mediates the chemistry of the coordinated NO. Understanding the dynamics, thermodynamics, and mechanisms of the relevant fundamental processes provides insight into how the chemical biology of NO and other relevant nitrogen oxides function.

Acknowledgements Reactivity studies of nitrogen oxides in the UCSB laboratory of PCF have long been supported by the Division of Chemistry of the US National Science Foundation (Current grant CHE-1058794). JCMP thanks Coordenação de Aperfeiçoamento de Pessoal de Nível Superior (CAPES) for fellowship support.

References

1. Ignarro LJ (1999) *Angew Chemie I Ed* 38:1882
2. Furchgott RF (1999) *Angew Chemie I Ed* 38:1870
3. Murad F (1999) *Angew Chemie I Ed* 38:1856
4. Ignarro LJ (2010) *Nitric oxide: biology and pathobiology*. 2nd edn. Elsevier Inc., Burlington
5. Bellamy TC, Garthwaite J (2001) *J Biol Chem* 276
6. Boon EM, Huang SH, Marletta MA (2005) *Nature Chem Biol* 1:53
7. Griffith OW, Stuehr DJ (1995) *Ann Rev Physiol* 57:707
8. Greenwood NN, Earnshaw A (1993) *Chemistry of the elements*. Pergamon, Oxford, Chapter 11
9. Coppens P, Novozhilova I, Kovalevsky A (2002) *Chem Rev* 102:861
10. Novozhilova IV, Coppens P, Lee J, Richter-Addo GB, Bagley KA (2006) *J Am Chem Soc* 128:2093
11. Tocheva EI, Rosell FI, Mauk AG, Murphy MEP (2004) *Science* 304:867
12. Tocheva EI, Rosell FI, Mauk AG, Murphy MEP (2007) *Biochemistry* 46:12366
13. Merkle AC, Lehnert N (2012) *Dalton Trans* 41:3355
14. Periyasamy G, Sundararajan M, Hillier IH, Burton NA, McDouall JJW (2007) *Phys Chem* 9:2498
15. Mingos DMP (1973) *Inorg Chem* 12:1209
16. Enemark JH, Feltham RD (1974) *Coord Chem Rev* 13:339
17. Wyllie GRA, Scheidt WR (2002) *Chem Rev* 102:1067
18. Copeland DM, Soares AS, West AH, Richter-Addo GB (2006) *J Inorg Biochem* 100:1413
19. Cohn JN, McInnes GT, Shepherd AM (2011) *J Clin Hyperten* 13:690
20. Roussin J (1858) *Ann Chim Phys* 52:285
21. Rauchfuss TB, Weatherill TD (1982) *Inorg Chem* 21:827
22. Mokh VP, Poltorakov AP, Serezhenkov VA, Vanin AF (2010) *Nitric Oxide Biol Chem* 22:266
23. Flitney FW, Megson IL, Thomson JLM, Kennovin GD, Butler AR (1996) *Br J Pharmacol* 117:1549
24. Bourassa J, DeGraff W, Kudo S, Wink DA, Mitchell JB, Ford PC (1997) *J Am Chem Soc* 119:2853
25. Kudo S, Bourassa JL, Boggs SE, Sato Y, Ford PC (1997) *Analyt Biochem* 247:193
26. Conrado CL, Bourassa JL, Egler C, Weckler S, Ford PC (2003) *Inorg Chem* 42:2288
27. Weckler SR, Mikhailovsky A, Korystov D, Ford PC (2006) *J Amer Chem Soc* 128:3831
28. Zheng Q, Bonoiu A, Ohulchanskyy TY, He GS, Prasad PN (2008) *Mol Pharm* 5:389
29. Chen TN, Lo FC, Tsai ML, Shih KN, Chiang MH, Lee GH, Liaw WF (2006) *Inorg Chim Acta* 359:2525
30. Kim YM, Chung HT, Simmons RL, Billiar TR (2000) *J Biol Chem* 275:10954

31. Butler AR, Megson IL (2002) *Chem Rev* 102:1155
32. Bosworth CA, Toledo JC Jr, Zmijewski JW, Li Q, Lancaster JR Jr (2009) *Proc Natl Acad Sci USA* 106:4671
33. Tonzetich ZJ, McQuade LE, Lippard SJ (2010) *Inorg Chem* 49:6338
34. Hickok JR, Sahni S, Shen H, Arvind A, Antoniou C, Fung LWM, Thomas DD (2011) *Free Radic Biol Med* 51:1558
35. Manoharan PT, Hamilton WC (1963) *Inorg Chem* 2:1043
36. Lu TT, Tsou CC, Huang HW, Hsu IJ, Chen JM, Kuo TS, Wang Y, Liaw WF (2008) *Inorg Chem* 47:6040
37. Bryar TR, Eaton DR (1992) *Canad J Chem* 70:1917
38. Johansson G, Lipscomb WN (1957) *J Chem Phys* 27:1417
39. Ruggiero CF, Carrier SM, Antholine WE, Whitaker JW, Cramer CJ, Tolman WB (1993) *J Am Chem Soc* 115:11285
40. Fujisawa K, Tateda A, Miyashita Y, Okamoto K, Paulat F, Praneeth VKK, Merkle A, Lehnert N (2008) (I) *J Am Chem Soc* 130:1205
41. Wright AM, Wu G, Hayton TW (2010) *J Am Chem Soc* 132:14336
42. Scheidt WR, Frisse ME (1975) *J Am Chem Soc* 97:17
43. Nasri H, Haller KJ, Wang Y, Huynh BH, Scheidt WR (1992) *Inorg Chem* 31:3459
44. Scheidt WR, Brinegar AC, Ferro EB, Kerner JF (1977) *J Am Chem Soc* 99:7315
45. Brucker EA, Olson JS, Ikeda-Saito M, Philips GN Jr (1998) *Proteins Struct Funct Genet* 30:352
46. Chan NL, Kavanaugh JS, Rogers PH, Arnone A (2004) *Biochemistry* 43:118
47. Wayland BB, Olson LW (1974) *J Am Chem Soc* 95:6037
48. Hoffman BM, Weschler CJ, Basolo F (1976) *J Am Chem Soc* 98:5473
49. Palmer G (1979) In: Dolphin D (ed) *The porphyrins*, vol 4. Academic, New York, Chap. 6
50. Gouterman M (1961) *J Mol Spectrosc* 6:138
51. Westcott BL, Enemark JH (1999) In: Solomon EI, Lever ABP (eds) *Inorganic electronic structure and spectroscopy*, vol 2. Wiley, New York pp 403–450
52. Scheidt WR, Hatano K, Rupprecht GA, Piciulo PL (1979) *Inorg Chem* 18:292
53. Traylor TG, Sharma VS (1992) *Biochemistry* 31:2847
54. Perutz MF, Kilmartin JV, Nagai K, Szabo A, Simon SR (1976) *Biochem* 15:378
55. Dierks EA, Hu S, Vogel KM, Yu AE, Sprio TG, Burstyn JN (1997) *J Am Chem Soc* 119:7316
56. Derbyshire ER, Marletta MA (2012) *Ann Rev Biochem* 81:559
57. Patterson JC, Lorkovic IM, Ford PC (2003) *Inorg Chem* 42:4902
58. Toledo JC, Silva HAS, Scarpellini M, Mori V, Camargo AJ, Bertotti M, Franco DW (2004) *Eur J Inorg Chem* 1879
59. Goodrich LE, Paulat F, Praneeth VKK, Lehnert N (2010) *Inorg Chem* 49:6293
60. Caramori GF, Kunitz AG, Andriani KF, Doro FG, Frenking G, Tfouni E (2012) *Dalton Trans* 41:7327
61. Heinecke JL, Khin C, Pereira JCM, Suárez SA, Iretskii AV, Doctorovich F, Ford PC (2013) *J Am Chem Soc* 135:4007
62. Conradie J, Hopmann KH, Ghosh A (2010) *J Phys Chem B* 114:8517
63. Olson JS, Phillips GN (1996) *J Biol Chem* 271:17593
64. Strickland N, Harvey JN (2007) *J Phys Chem B* 111:841
65. Praneeth VKK, Paulat F, Berto TC, George SD, Näther C, Sulok CD, Lehnert N (2008) *J Am Chem Soc* 130:15288
66. Walda KN, Liu XY, Sharma VS, Magde D (1994) *Biochem* 33:2198
67. Benabbas A, Ye X, Kubo M, Zhang ZY, Maes EM, Montfort WR, Champion PM (2010) *J Am Chem Soc* 132:2811
68. Park J, Lee T, Park J, Lim M (2013) *J Phys Chem B* 117:2850
69. Armor JN, Scheidegger HA, Taube H (1973) *J Am Chem Soc* 90:1968
70. Armor JN, Pell SD (1973) *J Am Chem Soc* 95:7625
71. Czap A, van Eldik R (2003) *Dalton Trans* 32:665

72. Ford PC, Fernandez BO, Lim MD (2005) *Chem Rev* 105:2439
73. Moore EG, Gibson QH (1976) *J Biol Chem* 251:2788
74. Tamura M, Kobayashi K, Hayashi K (1978) *FEBS Let* 88:124
75. Hoffman BM, Gibson QH (1978) *Proc Natl Acad Sci USA* 75:21
76. Rose EJ, Hoffman BM (1983) *J Am Chem Soc* 105:2866
77. Hoshino M, Arai S, Yamaji M, Hama Y (1986) *J Phys Chem* 90:2109
78. Ionascu D, Gruia F, Ye X, Yu A, Rosca F, Beck C, Demidov A, Olson JS, Champion PM (2005) *J Am Chem Soc* 127:16921
79. Purwar N, McGarry JM, Kostera J, Pacheco AA, Schmidt M (2011) *Biochemistry* 50:4491
80. Hoshino M, Kogure M (1989) *J Phys Chem* 93:5478
81. Hoshino M, Ozawa K, Seki H, Ford PC (1993) *J Am Chem Soc* 115:9568
82. Laverman LE, Ford PC (2001) *J Am Chem Soc* 123:11614
83. Laverman LE, Wanat A, Oszajca J, Stochel G, Ford PC, van Eldik R (2001) *J Am Chem Soc* 123:285
84. Ford PC (2010) *Inorg Chem* 49:6226
85. Wolak M, van Eldik R (2005) *J Am Chem Soc* 127:13312
86. Abu-Soud HM, Ichimori K, Presta A, Stuehr DJ (2000) *J Biol Chem* 275:17349
87. Scheele JS, Bruner E, Kharitonov VG, Martasek P, Roman LJ, Masters BS, Sharma VS, Magde D (1999) *J Biol Chem* 274:13105
88. Andersen JF, Ding XD, Balfour C, Shokhireva TK, Champagne DE, Walker FA, Montfort WR (2000) *Biochem* 39:10118
89. Ouellet H, Lang J, Couture MR, Ortiz de Montellano P (2009) *Biochem* 48:863
90. Franke A, Stochel G, Jung C, Van Eldik R (2004) *J Am Chem Soc* 126:4181
91. Kharitonov VG, Russwurm M, Madge D, Sharma VS, Koesling D (1997) *Biochem Biophys Res Comm* 239:284
92. Quaroni LG, Seward HE, McLean KJ, Girvan HM, Ost, TWB, Noble MA, Kelly SM, Price NC, Cheesman MR, Smith WE, Munro AW (2004) *Biochem* 43:16416
93. Rinaldo S, Arcovito A, Brunori M, Cutruzzolà F (2007) *J Biol Chem* 282:14761
94. Kakar S, Hoffman FG, Storz JF, Fabian M, Hargrove MS (2010) *Biophys Chem* 152:1
95. Abbruzzetti S, Faggiano S, Spyrakis F, Bruno S, Mozzarelli A, Astegno A, Dominici P, Viappiani C (2011) *IUBMB Life* 63:1094
96. Condorelli P, George SC (2001) *Biophys J* 80:2110
97. Ostrich IJ, Gordon L, Dodgen HW, Hunt JP (1980) *Inorg Chem* 19:619
98. Schnepfenseper T, Zahl A, van Eldik R (2001) *Angew Chemie Int Ed Eng* 40:1678
99. Hickok JR, Vasudevan D, Thatcher GRJ, Thomas DD (2012) *Antioxi Redox Sig* 17:962
100. Nhut G T, Kalyvas H, Skodje KM, Hayashi T, Moenne-Loccoz P, Callan PE, Shearer J, Kirschenbaum LJ, Kim E (2011) *J Am Chem Soc* 133 5 1184
101. Lin ZS, Lo FC, Li CH, Chen CH, Huang WN, Hsu IJ, Lee JF, Horng JC, Liaw WF (2011) *Inorg Chem* 50:10417
102. Vanin AF (2009) *Nitric Oxide Biol Chem* 21:1
103. Tonzetich ZJ, Do LH, Lippard SJ (2009) *J Am Chem Soc* 131:7964
104. Bourassa JL, Ford PC (2000) *Coord Chem Rev* 200:887
105. Sanina NA, Syrsova LA, Shkondina NI, Rudneva TN, Malkova ES, Bazanov TA, Kotelnikov AI, Aldoshin SM (2007) *Nitric Oxide Biol Chem* 16:181
106. Bourassa J, Lee B, Bernhard S, Schoonover J, Ford PC (1999) *Inorg Chem* 38:2947
107. Vanin AF, Papina AA, Serezhenkov VA, Koppenol WH (2004) *Nitric Oxide* 10:60
108. Wanat A, Schnepfenseper T, Stochel G, van Eldik R, Bill E, Wieghardt K (2002) *Inorg Chem* 41:2
109. Schnepfenseper T, Wanat A, Stochel G, Goldstein S, Meyerstein D, van Eldik R (2001) *Euro J. Inorg Chem* 2317
110. Lucas HR, Meyer GJ, Karlin KD (2009) *J Am Chem Soc* 131:13924
111. Zheng D, Birke R (2001) *J Am Chem Soc* 123:4637

112. Wolak M, Zahl A, Schnepfensieper T, Stochel G, van Eldik R (2001) *J Am Chem Soc* 123:9780
113. Bakac A, Pestovsky O, Durfey BL, Kristian KE (2013) *Chem Sci* 4:2185
114. Gladwin MT, Grubina R, Doyle MP (2009) *Accts Chem Res* 42:157
115. He C, Knipp M (2009) *J Am Chem Soc* 131:12042
116. Yi J, Heinecke J, Tan H, Ford PC, Richter-Addo GB (2009) *J Am Chem Soc* 131:18119
117. Heinecke J, Ford PC (2010) *Coord Chem Rev* 254:235
118. Olabe JA (2008) *Dalton Trans* 3633
119. Cohn JN, McInnes GT, Shepherd AMJ (2011) *Clin Hyperten* 13:690
120. Vaughan CJ, Delanty N (2000) *Lancet* 356:411
121. Ascenzi P, Pesce A, Nardini M, Bolognesi M, Ciaccio C, Coletta M, Dewilde S (2013) *Biochem Biophys Res Comm* 430:1301
122. Hoshino M, Maeda M, Konishi R, Seki H, Ford PC (1996) *J Am Chem Soc* 118:5702
123. Koppenol WH (2012) *Inorg Chem* 51:5637
124. Reichenbach G, Sabatini S, Palombari R, Palmerini CA (2001) *Nitric Oxide* 5:395
125. Luchsinger BP, Rich EN, Gow AJ, Williams EM, Stamler JS, Singel DJ (2003) *Proc Natl Acad Sci USA* 100:461
126. Broniowska KA, Keszler A, Basu S, Kim-Shapiro DB, Hogg N (2012) *Biochem J* 442:191
127. Fernandez BO, Lorkovic IM, Ford PC (2004) *Inorg Chem* 43:5393
128. Fernandez BO, Ford PC (2003) *J Am Chem Soc* 125:10510
129. Basu S, Grubina R, Huang J, Conradie J, Huang Z, Jeffers A, Jiang A, He X, Azarov I, Seibert R, Mehta A, Patel R, King SB, Hogg N, Ghosh A, Gladwin MT, Kim-Shapiro DB (2007) *Nature Chem Biol* 3:785
130. Tejero J, Basu S, Helms C, Hogg N, King SB, Kim-Shapiro DB, Gladwin MT, Low NO (2012) *J Biol Chem* 287:18262
131. Lundberg J, Weitzberg E, Gladwin MT (2008) *Nat Rev Drug Discov* 7:156
132. Feelisch M, Fernandez BO, Bryan NS, Garcia-Saura MF, Bauer S, Whitlock DR, Ford PC, Janero DR, Rodriguez J, Ashrafiyan H (2008) *J Biol Chem* 283:33927
133. Lei Y, Anson FC (1994) *Inorg Chem* 33:5003
134. Tran D, Shelton BW, White AI, Laverman LE, Ford PC (1998) *Inorg Chem* 37:2505
135. Lim MD, Capps KB, Karpishin TB, Ford PC (2005) *Nitric Oxide* 12:244
136. Tsuge K, DeRosa F, Lim MD, Ford PC (2004) *J Am Chem Soc* 126:6564
137. Khin C, Lim MD, Tsuge K, Iretskii A, Wu G, Ford PC (2007) *Inorg Chem* 46:9323
138. Weichsel W, Maes EM, Andersen JF, Valenzuela JG, Shokhireva TK, Walker FA, Montfort WR (2005) *Proc Natl Acad Sci USA* 102:594
139. Franke A, Stochel G, Suzuki N, Higuchi T, Okuzono K, van Eldik R (2005) *J Am Chem Soc* 127:5360
140. Dicks AP, Swift HR, Williams DL, H, Butler AR, Al-Sa'doni HH, Cox BG (1996) *J Chem Soc Perkin Trans* 2:481
141. Melzer Marie M, Mossin S, Cardenas AJP, Williams KD, Zhang S, Meyer K, Warren TH (2012) *Inorg Chem* 51:8658
142. Franz KJ, Singh N, Lippard SJ (2000) *Angew Chem I E* 39:2120
143. Riklin M, Tran D, Bu X, Laverman LE, Ford PC (2001) *JCS Dalton Trans* 1813:1819
144. McMillin DR, Kirchoff JR, Goodwin KV (1985) *Coord Chem Rev* 64:83
145. Lim MH, Lippard SJ (2005) *J Am Chem Soc* 127:12170
146. Lim MH, Xu D, Lippard (2006) *SJ Nat Chem Biol* 2:375
147. McQuade LE, Pluth MD, Lippard SJ (2010) *Inorg Chem* 49:8025
148. Kumar P, Kalita A, Mondal B (2012) *Dalton Trans* 41:10543
149. Sarma M, Kalita A, Kumar P, Mondal B (2010) *J Am Chem Soc* 132:7846
150. Sarma M, Mondal B (2011) *Inorg Chem* 50:3206
151. Shiva S, Wang X, Ringwood LA, Xu X, Yuditskaya S, Annavaajihala V, Miyajima H, Hogg N, Harris ZL, Gladwin MT (2006) *Nature Chem Biol* 2:486
152. Grundy KR, Reed CA, Roper WR (1970) *Chem Commun* 1501

153. Wilson RD, Ibers JA (1979) *Inorg Chem* 18:336
154. Marhenke J, Joseph CA, Corliss MZ, Dunn T, Ford PC (2007) *Polyhedron* 26:4638
155. Lin R, Farmer PJ (2000) *J Am Chem Soc* 122:2393
156. Montenegro AC, Amorebieta VT, Slep LD, Martin DF, Roncaroli F, Murgida DH, Bari SE, Olabe JA (2009) *Angew Chem Int Ed* 48:4213
157. Khin C, Heinecke JL, Ford PC (2008) *J Am Chem Soc* 130:13830
158. Smith PAS, Hein GE (1960) *J Am Chem Soc* 82:5731
159. Miranda KM (2005) *Coord Chem Rev* 249:433
160. Doctorovich F, Bikiel D, Pellegrino J, Suarez SA, Larsen A, Marti MA (2011) *Coord Chem Rev* 255:2764
161. Fukuto JM, Cisneros CJ, Kinkade RL (2013) *J Inorg Biochem* 118:201
162. Ford PC, Wink DA, Stanbury DM (1993) *FEBS Lett* 326:1
163. Wink DA, Darbyshire JF, Nims RW, Saveedra JE, Ford PC (1993) *Chem Res Toxicol* 6:23
164. Silkstone RS, Mason MG, Nicholls P, Cooper CE (2012) *Free Rad Biol Med* 52:80
165. Ford E, Hughes MN, Wardman P (2002) *Free Rad Biol Med* 32:1314
166. Liu X, Miller MJS, Joshi MS, Thomas DD, Lancaster JR Jr (1998) *Proc Natl Acad Sci USA* 95:2175
167. Doyle MP, Hoekstra JW (1981) *J Inorg Biochem* 14:351
168. Herold S, Exner M, Nauser T (2001) *Biochemical* 40:3385
169. Olson JS, Foley EW, Rogge C, Tsai AL, Doyle MP, Lemon DD (2004) *Free Rad. Biol Med* 36:685
170. Gardner PR, Gardner AM, Brashear WT, Suzuki T, Hvitved AN, Satchell KDR, Olson JS (2006) *J Inorg Biochem* 100:542
171. Kurtikyan TS, Ford PC (2010) *Chem Commun* 46:8570
172. Blomberg LM, Blomberg MRA, Siegbahn PEM (2004) *J Inorg Biol Chem* 9:923
173. Mishra S, Meuwly M (2010) *J Am Chem Soc* 132:2968
174. Møller JKS, Skibsted LH (2004) *Chem Eur J* 10:2291
175. Arnold EV (1996) *Bohle DS* 269:41
176. Munk MB, Huvaere K, Van Bocxlaer J, Skibsted LH (2010) *Food Chem* 121:472
177. Sarti P, Forte E, Mastronicola D, Giuffre A, Arese M (2012) *Biochim Biophys Acta Bioenerget* 1817:610

Synthetic Models of Copper–Nitrosyl Species Proposed as Intermediates in Biological Denitrification

Debra J. Salmon and William B. Tolman

Abstract Copper-containing nitrite reductase enzymes catalyze the reduction of nitrite to nitric oxide during denitrification, a key component of the global nitrogen cycle. Insights into the properties of proposed copper–nitrosyl intermediates have been obtained through studies of model complexes. Such complexes comprising both copper and nickel exhibit variable geometries and electronic structures that are influenced by the supporting ligands.

Keywords Copper · Model complex · Nitric oxide · Nitrite · Nitrite reductase

Contents

1	Introduction	138
2	[CuNO] ¹¹ Complexes	141
3	[CuNO] ¹⁰ Complexes	144
4	[NiNO] ¹⁰ Complexes	146
5	Summary, Conclusions, and Outlook	150
	References	150

Abbreviations

Ar	Aryl
atm	Atmosphere
Bpy	2,2'-Bipyridyl
Bu	Butyl
Cp	Cyclopentadienyl
Cu-NiR	Copper nitrite reductase enzyme

D.J. Salmon and W.B. Tolman (✉)
Department of Chemistry and Center for Metals in Biocatalysis, University of Minnesota,
207 Pleasant St. SE, Minneapolis, MN 55455, USA
e-mail: wtolman@umn.edu

Cy	Cyclohexyl
dmp	2,9-Dimethyl-1,10-phenanthroline
ENDOR	Electron-nuclear double resonance
EPR	Electron paramagnetic resonance
equiv	Equivalent(s)
ESI-MS	Electrospray ionization mass spectrometry
Et	Ethyl
h	Hour(s)
His	Histidine
Im	Imidazole
<i>i</i> Pr	Isopropyl
IR	Infrared spectroscopy
MCD	Magnetic circular dichroism
Me	Methyl
Mes	Mesityl 2,4,6-trimethylphenyl (not methanesulfonyl)
min	Minute(s)
mol	Mole(s)
NMR	Nuclear magnetic resonance
Ph	Phenyl
py	Pyridine
pz	Pyrazolyl
rt	Room temperature
s	Second(s)
<i>t</i> Bu	<i>tert</i> -Butyl
THF	Tetrahydrofuran
TMEDA	<i>N,N,N',N'</i> -tetramethyl-1,2-ethylenediamine
Tol	4-Methylphenyl
Trp	Tris(pyrazolyl)hydroborate
UV-vis	Ultraviolet-visible
XAS	X-ray absorption spectroscopy

1 Introduction

Biological denitrification plays a major role in the global nitrogen cycle and involves the reduction of nitrate to dinitrogen, through several nitrogen oxide intermediates (Scheme 1). The various steps in this process are catalyzed by metalloenzymes that have been extensively studied [1–23]. These enzymes include the molybdopterin-containing nitrate reductase [4] and the heme–nonheme iron-containing nitric oxide reductase [5], which bears key similarities to the large heme-copper oxidase family, members of which also react in physiologically relevant



Scheme 1 Chemical steps involved in denitrification

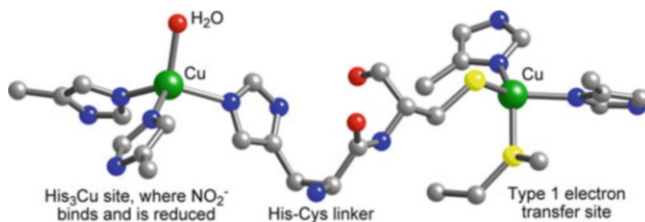
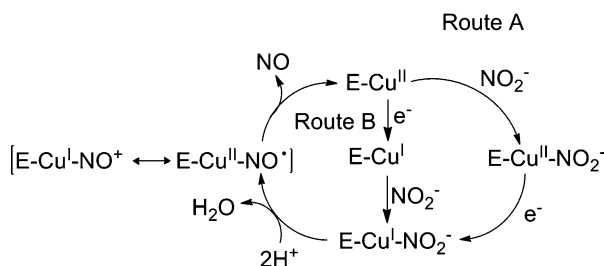


Fig. 1 The copper sites in nitrite reductase (PDB 1NIA), with the Cu atoms labeled. Key: blue = N, yellow = S, red = O, gray = C. Drawing adapted from [17]

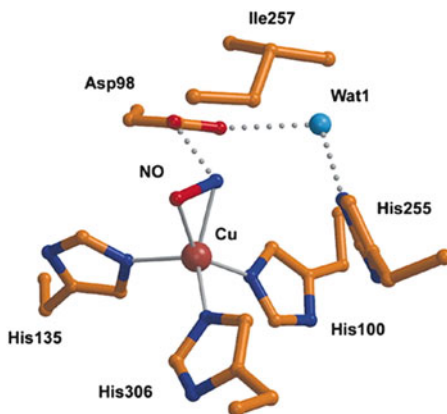


Scheme 2 Proposed mechanisms for catalysis by Cu-NiR, adapted from [18]

ways with nitrogen oxides [6]. The final step in denitrification is catalyzed by a multicopper enzyme nitrous oxide reductase [7]. The reduction of nitrite to nitric oxide is performed by heme ($\text{cd}_1\text{-NiR}$) or copper (Cu-NiR) enzymes [8], of which the latter forms the basis of discussion in this chapter.

Extensive structural, spectroscopic, and mechanistic studies of Cu-NiR's have been performed; a recent review summarizes the characterization of key intermediates in the enzyme and in model complexes [9]. Nitrite reduction is proposed to occur at the $(\text{His})_3\text{Cu}$ center in the enzyme, which is located near a type 1 electron transfer copper site (Fig. 1). Two routes for reduction of nitrite to NO by Cu-NiR have been proposed. Route A (Scheme 2) involves binding of nitrite to the oxidized Cu(II) center, followed by electron transfer from the type 1 copper center to achieve a Cu(I)-NO_2^- species suggested to adopt a nitrito (*O*-bound) form [10, 11]. In route B, reduction occurs prior to nitrite binding, and the Cu(I)-NO_2^- species is proposed to be nitro (*N*-bound) [8]. Either Cu(I)-NO_2^- species is then protonated, to yield a nitrous acid intermediate, which would then lose H_2O to yield a copper nitrosyl at the $[\text{CuNO}]^{10}$ oxidation level, described according to the Enemark–Feltham formalism for metal–nitrosyls ($[\text{MNO}]^n$, where n is the sum of metal d and nitrosyl π^* electrons) [12–14]. Additional studies have proposed a random-sequential mechanism in which both routes A and B run in parallel [15]. In any case, the $[\text{CuNO}]^{10}$ species is proposed to be highly susceptible to NO (product)

Fig. 2 Representation of the active site of the proposed side-on copper–nitrosyl in NiR. Reproduced with permission from [19]



loss, which would yield the resting Cu(II) enzyme active site. A one-electron reduced $[\text{CuNO}]^{11}$ species has also been considered, but while it is not currently implicated as a player in the major catalytic pathway for reduction of nitrite to NO, it has been suggested to be involved in the reduction of NO under anaerobic conditions [16].

While the proposed $[\text{CuNO}]^n$ ($n = 10$ or 11) species have not been directly observed as catalytic intermediates, such copper nitrosyls have been identified as products of reactions of Cu-NiR with NO. For example, treatment of crystals of the reduced enzyme from the bacterium *Alcaligenes faecalis* with exogenous NO yielded a novel species that was characterized by X-ray crystallography [19]. The 1.4 Å resolution data were interpreted to indicate the presence of a side-on bound nitrosyl (Fig. 2), a provocative conclusion because such coordination is unprecedented for a metallo-enzyme active site. Notable geometric parameters include N and O atoms nearly equidistant from the Cu atom (1.97–2.01 Å and 1.95–2.12 Å), an average Cu–N–O bond angle of 71°, and a long N–O distance of 1.45–1.67 Å. X-ray crystal structures were reported in separate work that also feature a side-on bound nitrosyl, albeit with slightly different structural parameters (cf. Cu–N/O = 2.2 Å, N–O = 1.4 Å) [11]. Wild-type NiR and two mutants with little or no enzymatic activity, one incapable of electron transfer from the type 1 Cu to the catalytic type 2 Cu site (H145A) and the other without the hydrogen-bonding Asp98 residue (D98N), both showed side-on bound NO when crystals were soaked in NO solutions [20]. The NO was more disordered in the D98N mutant, however, which was partially modeled as end-on bound NO. In all of these cases, the copper–nitrosyl was assigned as $[\text{CuNO}]^{11}$, derived from the binding of NO to a Cu(I) center, either present initially or derived from reduction of a Cu(II) site by excess NO.

The novelty of the side-on coordination in the aforementioned species inspired studies by experiment and theory aimed at evaluating the relative stabilities of the side-on versus end-on geometries and the oxidation state assignments $\text{Cu(II)}\text{-NO}^-$ versus $\text{Cu(I)}\text{-NO}^\bullet$. With regard to the latter issue, an assignment as $\text{Cu(II)}\text{-NO}^-$

based on EPR spectroscopy data [20] was disputed in favor of the alternate Cu(I)–NO• formulation on the basis of analysis of EPR, MCD, and ENDOR spectroscopy data in conjunction with theory [21, 22]. This conclusion was corroborated in separate computational studies, which together with others [23–25] indicated that the end-on geometry was energetically favored relative to the side-on structure in most models comprising either simple ligands or ones incorporating surrounding amino acid residues found in the protein. On the other hand, other DFT studies showed that the side-on geometry modeled using the X-ray structure coordinates was a local energy minimum due to steric interactions of the end-on structure with an Ile-257 residue in the protein environment, despite the finding that the end-on geometry is a global minimum, 6–8 kcal/mol lower in energy than the side-on structure [26].

These types of issues centered on electronic and geometric structural preferences and reactivity of proposed metalloenzyme intermediates may be addressed through studies of synthetic complexes, which may be more readily studied in detail under abiological conditions (e.g., low temperature in organic solvent) and which can be modified through variation of supporting ligand properties [27]. In particular, studies of copper–nitrosyl complexes have provided important insights into bonding, oxidation states and reactivity that are helpful for understanding the putative [CuNO]ⁿ ($n = 10$ or 11) species proposed for Cu-NiR, as well as for other enzymes [3] or catalytic systems [28]. We summarize these advances herein and include discussion of additional work on nickel congeners that provides complementary understanding.

2 [CuNO]¹¹ Complexes

Although not a monocopper species of specific relevance to Cu-NiR intermediates, it is important to note the first structurally characterized copper–nitrosyl complex to be reported (**1**, Fig. 3). This complex was prepared by reaction of a dicopper(I) precursor with NO⁺ and was proposed to contain a Cu(II)–(NO[−])–Cu(II) core on the basis of structural and spectroscopic evidence [29]. The geometry of **1** is similar to phenoxo and hydroxo-bridged dicopper(II) analogs [30] and features a Cu–Cu distance of 3.141(0) Å. The N–O bond length (1.176 Å), Cu–N–O bond angle (129.5°), and IR ($\nu(\text{NO}) = 1,536 \text{ cm}^{-1}$) are characteristic of a bridging NO[−] ligand.

The first well-defined mononuclear copper nitrosyl complexes to be isolated (**2**, Fig. 3) are supported by tris(pyrazolyl)hydroborate (Tp^{R,R'}) ligands with variable substituents R and R' that confer differing steric and electronic properties to the complexes [31–35]. These complexes were prepared by addition of NO (1 atm) to solutions of TpCu(I) precursors, resulting in a color change from pale yellow to deep red. The reactions were reversible, as evinced by bleaching under vacuum. The X-ray structure of **2a** (R = *t*Bu, R' = H; Fig. 4) shows end-on coordination of the nitrosyl with a Cu–N–O angle of 163.4(6)°, intermediate between linear and fully bent (120°) geometries [32]. The subsequently determined structure of **2f** (R = *t*Bu, R' = *i*Pr) features an Cu–N–O angle closer to linearity (171.9(5)°) [35].

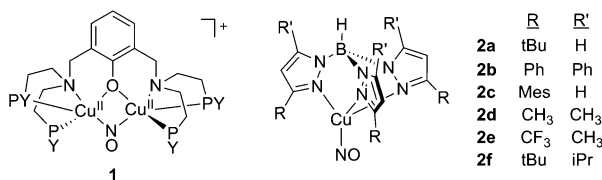


Fig. 3 Examples of well-defined copper–nitrosyl complexes

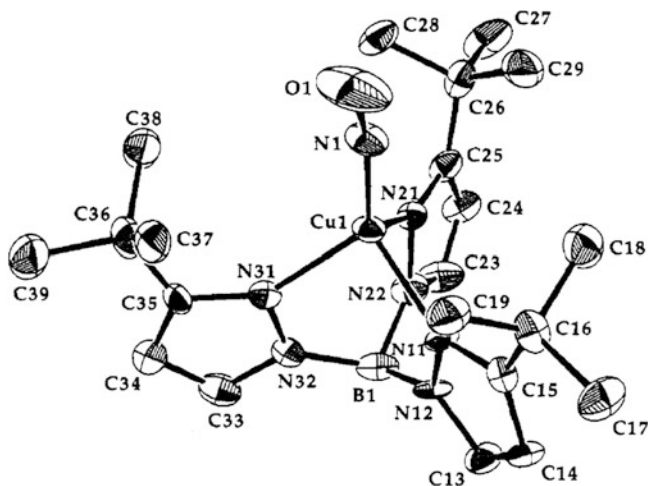
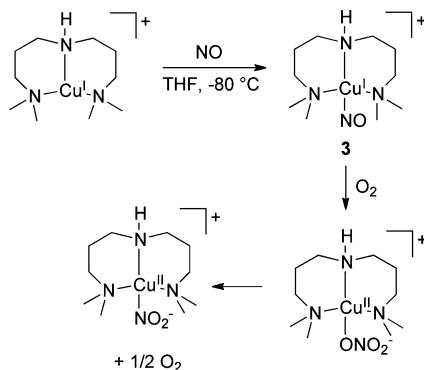


Fig. 4 Representation of the X-ray crystal structure of **2a** ($R = t\text{Bu}$, $R' = \text{H}$). Reprinted with permission from [31]. Copyright 1992 American Chemical Society

The red color of the complexes is due to an electronic absorption with a λ_{max} in the range 436–506 nm (Table 1). These absorption energies vary as a function of the electron donor ability of the supporting ligand substituents, as do the corresponding nitrosyl stretching frequencies and $\nu(\text{CO})$ values for carbonyl analogs [36, 37]. Thus, the more electron withdrawing the substituents (e.g., $R' = \text{CF}_3$), the greater the Lewis acidity of the copper ion and the higher the $\nu(\text{CO})$ and $\nu(\text{NO})$ values. The same effect is also seen in a comparison of **2f** ($R = t\text{Bu}$, $R' = i\text{Pr}$; $\nu(\text{NO}) = 1,698 \text{ cm}^{-1}$) to an analogous complex supported by the less electron-donating, neutral tris(pyrazolyl)methane ligand ($\nu(\text{NO}) = 1,742 \text{ cm}^{-1}$) [35]. The accompanying trend in the electronic absorption feature (more Lewis acidic center has shorter wavelength λ_{max}) is consistent with its assignment as a transition with $\text{Cu } d \rightarrow \text{NO } \pi^*$ MLCT character. This assignment, which was confirmed in more detailed later work [35], supports a $\text{Cu(I)}\text{-NO}\cdot$ formulation for these complexes. Further corroboration of this conclusion comes from theoretical calculations [38], the absence of d–d transitions typical for Cu(II) ions in the electronic absorption and MCD spectra, and the finding that the EPR spectra features a signal only observable at $T < 40 \text{ K}$ with $g \sim 1.84$, both well below what is typical for Cu(II) compounds, with a large A_{N} value of $\sim 30 \times 10^{-4} \text{ cm}^{-1}$ indicative of significant spin density on the nitrosyl N atom

Scheme 4 Synthesis of a copper-nitrosyl complex and its O₂ reactivity



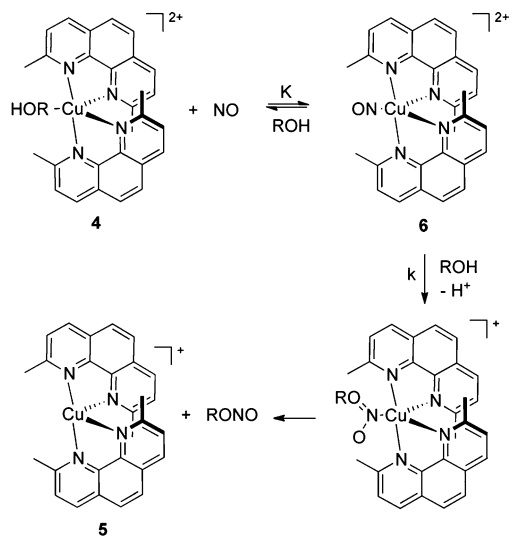
Another example of a [CuNO]¹¹ complex is supported by 3,3'-iminobis(*N,N'*-dimethylpropylamine) (**3**, Scheme 4; $\nu(\text{NO}) = 1,736 \text{ cm}^{-1}$) [39]. It was suggested to be a Cu(I)–NO• species on the basis of DFT calculations and EPR spectroscopy. This complex reacted with O₂ to yield a novel peroxynitrite complex that upon heating regenerated O₂ (0.5 equiv) and a copper(II)–nitrite product.

3 [CuNO]¹⁰ Complexes

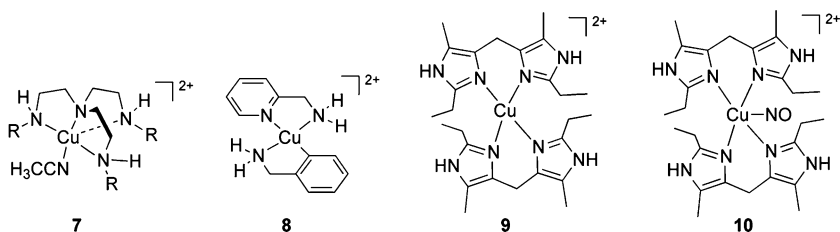
There have been many attempts to access the [CuNO]¹⁰ core proposed to be an intermediate during catalysis by Cu-NiR. In early work, adduct formation between simple Cu(II) salts and NO was postulated, but characterization data was sparse and structural information from these studies is lacking [40–42]. The intermediacy of [CuNO]¹⁰ in various other transformations has been suggested in several reports, and in some cases these proposals have been supported by direct spectroscopic data. In this section we summarize these reports as well as the more recent description of the first X-ray structure of a [CuNO]¹⁰ complex.

In a number of instances, treatment of copper(II) complexes with NO results in reduction to yield copper(I) species, and mechanisms involving initial Cu(II)–NO adduct formation have been proposed. For example, the complex **4** (dmp = 2,9-dimethyl-1,10-phenanthroline) in water or methanol solution reacts with NO to yield **5** and RONO (R = H or Me; Scheme 5) [43, 44]. The results of kinetics experiments were interpreted to support the mechanism shown in Scheme 5, and the observation of reversible color changes upon exposure of **4** on a solid support to NO was cited in support of the feasibility of the 5-coordinate [CuNO]¹⁰ intermediate **6**.

In a related example, Cu(II) complexes **7** of tripodal tris(2-*R*-aminoethyl)amines (R = H, Et, *i*Pr) react with NO in CH₃CN to yield [Cu(I)(CH₃CN)₄]⁺ and nitrosated ligands (Scheme 6) [45, 46]. Transient intermediates were observed by UV–vis spectroscopy, which were found to be EPR silent and, in one case (R = H), to exhibit an intense peak in the IR spectrum at 1,650 cm⁻¹ assigned to $\nu(\text{NO})$. These results were interpreted to suggest the intermediacy of a copper–nitrosyl complex. Similar data and conclusions were drawn for the reactions of **8** with NO [47].



Scheme 5 Reactivity of a Cu(II) complex with NO



Scheme 6 Copper(II) complexes that react with NO, and the product in one case (**10**)

A thermally stable Cu(II)–NO adduct was isolated upon treatment of **9** with NO (Scheme 6) [48]. This adduct (**10**) was identified by ESI-MS and elemental analysis and was shown to be diamagnetic (EPR silent, sharp peaks in ^1H NMR spectrum) with $\nu(\text{NO}) = 1,662\text{ cm}^{-1}$ ($\Delta^{15}\text{N} = 31\text{ cm}^{-1}$). Interestingly, treatment of **10** with H_2O_2 yielded a Cu(I)–nitrate product, which was proposed to evolve from a Cu(I)–peroxynitrite intermediate [49]. Also, complex **10** reacted with added H_2O to yield a unique N-donor ligand supported Cu(I)–nitrite complex, a conversion that is reverse of that catalyzed by NiR [48].

Only one X-ray crystal structure of a $[\text{CuNO}]^{10}$ complex (**11**) has been reported to date (Fig. 5) [50]. This purple complex was prepared by addition of 2 equiv of $[\text{NO}][\text{PF}_6]$ to copper metal powder at $-25\text{ }^\circ\text{C}$ in CH_3NO_2 . It binds NO reversibly to yield $[\text{Cu}(\text{CH}_3\text{NO}_2)_5](\text{PF}_6)_2$ (**12**), as monitored by following the $\nu(\text{NO})$ ($1,933\text{ cm}^{-1}$, $\Delta^{15}\text{N} = 40\text{ cm}^{-1}$) for **11** and the EPR spectrum of **12** during cycling between vacuum and NO (1 atm). The nitrosyl ligand adopts a bent geometry $[(\text{Cu}-\text{N}-\text{O}) = 121.0(3)^\circ]$ at an equatorial site. A weak Cu–NO interaction is indicated by a Cu–N bond length [$1.955(4)\text{ \AA}$] that is longer than in $[\text{CuNO}]^{11}$

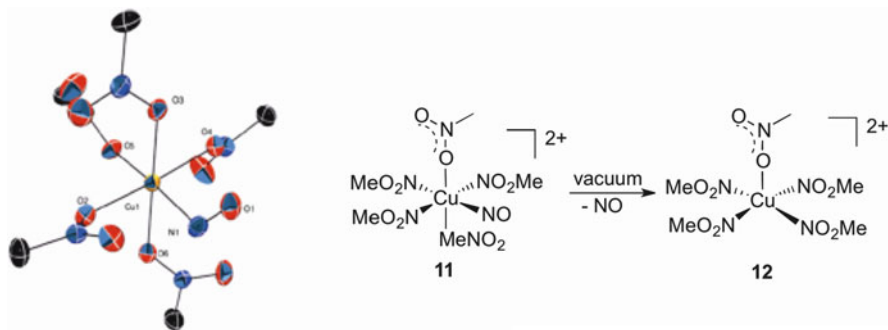


Fig. 5 Complexes **11** and **12** and a representation of the X-ray crystal structure of **11**, reprinted with permission from [50]. Copyright 2010 American Chemical Society

complexes **2a** and **2f** (1.76–1.79 Å). It was argued that the $[\text{CuNO}]^{10}$ moiety is best formulated as a $\text{Cu(II)}\text{-NO}\cdot$ species, but additional evaluation of this hypothesis is needed. Importantly, as noted [50], complex **11** “may provide a model of how nitric oxide coordinates to Cu(II) during the Cu-NIR catalytic cycle.”

4 $[\text{NiNO}]^{10}$ Complexes

It can be useful to compare the small molecule activation chemistry of nickel complexes to copper congeners, as in many cases complementary structures and related reactivity may be observed (cf. dioxygen activation [51, 52]). A number of complexes comprising the $[\text{NiNO}]^{10}$ core have been characterized, which while featuring the same overall electron count as the $[\text{CuNO}]^{10}$ moiety may be considered to adopt different metal oxidation states ($\text{Ni(I)}\text{-NO}\cdot/\text{Ni(II)}\text{-NO}^-$ vs. $\text{Cu(II)}\text{-NO}\cdot/\text{Cu(III)}\text{-NO}^-$).

Because they are supported by the same $\text{Tp}^{\text{R,R'}}$ ligand set, it is particularly useful to draw comparisons among the complexes $\text{Tp}^{\text{R,R'}}\text{M(NO)}$ ($\text{M} = \text{Cu, Ni, Co}$; Table 2) [38, 53, 54]. While there is general agreement that the $\text{Cu(I)}\text{-NO}\cdot$ formulation is appropriate for **2a**, in which the $[\text{CuNO}]^{11}$ moiety is distorted from linearity, quite disparate views on the bonding for the linear Ni complex **13** have been proposed, including $\text{Ni(0)}\text{-NO}^+$ [53], $\text{Ni(II)}\text{-NO}^-$ [38], and $\text{Ni(IV)}\text{-NO}^{3-}$ [54]. The $\text{Ni(0)}\text{-NO}^+$ hypothesis merely reflects a formalized view with no basis in experimental data or theory. The $\text{Ni(IV)}\text{-NO}^{3-}$ view was suggested on the basis of the short Ni-N distance, which was noted to be similar to that in the hypothetical nitride $\text{Tp}^{\text{CH}_3, \text{CH}_3}\text{NiN}$, and an interpretation of DFT calculations that relied, essentially, on not attributing electrons involved in Ni-NO π bonding to the d electron count [54]. This view is disputed in a more recent study [38] that drew specific comparisons to the Co analog **14** (Table 2), which was shown by extensive experimental data (cf. EPR and XAS) and multiconfigurational calculations to be best described as high-spin Co(II) ($S_{\text{Co}} = 3/2$) antiferromagnetically coupled to a triplet NO^- ($S_{\text{NO}} = 1$). Calculations for **13** led to a similar

Table 2 Selected properties for $\text{Tp}^{\text{R,R'}}\text{M}(\text{NO})$ complexes ($\text{M} = \text{Cu}, \text{Ni}, \text{Co}$)

Complex	$\nu(\text{NO})$ (cm^{-1})	M–N–O (deg)	M–N (\AA)	N–O (\AA)	Reference
$\text{Tp}^{\text{tBu,H}}\text{Cu}(\text{NO})$ (2a)	1,712	163.4(6)	1.759(6)	1.108(7)	[32]
$\text{Tp}^{\text{CH}_3,\text{CH}_3}\text{Ni}(\text{NO})$ (13)	1,786	178.5(6)	1.619(6)	1.170(7)	[54]
$\text{Tp}^{\text{CH}_3,\text{CH}_3}\text{Co}(\text{NO})$ (14)	1,732	175.5(6)	1.628(5) ^a	1.167(6)	[38]

^aData for one of two molecules in the asymmetric unit

conclusion, whereby the ground state is dominated by Ni(II) configurations. The authors of this work further argued that the higher $\nu(\text{NO})$ value for **13** than for **14** is not consistent with a lower N–O bond order implied by the Ni(IV)–NO³⁻ formulation, and rationalized the divergent $\nu(\text{NO})$ values for the two complexes on the basis of differing contributions of M(O)–NO• configurations to their respective ground state wave functions.

Nickel–nitrosyls supported by facially coordinating tridentate ligands geometrically akin to $\text{Tp}^{\text{R,R'}}$ (Fig. 6) feature linear $[\text{NiNO}]^{10}$ cores like in **13** [54–59]. Presumably, similar bonding conclusions as drawn for the $\text{Tp}^{\text{R,R'}}$ case apply, although these issues have not yet been explored fully for these systems. Comparison of $\nu(\text{NO})$ among the linear 4-coordinate $[\text{NiNO}]^{10}$ complexes supported by the full range of tridentate ligands has been made [57], revealing trends in electron-donating abilities of the ligands (Table 3). For example, the strong electron donor characteristics of the heterocyclic carbenes in **17–19** induce lower $\nu(\text{NO})$ values than for complexes of $\text{Tp}^{\text{R,R'}}$ ligands or S/Se analogs **15–16**.

Linear nitrosyls have also been isolated in non- C_3 -symmetric complexes (Fig. 7). A Ni analog **23** of the $[\text{CuNO}]^{10}$ complex **11** was prepared similarly, but exhibited a Ni–N–O angle of 174.1(8)° ($\nu(\text{NO}) = 1,877 \text{ cm}^{-1}$) in distinct contrast to the bent geometry observed for the Cu complex (121.0(3)°) [60]. The weakly bound nitromethane ligands in **23** can be readily displaced, by arenes such as mesitylene, to yield **24**. Several three-coordinate $[\text{NiNO}]^{10}$ complexes have been reported [60–62], including **25** and those supported by β -diketiminato ligands that were synthesized from d⁹ Ni(I) precursors [63]. Complexes such as **26** contain linear nitrosyls, as analyzed from their X-ray crystal structures (Ni–N–O = 171–174°).

Bent geometries for $[\text{NiNO}]^{10}$ complexes have also been observed. For example, bidentate Se and S donor ligand variants of the tridentate ligands in **27–28** result in non- C_3 -symmetric structures with nonlinear nitrosyls (Fig. 8) [55, 64]. A rationale for the observed nitrosyl geometries was invoked wherein the Ni–N σ^* orbital is stabilized by mixing of the nitrosyl π^* orbital through bending [64]. The first anionic mononuclear $[\text{NiNO}]^{10}$ complex **29**, supported by thiolate ligands, features $\nu(\text{NO}) = 1,655 \text{ cm}^{-1}$ in the solid state or Nujol mull (1,756 cm^{-1} in CH_3CN) and a bent Ni–N–O bond angle of 156.6°. The low nitrosyl stretching frequency presumably derives from the anionic nature of the complex and the strong electron-donating characteristics of the supporting thiolate ligands. In another example, reaction of the 3-coordinate complex **25** with bipy or 2,9-dimethyl-1,10-phenanthroline yields the 5-coordinate species **30**. The nitrosyl in **30** is best described as NO⁻ (Ni–N–O = 129.5(2)° and $\nu(\text{NO}) = 1,567 \text{ cm}^{-1}$), in

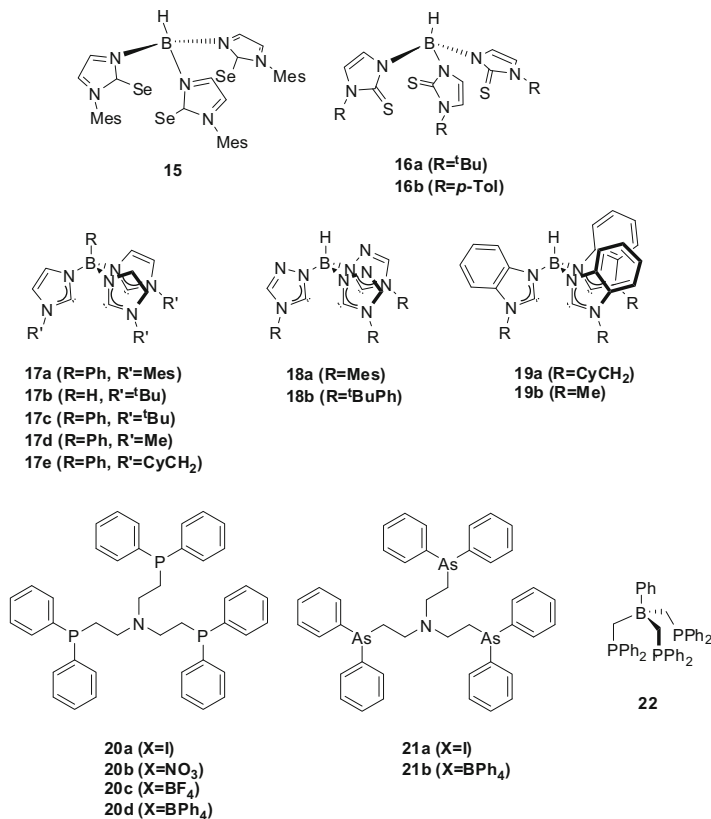


Fig. 6 Ligands used to support 4-coordinate, approximately C_3 -symmetric $[\text{NiNO}]^{10}$ complexes. For **18** and **19**, X = counterion of the cationic complex

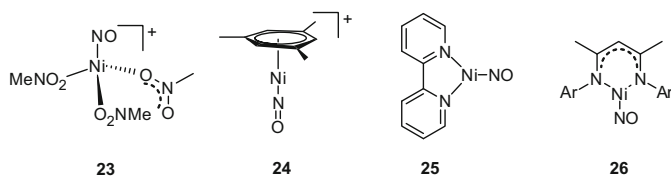
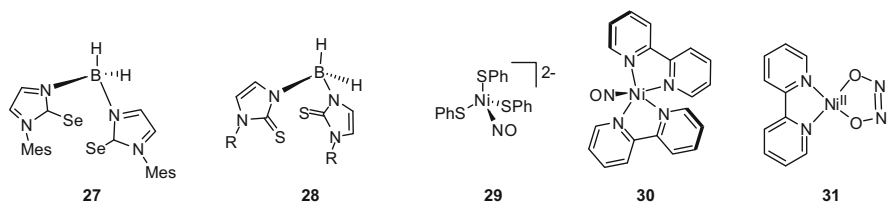
contrast with the linear nitrosyl in three-coordinate **25** ($\text{Ni-N-O} = 176.2(3)^\circ$ and $\nu(\text{NO}) = 1,869 \text{ cm}^{-1}$). Complex **30** decomposed upon standing via a characterized $[\text{N}_2\text{O}_2]^{2-}$ intermediate **31** to form N_2O , a reaction similar to the disproportionation of the $[\text{CuNO}]^{11}$ species **2a–e**.

Finally, a particularly apropos case relevant to proposals for the nitrosyl intermediate invoked in Cu-NiR catalysis centers on the Cp^*Ni system (Fig. 9) [65]. X-ray structures of the ground state complex $\text{Cp}^*\text{Ni}(\text{NO})$ (**32**) and its metastable form **33** resulting from irradiation were solved, revealing conversion of the linear nitrosyl to a side-on bound form upon photolysis. This latter $[\text{NiNO}]^{10}$ structure provides key precedent for the putative $[\text{CuNO}]^{10}$ variant proposed for Cu-NiR.

Table 3 Comparison of $\nu(\text{NO})$ values for 4-coordinate $[\text{NiNO}]^{10}$ complexes supported by tridentate ligands

Ligand	$\nu(\text{NO})$ (cm^{-1})	Reference
$\text{Tp}^{\text{CH}_3, \text{CH}_3}$ (as in 13)	1,786	[54]
15	1,763, 1,752	[54]
16a	1,741	[55]
16b	1,752	[55]
17a	1,724	[56]
17b	1,703	[56]
17c	1,701	[56]
17d	1,697	[56]
17e	1,693	[57]
18a	1,742	[57]
18b	1,746	[57]
19a	1,711	[57]
19b	1,714	[57]
20a	1,760	[58]
20b	1,770	[58]
20c	1,775	[58]
20d	1,755	[58]
21a	1,760	[58]
21b	1,778	[58]
22	1,737	[59]

The counterion (X) in the cationic complexes formed from **20** and **21** altered $\nu(\text{NO})$

**Fig. 7** Examples of complexes with linear nickel–nitrosyls**Fig. 8** Examples of complexes with bent nickel–nitrosyls

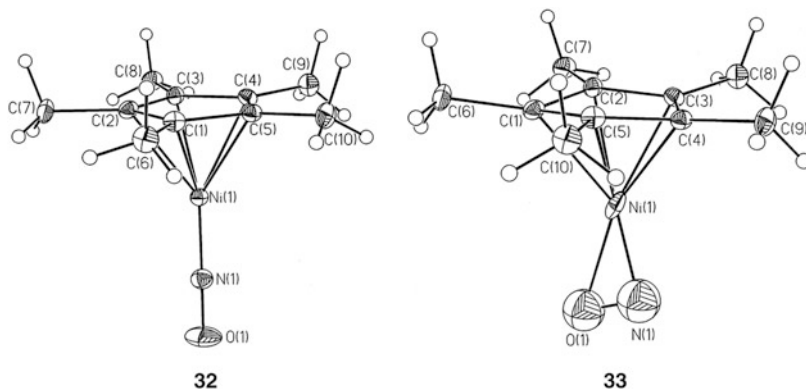


Fig. 9 Comparison of ground state complex **32** and its metastable form **33**. Reprinted with permission from [65]. Copyright 1998 American Chemical Society

5 Summary, Conclusions, and Outlook

Studies of copper– and nickel–nitrosyl complexes have provided new understanding of bonding, geometries, and electronic structures of the $[MNO]^n$ units that has informed and complemented spectroscopic and theoretical studies of elusive intermediates in the reactions of Cu–NiR. While more success has been attained to date in modeling $[CuNO]^{11}$ species, one electron more reduced than the purported active intermediate, recent advances in characterizing $[CuNO]^{10}$ compounds have led to more direct information on how nitric oxide binds to the metal center during enzymatic catalysis. The appearance of a side-on nitrosyl in the native enzyme has not yet been duplicated in copper complexes; this remains as a synthetic objective in future work. Nickel–nitrosyl congeners of the electron count $[NiNO]^{10}$ have enabled useful comparisons to their copper analogs, and the identification of a side-on bound variant provides key precedent for this geometry in Cu–NiR. The varied coordination modes of nitrosyl ligands as a function of supporting ligand geometries and properties are fascinating from a structural perspective and provide a framework for future reactivity studies. Such studies will add to the wealth of information on Cu–NiR models aimed at better understanding nitrosyl bonding and the nature of intermediates involved in the Cu–NiR catalytic cycle.

References

1. Zumft WG (1997) Cell biology and molecular basis of denitrification. *Microbiol Rev* 61:533
2. Eady RR, Hasnain SS (2004) Denitrification. In: McCleverty JA, Meyer TJ (eds) *Comprehensive coordination chemistry II*, vol 8. Elsevier, Amsterdam, pp 759–786
3. Wasser IM, de Vries S, Moënné-Loccoz P, Schröder I, Karlin KD (2002) Nitric oxide in biological denitrification: Fe/Cu metalloenzyme and metal complex NO_x redox chemistry. *Chem Rev* 102:1201

4. Campbell WH (1999) Nitrate reductase structure, function and regulation: bridging the gap between biochemistry and physiology. *Annu Rev Plant Physiol Plant Mol Biol* 50:277
5. Moënné-Loccoz P, Richter O-MH, Huang H-W, Wasser IM, Ghiladi RA, Karlin KD, de Vries S (2000) Nitric oxide reductase from *Paracoccus denitrificans* contains an oxo-bridged heme/non-heme diiron center. *J Am Chem Soc* 122:9344
6. Zumft W (2005) Nitric oxide reductases of prokaryotes with emphasis on the respiratory, heme-copper oxidase type. *J Inorg Biochem* 99:194
7. Dell Acqua S, Pauleta SR, Moura I, Moura JGG (2011) The tetranuclear copper active site of nitrous oxide reductase: the CuZ center. *J Biol Inorg Chem* 16:183
8. Averill BA (1996) Dissimilatory nitrite and nitric oxide reductases. *Chem Rev* 96:2951
9. Merkle A, Lehnert N (2012) Binding and activation of nitrite and nitric oxide by copper nitrite reductase and corresponding model complexes. *Dalton Trans* 41:3355
10. Suzuki S, Kataoka K, Yamaguchi K (2000) Metal coordination and mechanism of multicopper nitrite reductase. *Acc Chem Res* 33:728
11. Antonyuk SV, Strange RW, Sawers G, Eady RR, Hasnain SS (2005) Atomic resolution structures of resting-state, substrate- and product-complexed Cu-nitrite reductase provide insight into catalytic mechanism. *Proc Natl Acad Sci USA* 102:12041
12. Enemark JH, Feltham RD (1974) Principles of structure, bonding, and reactivity for metal nitrosyl complexes. *Coord Chem Rev* 13:339
13. McCleverty JA (2004) Chemistry of nitric oxide relevant to biology. *Chem Rev* 104:403
14. Hayton TW, Legzdins P, Sharp WB (2002) Coordination and organometallic chemistry of metal – NO complexes. *Chem Rev* 102:935
15. Wijma HJ, Jeuken LJC, Verbeet MP, Armstrong FA, Canters GW (2006) A random-sequential mechanism for nitrite binding and active site reduction in copper-containing nitrite reductase. *J Biol Chem* 281:16340
16. Ye RW, Toro-Suarez I, Tiedje JM, Averill BA (1991) H₂¹⁸O isotope exchange studies on the mechanism of reduction of nitric oxide and nitrite to nitrous oxide by denitrifying bacteria. *J Biol Chem* 266:12848
17. Tolman W (2006) Using synthetic chemistry to understand copper protein active sites: a personal perspective. *J Biol Inorg Chem* 11:261
18. Kujime M, Fujii H (2006) Spectroscopic characterization of reaction intermediates in a model for copper nitrite reductase. *Angew Chem Int Ed* 45:1089
19. Tocheva EI, Rosell FI, Mauk AG, Murphy MEP (2004) Side-on copper-nitrosyl coordination by nitrite reductase. *Science* 304:867
20. Tocheva EI, Rosell FI, Mauk AG, Murphy MEP (2007) Stable copper-nitrosyl formation by nitrite reductase in either oxidation state. *Biochemistry* 46:12366
21. Usov OM, Sun Y, Grigoryants VM, Shapleigh JP, Scholes CP (2006) EPR-ENDOR of the Cu(I)NO complex of nitrite reductase. *J Am Chem Soc* 128:13102
22. Ghosh S, Dey A, Usov OM, Sun Y, Grigoryants VM, Scholes CP, Solomon EI (2007) Resolution of the spectroscopy versus crystallography issue for NO intermediates of nitrite reductase from *Rhodobacter sphaeroides*. *J Am Chem Soc* 129:10310
23. Silaghi-Dumitrescu R (2006) Copper-containing nitrite reductase: a DFT study of nitrite and nitric oxide adducts. *J Inorg Biochem* 100:396
24. Sundararajan M, Surendran R, Hillier IH (2006) How is NO bound to reduced copper nitrite reductase? A DFT study. *Chem Phys Lett* 418:96
25. Periyasamy G, Sundararajan M, Hillier IH, Burton NA, McDouall JJW (2007) The binding of nitric oxide at the Cu(I) site of copper nitrite reductase and of inorganic models: DFT calculations of the energetics and EPR parameters of side-on and end-on structures. *Phys Chem Chem Phys* 9:2498
26. Merkle AC, Lehnert N (2009) The side-on copper(I) nitrosyl geometry in copper nitrite reductase is due to steric interactions with isoleucine-257. *Inorg Chem* 48:11504
27. Karlin KD (1993) Metalloenzymes, structural motifs, and inorganic models. *Science* 261:701

28. Shelef M (1995) Selective catalytic reduction of NO_x with N-free reductants. *Chem Rev* 95:209
29. Paul PP, Tyeklar Z, Farooq A, Karlin KD, Liu S, Zubieta J (1990) Isolation and X-ray structure of a dinuclear copper-nitrosyl complex. *J Am Chem Soc* 112:2430
30. Karlin KD, Hayes JC, Gultneh Y, Cruse RW, McKown JW, Hutchinson JP, Zubieta J (1984) Copper-mediated hydroxylation of an arene: model system for the action of copper monooxygenases. Structures of a binuclear copper(I) complex and its oxygenated product. *J Am Chem Soc* 106:2121
31. Carrier SM, Ruggiero CE, Tolman WB, Jameson GB (1992) Synthesis and structural characterization of a mononuclear copper nitrosyl complex. *J Am Chem Soc* 114:4407
32. Ruggiero CE, Carrier SM, Antholine WE, Whittaker JW, Cramer CJ, Tolman WB (1993) Synthesis and structural and spectroscopic characterization of mononuclear copper nitrosyl complexes: models for nitric oxide adducts of copper proteins and copper-exchanged zeolites. *J Am Chem Soc* 115:11285
33. Ruggiero CE, Carrier SM, Tolman WB (1994) Reductive disproportionation of NO mediated by copper complexes: modeling N₂O generation by copper proteins and heterogeneous catalysts. *Angew Chem Int Ed Engl* 33:895
34. Schneider JL, Carrier SM, Ruggiero CE, Young VG Jr, Tolman WB (1998) Influences of ligand environment on the spectroscopic properties and disproportionation reactivity of copper-nitrosyl complexes. *J Am Chem Soc* 120:11408
35. Fujisawa K, Tateda A, Miyashita Y, Okamoto K, Paulat F, Praneeth VKK, Merkle A, Lehnert N (2008) Structural and spectroscopic characterization of mononuclear copper(I) nitrosyl complexes: end-on versus side-on coordination of NO to copper(I). *J Am Chem Soc* 130:1205
36. Mealli C, Arcus CS, Wilkinson JL, Marks TJ, Ibers JA (1976) Structural studies of copper(I) binding by hydrotris(1-pyrazolyl)borate and hydrotris(3,5-dimethyl-1-pyrazolyl)borate in the solid state and in solution. *J Am Chem Soc* 98:711
37. Kitajima N, Fujisawa K, Fujimoto C, Moro-oka Y, Hashimoto S, Kitagawa T, Toriumi K, Tatsumi K, Nakamura A (1992) A new model for dioxygen binding in hemocyanin. Synthesis, characterization, and molecular structure of the $\mu\text{-}\eta^2\text{-}\eta^2$ peroxo dinuclear copper(II) complexes, [Cu(HB(3,5-R₂pz)₃)](O₂) (R = *i*-Pr and Ph). *J Am Chem Soc* 114:1277
38. Tomson NC, Crimmin MR, Petrenko T, Rosebrugh LE, Sproules S, Boyd WC, Bergman RG, DeBeer S, Toste FD, Wieghardt K (2011) A step beyond the Feltham–Enemark notation: spectroscopic and correlated *ab Initio* computational support for an antiferromagnetically coupled M(II)–(NO) – description of Tp*M(NO) (M = Co, Ni). *J Am Chem Soc* 133:18785
39. Park GY, Deepalatha S, Puiui SC, D-H L, Mondal B, Sarjeant AAN, del Rio D, Pau MYM, Solomon EI, Karlin KD (2009) A peroxynitrite complex of copper: formation from a copper-nitrosyl complex, transformation to nitrite and exogenous phenol oxidative coupling or nitration. *J Biol Inorg Chem* 14:1301
40. Mercer M, Fraser RTM (1963) Formation and dissociation of copper (II) nitrosyl complexes in non-aqueous solvents. *J Inorg Nucl Chem* 25:525
41. Doyle MP, Siegfried B, Hammond JJ (1976) Oxidative deamination of primary amines by copper halide nitrosyls. The formation of geminal dihalides. *J Am Chem Soc* 98:1627
42. Deters D, Weser U (1995) The analogous reaction of a diSchiff base coordinated copper and Cu₂Zn₂ superoxide dismutase with nitric oxide. *Biometals* 8:25
43. Tran D, Ford PC (1996) Nitric oxide reduction of the copper (II) complex Cu(dmp)₂²⁺ (dmp = 2,9-dimethyl-1,10-phenanthroline). *Inorg Chem* 35:2411
44. Tran D, Skelton BW, White AH, Laverman LE, Ford PC (1998) Investigation of the nitric oxide reduction of the bis(2,9-dimethyl-1,10-phenanthroline) complex of copper(II) and the structure of [Cu(dmp)₂(H₂O)](CF₃SO₃)₂. *Inorg Chem* 37:2505
45. Sarma M, Singh A, Subrahmanyam Gupta G, Das G, Mondal B (2010) Nitric oxide reduction of copper(II) complex with tetradentate amine ligand followed by ligand transformation. *Inorg Chim Acta* 363:63

46. Sarma M, Kalita A, Kumar P, Singh A, Mondal B (2010) Reduction of copper(II) complexes of tripodal ligands by nitric oxide and trinitrosation of the ligands. *J Am Chem Soc* 132:7846
47. Sarma M, Mondal B (2011) Nitric oxide reduction of copper(II) complexes: spectroscopic evidence of copper(II) – nitrosyl intermediate. *Inorg Chem* 50:3206
48. Kalita A, Kumar P, Deka RC, Mondal B (2012) First example of a Cu(I)–(η^2 -O, O)nitrite complex derived from Cu(II)–nitrosyl. *Chem Commun* 48:1251
49. Kalita A, Kumar P, Mondal B (2012) Reaction of a copper(II)–nitrosyl complex with hydrogen peroxide: putative formation of a copper(I)–peroxynitrite intermediate. *Chem Commun* 48:4636
50. Wright AM, Wu G, Hayton TW (2010) Structural characterization of a copper nitrosyl complex with a {CuNO}¹⁰ configuration. *J Am Chem Soc* 132:14336
51. Kieber-Emmons M, Riordan C (2007) Dioxxygen activation at monovalent nickel. *Acc Chem Res* 40:618
52. Yao S, Driess M (2011) Lessons from isolable nickel(I) precursor complexes for small molecule activation. *Acc Chem Res* 45:276
53. Harding DJ, Harding P, Adams H, Tuntulani T (2007) Synthesis and characterization of sterically hindered tris(pyrazolyl)borate Ni complexes. *Inorg Chim Acta* 360:3335
54. Landry VK, Pang K, Quan SM, Parkin G (2007) Tetrahedral nickel nitrosyl complexes with tripodal [N₃] and [Se₃] donor ancillary ligands: structural and computational evidence that a linear nitrosyl is a trivalent ligand. *Dalton Trans* 820
55. Maffett LS, Gunter KL, Kreisel KA, Yap GPA, Rabinovich D (2007) Nickel nitrosyl complexes in a sulfur-rich environment: the first poly(mercaptoimidazolyl)borate derivatives. *Polyhedron* 26:4758
56. Nieto I, Bontchev RP, Ozarowski A, Smirnov D, Krzystek J, Telser J, Smith JM (2009) Synthesis and spectroscopic investigations of four-coordinate nickel complexes supported by a strongly donating scorpionate ligand. *Inorg Chim Acta* 362:4449
57. Muñoz SB III, Salvador B, Foster WK, Lin H-J, Margarit CG, Dickie DA, Smith JM (2012) Tris(carbene)borate ligands featuring imidazole-2-ylidene, benzimidazol-2-ylidene, and 1,3,4-triazol-2-ylidene donors. Evaluation of donor properties in four-coordinate {NiNO}¹⁰ complexes. *Inorg Chem* 51:12660
58. Di Vaira M, Ghilardi CA, Sacconi L (1976) Synthesis and structural characterization of some nitrosyl complexes of iron, cobalt, and nickel with poly(tertiary phosphines and arsines). *Inorg Chem* 15:1555
59. MacBeth CE, Thomas JC, Betley TA, Peters JC (2004) The coordination chemistry of “[BP₃]NiX” platforms: targeting low-valent nickel sources as promising candidates to L₃Ni=E and L₃Ni≡E linkages. *Inorg Chem* 43:4645
60. Wright AM, Wu G, Hayton TW (2011) Late-metal nitrosyl cations: synthesis and reactivity of [Ni(NO)(MeNO₂)₃][PF₆]. *Inorg Chem* 50:11746
61. Iluc VM, Miller AJM, Hillhouse GL (2005) Synthesis and characterization of side-bound aryldiazo and end-bound nitrosyl complexes of nickel. *Chem Commun* 5091
62. Wright AM, Wu G, Hayton TW (2012) Formation of N₂O from a nickel nitrosyl: isolation of the cis-[N₂O₂]²⁻ intermediate. *J Am Chem Soc* 134:9930
63. Puiu SC, Warren TH (2003) Three-coordinate β -diketiminato nickel nitrosyl complexes from nickel(I)-lutidine and nickel(II)-alkyl precursors. *Organometallics* 22:3974
64. Landry VK, Parkin G (2007) Synthesis and structural characterization of [Bse^{Me}]Ni(PPh₃)(NO), a nickel complex with a bent nitrosyl ligand. *Polyhedron* 26:4751
65. Fomitchev DV, Furlani TR, Coppens P (1998) Combined X-ray diffraction and density functional study of [Ni(NO)(η^5 -Cp^{*})] in the ground and light-induced metastable states. *Inorg Chem* 37:1519

Structure and Bonding in Heme–Nitrosyl Complexes and Implications for Biology

Nicolai Lehnert, W. Robert Scheidt, and Matthew W. Wolf

Abstract This review summarizes our current understanding of the geometric and electronic structures of ferrous and ferric heme–nitrosyls, which are of key importance for the biological functions and transformations of NO. In-depth correlations are made between these properties and the reactivities of these species. Here, a focus is put on the discoveries that have been made in the last 10 years, but previous findings are also included as necessary. Besides this, ferrous heme–nitroxyl complexes are also considered, which have become of increasing interest recently due to their roles as intermediates in NO and multiheme nitrite reductases, and because of the potential role of HNO as a signaling molecule in mammals. In recent years, computational methods have received more attention as a means of investigating enzyme reaction mechanisms, and some important findings from these theoretical studies are also highlighted in this chapter.

Keywords Crystallography · DFT calculations · Electronic structure · Heme proteins · HNO · Iron porphyrins · Nitric oxide · Nitrosyl complexes · Nitroxyl complexes · Non-innocent ligands · Spectroscopy

Contents

1	Introduction	157
2	Geometric Structures of Heme–Nitrosyls	160
	2.1 Ferrous Heme–Nitrosyls	160

N. Lehnert (✉) and M.W. Wolf
Department of Chemistry, The University of Michigan, Ann Arbor, MI 48109-1055, USA
e-mail: lehnertn@umich.edu

W.R. Scheidt (✉)
Department of Chemistry and Biochemistry, University of Notre Dame, 251 Nieuwland Science Hall, Notre Dame, IN 46556, USA
e-mail: Scheidt.1@nd.edu

2.2	Ferric Heme–Nitrosyls	169
2.3	Related Nitrosyls (Mn and Co)	173
3	Spectroscopic Properties of Heme–Nitrosyls	174
3.1	Ferrous Heme–Nitrosyls	174
3.2	Ferric Heme–Nitrosyls	186
4	Electronic Structures of Heme–Nitrosyls	193
4.1	Ferrous Heme–Nitrosyls	193
4.2	Ferric Heme–Nitrosyls	204
5	Ferrous Heme–Nitroxyl Complexes	210
6	Heme–Nitrosyl Complexes as Intermediates in Enzyme Catalysis: New Computational Insight	213
6.1	Fungal Nitric Oxide Reductase	213
6.2	Bacterial Nitric Oxide Reductase	215
6.3	Multiheme Cytochrome <i>c</i> Nitrite Reductase	217
7	Conclusions	218
	References	218

Abbreviations

2-MI	2-Methylimidazole
3,5-Me-BAFP	3,5-Methyl-bis(aryloxy)-fence porphyrin
4-MePip	4-Methylpiperidine
5C	Five-coordinate
6C	Six-coordinate
CcNIR	Multiheme cytochrome <i>c</i> nitrite reductase
CcO	Cytochrome <i>c</i> oxidase
Cys	Cysteine, cysteinate
Cyt <i>c</i>	Cytochrome <i>c</i>
Deut ²⁻	Deuteroporphyrin IX dimethylester dianion
ENDOR	Electron-nuclear double resonance spectroscopy
eNOS	Endothelial nitric oxide synthase
EPR	Electron paramagnetic resonance spectroscopy
Hb	Hemoglobin
His	Histidine
HNOX	Heme-nitric oxide or oxygen binding (domain)
HOMO	Highest occupied molecular orbital
HRP	Horseradish peroxidase
hs	High-spin
iNOS	Inducible nitric oxide synthase
Iz	Indazole
ls	Low-spin
LUMO	Lowest unoccupied molecular orbital
Mb	Myoglobin
MCD	Magnetic circular dichroism spectroscopy
MI	1-Methylimidazole (also called <i>N</i> -methylimidazole)
MO	Molecular orbital

NIR	Nitrite reductase
nNOS	Neuronal nitric oxide synthase
NO	Nitric oxide
NOD	Nitric oxide dioxygenation
NOR	Nitric oxide reductases
NorBC	Bacterial respiratory NO reductase
NOS	Nitric oxide synthase
Np	Nitrophorins
NRVS	Nuclear resonance vibrational spectroscopy
OEP ²⁻	Octaethylporphyrin dianion
OETPP ²⁻	Octaethyltetraphenylporphyrin dianion
oxoOEC ²⁻	Oxo-octaethylchlorin
P ²⁻	Porphine dianion
P450nor	Fungal cytochrome P450 NO reductase
<i>p</i> -C ₆ H ₄ F ⁻	4-Fluorophenyl anion
PCET	Proton-coupled electron transfer
PES	Potential energy surface
Prz	Pyrazine
Py	Pyridine
Pz	Pyrazole
rNp	<i>Rhodnius prolixus</i> nitrophorins
sGC	Soluble guanylate cyclase
SOMO	Singly occupied molecular orbital
<i>To</i> -F ₂ PP ²⁻	Tetra(<i>ortho</i> -difluoro-phenyl)-porphyrin dianion
<i>Tp</i> -CF ₃ PP ²⁻	Tetra(<i>para</i> -trifluoromethylphenyl)-porphyrin dianion
<i>Tp</i> -FPP ²⁻	Tetra(<i>para</i> -fluorophenyl)-porphyrin dianion
<i>Tpiv</i> PP ²⁻	Picket fence porphyrin
<i>Tp</i> -NO ₂ PP ²⁻	Tetra(<i>para</i> -nitrophenyl)-porphyrin dianion
<i>Tp</i> -OCH ₃ PP ²⁻	Tetra(<i>para</i> -methoxyphenyl)-porphyrin dianion
TPP* ²⁻	Phenyl-substituted tetraphenylporphyrin dianion
TPP ²⁻	Tetraphenylporphyrin dianion
TPPBr ₄ ²⁻	2,3,12,13-Tetrabromotetraphenylporphyrin dianion

1 Introduction

Heme proteins play a central role in biology as catalysts for the transformations of organic molecules (biosynthesis and degradation of organic compounds), electron transfer, molecular transport, gas and redox sensing, and the detoxification of reactive oxygen and nitrogen species [1]. One important biomolecule that is produced, sensed, and detoxified by heme proteins is the diatomic gas nitric oxide (NO) [2, 3]. This molecule is produced in mammals by the nitric oxide synthase (NOS) enzyme family for the purpose of signal transduction [in the cardiovascular system (endothelial

NOS – eNOS) and the brain (neuronal NOS – nNOS)] and for immune defense (inducible NOS – iNOS) [3–7]. The NOS isozymes are relatives of Cyt P450s and contain a heme *b* in the active site with axial cysteinate (Cys) coordination [8], and an additional, redox active, tetrahydropterin (H₄B, in the reduced form) cofactor in close proximity to the active site heme. These enzymes oxidize L-arginine in a two-step process using O₂ to yield NO and citrulline as final products. Once NO is produced by eNOS or nNOS, it is detected by the universal mammalian NO sensor protein soluble guanylate cyclase (sGC) [3, 9], the heme-based sensing domain of which was later identified to be part of the larger group of heme-nitric oxide or oxygen binding (HNOX) domains that are also found in bacteria [10]. Nitric oxide can further be produced in vivo by reduction of nitrite [11]. This process is catalyzed by heme *cd*₁ nitrite reductases (NIR) in denitrifying bacteria [12], and by deoxy-hemoglobin (Hb) and -myoglobin (Mb) in mammals [13]. The active site heme *d* of *cd*₁ NIRs is unusual with two adjacent pyrrol rings being functionalized by carbonyl groups, a modification that is thought to reduce the affinity of the heme for NO in order to promote NO release after nitrite reduction. In mammals, deoxy-Hb and -Mb are thought to bind nitrite and reduce it to NO as part of hypoxic signaling [14]. Recently, evidence has been provided that cytochrome *c* oxidases (CcOs) are also capable of reducing nitrite to NO under hypoxic conditions [15]. It has been proposed that NO produced this way then plays a role in the dilation of arteries to increase blood flow, and the induction of hypoxic nuclear genes (hypoxic signaling) for the physiological adaptation to hypoxia [16], including the expression of CcO isozymes with altered activities [17].

Since NO is toxic, it is important that efficient detoxification pathways are in place wherever this gas is produced in living systems. In mammals, the main degradation pathway of NO seems to be the reaction with oxy-Hb and -Mb, although other pathways may also exist [18, 19]. This pathway is also used by certain bacteria as a means of defense against nitrosative stress. This reaction, NO dioxygenation (NOD), leads to the generation of nitrate as the final product, presumably via formation of a heme-bound peroxynitrite intermediate [20, 21]. In denitrifying bacteria and fungi, mostly anaerobes, the degradation of NO is achieved by reduction to N₂O, catalyzed by NO reductases (NOR) [3]. The most common bacterial NORs are heterodimers and contain a catalytic domain (NorB) and a Cyt *c* electron transfer subunit, and are therefore termed NorBC or cNOR [22]. The active site of these proteins contains a heme *b*₃ with axial histidine (His) coordination and a non-heme iron center (termed Fe_B) in close proximity [23]. On the other hand, the fungal NOR belongs to the Cyt P450 family and correspondingly, uses a single heme *b* with axial Cys coordination for the reduction of NO [24]. Another potential pathway for NO degradation would be disproportionation, $3\text{NO} \rightarrow \text{NO}_2 + \text{N}_2\text{O}$, which is catalyzed by a number of transition metals, for example copper and manganese [25, 26]. In particular, copper NIR has been proposed to catalyze this reaction [27]. However, the apparent disadvantages of this process are the dependence of the reaction rate on the NO concentration in the third power, and the fact that NO₂ is generated as one of the products, which is a strongly oxidizing and nitrosating species. Accordingly, this pathway does not seem to be used for NO degradation in vivo.

Another interesting class of heme proteins are nitrophorins (Np), which serve as NO transporters in the saliva of certain blood-sucking insects [28]. The Nps from *Rhodnius prolixus* (the kissing bug) show a lipocalin-like fold with the heme being positioned in a barrel, formed from β -sheets. The heme shows axial His coordination and is located in close proximity to the open end of this barrel. In contrast, the Np from *Cimex lectularius* (the bedbug) has a β -sandwich structure where the heme is located in the periphery of the protein. Both types of Nps are active for NO transport in the ferric oxidation state. Most recently, a new protein has been discovered that is very similar in structure to the *R. prolixus* Nps. The exact function of this protein is not known, but it is thought to be utilized for NO binding. It was therefore named nitrobindin [29].

Recently, the one-electron reduced form of NO, HNO, has also gained increased attention not only as an intermediate in NOR catalysis, but also as a potential signaling molecule in biology with distinctively different physiological effects from NO [30]. This is currently a controversial topic in the literature. Corresponding heme complexes with bound nitroxyl anions (NO^-) have been published in the literature, and their reactivities have been explored [31].

In order to better understand the biological functions and transformations of nitric oxide, detailed studies into the geometric and electronic structures of corresponding heme–NO complexes in proteins and model complexes have been undertaken, and the reactions that lead to the generation of NO and that are responsible for its degradation have been investigated in detail. Great progress has been made in the last decade in furthering our understanding of those issues that relate to the role of NO in biological systems. The goal of this review is to provide a concise overview of the geometries, electronic structures, and reactivities of heme–nitrosyl complexes and, in particular, to summarize the most recent developments in the field that have been reported within the last 5 years. For earlier studies, the reader is referred to a number of comprehensive reviews. The geometric structures of manganese, iron, cobalt, and ruthenium porphyrin complexes with NO were reviewed in detail in 2002 by one of us [32]. The reactions of NO_x species with metalloporphyrins have been the focus of a number of reviews, for example [2, 3, 33–41]. The most recent reviews on the spectroscopic and electronic structures of heme–nitrosyls were published by one of us in 2010 [42], and by Ghosh et al. in 2011 [43].

Recent highlights in the field with respect to the structural characterization of heme–nitrosyls include new high-resolution crystal structures of five- and six-coordinate (5C and 6C) ferrous heme–nitrosyl model complexes and investigations into the structural dynamics of NO in the solid state in these systems [44–46], and the first crystal structure of a heme-hyponitrite dimer [47]. New spectroscopic accomplishments include the characterization of isomers of deoxy-Mb NO adducts via ENDOR [48], investigations into NO binding in sGC via multifrequency electron paramagnetic resonance (EPR) methods [49], the first detailed analysis of single-crystal nuclear resonance vibrational spectroscopy (NRVS) data for a 6C heme–nitrosyl model complex [50], and the characterization of a cobalt-porphyrin peroxynitrite adduct [21]. Important recent computational results provide more insight

into the mechanistic alternatives for different NO and nitrite reductases [51–53], and a detailed understanding of the electronic structure of ferric heme–nitrosyls [54].

2 Geometric Structures of Heme–Nitrosyls

The earliest structure determinations of nitrosyl derivatives of iron porphyrinates were carried out in the laboratories of one of us (Scheidt), and date back to the early to mid-1970s. Although these structures delineated some of the systematic features of the geometric structures, more recent studies have also revealed important general structural features. These more recent attributes will be emphasized in this review. The earlier work has been reviewed most recently in *Accounts of Chemical Research* [55] and *Chemical Reviews* [32].

2.1 Ferrous Heme–Nitrosyls

The members of this group are all odd molecules with a single unpaired electron formally derived from the NO ligand, e.g., $S = 1/2$. Although some closely related macrocyclic complexes of iron(II) and NO have an intermediate-spin state, no such species are known for porphyrinic derivatives; however, low-lying excited states of higher multiplicity have been suggested. The structures are typically those expected for low-spin iron(II) species [56]. In all cases, the iron is displaced toward the axial NO, with larger displacements expected, and found, for the five-coordinate derivatives. The iron displacements are in the range of 0.2–0.3 Å for the five-coordinate species and less than 0.1 Å for the analogous six-coordinate species. In-plane Fe–N_p distances are typical for low-spin iron at around 2.0 Å (often just slightly less). One of the striking features of this group of nitrosyl derivatives is the axial ligand-based equatorial asymmetry.

2.1.1 Five-Coordinate Nitrosyls

The first iron porphyrinate derivative to be structurally characterized was that of [Fe(TPP)(NO)] [57]. This structure demonstrated a recurrent problem in structural NO chemistry, rotational disorder in the MNO group when the group does not have a linear geometry. This molecule has crystallographically demanded 4/m symmetry leading to disorder in this particular species that is rather extreme, with a total of eight positions of the NO group, a real “hydra” of disorder as shown in Fig. 1. Fifteen years would pass before new five-coordinate derivatives were obtained for structural analyses, the most important of these was the structure determination of two crystalline forms of [Fe(OEP)(NO)] which unequivocally showed a distinct pattern for five-coordinate nitrosyls. In some respects this time gap between structure determinations was fortuitous since the two structures of [Fe(OEP)(NO)] were determined at low temperature and with area detector diffractometers,

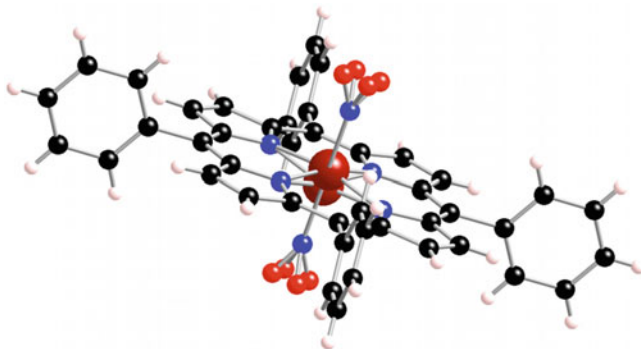


Fig. 1 The molecular structure observed for $[\text{Fe}(\text{TPP})(\text{NO})]$, which has crystallographically demanded symmetry far higher than the molecule possesses

which provided more accurate structures than those that would have been obtained earlier. It is thus possible that those features would not have been detected.

These two structures were completely ordered with a single orientation of the NO group. An unexpected feature of the first structure was the off-axis tilt of the Fe–NO vector from the heme normal. A second crystalline form showed exactly the same phenomenon. The two crystalline forms were true polymorphs with no solvent contained in either crystal. We thus concluded that this molecular feature was integral to the five-coordinate nitrosyls [58]. A second, apparently general, feature was even more unexpected. There was an asymmetry in the *equatorial* bond distances correlated with the direction of the off-axis tilt. This is shown in Fig. 2. The diagram at the bottom right of the figure shows the general pattern, whereas the diagram at the upper left gives actual values of the equatorial distances in one crystal; although the distance differences are small they are statistically significant. As can be seen, the Fe–N_p bond distances in the direction of the tilt are shorter than the equatorial distances opposite the tilt. This general pattern of equatorial asymmetry was further observed in several additional structures [59], indeed all five-coordinate nitrosyl complexes with sufficiently ordered nitrosyl groups display the off-axis tilt and the equatorial asymmetry. The deuteroporphyrin derivative [60], one of the very few porphyrin X-ray structures based on the biologically important protoporphyrin IX derivatives, shows this behavior as well. This molecule is illustrated in Fig. 3.

Table 1 lists structural parameters for a number of five-coordinate species, including the averaged values of the equatorial Fe–N_p distances when sufficient ordering of the NO group makes this sensible. The equatorial distance differences are seen to be of the order of 0.02–0.03 Å which, given the generality of the pattern, is very striking. One entry in the table requires special emphasis, the second set of entries for $[\text{Fe}(\text{TPP})(\text{NO})]$. Crystals of $[\text{Fe}(\text{TPP})(\text{NO})]$ were found to undergo a gradual phase change over a range of temperatures centered around 250 K [44]. The phase change is quite reversible with no apparent loss of crystallinity as samples

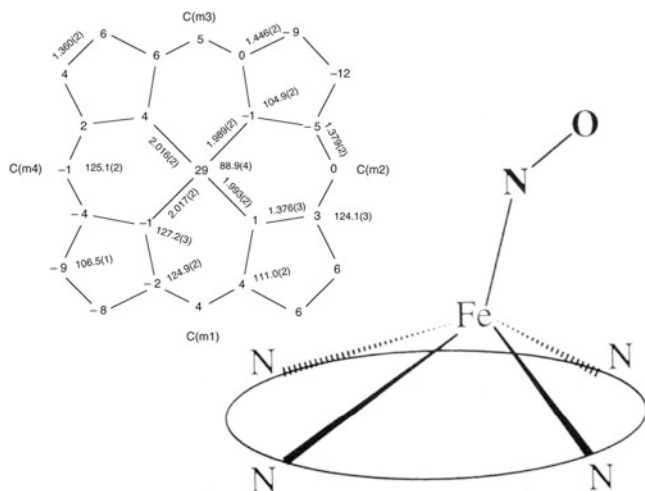


Fig. 2 Diagrams illustrating the off-axis NO tilt and its effect on the length of the equatorial Fe–N_p distances

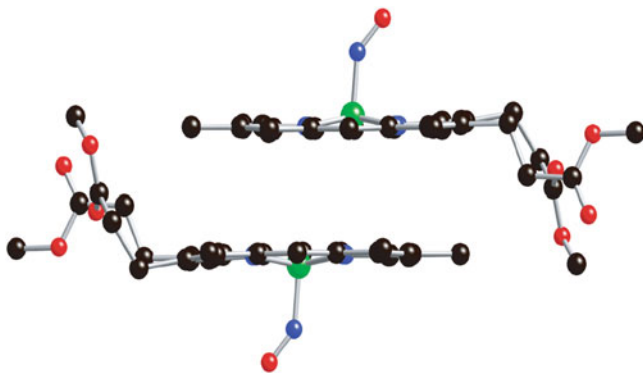


Fig. 3 Diagram illustrating the structure and the interplanar interaction of [Fe(Deut)(NO)]

are warmed or cooled past the transition point. The required symmetry for the molecule changes from $4/m$ to inversion symmetry below the transition temperature, and the Fe–NO tilt is observed as can be seen in Fig. 4 that shows the structure at 33 K.

From the determination of the first structure, it was already clear that the Fe–N–O group will not be linear, nor fully bent, but that of a “half-bent” system. The original structure determination provided an estimate for this angle; subsequent structures suggest a value of about 143° as the most likely estimate. Some comparisons of the structures of five- versus six-coordinate species are given in the next section.

Table 1 Structural and vibrational data for several 5C ferrous heme–nitrosyls

Complex	T (K)	Fe–NO ^a	N–O ^a	Fe–N–O ^b	Tilt ^b	Short Fe–N _p ^{a,c}	Long Fe–N _p ^{a,d}	References
[Fe(TPP)(NO)]	RT	1.717(7)	1.12(1)	149.2(6)	NA ^e	NA	NA	[57]
[Fe(OEP)(NO)] (A)	130	1.722(2)	1.167(3)	144.4(2)	6.5	1.991(3)	2.016(1)	[58, 59]
[Fe(OEP)(NO)] (B)	130	1.731(1)	1.168(1)	142.7(1)	8.2	1.999(1)	2.020(4)	[58, 59]
[Fe(OEP)(NO)] (B)	213	1.727(1)	NR ^f	143.3(1)	7.8	1.997(1)	2.017(5)	[59]
[Fe(OEP)(NO)] (B)	293	1.724(1)	NR ^f	144.6(2)	7.0	1.999(3)	2.016(4)	[59]
[Fe(TPPBr ₄)(NO)] (A)	130	1.734(8)	1.119(11)	147.9(8)	5.6	2.031(8)	2.041(9)	[59]
[Fe(TPPBr ₄)(NO)] (A)	130	1.726(9)	1.144(12)	146.9(9)	7.1	2.004(7)	2.027(7)	[59]
[Fe(TPPBr ₄)(NO)] (B)	293	1.691(11)	1.145(16)	145(1)	NA	NA	NA	[59]
[Fe(oxoOEC)(NO)]	130	1.732(1)	1.170(2)	143.1(1)	7.1	1.997(1)	2.011(4)	[59]
[Fe(Deut)(NO)]	100	1.723(3)	1.187(4)	143.1(3)	6.2	1.990(4)	2.020(20)	[60]
[Fe(TpivPP)(NO)]	294	1.72(2)	1.197(9)	143(3)	– ^e	–	–	[61]
[Fe(TpivPP)(NO)]	158	1.65(5)	1.17(5)	137(4)	–	–	–	[62]
[Fe(T _o -F ₂ PP)(NO)]	100	1.738(5)	NR ^f	140.4	NA	–	–	[63]
[Fe(TPP)(NO)]	33	1.739(6)	1.163(5)	144.4(5)	6.3	–	–	[44]
[Fe(TPP)(NO)]	90	1.740(5)	1.153(4)	145.6(4)	5.8	–	–	[44]
[Fe(TPP)(NO)]	180	1.737(5)	1.131(4)	147.3(4)	4.7	–	–	[44]
[Fe(TPP)(NO)]	293	1.720(6)	1.107(11)	149.5(7)	NA	–	–	[44]
[Fe(3,5-Me-BAFP)(NO)] (A)	95	1.713(4)	1.149(5)	146.3(4)	NR ^f	1.969(3)	1.997(5)	[64]
[Fe(3,5-Me-BAFP)(NO)] (B)	95	1.714(4)	1.142(5)	146.6(4)	NR ^f	1.975(3)	1.999(10)	[64]

^aValues in Å^bValues in degrees^cIn direction of tilt^dOpposite direction of tilt^eAn entry of NA or a *dashed line* indicates that the value is unavailable owing to disorder^fNot reported

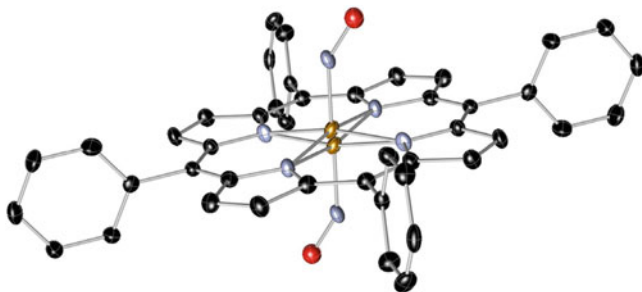


Fig. 4 Thermal ellipsoid plot showing the crystal structure of $[\text{Fe}(\text{TPP})(\text{NO})]$ at 33 K after the crystal system has undergone the tetragonal to triclinic phase change. The molecule retains a crystallographically demanded inversion center

2.1.2 Six-Coordinate Nitrosyls

A summary of selected structural properties of the six-coordinate iron(II)-nitrosyl derivatives is given in Table 2. Also given in the table is the value of the N–O stretching frequency (when available). It is important to note that this value is quoted for the same temperature as that used for the structure determination.

The first six-coordinate derivative to be structurally characterized was $[\text{Fe}(\text{TPP})(\text{MI})(\text{NO})]$ [65], which is a low-spin complex. The diatomic NO group is coordinated end-on with a “half-bent” FeNO group that was disordered over at least two distinct positions. The Fe–N–O angle found was $142.1(1)^\circ$, a value that is slightly smaller than that found for the five-coordinate species $[\text{Fe}(\text{TPP})(\text{NO})]$. Subsequent determinations of this angle suggested that the value found was somewhat larger than the true value (as shown when it can be determined in a non-disordered structure). The equatorial Fe–N_p bond distances were those expected for low-spin iron(II) derivatives and will be commented on further only in special circumstances. The most striking feature of the structure, however, was the axial Fe–N(Im) distance *trans* to the NO. The value found, 2.180 Å, was about 0.2 Å longer than that expected for the axial distance in low-spin iron(II) complexes. This bond distance elongation reflects the strong *trans* effect seen for six-coordinate nitrosyl derivatives.

The *trans* directing effect of the coordinated NO group was further explored by the structure determination of $[\text{Fe}(\text{TPP})(4\text{-MePip})(\text{NO})]$ [66]. The increased steric hindrance of the saturated six-membered ring of 4-methylpiperidine with an N–H substituent at the coordinating nitrogen atom was expected to lead to an even longer *trans* Fe–N bond distance. This was indeed observed along with an even more surprising result. The two crystalline modifications of $[\text{Fe}(\text{TPP})(4\text{-MePip})(\text{NO})]$ that were obtained had *trans* bond distances in the crystalline forms which were distinctly different at 2.328(10) and 2.463(7) Å. The $\nu(\text{N–O})$ values were also quite different at 1,640 and 1,653 cm^{-1} . The variation in the N–O stretching frequency shows sensitivity to small variations in the electron density at the iron. Indeed, a plot of $\nu(\text{N–O})$ versus the *trans* Fe–NO distance shows a linear relationship between the two variables [66]. Although such dramatic shifts in *trans* distance

Table 2 Structural and vibrational data for several 6C ferrous heme–nitrosyls

Complex	T (K)	Ordered ^a	Fe–NO ^b	N–O ^b	Fe–N–O ^c	N(<i>r</i> trans) ^{b,d}	$\nu(\text{N–O})^e$	References
[Fe(TPP)(MD)(NO)]	293	No (2)	1.743(4)	1.121(8)	142.1(6)	2.180(4)	1,625 ^f	[65]
[Fe(TPP)(MD)(NO)] ⁱ	100	No (2)	1.749(1)	1.184(2)	137.2(1)	2.170(1)	–	[46]
[Fe(TPP)(MD)(NO)] ⁱ	293	No (3)	1.745(2)	1.163(10)	137.6(8)	2.186(2)	–	[46]
[Fe(TPP)(MD)(NO)] ⁱ	100	No (2)	1.750(2)	1.182(3)	137.7(2)	2.173(2)	1,628 ^f	[67]
[Fe(TPP)(4-NH ₂ Py)(NO)]	100	Yes	1.758(1)	1.170(1)	139.8(1)	2.278(1)	1,653 ^g	[67]
[Fe(TPP)(4-MePip)(NO)] ⁱ	100	Yes	1.752(2)	1.171(2)	138.0(2)	2.285(2)	1,642 ^g	[67]
[Fe(TPP)(4-MePip)(NO)]	293	Yes	1.721(10)	1.141(13)	138.5(1)	2.328(10)	1,640 ^f	[66]
[Fe(TPP)(4-MePip)(NO)]	293	Yes	1.740(7)	1.112(9)	143.7(6)	2.463(7)	1,653 ^g	[66]
[Fe(To-F ₂ PP)(MI)(NO)]	293	No (2)	1.752(2)	1.202(2)	138.0(2)	2.188(2)	1,636 ^h	[69]
[Fe(TpivPP)(Py)(NO)]	100	No (2,4,?)	1.742(5)	1.1941(9)	133.4(5)	2.260(5)	1,635 ^h	[67]
<i>tri</i> -[Fe(Tp-FPP)(MD)(NO)]	100	Yes	1.752(1)	1.182(1)	138.6(1)	2.169(1)	1,636 ^f	[45]
<i>tri</i> -[Fe(Tp-FPP)(MD)(NO)] ⁱ	100	Yes	1.759(1)	1.184(2)	138.1(1)	2.167(1)	1,636 ^f	[45]
<i>tri</i> -[Fe(Tp-FPP)(MD)(NO)]	150	Yes	1.748(1)	1.181(2)	138.9(1)	2.172(1)	1,637 ^f	[45]
<i>tri</i> -[Fe(Tp-FPP)(MD)(NO)]	175	Yes	1.743(2)	1.182(3)	138.9(1)	2.172(2)	1,637 ^f	[45]
<i>tri</i> -[Fe(Tp-FPP)(MD)(NO)]	200	No (2)	1.748	1.179(2)	139.0(1)	2.177(3)	1,638 ^f	[45]
<i>tri</i> -[Fe(Tp-FPP)(MD)(NO)]	224	No (2)	1.747(1)	1.180(2)	139.0(1)	2.181(1)	1,638 ^f	[45]
<i>tri</i> -[Fe(Tp-FPP)(MD)(NO)] ⁱ	224	No (2)	1.758(1)	1.182(2)	138.1(2)	2.188(1)	1,638 ^f	[45]
<i>tri</i> -[Fe(Tp-FPP)(MD)(NO)]	293	No (2)	1.743(1)	1.188(2)	138.8(2)	2.191(1)	1,640 ^f	[45]
<i>tri</i> -[Fe(Tp-FPP)(MD)(NO)] ⁱ	293	No (2)	1.752(1)	1.184(2)	138.3(2)	2.188(2)	1,640 ^f	[45]
<i>tri</i> -[Fe(Tp-FPP)(MD)(NO)]	350	No (2)	1.724(3)	1.194(6)	139.1(3)	2.193(3)	1,641 ^f	[45]
<i>mono</i> -[Fe(Tp-FPP)(MI)(NO)]	100	Yes	1.748(1)	1.181(1)	137.3(1)	2.131(1)	1,624 ^f	[45]
<i>mono</i> -[Fe(Tp-FPP)(MI)(NO)]	125	Yes	1.748(3)	1.215(3)	135.7(3)	2.128(3)	1,625 ^f	[45]
<i>mono</i> -[Fe(Tp-FPP)(MI)(NO)]	150	No (2)	1.756(2)	1.201(2)	136.5(1)	2.132(1)	1,626 ^f	[45]
<i>mono</i> -[Fe(Tp-FPP)(MI)(NO)]	293	No (2)	1.753(3)	1.200(4)	138.2(3)	2.158(2)	1,630 ^f	[45]
[Fe(TpivPP)(NO ₂)(NO)] ^{-j}	124	Yes	1.792(8)	1.176(8)	137.4(6)	2.086(8)	1,616 ^f	[68]
[Fe(TpivPP)(NO ₂)(NO)] ^{-j}	124	No (2)	1.774(8)	1.156(10)	139.4(7)	2.080(8)	1,616 ^f	[68]
[Fe(TpivPP)(NO ₂)(NO)] ^{-k}	127	No (2)	1.840(6)	1.134(8)	137.4(6)	2.060(7)	1,668 ^g	[68]

(continued)

Table 2 (continued)

Complex	T (K)	Ordered ^a	Fe–NO ^b	N–O ^b	Fe–N–O ^c	N(<i>trans</i>) ^{b,d}	$\nu(\text{N–O})^e$	References
[Fe(Tp–OCH ₃ PP)(MI)(NO)]	100	Yes	1.749(1)	1.186(1)	136.1(1)	2.166(8)	1,616 ^f	[45]
[Fe(Tp–OCH ₃ PP)–(MI)(NO)] ^g	100	Yes	1.753(1)	1.190(1)	135.9(1)	2.170(1)	1,616 ^f	[45]
[Fe(Tp–OCH ₃ PP)(MI)(NO)]	293	No (2)	1.746(1)	1.200(2)	135.8(1)	2.199(1)	1,620 ^f	[45]
[Fe(Tp–OCH ₃ PP)(MI)(NO)]	330	No (2)	1.744(1)	1.210(2)	135.9(1)	2.203(1)	1,620 ^f	[45]
[Fe(Tp–NO ₂ PP)(MI)(NO)]	100	No (3)	1.755(2)	1.232(3)	133.2(2)	2.164(3)	–	[46]
[Fe(Tp–CF ₃ PP)(MI)(NO)]	100	No (2)	1.753(2)	1.192(2)	138.1(2)	2.146(2)	–	[46]
[Fe(Tp–CF ₃ PP)(MI)(NO)]	290	No (2)	1.750(2)	1.254(3)	133.7(2)	2.169(2)	–	[46]
[Fe(OEPO)(Py)(NO)]	90	Yes	1.744(2)	1.190(3)	138.3(2)	2.310(2)	1,645	[70]

^aThe number in parentheses is the number of crystallographically defined NO positions

^b ν value in Å

^cValue in degrees

^dDistance *trans* to NO

^eValue in cm⁻¹

^fKBr

^gNujol

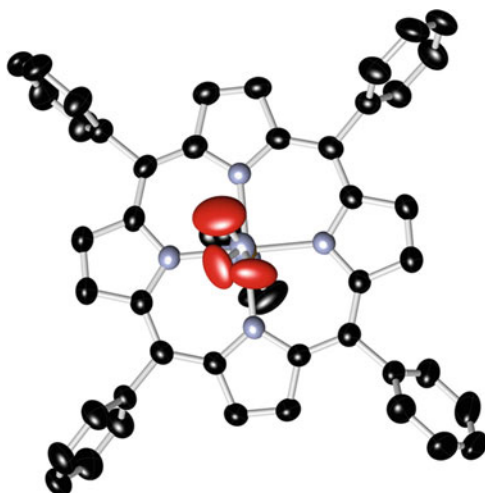
^hIn solution

ⁱDuplicate measurement of different crystal

^jPerpendicular form

^kParallel form

Fig. 5 Thermal ellipsoid plot showing the structure of [Fe(TPP)(MI)(NO)] at 293 K with the most extensive diffraction data available. Note the three locations of the NO oxygen atom



have not been seen subsequently, it is to be noted that in temperature-dependent structure determinations, both the N–O stretching frequency and the *trans* bond distance show the same behavior of increased distance and increased frequency. It should be recognized that such correlations require a constant equatorial porphyrin ligand; each porphyrin ligand system displays a unique relationship between the two variables (see Table 2).

Among the entries in Table 2, a large number are duplicates of some sort. The first duplicates are those related to the original [Fe(TPP)(MI)(NO)] structure, which has been subsequently restudied at both 293 and 100 K [46, 67]. All of the redeterminations have made good use of new data collection instrumentation and probably enhanced computing capabilities as well. The 100 K results still show a disordered FeNO group with two distinct orientations that are closely similar in all examples. The enhancement of data/parameter ratios available for all, but especially that of the 293 K data set, led to the unexpected finding that there are three distinct FeNO orientations in the crystal at room temperature as shown in Fig. 5. In the earlier 293 K analysis, the two closest orientations were merged into an average orientation with a much larger apparent thermal motion for the terminal oxygen atom of the NO (this shows how much can be hidden in the larger thermal motion parameters obtained at higher temperatures).

As has already been noted, two or more FeNO orientations of the group are a common feature of their solid-state structures. This phenomenon suggests that the barrier to rotation around the Fe–NO bond is of low energy. This has been thoroughly studied with a series of temperature-dependent structure determinations, with some studies involving two distinct crystalline samples. Four different samples have been studied at varying temperatures [45, 46]. In all cases, there is less or no FeNO group disorder at the lower temperatures. The two crystalline polymorphs of [Fe(*Tp*-FPP)(MI)(NO)] both display completely ordered FeNO groups at 100 K, and increasing amounts of disorder as the temperature is raised. Details of the study

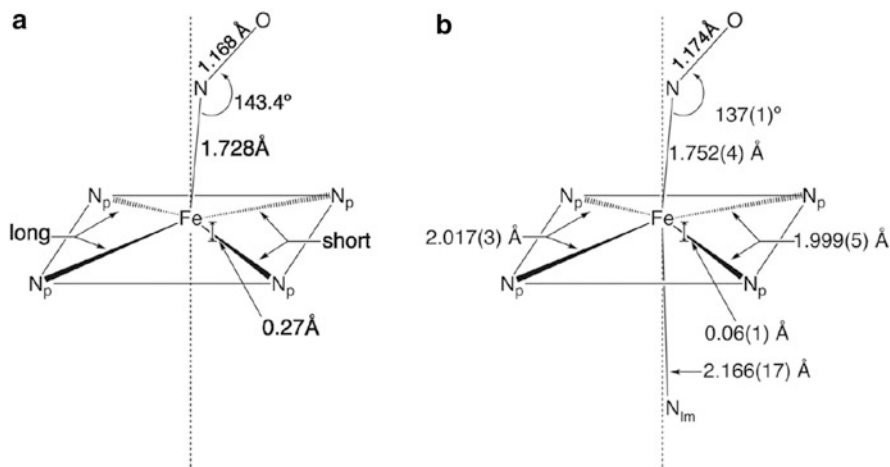


Fig. 6 Diagram illustrating and comparing the “best” structural values for 5C [Fe(por)(NO)] and 6C [Fe(por)(MI)(NO)] derivatives

of the triclinic form of [Fe(*Tp*-FPP)(MI)(NO)] are especially informative. Two different crystals, when measured at the same temperature, effectively show the same amount of disorder, which increases to a 74:26 split as the temperature increases to 350 K. Although the temperature at which disorder begins to appear varies substantially with the particular complex, for *tri*-[Fe(*Tp*-FPP)(MI)(NO)] the disorder onset begins at about 200 K. Importantly, the experiments have also clearly demonstrated that the effect of order/disorder was completely reversible as experiments were performed with both increasing and decreasing temperatures.

An analysis of changes in the observed crystal packing, including calculations of the potential energy for six different [Fe(Porph)(MI)(NO)] complexes, as the temperature is increased, shows that the packing distances close to the NO increase sufficiently to allow for local minima and alternative orientations of the FeNO group. Further details of this analysis are available in the original publication [46].

An examination of Table 2 shows that with one exception, all six-coordinate porphyrin derivatives are those with *meso*-substituted tetraarylporphyrin ligands. Most have 1-methylimidazole as the axial ligand *trans* to NO. The relatively large number of equivalent six-coordinate complexes with an axial 1-methylimidazole permits the construction of a diagram illustrating the expected features of the six-coordinate derivatives, and which are compared to the corresponding features for five-coordinate species in Fig. 6. The asymmetry in the coordination group, first clearly shown for five-coordinate complexes, is also seen in the six-coordinate species. As schematically depicted in the diagram, the Fe–NO vector is tilted off the heme normal, although with somewhat less of a tilt than that observed for the five-coordinate species. The *trans* Fe–N(Im) bond is also tilted off axis, in the same general direction as the Fe–NO tilt. The *trans* bond distance is always large, the value given in the figure is the average with the value in parentheses being the standard deviation calculated on the assumption that all values are drawn from the same population. This assumption is

much more likely for the other values entered in the figure; the observed range for the Fe–N(Im) distance is 2.128–2.203 Å. The asymmetry in the equatorial Fe–N_p bond distances, first noted for five-coordinate species, is also observed in the six-coordinate cases, with values indicated in the diagram. Finally we note that the axial Fe–NO distances are clearly longer in the six-coordinate species, but the Fe–N–O angle is definitely smaller. All of the structural changes between the two coordination numbers are consistent with a differing distribution of the unpaired electron over the FeNO unit.

Calculations for the model complex [Fe(Porph)(MI)(NO)] show that there is an orientational preference for the relative orientation of the imidazole and the FeNO planes [46]. The preference is for both to be coplanar rather than to have a relative perpendicular orientation. Interestingly, these results also show that the equatorial asymmetry follows the rotation of the FeNO group in the calculations.

Except for a pair of unusual derivatives, the anions [Fe(TpivPP)(NO₂)(NO)][−] [68], the issue of preferred relative orientations of the axial ligands has not been explored experimentally. In the [Fe(TpivPP)(NO₂)(NO)][−] species, which has two crystallographically distinct forms where the FeNO and NO₂[−] planes are either coplanar or perpendicular, experimental spectroscopic data show differences for the electronic structure. This includes distinctly different Mössbauer spectra for the two forms as well as differing IR spectra of both the NO and NO₂[−] groups. The 52 cm^{−1} difference in the N–O stretches clearly demonstrates significant differences in the electron distribution [68].

2.2 Ferric Heme–Nitrosyls

The ferric nitrosyl derivatives are all formally formed from the paramagnetic d⁵ iron center and a paramagnetic NO ligand. Although precise details of coupling may be controversial, all known species are coupled to yield diamagnetic complexes and hence are low-spin. As in the iron(II) systems, the basic structural features are comparable to those of corresponding low-spin complexes [56].

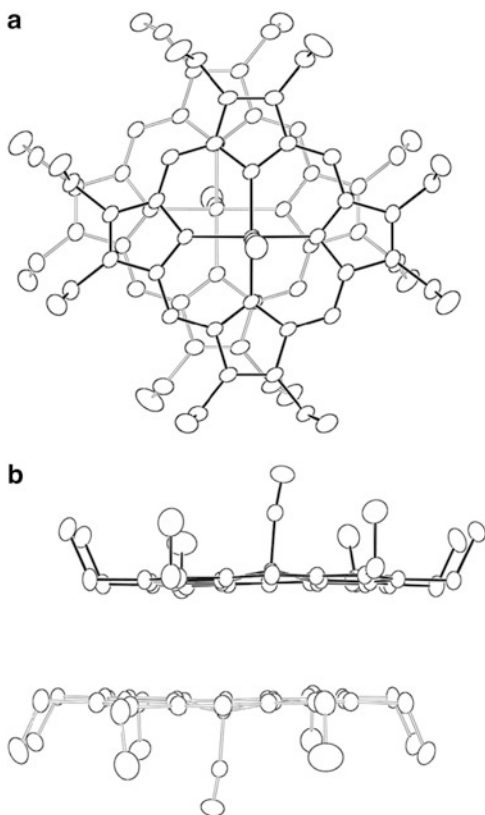
Although NO forms a number of iron(III) derivatives, their formation generally requires starting from an iron(III) porphyrinate with an easily displaced anion or an effectively open coordination site. The first derivatives isolated and crystallographically characterized used the easily displaced perchlorate anion in five-coordinate [Fe(Porph)(ClO₃)] to prepare the new iron(III) derivatives. Two derivatives were prepared [71], both are cationic species. The first was five-coordinate [Fe(OEP)(NO)]⁺, which forms a π–π dimer in the solid state with a mean plane separation of about 3.3 Å (see discussion below). The second derivative, [Fe(TPP)(H₂O)(NO)]⁺, has a water molecule coordinated *trans* to the NO with an Fe–O distance of 2.001(5) Å, clearly there is not an NO *trans* effect. This is of course consistent with an unpopulated *d*_{z²} orbital. This complex also points out a significant chemical feature of this class, there is a strong driving force to add a ligand *trans* to NO; the water concentration in the synthesis of [Fe(TPP)(H₂O)(NO)]⁺ was quite small. These two structures and the other known iron(III) derivatives are summarized in Table 3.

Table 3 Structural and vibrational data for several 6C ferric heme-nitrosyls

Complex	<i>T</i> (K)	Fe-NO ^a	N-O ^a	Fe-N-O ^b	Fe-L ^{a,c}	$\nu(\text{N-O})^d$	References
[Fe(OEP)(NO)] ⁺ · CHCl ₃	292	1.644(3)	1.112(4)	176.9(3)	–	1,868 ^e	[71]
[Fe(TPP)(H ₂ O)(NO)] ⁺	96	1.652(5)	1.150	174.4(10)	2.001(5)	1,937 ^e	[71]
[Fe(OEP)(NO)] ⁺	130	1.653(1)	1.140(2)	173.2(1)	–	1,838 ^{c,f}	[72]
[Fe(TPP)(HO- <i>i</i> -C ₅ H ₁₁)(NO)] ⁺	153	1.776(5)	0.925(6)	177.1(7)	2.063(3)	1,935 ^e	[79]
[Fe(OEP)(MI)(NO)] ⁺	130	1.646(2)	1.135(2)	177.3(2)	1.989(2)	1,921 ^f	[78]
[Fe(OEP)(Pz)(NO)] ⁺	130	1.627(2)	1.141(3)	176.9(3)	1.988(2)	1,894 ^f	[78]
[Fe(OEP)(Iz)(NO)] ⁺	130	1.632(3)	1.136(4)	177.6(3)	2.010(3)	1,914 ^f	[78]
[(Fe(OEP)(NO)) ₂ (Prz)] ²⁺	130	1.632(3)	1.131(4)	176.5(3)	2.039(2)	1,899 ^f	[78]
[Fe(OETPP)(MI)(NO)] ⁺	130	1.650(2)	1.130(3)	177.0(3)	1.983(2)	1,871 ^f	[77]
[Fe(OEP)(2-MI)(NO)] ⁺ (A)	130	1.649(2)	1.132(3)	175.6(2)	2.053(2)	1,917 ^f	[77]
[Fe(OEP)(2-MI)(NO)] ⁺ (B)	130	1.648(2)	1.139(2)	177.4(2)	2.032(2)	1,917 ^f	[77]
[Fe(TPP)(H ₂ O)(NO)] ⁺	100	1.63	1.15	173.0(3)	1.961(3)	1,897 ^g	[80]
[Fe(OEP)(<i>p</i> -C ₆ H ₄ F)(NO)]	130	1.728(2)	1.153(3)	157.4(2)	2.040(3)	1,791 ^f	[75]
[Fe(OEP)(SR-H ₂)(NO)]	100	1.671(9)	1.187(9)	159.6(8)	2.356(3)	1,839 ^f	[74]
[Fe(TPP)(O ₂ CCF ₃)(NO)]	100	1.618(8)	1.151(8)	175.8(6)	1.899(6)	1,907 ^g	[81]
[Fe(TpivPP)(NO ₂)(NO)]	130	1.671(2)	1.144(3)	169.3(2)	1.998(2)	1,893 ^g	[76]
[Fe(TpivPP)(NO ₂)(NO)]	130	1.688(2)	1.132(3)	180	2.002(2)	1,893 ^g	[76]

^aValue in Å^bValue in degrees^cLigand *trans* to NO^dValue in cm⁻¹^eKBr pellet^fNujol mull^gIn solution

Fig. 7 Thermal ellipsoid plots illustrating the intermolecular interactions in $[\text{Fe}(\text{OEP})(\text{NO})]^+$. Both top and side views are given (reprinted with permission from [72]. Copyright 2000 American Chemical Society)



A subsequent preparation and structural determination of crystalline $[\text{Fe}(\text{OEP})(\text{NO})]\text{ClO}_4$ from a different solvent led to some notable results [72]. As can be seen in Table 3, the structural parameters of interest for the two forms are almost identical. Moreover, both the original and the new crystalline forms are found as π - π dimers with inversion symmetry between pairs of porphyrin rings and with very similar interplanar separations. This intermolecular interaction is illustrated for the unsolvated form of $[\text{Fe}(\text{OEP})(\text{NO})]^+$ in Fig. 7. Given the close similarity of the molecular structures of the two crystalline forms, it was unexpected that the NO stretching frequencies should be found to differ by about 30 cm^{-1} . Differences in electronic structure, as monitored by Mössbauer spectroscopy, are nil, as shown by the data summarized for the two in Fig. 8. The figure also illustrates the position of the perchlorate anion with respect to the porphyrin complex. The spectroscopic issues, particularly the relationship between $\nu(\text{N}-\text{O})$ and $\nu(\text{Fe}-\text{NO})$, were further studied [73]. An interesting conclusion presented there was that the topmost molecular orbitals are very different than those of the analogous CO complexes. The π -backbonding model, attractive though it is, might not apply in the same way as that for the CO species.

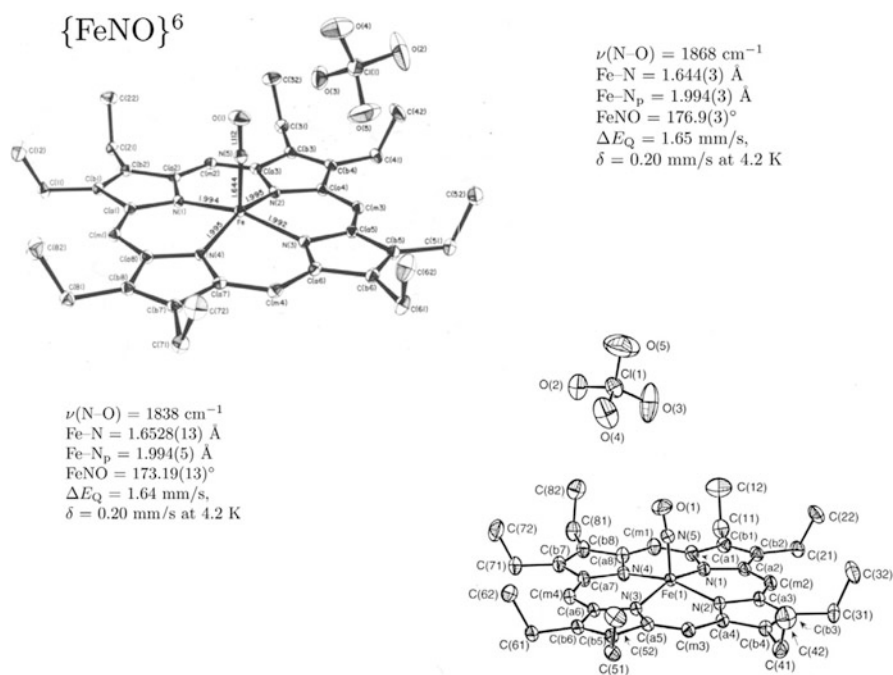


Fig. 8 ORTEP diagrams illustrating the relative position of the perchlorate anion, and physical properties of the two crystalline forms of $[\text{Fe}(\text{OEP})(\text{NO})]^+$

All other $\{\text{FeNO}\}^6$ species are six-coordinate. Despite the fairly large number of complexes given in Table 3, which would suggest that the preparation and isolation of iron(III) nitrosyls would be relatively straightforward, their preparation can be challenging. A particular difficulty is reductive nitrosylation in which NO acts both as a ligand and as a reducing agent to form the very stable $\{\text{FeNO}\}^7$ species [33]. These difficulties have been circumvented by careful attention to detail or by the use of specialized solid-state syntheses [74]. Thus, complexes with a number of ligands *trans* to NO have been prepared including neutral nitrogen donors, water, and anionic ligands including thiolate, carboxylate, and nitrite.

The geometry of the FeNO group is expected to be linear; however, the only known complexes that have Fe–N–O angles of exactly 180° are found in systems with both crystallographic disorder and required crystallographic symmetry (only one such species is included in Table 3). It can be seen from Table 3 that the Fe–N–O angles do vary over a substantial range – from near linearity ($\sim 177^\circ$) to those that are substantially nonlinear ($\sim 160^\circ$; see Sect. 3.2.2). The deviation from linearity does depend on the nature of the *trans* ligand. These geometrical features are correlated with the value of $\nu(\text{N-O})$ as discussed in Sect. 4.2.2. Table 3 shows that the complexes with a neutral nitrogen donor have N–O stretching frequencies over a relatively narrow range and the Fe–N–O bond angle is near linear. The first significant outlier was the complex $[\text{Fe}(\text{OEP})(p\text{-C}_6\text{H}_4\text{F})(\text{NO})]$ [75] with an organometallic *trans* ligand. This complex has a significantly different $\nu(\text{N-O})$, that at

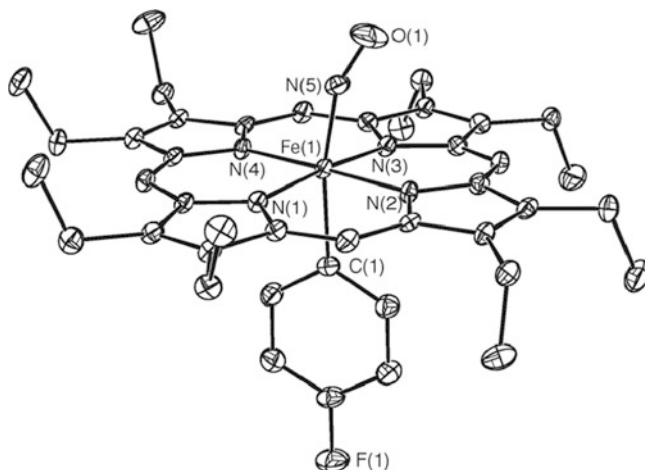


Fig. 9 ORTEP diagram of [Fe(OEP)(*p*-C₆H₄F)(NO)] illustrating the off-axis tilt of both axial ligands toward each other (reprinted with permission from [75]. Copyright 2001 American Chemical Society)

1,791 cm⁻¹ is at a substantially lower frequency than other derivatives. Equally notable is the substantially bent Fe–N–O bond (value of angle = 157.4(2)°) and the Fe–NO bond distance, which is substantially longer than other derivatives. This behavior was subsequently found to be largely mirrored by a thiolate complex that required a solid-state synthetic procedure [74]. A final unusual feature is the simultaneous tilt of both axial ligands. The tilts are toward each other to form a sort of “bowed” species with an C–Fe–N bond angle of 168.8(1)°. This is illustrated in the ORTEP diagram (Fig. 9). This frequency lowering, Fe–N–O bending, and Fe–NO lengthening are correlated with the character of the σ -donor *trans* to the NO, with larger effects with the strongest σ -donors. We believe that this σ -bonding effect is also manifested in the FeNO bend found in [Fe(TpivPP)(NO₂)(NO)] [76]. The issue is addressed in Sect. 4.2.2.

A final issue: there had been a suggestion that the porphyrin core conformation could play a role in the geometry of the FeNO group. An investigation into this possible effect was able to isolate derivatives with substantially nonplanar core conformations, but the effects of the core conformation, if any, are quite small [77]. The FeNO geometries of these derivatives, either with a sterically demanding axial ligand or a sterically congested porphyrin core, are quite similar to those of the other derivatives with a neutral nitrogen donor *trans* to NO [78].

2.3 Related Nitrosyls (Mn and Co)

The metalloporphyrinate derivatives on either side of iron in the periodic table also form MNO complexes but only in a single oxidation state. The total number of known structures is relatively limited and only a few will be cited here. The cobalt derivatives

are $\{\text{CoNO}\}^8$ species and all are five-coordinate in the solid state. The strongly developed five-coordinate nature is apparently the result of a strong *trans* directing effect consistent with addition of another electron to the MNO unit relative to iron. The first derivative characterized was the $[\text{Co}(\text{TPP})(\text{NO})]$ complex, which exhibited the same disorder as the iron analogue [82]. Subsequently, crystalline $[\text{Co}(\text{OEP})(\text{NO})]$ was obtained and ordered structures were found. There is a smaller off-axis tilt than in the iron derivatives, but the equatorial asymmetry is still observed. The Co–N–O bond angle is fully bent with a value of $122.70(8)^\circ$. The Co–NO bond length is $1.8444(9)$ Å, fully 0.1 Å longer than in the iron derivatives [83, 84]. These values appear typical for cobalt derivatives. More recently, $[\text{Co}(\text{TPP})(\text{NO})]$ has been reinvestigated. It, just like the iron species, undergoes a phase change with ordering of the axial ligand at lower temperatures [85]. The phase transition is much sharper in the cobalt system than in the iron systems and the study trapped an intermediate structure (CoNO rotamers) during the phase change transition [85].

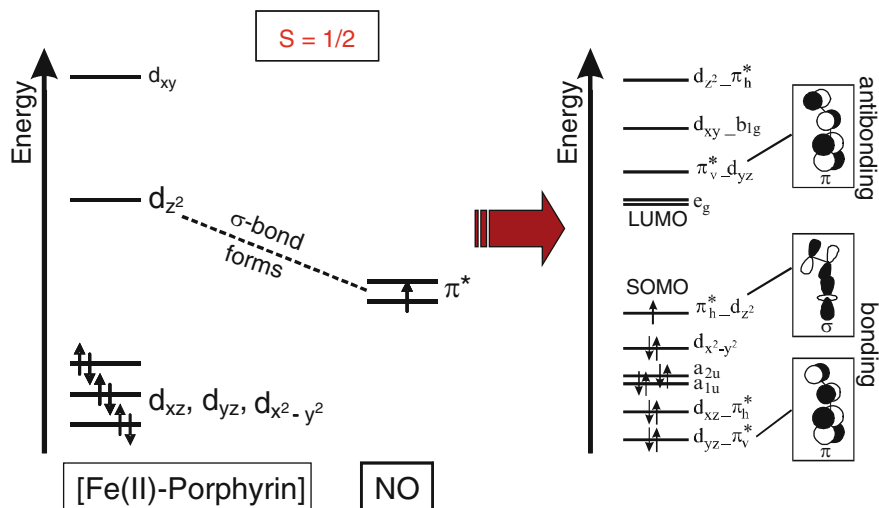
The manganese derivatives are $\{\text{MnNO}\}^6$ species and are expected to be closely similar in structure to the ferric derivatives with linear Mn–N–O groups. A single five-coordinate species [86] and a limited number of six-coordinate species have been structurally characterized [86, 87]. All have Mn–NO distances of about 1.645 Å and are otherwise not especially notable. Thus, both the cobalt and manganese species underline the unique properties of the ferrous NO derivatives.

3 Spectroscopic Properties of Heme–Nitrosyls

In the following, a comprehensive summary of the spectroscopic and thermodynamic properties of ferrous and ferric heme–nitrosyls is provided, and recent results are highlighted. In the case of ferrous heme–nitrosyls, both five- and six-coordinate (5C and 6C) species exist under physiological conditions, and their properties are compared side by side. In the case of ferric heme–nitrosyls, 6C species are usually formed, but interesting differences are observed between corresponding imidazole- and thiolate-coordinated systems, and their spectroscopic properties are compared. These results form the basis for understanding the electronic structures and the nature of the bonding in these metal–NO systems.

3.1 Ferrous Heme–Nitrosyls

Ferrous heme–nitrosyls generally contain low-spin ferrous hemes ($S = 0$) with a bound NO ligand ($S = 1/2$) as shown in Scheme 1, left, so the total spin of these complexes in the ground state is $S = 1/2$. Since these compounds are therefore paramagnetic, they are amenable to paramagnetic spectroscopic methods. In particular, (pulsed) EPR methods have been used to characterize these species. In addition, vibrational spectroscopy has been a key technique for exploring the properties of these compounds.



Scheme 1 Electronic structure of ferrous heme–nitrosyls. The Fe–NO σ -interaction is indicated. In addition, a π -backbond is formed between d_{yz} and the empty π^* orbital of NO (in the coordinate system applied here where the z axis is aligned with the heme normal, and x and y point toward the meso carbons in the heme plane) (reprinted with permission from [42]. Copyright 2010 American Chemical Society)

3.1.1 Electron Paramagnetic Resonance

For recent reviews of the EPR-spectroscopic properties of heme–nitrosyls, see [3, 42, 88, 89]. Five-coordinate (5C) ferrous heme–nitrosyls in model systems and proteins show characteristic, rhombic EPR spectra with g values of about 2.1, 2.04–2.06, and 2.01 for g_{\max} , g_{mid} , and g_{\min} , respectively (see [89] and references therein). The principal axis of g_{\min} is closely aligned with the Fe–NO bond [90, 91]. This g -value shows a very characteristic, three-line ^{14}N hyperfine splitting with coupling constants of $^{\text{NO}}A = 45\text{--}50$ MHz that result from coupling of the unpaired electron in the complex with the nuclear spin of the nitrogen atom of NO (the ^{14}N nucleus has a nuclear spin $I = 1$). Importantly, the ^{14}N hyperfine tensor is actually quite isotropic, but for g_{\max} and g_{mid} the hyperfine splittings are washed out and in almost all cases not well resolved in the spectra. One exception is the model complex [Fe(*To*-F₂PP)(NO)] (*To*-F₂PP²⁻ = tetra(*ortho*-difluorophenyl)porphyrin dianion) as shown in Fig. 10, left [64]. In this rare case, the ^{14}N hyperfine couplings of all three g values are in fact well resolved in the frozen solution EPR data. As evident from these data and the literature, the ^{14}N hyperfine coupling constants for all three g values are quite similar and typically fall in the range of $^{\text{NO}}A = 40\text{--}50$ MHz (see [89] and references therein).

In six-coordinate (6C) complexes with axial N-donor ligands bound *trans* to NO (especially imidazole derivatives in model complexes and His in proteins) a number of characteristic changes are observed in the EPR spectra. First, the g -values decrease to about 2.08, 2.00, and 1.97 for g_{\max} , g_{mid} , and g_{\min} , respectively (see [89] and references therein), which, together with MCD results, provides

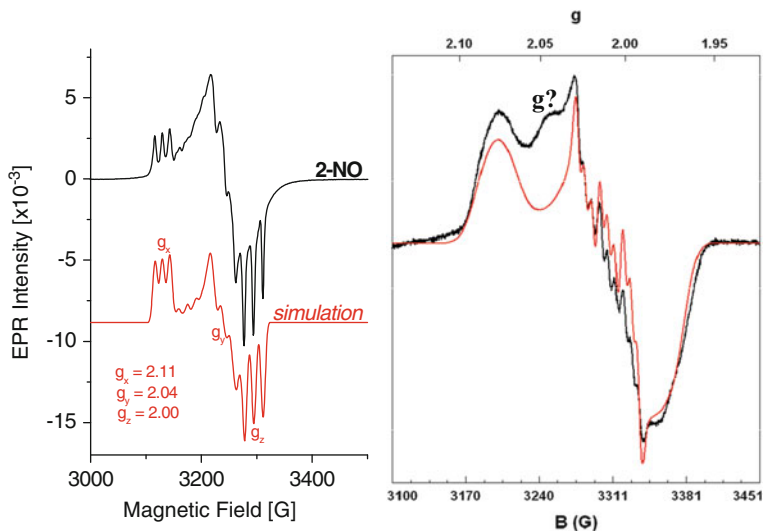


Fig. 10 *Left*: EPR spectrum of the 5C model complex $[\text{Fe}(\text{To-F}_2\text{PP})(\text{NO})]$ (black) and simulation of the data (red). ^{14}N hyperfine coupling constants for g_{max} , g_{mid} , and g_{min} are: 39, 46, and 47 MHz, respectively [64]. *Right*: EPR spectrum of the 6C model system $[\text{Fe}(\text{To-F}_2\text{PP-BzIM})(\text{NO})]$ in frozen DMSO at 77 K (black). Red: fit of the spectrum using the parameters: $g_{\text{max}} = 2.077$, $g_{\text{mid}} = 2.009$, $g_{\text{min}} = 1.978$; ^{14}N hyperfine: $^{\text{NO}}A = 37, 62, 39$ MHz, for $g_{\text{max}}, g_{\text{mid}}, g_{\text{min}}$, respectively. $^{\text{IM}}A = 19$ MHz for g_{mid} (reprinted with permission from [93]. Copyright 2009 American Chemical Society)

evidence for a shift in spin density from iron toward NO in the 6C compared to the 5C complexes [91, 92]. The g value that shows the well-resolved hyperfine splittings is g_{mid} in the 6C case. The spectral signal for this g value is split into nine lines, due to strong hyperfine couplings to the nuclear spin of the nitrogen atom of NO (with $^{\text{NO}}A = 60\text{--}65$ MHz) and weaker hyperfine couplings to the nitrogen atom of the imidazole ring (with $^{\text{IM}}A \approx 20$ MHz) bound *trans* to NO as shown in Fig. 10, right [93]. The hyperfine couplings for the other g -values, g_{max} and g_{min} , are again not well resolved in the frozen solution spectra, but have been determined from single crystal EPR to be around 30–45 and 25–35 MHz, respectively [94]. Hence, the ^{14}N hyperfine tensor of NO becomes more anisotropic in the 6C compared to the 5C case. The fact that one g value (g_{min} in 5C and g_{mid} in 6C complexes) shows very small g strain and correspondingly, very sharp hyperfine lines has been taken as evidence that the principal axis of this g value is oriented along the Fe–NO bond [42]. Hence, even if several different rotational isomers (where the NO ligand rotates around the Fe–NO bond; see Sect. 2.1.2) are present in a frozen solution sample, the g strain would be small for this g value. In contrast, the remaining two g values with principal axes within the porphyrin plane would be more strongly affected by this disorder, washing out their hyperfine lines [42]. Computational evidence supports this idea, showing that the calculated principal axis of g_{mid} is indeed closest to the Fe–NO vector in the 6C case, although their directions are not collinear: in the DFT calculations, both g_{min} and g_{mid} are located

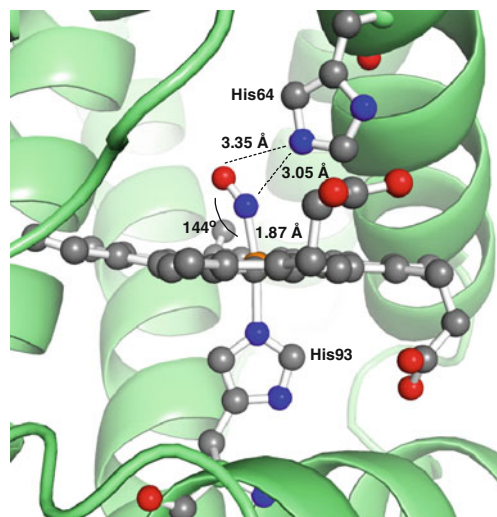


Fig. 11 Crystal structure of the Fe(II)–NO complex in horse heart Mb as obtained by the reaction of met-Mb with nitrite/dithionite. The image was generated using PyMOL from PDB code 2FRJ [100]

in the Fe–NO plane, but the Fe–NO vector and the principal axis of g_{mid} deviate by about 30° [69, 91, 92, 95]. Recently, overall similar g tensor orientations were calculated for the 6C nitrosyl adducts of Mb and of *Pseudomonas aeruginosa* cd_1 nitrite reductase, using QM/MM approaches in both cases that include the complete protein [48, 96]. However, in these calculations the observed deviation between the Fe–NO vector and the principal axis of g_{mid} was quite large ($\sim 50^\circ$), and it was pointed out that a better interpretation of the computational result is that the principal axis of g_{min} is actually aligned with the N–O bond in the 6C case. In this point of view, g_{mid} is then close to orthogonal to the N–O vector and located within the Fe–N–O plane [48]. Although the computational predictions are relatively consistent in this sense, it is not clear why this orientation would lead to the particularly small g strain for g_{mid} . Considering the significant approximations that go into the calculation of g tensors for transition metal complexes [97] and in particular, the fact that the DFT-calculated excitation energies, which are implicitly involved in g -tensor calculations, are prone to significant errors, it is possible that this result is not accurate, and that experimentally, the principal axis of g_{mid} is in fact more closely aligned with the Fe–NO bond. These potential problems in the DFT calculations are further documented by the fact that the calculated g shifts (Δg) show substantial deviations from experiment, in particular for g_{max} : for example, in the most recent QM/MM calculations for Mb(II)–NO, the error in Δg_{max} is around 100% [48]. The single-crystal EPR data for Hb(II)–NO adducts particularly support the idea that g_{mid} should be more closely aligned with the Fe–NO bond: here, the principal axes of g_{mid} were found within $8\text{--}10^\circ$ of the heme normal; i.e., close to the Fe–NO vector [94]. The corresponding data for Mb

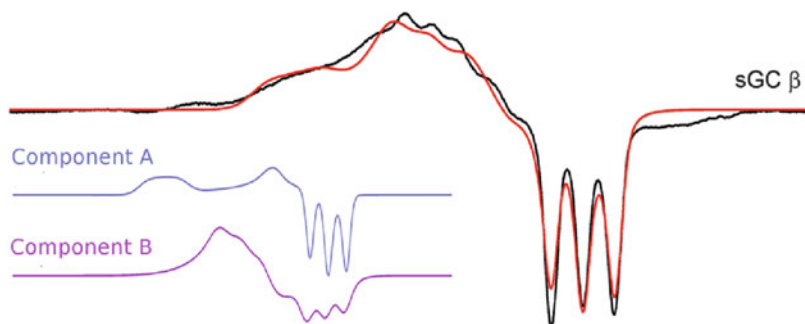


Fig. 12 X-band EPR spectra of the $\beta 1$ heme domain of sGC with bound NO (*black trace*), indicative of formation of a 5C ferrous heme–nitrosyl. The *red trace* corresponds to a simulation of the spectrum using a two-component model. The *insert* shows the two components required to fit these data (and Q- and S-band data simultaneously) individually (reprinted with permission from [49]. Copyright 2012 American Chemical Society)

(II)–NO single crystals show a larger deviation of the g_{mid} principal axis from the heme normal by 20–30° (depending on temperature) [98]. More work is necessary to ultimately determine the exact g tensor orientation in 6C ferrous heme–nitrosyls.

An interesting peculiarity of 6C heme–nitrosyls is the observation of a second, axial minority component in the frozen solution EPR spectra of both proteins and model complexes [89]. This species is also present in the model system [Fe(*To*-F₂PP-BzIM)(NO)] shown in Fig. 10, right, labeled as “*g?*” [93]. In pioneering studies on protoporphyrin IX model complexes and selected protein NO adducts (including Mb(II)–NO), Morse and Chan proposed that this additional species corresponds to another conformer of the complex where the positioning of iron relative to the heme plane and the other ligands is different [99]. Another possible explanation is that both species differ in the relative orientation of the NO and the *trans* N-donor (imidazole) ligand, i.e., the dihedral angle between these ligands could differ, especially since a similar effect is not observed in the 5C case (see also [89]). Recently, ENDOR studies coupled with high-level DFT calculations on Mb–NO were used to further investigate this point [48]. The ENDOR results show hyperfine couplings between the Fe–N–O unit and the ¹⁵N proton of His64 in the major, rhombic EPR species, in agreement with the crystal structure of Mb(II)–NO which also indicates the presence of this hydrogen bond (see Fig. 11) [100]. On the other hand, this hydrogen bond is weaker, and might even be absent, in the minor, axial EPR species. Based on these findings, it is proposed that (a) the major, rhombic EPR species corresponds closely to the Mb–NO crystal structure 2FRJ (Fig. 11), whereas (b) the second, axial conformer is also a six-coordinate complex with an overall similar electronic structure, but with a different N₃(heme)–Fe–NO dihedral angle and/or diminished hydrogen bonding to His64 [48]. Recently, similar differences have also been observed in the EPR spectra of the Fe–NO complexes of low- and high-activity sGC, which can be deconvoluted into a rhombic and an axial component as shown in Fig. 12 [49].

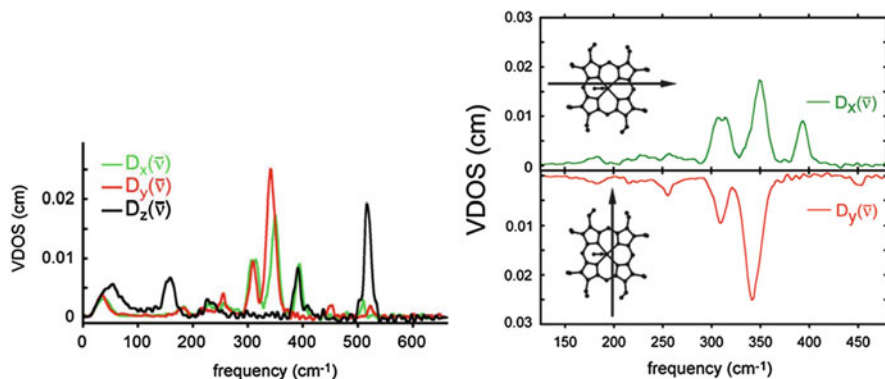


Fig. 13 *Left:* Directional contributions to the VDOS of $[^{57}\text{Fe}(\text{OEP})(\text{NO})]$ for x , y , and z directions. For x , the beam is parallel to the porphyrin plane and to the Fe–N–O plane, for y the beam is parallel to the porphyrin plane and perpendicular to the Fe–N–O plane (see *right*), and for z , the beam is perpendicular to the porphyrin plane. *Right:* comparison of the in-plane polarized data. Adapted from [105]

Hydrogen bonds between ferrous heme-bound NO and active site His and tyrosine (Tyr) residues might be quite common in heme proteins, and have also been detected (via ENDOR) for *P. aeruginosa* cd_1 nitrite reductase [96]. However, computational and vibrational spectroscopic studies indicate that the hydrogen bonds are rather weak and only have a small effect on the properties of the Fe–NO bond. This aspect is further discussed in Sect. 3.1.3.

3.1.2 Vibrational Spectroscopy

For recent reviews on the vibrational properties of heme–nitrosyls see [2, 3, 42, 101]. The vibrational spectra of 5C ferrous heme–nitrosyls show very characteristic vibrational features associated with the Fe–N–O unit (see [3, 42] for current reviews). The N–O stretching mode, $\nu(\text{N–O})$, is observed at $1,670\text{--}1,700\text{ cm}^{-1}$ (most conveniently by IR spectroscopy). The Fe–NO stretch, $\nu(\text{Fe–NO})$, appears at $520\text{--}540\text{ cm}^{-1}$ and is most conveniently observed by NRVS, but is also detected quite straightforwardly with resonance Raman spectroscopy using Soret excitation [102]. The in-plane Fe–N–O bend is most elusive, but has been safely assigned by NRVS to a feature around $370\text{--}390\text{ cm}^{-1}$ [103, 104]. These assignments were initially based on isotope labeling in conjunction with normal coordinate simulations of the obtained data. More recently, oriented single-crystal NRVS data for the model complex $[^{57}\text{Fe}(\text{OEP})(\text{NO})]$ have been reported that further confirm these assignments [105]. Excitingly, these NRVS measurements allow for the determination of the direction of iron motion within the molecular framework. For example, if the single crystal is oriented in a way that the heme is orthogonal to the plane of polarization of the incident electromagnetic radiation, then only those vibrations where the iron moves orthogonal to the heme plane (i.e., where iron moves in the direction of polarization of the incident light) contribute to the spectral intensity [106]. As shown in Fig. 13, the intense feature observed at 517 cm^{-1} for

[Fe(OEP)(NO)] is fully out-of-plane polarized (the z direction in the applied coordinate system), which means that the iron center moves exclusively in the orthogonal direction to the heme. This is in agreement with previous assignments of this feature to the Fe–NO stretch [104]. The feature at 394 cm^{-1} shows equal intensities in z and x direction, where the x axis is located within the Fe–N–O plane (see Fig. 13, right). This band therefore clearly corresponds to the Fe–N–O in-plane bending mode, in agreement with previous work [69, 103]. Note that the NRVS signal for the bending mode is much weaker in the TPP^{2-} derivatives [104]. The in-plane polarized spectra show further differences for the x and y directions as shown in Fig. 13, right [105]. This apparent symmetry lowering is due to the fact that the porphyrin in-plane vibrations of E_u symmetry are now localized relative to the Fe–N–O plane, where the components in x direction (in-plane with respect to the Fe–N–O unit) couple with the Fe–N–O in-plane bend, whereas the components in y direction (out-of-plane with respect to the Fe–N–O unit) couple with the Fe–NO torsion. This effect was analyzed for a corresponding 6C complex in detail in [50] (see below).

In the case of six-coordinate complexes with axial N-donor coordination, interesting spectral changes are observed. The N–O stretching frequency shifts down to $1,610\text{--}1,640\text{ cm}^{-1}$ as easily observed by IR spectroscopy. On the other hand, the assignment of the Fe–NO stretch and Fe–N–O bend has resulted in a long-standing debate in the literature. From resonance Raman spectroscopy, only one low-energy isotope-sensitive band is identified from the spectra, usually around $550\text{--}570\text{ cm}^{-1}$. Chottard and Mansuy initially reported this feature at 549 cm^{-1} for the NO adduct of deoxy-Hb and assigned it to the Fe–NO stretch [107]. This assignment was subsequently supported by other groups [108, 109]. Doubts about this assignment were later voiced by Benko and Yu, who performed detailed isotope-labeling studies on Hb(II)–NO and Mb(II)–NO, and based on these results, assigned the 550 cm^{-1} Raman feature to the Fe–N–O in-plane bend [110], but this assignment was not generally accepted in the literature [111, 112]. More recently, resonance Raman and in particular NRVS investigations finally identified a second vibration associated with the Fe–N–O unit around 440 cm^{-1} in both the 6C model complex [Fe(TPP)(MI)(NO)] (TPP^{2-} = tetraphenylporphyrin dianion; MI = 1-methylimidazole) and related derivatives, and Mb(II)–NO [69, 113, 114]. A careful examination of earlier resonance Raman data on Mb(II)–NO and corresponding mutants from [111] shows that this feature is in fact present in these data as a very weak band. These results cast further doubt on the initial assignment of the $550\text{--}570\text{ cm}^{-1}$ Raman feature to the Fe–NO stretch [115]. This issue was finally resolved recently using again single-crystal NRVS experiments on the model complex [^{57}Fe (TPP)(MI)(NO)] [50].

NRVS data on powder samples of [^{57}Fe (TPP)(MI)(NO)] and the corresponding $^{15}\text{N}^{18}\text{O}$ -labeled complex identified two isotope-sensitive features at 437 and 563 cm^{-1} that shift to 429 and 551 cm^{-1} in the $^{15}\text{N}^{18}\text{O}$ -labeled complex [115]. Very similar vibrational features are observed in the NRVS spectra of Mb(II)–NO; in this case at 443 and 547 cm^{-1} [113]. Major insight into the assignments of these features comes from oriented single-crystal NRVS data on the model complex [^{57}Fe (TPP)(MI)(NO)], as shown in Fig. 14, and detailed normal coordinate analysis (NCA) simulations of these data [50]. Importantly, the NRVS data in Fig. 14 show that the band at about

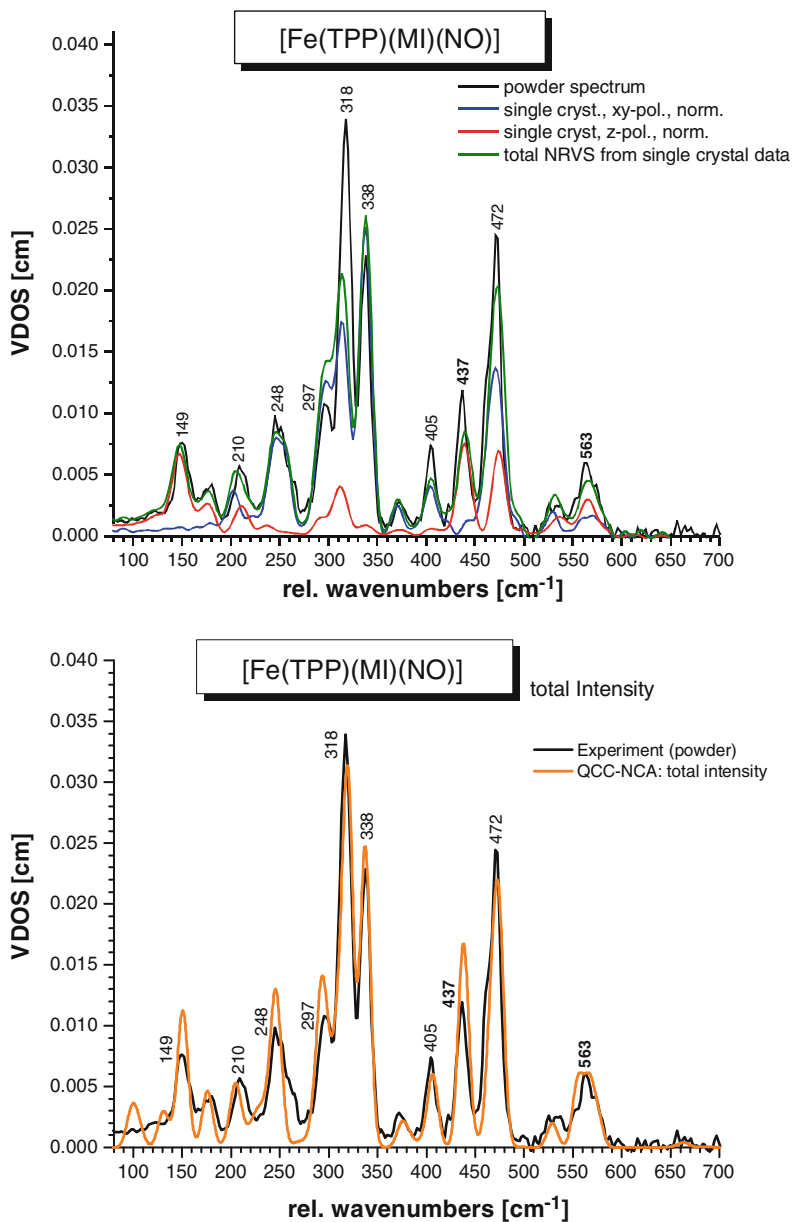


Fig. 14 *Top:* NRVs VDOS spectra of [$^{57}\text{Fe}(\text{TPP})(\text{MI})(\text{NO})$]. *Black:* powder spectrum; *blue and red:* normalized single crystal in-plane (*blue*) and out-of-plane (*red*) polarized spectra; *green:* predicted powder spectrum calculated by adding the in-plane and out-of-plane polarized contributions (total NRVS = $1/3$ ip + $2/3$ oop intensity). *Bottom:* experimental powder data (*black*) and total NRVS VDOS intensity from a simulation using the QCC–NCA approach (*orange*) (reprinted with permission from [50]. Copyright 2010 American Chemical Society)

440 cm^{-1} is almost exclusively out-of-plane (z) polarized, which, by itself, is already a very strong indication that this feature corresponds to the Fe–NO stretch where iron moves orthogonal to the plane of the heme [115]. The band at about 560 cm^{-1} , on the other hand, shows more mixed polarizations, but the exact nature of the corresponding normal mode can now be understood based on the single-crystal NRVS and NCA results. These NCA simulations provide the best eigenvectors (normal coordinate descriptions) available to this date for the Fe–NO stretch and the Fe–N–O bend in 6C ferrous heme–nitrosyls, which provides quantitative insight into the nature of these features [50]. The data simulations unambiguously assign the $\sim 440\text{ cm}^{-1}$ feature to the Fe–NO stretch, $\nu(\text{Fe–NO})$, which is the only way that the dominant z -polarization of this band can be reproduced. On the other hand, the Fe–N–O bending internal coordinate is actually distributed over a number of porphyrin-based vibrations in the $520\text{--}580\text{ cm}^{-1}$ region (see Fig. 14) due to strong mode mixing, and the main feature assigned to $\delta_{\text{ip}}(\text{Fe–N–O})$ is observed at 563 cm^{-1} in [$^{57}\text{Fe}(\text{TPP})(\text{MI})(\text{NO})$]. These modes also show strong admixtures of the Fe–NO stretching internal coordinate as evidenced by their out-of-plane polarized intensity. The assignment of the $\sim 560\text{ cm}^{-1}$ feature to $\delta_{\text{ip}}(\text{Fe–N–O})$ is based on the finding (a) that the contribution of the Fe–N–O bending internal coordinate is more pronounced than the contribution from the Fe–NO stretch, and (b) that the atomic motions of the Fe–N–O unit in this normal mode are largely dominated by the displacement of the N-atom, and hence the atomic motions and kinetic energies of this mode resemble more closely a Fe–N–O bending mode. Importantly, based on the similar vibrational energies and spectral (Raman, NRVS) properties, a similar situation is likely encountered in other 6C ferrous heme–nitrosyls in model systems and in proteins [113, 114]. These assignments therefore represent general vibrational features of 6C ferrous heme–nitrosyls. In this way, NRVS data have resolved a long-standing controversy in the literature about the assignment of $\nu(\text{Fe–NO})$ in six-coordinate ferrous heme–nitrosyls in proteins and model complexes.

Full normal coordinate simulation of the NRVS data delivered force constants for the Fe–NO and N–O bonds in [$\text{Fe}(\text{TPP})(\text{MI})(\text{NO})$] of 2.57 and 11.55 mdyn/Å, respectively [50]. Importantly, these are distinctively smaller than force constants for corresponding 5C complexes; for example, for the analogous complexes [$\text{Fe}(\text{TPP})(\text{NO})$] and [$\text{Fe}(\text{OEP})(\text{NO})$], the Fe–NO and N–O force constants are 2.98 and 12.53 mdyn/Å [69] and 2.94 and 12.14 mdyn/Å [103], respectively. The implications of this result for the electronic structures of these complexes are discussed below.

3.1.3 General and Biological Implications

The new vibrational assignments for 6C ferrous heme–nitrosyls are highly significant with respect to the ongoing efforts to establish Fe–NO versus N–O vibrational correlation diagrams for corresponding heme complexes that could then be used to obtain insight into the properties of the protein's active site and the hydrogen bonding present based solely on vibrational data. This approach has been very successful for corresponding ferrous heme–CO complexes, where such relationships have been

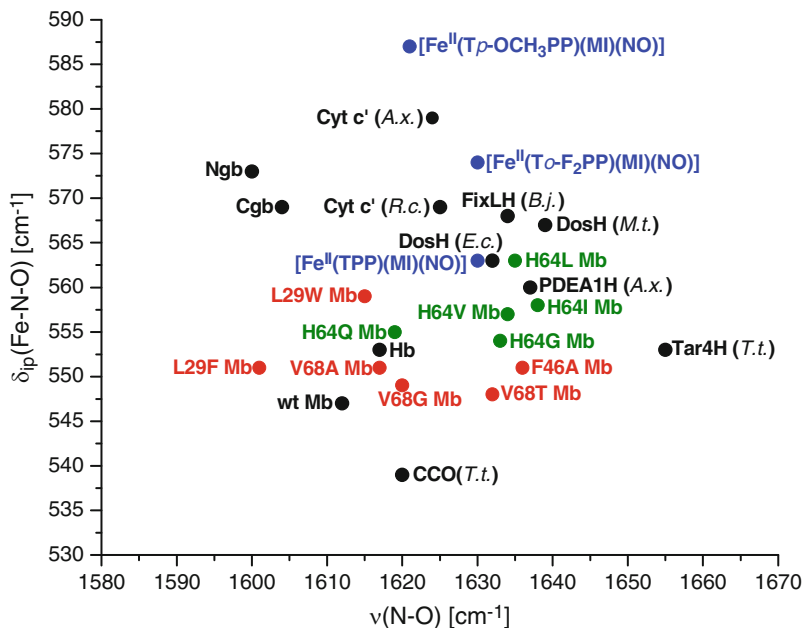
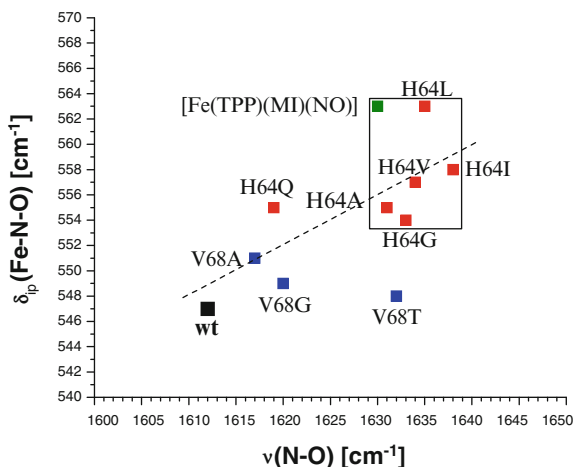


Fig. 15 Correlation diagram for $\nu(\text{N-O})$ and $\delta_{\text{ip}}(\text{Fe-N-O})$ in six-coordinate ferrous heme–nitrosyls in proteins and model complexes, using data from [111, 112]. Data for wt Mb (II)–NO and [Fe(TPP)(MI)(NO)] are taken from [50, 113]. *Black*: heme proteins with proximal His coordination; *blue*: model complexes with bound 1-methylimidazole (MI); *red*: Mb mutants; *green*: Mb mutants where the distal His64 has been altered to remove the potential hydrogen bond to the coordinated NO (reprinted with permission from [42]). Copyright 2010 American Chemical Society)

established and are commonly used in the literature when exploring the properties of new heme proteins [116, 117]. From the original Raman investigations described above, the 550–570 cm^{-1} Raman band of 6C ferrous heme–nitrosyls was believed to be the Fe–NO stretch, and correspondingly correlations of this feature with the N–O stretch were attempted [101, 118]. In particular, an inverse correlation of the 550–570 cm^{-1} Raman band with $\nu(\text{N-O})$ was proposed (analogous to correlations observed for heme–CO complexes) [118], and this approach has in fact found some application in the literature (see, for example, the recent publications [119, 120]). As shown in Fig. 15, however, if a large number of 6C ferrous heme–nitrosyls is considered, no clear correlation is evident from the data [42]. Moreover, if only Mb(II)–NO adducts in wt Mb and corresponding Mb mutants are considered, a direct correlation is observed as shown in Fig. 16, opposite to the initially proposed inverse correlation [118]. These findings can be understood based on the new assignment of the 550–570 cm^{-1} feature to $\delta_{\text{ip}}(\text{Fe-N-O})$. Based on the detailed properties of this mode as described above, the lack of correlation of $\delta_{\text{ip}}(\text{Fe-N-O})$ with $\nu(\text{N-O})$ is in fact due to the complex and strongly mixed nature of this vibration. Because of this, the energy of this feature is influenced by many factors, including the mixing with porphyrin-based vibrations, heme distortions, hydrogen bonding, etc. Caution

Fig. 16 Correlation of $\delta_{\text{ip}}(\text{Fe-N-O})$ and $\nu(\text{N-O})$ in human myoglobin (Mb) wild-type (wt) and mutants. Importantly, in the His64 mutants the distal His that is able to form a hydrogen bond with a bound diatomic has been removed. This correlation shows that the complex $[\text{Fe}(\text{TPP})(\text{MI})(\text{NO})]$ actually represents a model for the Mb(II)-NO adduct in the *absence* of hydrogen bonding. The data are taken from [111, 112] (reprinted with permission from [50]. Copyright 2010 American Chemical Society)



therefore needs to be exercised when conclusions are drawn about heme-nitrosyl properties that are based on such vibrational correlations.

As evident from the crystal structure of Mb(II)-NO shown in Fig. 11 and confirmed by recent ENDOR studies, the ferrous heme-bound NO ligand in proteins can form hydrogen bonds with distal amino acid side chains such as His and Tyr [48, 96]. One interesting question, especially when comparing the NO, CO, and O₂ adducts of ferrous Mb and Hb, is the relative strength of the hydrogen bond between the distal His and the bound diatomic. In particular, the strength of the Fe(II)-NO...H-N(His64) interaction and its effect on the properties of the coordinated NO are not clear. Vibrational spectroscopy is a great method to gain further insight into this topic, since metal-NO stretching frequencies are very sensitive to changes in the metal-NO interaction. The comparison in Fig. 16, which is based on extensive resonance Raman studies on Mb and corresponding mutants [111, 112], shows that the Mb mutants that lack the distal His (H64X) have somewhat higher $\delta_{\text{ip}}(\text{Fe-N-O})$ and $\nu(\text{N-O})$ frequencies than wt Mb, and that the complex $[\text{Fe}(\text{TPP})(\text{MI})(\text{NO})]$ actually falls right into the same region of the correlation plot as the His64 mutants. The complex $[\text{Fe}(\text{TPP})(\text{MI})(\text{NO})]$ therefore serves as a general model for ferrous heme-nitrosyls *in the absence of hydrogen bonding* [3]. Correspondingly, the Fe-NO stretching frequency in the model complex can be used to estimate the energy of this mode in the His64 mutants where $\nu(\text{Fe-NO})$ could not be determined. Importantly, the Fe-NO stretching frequencies in wt Mb(II)-NO and $[\text{Fe}(\text{TPP})(\text{MI})(\text{NO})]$ are very similar, located at 443 and ~ 439 cm^{-1} (437 cm^{-1} with ⁵⁷Fe) [50, 113], respectively, which provides strong evidence that the effect of the hydrogen bond on the properties of the Fe-NO bond is rather small. This notion is further supported by DFT calculations, which estimate the Fe(II)-NO...H-N(His64) H-bond to equal 3–4 kcal/mol [121]. Experimental estimates for the free binding energy of the His-proton to NO are about -1 kcal/mol [122]. Based on the finding that the changes in the Fe-NO bond that are caused by the presence of the hydrogen bond are rather small, the lower N-O stretching frequency in wt

Mb(II)–NO compared to the His64 mutants is likely due to a polarization of the π/π^* orbitals of NO in the presence of the hydrogen bond, which would cause a slight weakening of the N–O bond. In this sense, the lower N–O stretch ($<1,620\text{ cm}^{-1}$) in wt Mb(II)–NO might be a hallmark for the presence of a hydrogen bond in proteins that contain 6C ferrous heme–nitrosyls with axial His coordination.

Recently, DFT calculations have been reported that provide further insight into the effect of hydrogen bonding on the Fe–N–O unit in 6C ferrous heme–nitrosyls [121, 123]. Here, three main types of H-bond geometries were investigated using constrained geometry optimizations. First, the hydrogen bond could be formed with either the oxygen or the nitrogen atom of NO, or it could be directed at the N–O bond. The latter possibility is actually closest to the crystal structure of Mb(II)–NO as shown in Fig. 11. This structure was also found to have the lowest energy when imidazole is used as the H-bond donor, albeit only by $\sim 0.1\text{ kcal/mol}$ [121]. The optimized structures indicate that H-bonding to either the oxygen atom or the N–O bond causes a slight strengthening of the Fe–NO bond (decrease in Fe–NO distance) accompanied by a slight weakening of the N–O bond (increase in N–O distance). Hence, this should lead to an inverse correlation of the $\nu(\text{Fe–NO})$ and $\nu(\text{N–O})$ vibrational frequencies. In contrast, H-bonding to the nitrogen atom leads to both a slight weakening of the Fe–NO and N–O bonds and hence, should be accompanied by a direct correlation of the $\nu(\text{Fe–NO})$ and $\nu(\text{N–O})$ vibrational frequencies, although the effect on the Fe–NO stretch is predicted to be very small [123]. Since the Fe–NO stretching frequency is not known for the Mb mutants, a further correlation with experiment cannot be attempted. In comparison to wt Mb(II)–NO, the model system [Fe(TPP)(MI)(NO)] shows a higher N–O and slightly lower Fe–NO frequency. This inverse correlation would be in agreement with hydrogen bonding to either the oxygen atom or the N–O bond in wt Mb(II)–NO, in agreement with the crystal structure in Fig. 11.

A stronger effect on the Fe–N–O bond is observed if divalent cations are placed in direct proximity of the heme–nitrosyl of Mb via genetic engineering. Lu and coworkers installed a second metal binding site in the active site of sperm whale Mb by mutating the distal residues Leu29 and Phe43 to His and Val68 to glutamic acid (Glu), creating a (His)₃(Glu) binding site (the Fe_B site in analogy to NorBC) for a second metal ion in direct proximity to the heme [124]. In this way, a synthetic model system for respiratory NorBC, called Fe_BMb, is obtained that is housed in a protein. The ferrous heme–nitrosyl obtained for Fe_BMb when the additional metal binding site is empty displays the N–O stretch at $1,601\text{ cm}^{-1}$, and a similar frequency is observed with Cu(I) bound in the Fe_B site (labeled Cu(I)–Fe_BMb). However, when the divalent metal ions Fe(II) or Zn(II) are present in the Fe_B site, the N–O stretch drops to $1,549$ and $1,550/1,577\text{ cm}^{-1}$, respectively [119]. This indicates a strong polarization of the Fe–NO bond and results in a complex that has distinct Fe(III)–NO(–) character due to increased Fe–NO π -backbonding. The strong coupling of the resulting (heme)Fe–NO \cdots M(II) unit is further evident from the fact that in the case of M(II) = Fe(II), the EPR spectrum below 30 K shows effective g values of ~ 6 , indicative of ferromagnetic coupling between the

heme–nitrosyl ($S = 1/2$, see above) and the high-spin Fe(II) ($S = 2$), leading to a total spin of $S_{\text{tot}} = 5/2$ [119]. Unfortunately, the Fe–NO stretches for these proteins are not known, so it is not clear whether the Fe–NO and N–O stretches show a direct or indirect correlation in these cases. An increase in π -backbonding as proposed in [119] should lead to an inverse correlation of these vibrational frequencies and could be diagnosed in this way. From resonance Raman, the Fe–N–O bending mode $\delta_{\text{ip}}(\text{Fe–N–O})$ for the protein with the empty Fe_{B} site is observed at 560 cm^{-1} , which shifts to 577 cm^{-1} in the Fe(II)– Fe_{B} Mb form. However, one caveat with these data is the apparent isotope shift of $\sim 25 \text{ cm}^{-1}$ of these features upon ^{15}NO substitution, identified from the corresponding difference spectra [119], which is physically impossible (the maximum possible shift would be about 15 cm^{-1}). It is not clear why such a large isotope shift is observed in these cases.

A similar shift of the N–O stretch below $1,600 \text{ cm}^{-1}$ is observed in ferrous heme–nitrosyls with thiolate ligation in *trans* position to NO. For example, the N–O stretch in the ferrous cytochrome P450cam NO complex is located at $1,591 \text{ cm}^{-1}$, which is surprisingly low in energy compared to 6C ferrous heme–nitrosyls with axial imidazole coordination, where this mode occurs at $\sim 1,630 \text{ cm}^{-1}$ in the absence of hydrogen bonding (see above) [125]. DFT calculations using the simplified model system $[\text{Fe}(\text{P})(\text{SR})(\text{NO})]^{-}$ (P^{2-} = porphine dianion; R = Me, Ph) with BP86/TZVP reproduce the experimental trend: [95] here, $\nu(\text{N–O})$ is predicted at $1,599$ (R = Me) and $1,617 \text{ cm}^{-1}$ (R = Ph), respectively, which is clearly lower in energy compared to the calculated value for $\nu(\text{N–O})$ in $[\text{Fe}(\text{P})(\text{MI})(\text{NO})]$ (MI = 1-methylimidazole), obtained at $1,662 \text{ cm}^{-1}$ with BP86/TZVP. The calculations also indicate that the proximal thiolate ligand induces a weakening of the Fe–NO bond in comparison to the imidazole-coordinated case. Here, the calculated Fe–NO force constant (BP86/TZVP) of $3.26 \text{ mdyn}/\text{\AA}$ in $[\text{Fe}(\text{P})(\text{MI})(\text{NO})]$ drops all the way to $2.38 \text{ mdyn}/\text{\AA}$ in $[\text{Fe}(\text{P})(\text{SMe})(\text{NO})]^{-}$. Although the magnitude of the effect is likely overestimated in the calculations, this indicates that the thiolate ligand exerts a stronger *trans* effect on the Fe–NO bond than imidazole or other N-donor ligands (see below) [95]. In addition, further computational analysis showed that the thiolate-coordinated 6C ferrous heme–nitrosyls have a distinct contribution of the Fe(III)–NO(–) resonance form in their ground states (about 20%), due to the presence of the thiolate ligand that stabilizes Fe(III) [126]. This was determined via a Löwdin–Amos–Hall paired orbital (LAH-PO) analysis of the DFT-calculated wavefunction for $[\text{Fe}(\text{P})(\text{SMe})(\text{NO})]^{-}$ [127, 128].

3.2 Ferric Heme–Nitrosyls

Ferric heme–nitrosyls generally show distinctively smaller NO binding constants (K_{eq}) compared to the analogous ferrous complexes, according to the reaction:

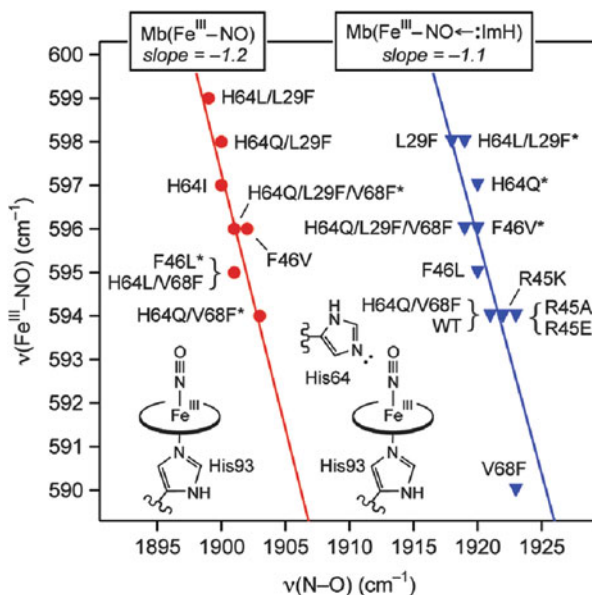


where L is the proximal ligand bound in *trans* position to NO (e.g., imidazole or thiolate), and the total charge n depends on the oxidation state of iron (+II or +III) and the charge of L, either neutral or anionic (keeping in mind that the porphyrin ligand is a dianion). For ferric hemes, K_{eq} is typically in the range of 10^3 – 10^5 M^{-1} , whereas for analogous ferrous complexes K_{eq} is usually about 10^{11} – 10^{12} M^{-1} [3, 129]. This translates to ΔG° values for NO binding of -15 to -16 kcal/mol for ferrous compared to -4 to -7 kcal/mol for ferric complexes. Hence, ferrous heme–nitrosyls are more stable by four to five orders of magnitude in K_{eq} or 8 – 11 kcal/mol in ΔG° . The underlying reasons for this important difference are further discussed below [54]. Since ferric heme–nitrosyls are diamagnetic, EPR and MCD do not provide further insight into the properties of these species. Hence, vibrational spectroscopy has been of key importance to elucidate the properties of these complexes (for recent reviews, see [3, 42, 122]).

3.2.1 Vibrational Spectroscopy

Ferric heme–nitrosyls with axial N-donor ligands (especially imidazole) bound *trans* to NO typically show N–O and Fe–NO stretching frequencies around $1,900$ – $1,930 \text{ cm}^{-1}$ and 580 – 600 cm^{-1} , respectively [3]. For example, the NO adduct of met Mb, Mb(III)–NO, shows the corresponding vibrations at $1,927$ and 596 cm^{-1} [110, 111, 130, 131]. Similarly, the NO complex of ferric *R. prolixus* nitrophorin 1 (rNP₁, see below) exhibits $\nu(\text{N–O})$ and $\nu(\text{Fe–NO})$ at $1,917$ and 591 cm^{-1} , respectively [132, 133]. Model complexes further corroborate these results; for example $\nu(\text{N–O})$ and $\nu(\text{Fe–NO})$ for $[\text{Fe}(\text{TPP})(\text{MI})(\text{NO})](\text{BF}_4)$ were identified at $1,896$ and 580 cm^{-1} (578 cm^{-1} measured with ^{57}Fe), respectively [54]. Since the Fe–N–O units in these complexes are essentially linear, these complexes also exhibit two Fe–N–O linear bending modes, $\delta_{\text{lb}}(\text{Fe–N–O})$, that are close to degenerate. These are found at similar energy as the Fe–NO stretches in these compounds. In the examples mentioned above, the bending modes are found at 572 (Mb), 578 (rNP₁), and 587 cm^{-1} in the above-mentioned model complex. While the N–O stretch is readily identified from IR spectroscopy, the low-energy stretching and bending modes of the Fe–N–O unit are usually determined by resonance Raman spectroscopy (see references above) and more recently, from NRVS measurements [54, 134]. Full NCA for the model complex $[\text{Fe}(\text{TPP})(\text{MI})(\text{NO})](\text{BF}_4)$ determined force constants for the N–O and Fe–NO bonds of 15.18 and 3.92 mdyn/\AA , respectively [54]. This is in good agreement with a more simplified NCA treatment applied to the vibrational data of rNP₄(III)–NO, where N–O and Fe–NO force constants of 15.11 and 4.09 were obtained [133]. A detailed investigation of the vibrational properties of a series of closely related ferric heme–nitrosyls in Mb and corresponding mutants clearly shows an inverse correlation of the $\nu(\text{N–O})$ and $\nu(\text{Fe–NO})$ vibrational frequencies as shown in Fig. 17 [122]. This is in agreement with the widely accepted idea that the Fe–N–O unit in these complexes has an Fe(II)–NO⁺ electronic structure in the ground state that is dominated by Fe(II) to NO⁺ π backbonding. This aspect is further discussed in Sect. 4.2. Importantly, a variation in the strength of this π backbond would then give rise to the observed

Fig. 17 Correlation of $\nu(\text{Fe-NO})$ and $\nu(\text{N-O})$ in ferric wild-type (wt) myoglobin (Mb) and corresponding mutants. Asterisks indicate minor components when two $\nu(\text{N-O})$ bands are detected. The slight slope of the curves relates to small variations in π backbonding between Fe(II) and NO^+ in the different mutants (reprinted with permission from [122]. Copyright 2010 American Chemical Society)



inverse correlation, in agreement with the experimental findings (see Fig. 17) and analogous to isoelectronic ferrous heme-CO complexes [116].

Interestingly, the large Fe-NO force constant in ferric heme-nitrosyls indicates that the Fe-NO bond is thermodynamically very strong in the ground state of these complexes, which is in contrast to the observed, relatively small binding constants of NO to ferric hemes (see above). This apparent contradiction is further discussed in Sect. 4.2.1.

3.2.2 The Effect of Axial Thiolate Ligation

The presence of an axial thiolate ligand leads to interesting variations in the geometric and electronic properties of ferric heme-nitrosyls. The first indication for this comes from the observation of a distinct bending of the Fe-N-O unit in these complexes with Fe-N-O angles of $\sim 160^\circ$. This was found both in the ferric NO adduct of the enzyme P450nor as shown in Fig. 18 and in the model complex $[\text{Fe}(\text{OEP})(\text{SR-H}_2)(\text{NO})]$ ($\text{SR-H}_2 = \text{S-2,6-(CF}_3\text{CONH)}_2\text{C}_6\text{H}_3$), the latter being the only structurally characterized ferric heme-nitrosyl model system with thiolate coordination [74]. In addition, vibrational data show that both the N-O and the Fe-NO stretch are shifted to distinctively lower energy in ferric heme-nitrosyls with axial thiolate coordination compared to analogous complexes with axially bound N-donor ligands [3, 73]. For example, the ferric NO adducts of P450nor and chloroperoxidase (CPO) exhibit these vibrations at 1,851 and 530 cm^{-1} and 1,868 and 538 cm^{-1} , respectively [135, 136]. The model complex $[\text{Fe}(\text{OEP})(\text{SR-H}_2)(\text{NO})]$ has similar vibrational properties and exhibits $\nu(\text{N-O})$ and $\nu(\text{Fe-NO})$ at

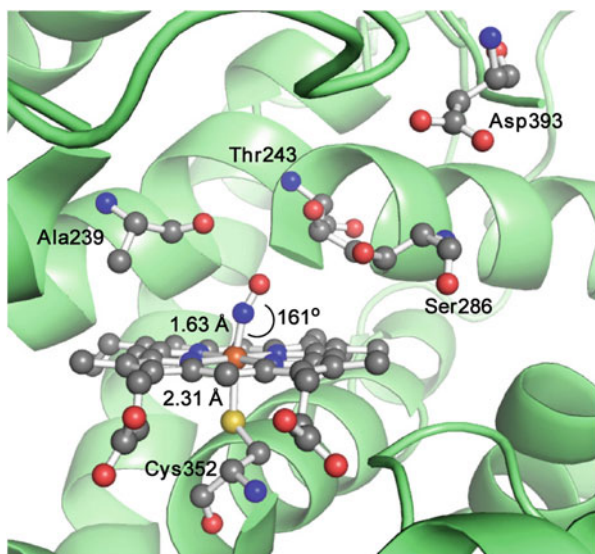


Fig. 18 Structure of the ferric NO complex in the Cytochrome P450nor active site. The image was generated using PyMOL from PDB code 1CL6

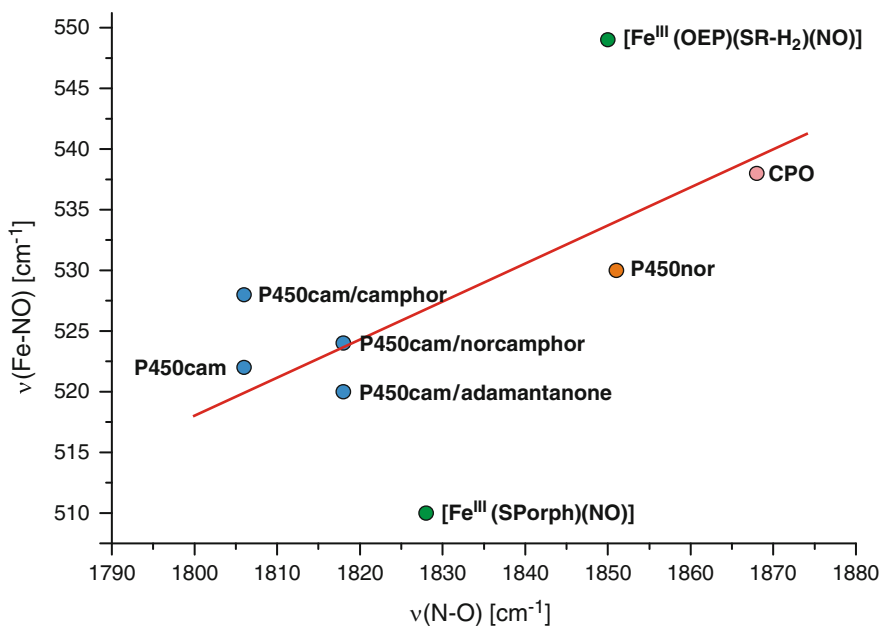


Fig. 19 Correlation of Fe–NO and N–O stretching vibrations in ferric heme–nitrosyls with axial thiolate coordination for various proteins and the two available model complexes

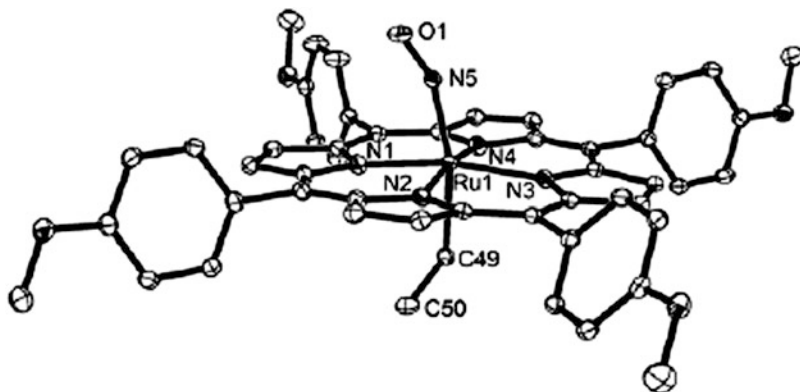


Fig. 20 Molecular structure of [Ru(T(*p*-OMe)PP)(Et)(NO)]. Hydrogen atoms have been omitted for clarity. Only one of the two disordered components is shown (reprinted with permission from [142]. Copyright 2012 American Chemical Society)

1,850 and 549 cm^{-1} , respectively [42, 74]. Importantly, a plot of the Fe–NO versus the N–O vibrational frequencies for the known thiolate-coordinated ferric heme–nitrosyls reveals a direct correlation of these vibrational energies as shown in Fig. 19 [3, 73]. This is surprising as in the generally accepted electronic structure description of ferric heme–nitrosyls, the Fe–N–O unit is described as having Fe(II)–NO⁺ character with dominant π backbonding (see above and Sect. 4.2). Hence, changes in the Fe–NO bond should lead to an inverse correlation of the Fe–NO and N–O vibrational frequencies, as observed for ferric heme–nitrosyls with axial imidazole coordination (see Fig. 17). The direct correlation, evident from Fig. 19, implies changes in the Fe–NO σ bond along this series of complexes, the origin of which was later identified to stem from a σ -*trans* effect of the strongly donating thiolate ligand [137]. This is further discussed in Sect. 4.2.

Interestingly, a similar bending of the Fe–N–O unit is also observed when other strongly donating, anionic ligands are bound in *trans* position to NO in corresponding Fe(III) and Ru(III) porphyrin complexes. Work by the Scheidt, Kadish, and Richter-Addo groups has identified strongly bent M–N–O (M = Fe, Ru, Os) units with M–N–O angles of 150–160° in complexes with axially coordinated organometallic ligands like phenyl derivatives [138, 139], in particular *para*-fluorophenyl [75, 140, 141]. These ligands can be envisioned to be even stronger σ donors than thiolates, and correspondingly should lead to an even stronger *trans* interaction with NO. In agreement with this idea, these compounds show low N–O stretching frequencies of only 1,750–1,800 cm^{-1} . Most recently, the first crystal structures of corresponding alkyl-coordinated Ru(III)–nitrosyl complexes of type [Ru(TPP*)(R)(NO)] (TPP*²⁻ = phenyl-substituted tetraphenylporphyrin dianion; R = methyl or ethyl) have been published [142]. Figure 20 shows the crystal structure of the complex [Ru(T(*p*-OMe)PP)(Et)(NO)] as an example. In this case, the Ru–N–O angle is 153° and the N–O stretch is observed at a record-setting low value of only 1,724 cm^{-1} .

3.2.3 Biological Implications

Investigations on ferrous heme–CO complexes in proteins with proximal His coordination had previously shown that the position of a protein on the $\nu(\text{C–O})/\nu(\text{Fe–CO})$ inverse correlation line provides information about the properties of the protein's distal pocket [116]. Proteins like wt Mb that lie on the low $\nu(\text{C–O})$, high $\nu(\text{Fe–CO})$ side usually exhibit polar pockets, often with hydrogen bond donors (the distal His in Mb). On the other hand, if a protein shows high $\nu(\text{C–O})$, low $\nu(\text{Fe–CO})$ frequencies, the distal pocket is rather nonpolar, like in Mb mutants where the distal His has been replaced by nonpolar amino acids. Investigations into the vibrational properties, usually via resonance Raman spectroscopy, of the ferrous CO adduct of a newly discovered heme protein therefore provides straightforward insight into the properties of the protein's active site pocket, and correspondingly, this methodology is frequently applied in the literature. On the other hand, as discussed above in detail, the same approach is unsuccessful for ferrous heme–nitrosyls, because the Fe–N–O bending mode, which is observed by Raman spectroscopy, does not show a meaningful correlation with $\nu(\text{N–O})$, and the Fe–NO stretch is not easily detected by resonance Raman. But what about ferric heme–nitrosyls? These complexes are isoelectronic with ferrous heme–CO complexes, and in particular, show very similar properties; i.e., they have linear Fe–N–O units and an electronic structure, best described as Fe(II)–NO⁺ (see Sect. 4), where the metal–ligand bond is also dominated by π -backbonding as in the Fe(II)–CO case. In this regard, NO⁺ is actually a stronger π -backbonding ligand than CO [54]. This indicates that ferric heme–nitrosyls might actually also be useful probes to investigate the properties of distal pockets in heme proteins. This idea was recently put to the test by Spiro and coworkers [122].

Surprisingly, as shown in Fig. 17, when the $\nu(\text{N–O})$ and $\nu(\text{Fe–NO})$ vibrational frequencies of wt Mb and of a collection of distal pocket mutants are plotted, two parallel, inverse correlation lines are obtained. The first correlation line (at lower N–O stretching frequencies) corresponds to His64 mutants that lack the distal His, so presumably this is a case where the bound NO is only influenced by the polarity of the active site pocket. The second correlation line (at higher N–O stretching frequencies) contains Mb variants that have either the distal His or a glutamine (Gln) in its place (H64Q). Spiro and coworkers investigated the underlying reason for this finding using DFT calculations and found that in ferric heme–nitrosyls, it is actually the lone pair of the distal His that weakly interacts with the positively charged (formally) NO⁺ ligand [122]. Since amino acid side chains like imidazole (His) and amides (Gln) are weak nucleophiles, the calculations predict a predominant interaction of the lone pairs of these groups with the O-atom of NO⁺. This is opposite to the proposed mechanism for nucleophilic addition of bases to these complexes where the base attacks the N-atom of the bound NO⁺ ligand [33]. The imidazole lone pair interaction with the Fe(II)–NO⁺ unit stabilizes the positive charge on the NO⁺ ligand, and in this way, increases the N–O bond strength and shifts $\nu(\text{N–O})$ to higher energy as shown in Fig. 17, while the Fe–NO bond is hardly affected [122]. Therefore, this interaction

does not correspond to a direct donation of significant electron density into the π^* orbitals of the bound NO^+ ligand, but rather to a polarization of the Fe(II)-NO^+ unit in the presence of the lone pair. This is a weak electrostatic effect (similar to the effect of hydrogen bonding on ferrous heme-nitrosyls and -carbonyls; see above) and not an effect of covalency. From the corresponding NO binding constants, it can be estimated that this interaction is worth about -1 kcal/mol in terms of free energy [122].

Importantly, as evident from Fig. 17, the $\nu(\text{N-O})/\nu(\text{Fe-NO})$ correlation can be used as a new reporter of heme pocket polarity and the accessibility of lone pair donors in the pocket. Comparison to existing vibrational data for nitrophorins, respiratory NO reductase (NorBC), and horseradish peroxidase (HRP) therefore provides some new insight with respect to the properties of these proteins [122]. The ferric NO adduct of *R. prolixus* nitrophorin 4 (rNP4) shows pH-dependent vibrational properties where the pH 7.5 and 5.5 forms fall on the two distinct correlations lines shown in Fig. 17. At low pH, the protein is in the closed form where the protein packs closely around the distal pocket [3]. Hence, there is no residue to interact with the bound NO^+ ligand, and correspondingly, $\nu(\text{N-O})$ and $\nu(\text{Fe-NO})$ at 1,904 and 590 cm^{-1} [143] put this form on the correlation line at lower $\nu(\text{N-O})$ where the Mb mutants are located that lack the distal His. The high pH form of the nitrophorins facilitates NO release, and excitingly, the vibrational properties of rNP4 at pH 7.5 with $\nu(\text{N-O})$ and $\nu(\text{Fe-NO})$ at 1,921 and 593 cm^{-1} [143] now place this form on the high-polarity line in Fig. 17. Since there are no suitable amino acid side chains available in the distal pocket to interact with NO, this indicates that the bound NO^+ is now exposed to water molecules (DFT predicts that the interaction with a lone pair from water could lead to a similar shift in $\nu(\text{N-O})$ as the interaction with imidazole [122]). This directly confirms the idea that a conformational change of rNPs is crucial in the process of NO release [3].

The ferric heme-nitrosyl adduct of NorBC shows $\nu(\text{N-O})$ and $\nu(\text{Fe-NO})$ at 1,904 and 594 cm^{-1} [144], which is right on the correlation line for the nonpolar distal pocket that lacks nucleophilic amino acid side chains. In contrast, the only functional model for NorBC reported so far by Collman and coworkers exhibits $\nu(\text{N-O})$ and $\nu(\text{Fe-NO})$ at 1,924 and 610 cm^{-1} , respectively [145], which is outside the range of vibrational energies observed for wt Mb and corresponding mutants (see Fig. 17), and other proteins. This is partly due to the application of a synthetic heme (picket fence porphyrin) in the dinuclear model complex, but could also indicate that the bound NO^+ in the model system is in a somewhat compressed environment, which would be in contrast to the protein [122]. This aspect warrants further investigation.

Interestingly, HRP(III)-NO shows an unusually high Fe-NO stretch at 604 cm^{-1} , whereas the N-O stretch is found at a relatively low value of 1,904 cm^{-1} [110, 131]. This could be related to lone pair donation from distal Arg and His residues to the bound NO^+ ligand as described above. In addition, the proximal His ligand in HRP has increased imidazololate character [146], and Spiro and coworkers speculate that this could also be a reason for the observed vibrational energies in HRP(III)-NO, in particular since the ferrous heme-CO complex of HRP also shows somewhat unusual $\nu(\text{C-O})/\nu(\text{Fe-CO})$ values [122]. The increase in $\nu(\text{Fe-NO})$ and decrease in

$\nu(\text{N–O})$ in the ferric heme–nitrosyl complex of HRP compared to other proteins could indeed indicate an increase in Fe(II)–NO^+ π -backbonding in HRP [54]. However, the presence of anionic axial ligands like thiolate, alkyl, and phenyl in ferric heme–nitrosyls usually leads to a simultaneous weakening of both the Fe–NO and N–O bonds, and correspondingly, a drop in both the Fe–NO and N–O stretching frequencies as described above [137]. It is therefore not clear how the increase in anionic imidazolate character of the proximal His by itself could be responsible for the observed vibrational properties of the ferric heme–NO adduct of HRP. This is an ideal problem for further investigations with large-scale DFT (e.g., QM–MM) calculations.

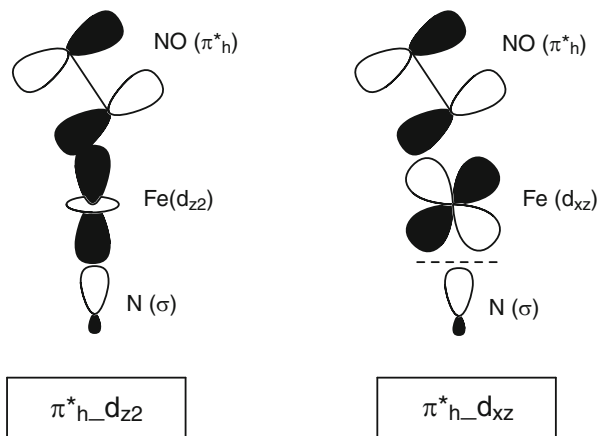
4 Electronic Structures of Heme–Nitrosyls

In pioneering work in the 1970s, Enemark and Feltham developed their famous classification system for transition metal NO complexes, $\{\text{MNO}\}^n$, where the superscript n refers to the sum of the valence electrons contributed by the d orbitals of the metal plus the electrons occupying the π^* orbitals of NO [147]. This allows for a straightforward classification of transition metal NO complexes and also defines the basic properties of these systems. NO is the smallest “non-innocent” ligand [148], i.e., this diatomic molecule is redox active and can coordinate to metal centers as NO^+ , NO(radical), and NO^- . The electronic structures of the resulting transition metal NO complexes exhibit extensive covalency and are often times complicated and difficult to understand. The modern spectroscopic and theoretical methods that are now in our hands in the twenty-first century provide the tools to go past the Enemark–Feltham classification to achieve more precise descriptions of the electronic structures of transition metal NO complexes. As formulated by one of us (Lehnert) recently [42], it is time to take on the challenge and strive to fully elucidate the electronic structures and electron distributions in transition metal NO complexes. Here we will discuss the progress in our understanding of the electronic structures of ferrous and ferric heme–nitrosyls, $\{\text{FeNO}\}^7$ and $\{\text{FeNO}\}^6$. Ferrous nitroxyl complexes, $\{\text{FeNO}\}^8$, are discussed in more detail in Sect. 5.

4.1 Ferrous Heme–Nitrosyls

The exact details of the electronic structures of ferrous heme–nitrosyls have been a matter of much debate in the recent literature. One of the main problems here is that DFT methods are not particularly good in describing the properties of these systems; so in order to obtain reliable electronic structure descriptions, extended comparisons between the calculations and experimental data need to be made. In addition, the exact spin distribution in these complexes is very sensitive to the applied functional, which further complicates matters. This aspect is discussed in detail in the following section for six-coordinate ferrous heme–nitrosyls.

Scheme 2 Variation of the SOMO of 6C ferrous heme–nitrosyls. *Left:* σ bonding orbital between the π_h^* orbital of NO and d_{z^2} of iron, as observed for 5C ferrous-heme nitrosyls. *Right:* π antibonding orbital between π_h^* and d_{xz}



4.1.1 Six-Coordinate Ferrous Heme–Nitrosyls

In order to elucidate the electronic structures of six-coordinate ferrous heme–nitrosyls, many different density functional/basis set combinations have been applied over the years. These studies generally agree that NO should be considered a σ donor and π acceptor ligand (see Scheme 1), but other key properties differ significantly. This is due to the fact that reported DFT results show distinct variations with respect to the exact composition of the singly occupied molecular orbital (SOMO) of the complex (labeled $d_{z^2}/d_{xz}-\pi_h^*$) and the spin density distribution. The SOMO could in principle vary all the way from a pure σ bonding orbital between π_h^* of NO (h = horizontal, the singly occupied π^* orbital of NO that is located within the Fe–N–O plane) and d_{z^2} of iron (see Scheme 1) to a π antibonding orbital between π_h^* and d_{xz} (in the applied coordinate system were the z direction corresponds to the heme normal, and the Fe–N–O unit lies within the xz plane), because the orbitals have the same symmetry within the C_s point group. These two extremes are shown in Scheme 2. However, as pointed out by Mingos and others for analogous $\{MNO\}^7$ and $\{MNO\}^8$ systems, this scenario should lead to the formation of a M–NO σ bond between d_{z^2} and π_h^* due to the stabilization of the resulting, bonding MO [149, 150].

In order to obtain further insight into the dependency of the electronic description of 6C ferrous heme–nitrosyls on the applied DFT method, we performed a number of single point calculations on the model $[Fe(P)(MI)(NO)]$. For this purpose, the BP86/TZVP-optimized structure of this species was used, which shows very good agreement with the crystal structure of $[Fe(TPP)(MI)(NO)]$ [69]. The results of these calculations are summarized in Table 4. As evident from the table, the spin density distribution, i.e., the exact localization of the unpaired electron of NO in the complex, shows a clear functional dependence (see also [151, 152]). With gradient-corrected functionals, the unpaired electron density is mostly metal centered (>50% on iron), whereas with hybrid functionals an NO-centered distribution of the spin density is observed (>50% on NO), i.e., the unpaired electron is in fact mostly localized on NO [42, 152]. CASSCF and CASPT2 calculations have been applied to further elucidate this issue,

Table 4 Calculated properties^a of the model system [Fe(P)(MI)(NO)] (using the BP86/TZVP optimized structure [69]) obtained with different functionals as indicated

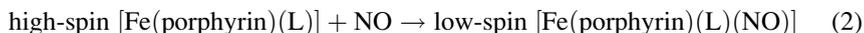
	Functional	Σ (Spin density)		$d_{z^2}/d_{xz}-\pi_n^*$		d orbital spin density		
		Fe	Σ (NO)	%Fe	%NO	d_{z^2}	d_{xz}	d_{yz}
Hybrid	B3LYP	26	75	27	58	0.41	-0.14	-0.04
	B3LYP-D	25	75	27	58	0.41	-0.14	-0.04
	B3LYP*	36	65	28	54	0.43	-0.10	-0.01
	O3LYP	51	51	33	54	0.46	-0.04	0.04
	TPSSH*	19	80	29	57	0.44	-0.19	-0.09
	O3LYP-D	51	51	24	44	0.46	-0.04	0.04
	O3LYP*	41	61	33	54	0.45	-0.09	0.01
	O3LYP-D*	41	61	24	44	0.45	-0.09	0.01
	TPSSH	35	66	32	55	0.45	-0.12	-0.03
	PBE0*	41	61	29	56	0.45	-0.10	0.01
	Gradient corrected	OLYP	69	33	43	44	0.49	0.05
TPSS		49	51	41	47	0.47	-0.04	0.01
BLYP		56	43	41	46	0.46	0.01	0.03
PBE		60	40	42	44	0.48	0.02	0.04

All calculations were performed with Ahlrich's triple-zeta basis set TZVP. For functionals in *bold*, the contour plot of the corresponding SOMO is included in Fig. 21

^aSpin densities and MO contributions were obtained from a Löwdin population analysis

and in initial studies metal-centered spin densities have been observed in these calculations that are similar to the results with the gradient-corrected functionals [152, 153]. These results have been taken as evidence that the metal-based spin densities should better reflect the properties of the real complexes. However, in contrast to these findings, more recent CASSCF investigations on the model system [Fe(NO)]²⁺ indicate that none of the DFT methods are able to reproduce the CASSCF spin densities well [154]. In addition, one has to keep in mind that results from CASSCF and CASPT2 calculations are greatly dependent on the applied active MO space as shown recently [154] and are also quite sensitive to basis sets. Consequently, the agreement between spin densities from CASSCF and CASPT2 calculations with those from gradient-corrected functionals by itself as reported in [153] is by no means a proof that this is really the most realistic description of the actual complexes. The best way to determine this is by extended quality checks of the calculated results against experimental findings. Here, the functional that gives the overall best agreement with experimental properties should then deliver the best description of the Fe–NO bond, and hence the electronic structure that is closest to the real system.

The first property that is often used to evaluate the quality of DFT methods are complex formation (free) energies; in our case this would be the binding energy of NO to a five-coordinate ferrous heme according to the equation:



This approach is somewhat problematic since NO binding energies according to (2) do not only depend on the properties of the actual NO product complex, but also on the spin state energetics (due to the spin state change in the reaction from high spin to low spin), which are not always well handled by DFT. Therefore, NO binding energies are a summation of many different contributions to the total energy, and hence are a more indirect measure of the quality of the description of the Fe–NO bond. Recently it has been shown that dispersion corrections are critically important for the calculation of accurate ligand binding energies, and that the dispersion correction accounts for roughly -10 kcal/mol for ligand binding to a heme center [155, 156]. Taking this into consideration, and applying a reasonably large and consistent basis set [54], hybrid functionals are able to reproduce the (free) binding energies of NO to ferrous heme centers well [155]. In contrast, gradient-corrected functionals tend to greatly overestimate the binding energy of NO to ferrous hemes, which is a first indication that gradient-corrected functionals overestimate the covalency, and hence, strength of the Fe–NO bond in heme–nitrosyls. This becomes very evident when calculated Fe–NO force constants and vibrational frequencies are considered (see below) [42]. Similar effects are also observed for other transition-metal nitrosyls [157, 158]. Based on all of these considerations, hybrid functionals give a better and more balanced description of the Fe–NO bond. The following discussion will therefore mostly focus on hybrid functionals.

Interestingly, Table 4 shows that although hybrid functionals give generally NO-centered spin densities as mentioned above, the variation between the different methods is still quite large and NO-based spin densities range all the way from 51% for O3LYP to 80% with TPSSH*. Intuitively, one would expect that this corresponds to a change in the amount of electron donation from the singly occupied π^* orbital of NO into the d_{z^2} orbital of iron. In contrast to this expectation, Table 4 shows that the Fe–NO σ bond is practically invariant in these cases, i.e., the charge contributions to the resulting SOMO, $d_{z^2}/d_{xz}-\pi_h^*$, are independent of the functional, and the spin density of d_{z^2} is about 45% with very little variation. A further examination of Table 4 shows that the variation in overall spin densities actually correlates with the spin density values of the d_{xz} and d_{yz} orbitals of iron, i.e., *the different functionals predict different degrees of spin polarization in the Fe–NO π backbond, and this is the underlying reason for the large variation in the calculated spin densities.* Note that this effect is much larger for the hybrid functionals compared to the gradient corrected functionals, which explains the overall larger variation of the spin densities in the former case. Corresponding to this result, the nature of the SOMO is, surprisingly, invariant between the different computational methods used, as shown in Fig. 21. In all cases, the SOMO corresponds to a σ interaction between d_{z^2}/d_{xz} of iron and π_h^* of NO.

In summary, our results show that the large variation in spin density observed with different hybrid functionals is clearly linked to the nature of the applied functional, whereas the variation of the SOMO noted in the literature [96] must then relate to other factors, for example the structure of the heme, the properties of

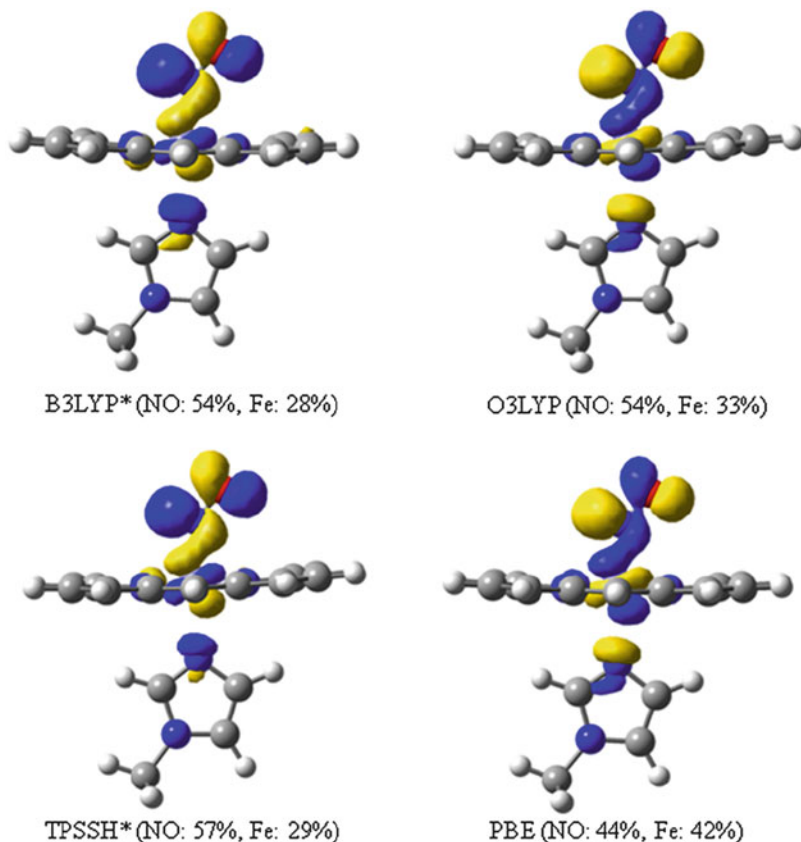


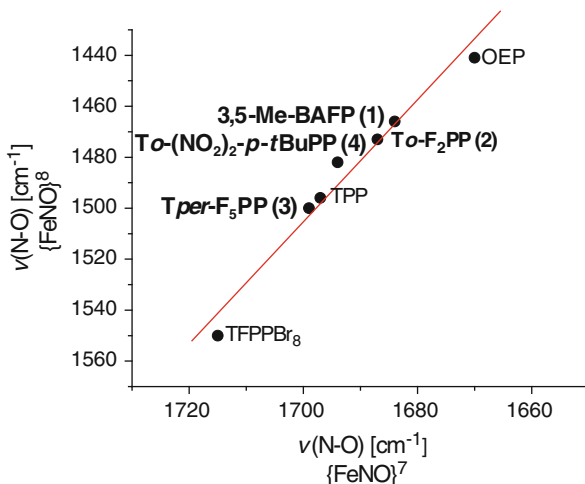
Fig. 21 The SOMO in 6C ferrous heme–nitrosyls, calculated for the model $[\text{Fe}(\text{P})(\text{MI})(\text{NO})]$ (P^{2-} = porphine dianion, MI = 1-methylimidazole) and different functionals as indicated

the proximal ligands, and the environment (solvent fields, etc.) used in the calculations. As shown here, the different functionals do not induce a variation in the nature of the SOMO by themselves, when the same structure is used for the calculations. At this point it is unclear what causes the variation in the SOMO noted in the literature, and whether or not this could be a computational artifact. Due to this uncertainty, it is important to correlate the DFT results with experiment as closely as possible to determine the exact nature of the Fe–NO bond in the real complexes.

4.1.2 Experimental Insight into the Nature of the SOMO

Key insight into the properties of the SOMO in ferrous heme–nitrosyls, i.e., whether it is more σ bonding or π antibonding in nature, can be obtained from the

Fig. 22 Comparison of N–O stretching frequencies in five-coordinate $\{\text{FeNO}\}^7$ and $\{\text{FeNO}\}^8$ porphyrin complexes with the indicated porphyrins as coligands [64]



general properties of these complexes, and by making correlations with the corresponding, one-electron reduced $\{\text{FeNO}\}^8$ species (see Sect. 5). As known for a long time, nitric oxide in ferrous heme–nitrosyls exhibits a very strong thermodynamic *trans* interaction with axially bound ligands that weakens both the Fe–NO bond and in particular, the Fe–{axial ligand} bond as described in Sects. 2.1 and 3.1 [65, 159]. The latter effect is evident from a distinct elongation of the Fe–{axial ligand} bond and a distinct drop in the corresponding stretching frequency. For example, for imidazole bound in *trans* position to NO, Fe–imidazole bond lengths of 2.18–2.20 Å and Fe–imidazole stretching frequencies of only approximately 150 cm^{-1} are observed [50, 67]. In addition, the binding constant of 1-methylimidazole in *trans* position to NO in corresponding model complexes is very small, generally observed below 50 M^{-1} [69]. In comparison, other strongly π accepting ligands like CO do not mediate much of a *trans* effect compared to NO [156, 160]. Besides the vibrational-spectroscopic insight described in Sect. 3.1, this provides further direct evidence that the strong thermodynamic *trans* effect of NO relates to the presence of a distinct Fe–NO σ bond. Since the Fe–NO σ bond is mediated by the SOMO of these complexes, this demonstrates that the SOMO should in fact be predominantly Fe–NO σ bonding in nature. Further support for this idea comes from recent investigations on the corresponding one-electron reduced $\{\text{FeNO}\}^8$ complexes [64]. As shown in Fig. 22, a very strong correlation is observed between the N–O stretching frequencies in related $\{\text{FeNO}\}^7$ and $\{\text{FeNO}\}^8$ complexes. This implies that the nature of the SOMO, which becomes doubly occupied in the $\{\text{FeNO}\}^8$ complexes, does not change in the one-electron reduction process; i.e., whatever the composition of this MO is in the $\{\text{FeNO}\}^7$ complexes is preserved in the $\{\text{FeNO}\}^8$ case. Importantly, the experimental data show that the double-occupation of the SOMO in the $\{\text{FeNO}\}^8$ case leads to (a) a further increase in the thermodynamic *trans* effect of NO (NO[−] in the reduced complex) [64] and (b) similar Fe–NO stretching frequencies compared to the $\{\text{FeNO}\}^7$ complexes [161]. This demonstrates that the SOMO is in fact dominantly

Fe–NO σ bonding in nature. If this orbital would be mostly π antibonding, its double occupation should not greatly affect the *trans* effect of NO, but this should induce a distinct weakening of the Fe–NO bond, accompanied by a significant drop in the Fe–NO stretching frequency in the reduced complex. This is not the case. DFT calculations further support this interpretation [64].

The question whether the SOMO is of σ -bonding or π -antibonding nature in low-spin {MNO}⁷ complexes will critically depend on the energy of the d_{z^2} orbital; in the first case (Scheme 2, left), d_{z^2} is relatively low in energy and available for binding to the singly occupied π_{h}^* orbital of NO, whereas in the latter case (Scheme 2, right), d_{z^2} is high in energy, and the nature of the SOMO then changes to a π -antibonding orbital between π_{h}^* and d_{xz} . The latter possibility, i.e., that the unpaired electron of NO is located in a strongly Fe–NO antibonding SOMO, has recently been proposed, based on DFT calculations, for the NO adduct of cd_1 NIR (calculated using the PBE functional) [96]. Between the two borderline cases shown in Scheme 2 a continuum of electronic structures exists, which result from variable mixing between the bonding $\pi_{\text{h}}^*d_{z^2}$ and the antibonding $\pi_{\text{h}}^*d_{xz}$ orbitals. The degree of this mixing will critically depend on the ability of the chosen computational method to accurately predict the energy of the d_{z^2} orbital, which then affects the balance between $\pi_{\text{h}}^*d_{z^2}$ and $\pi_{\text{h}}^*d_{xz}$ contributions in a delicate way. Hence, the SOMO in low-spin {MNO}⁷ complexes (M = Fe, Ru) should generally correspond to a superposition of $\pi_{\text{h}}^*d_{z^2}$ and $\pi_{\text{h}}^*d_{xz}$, and based on the strong experimental evidence described above, the contribution from $\pi_{\text{h}}^*d_{z^2}$ should dominate in ferrous heme–nitrosyls. Variation in the composition of the SOMO should be directly reflected by the properties of the complexes: in the case of a dominantly σ -bonding SOMO, the metal–NO bond should be relatively strong, and a distinct thermodynamic σ -*trans* effect should be observed in agreement with experiment as discussed above, whereas in cases where the SOMO is mostly π -antibonding in nature, the metal–NO bond should be weaker, and the thermodynamic *trans* effect should be less pronounced and equal to that of CO.

In this respect, comparison with analogous [Ru(porphyrin)(N-donor)(NO)] complexes of {RuNO}⁷ type with bound axial N-donor ligands is insightful. In general, the electronic structures of Fe(II)- and Ru(II)-porphyrin NO complexes are thought to be analogous. Interestingly, however, DFT calculations on the complex [Ru(OMP)(Py)(NO)] (OMP²⁻ = octamethylporphyrin dianion) by Kaim and coworkers indicate that the SOMO of this complex is in fact dominantly π -antibonding in nature [162]. In agreement with this, {RuNO}⁷ porphyrin complexes are unstable and generally difficult to isolate [32]. In the light of the above discussion, this can be explained with simple ligand field arguments: because Ru(II) is a second-row transition metal ion, the ligand field splitting observed for this species is generally much larger compared to Fe(II). This puts the d_{z^2} orbital at much higher energy in the Ru(II) complexes, leading to the SOMO being mostly π -antibonding in nature, which would greatly labilize the Ru–NO bond compared to the Fe–NO bond in the iron case. This further supports the idea that the SOMO in the {FeNO}⁷ heme complexes is dominantly σ -bonding in nature.

4.1.3 Experimental Evaluation of the Spin Density Distribution

EPR g values and hyperfine coupling constants available from EPR (especially for the $^{14/15}\text{N}$ -atom of NO) and Mossbauer (for the ^{57}Fe atom) spectroscopy should provide direct insight into the spin density distribution in the complexes, in particular since the gradient-corrected and hybrid functionals show such different tendencies in this respect (see above and Table 4). However, in practice this is not the case, and it is surprising that calculated g tensors and hyperfine coupling constants are relatively similar for both types of functionals. In general, gradient-corrected functionals perform better in reproducing experimental ^{14}N hyperfine coupling constants as noted first by Oldfield and coworkers who performed BPW91 and B3LYP calculations on the complex $[\text{Fe}(\text{OEP})(\text{NO})]$ [163], and similar observations were later made by others [48, 91]. However, the results obtained with hybrid functionals still agree reasonably well with experiment [91, 163], and more importantly, calculated g tensors and hyperfine coupling constants show quite large deviations from experiment with any functional used (due to intrinsic errors in the method used for these calculations; see Sect. 3.1) and are also strongly dependent on the basis set and the geometry. For example, using QM/MM calculations on the NO adduct of ferrous Mb yielded errors in the calculated g shifts for g_{max} of up to 100% (using the gradient-corrected functional PBE) [48]. Based on these rather large deviations, it seems that drawing conclusions about which functional gives a more accurate description of the electronic structure of ferrous heme–nitrosyls solely based on calculated hyperfine coupling constants is problematic.

On the other hand, the comparison of experimental and calculated Fe–NO force constants and stretching frequencies, which directly reflect the strength of the Fe–NO bond, is very straightforward and insightful in this regard [42]. Experimentally, six-coordinate ferrous heme–nitrosyls show Fe–NO stretching frequencies at about 440 cm^{-1} as discussed in Sect. 3.1 [50, 113]. Gradient-corrected functionals greatly overestimate the covalency and strength of the Fe–NO bond and predict $\nu(\text{Fe–NO})$ around 600 cm^{-1} , which is in stark contrast to the experimental results. In comparison, B3LYP calculations yield the Fe–NO stretch at about 420 cm^{-1} , indicating that this method certainly underestimates the strength of the Fe–NO bond, but the agreement with experiment is much better in this case. The largest deviations in the B3LYP calculations are observed for the N–O stretching frequency, which is predicted around $1,800\text{ cm}^{-1}$ (compared to $\sim 1,630\text{ cm}^{-1}$ experimentally). This deviation is in agreement with the idea that B3LYP underestimates the strength of the Fe–NO bond, in particular the π -backbond. So the fact that gradient-corrected functionals deliver better N–O stretching frequencies is actually mostly due to a fortunate error cancellation, where the overestimate of the π -backbond greatly lowers the N–O stretch, but the overestimate of the donation of the unpaired electron of NO toward iron (evident from the metal-based spin densities observed with gradient-corrected functionals) increases the N–O stretch (due to depopulation of the π_{h}^* orbital of NO). These effects cancel in a fortunate way, such that the calculated N–O stretching frequencies with gradient-corrected functionals are quite close to experiment. In summary, whereas gradient-

corrected functionals essentially fail to provide a reasonable estimate of the strength of the Fe–NO bond, the results from the hybrid functional B3LYP are in qualitative agreement with experiment and hence, give a more realistic (but certainly not perfect) description of the properties of the Fe–NO bond. This is further supported by the finding that gradient-corrected functionals greatly overestimate the binding energy of NO to ferrous hemes, whereas hybrid functionals are able to reproduce the NO binding energies well. Because of this, the NO-based spin-density distributions obtained from the B3LYP calculations can be expected to be more realistic, as the overestimate of the covalency of the Fe–NO bond by the gradient-corrected functionals leads to a significant quenching of the spin density of NO.

4.1.4 Electronic Structure Description of Ferrous-Heme Nitrosyls

Since hybrid functionals lead to a superior description of the properties of the Fe–NO bond, the interpretation of the electronic structure of ferrous heme–nitrosyls should take the spin-density distributions obtained from these calculations into consideration. Since ferrous heme–nitrosyls have total spins of $S = 1/2$, the details of the electronic structures of these complexes have to be analyzed within the spin-unrestricted scheme where majority (α) and minority (β) spin MOs have to be distinguished. As indicated in Scheme 1 and described in Sect. 3.1, NO is a σ -donor and π -acceptor ligand in ferrous heme–nitrosyls [50]. Here, the Fe–NO σ bond is mediated by medium strong donation from the singly occupied α - π_{h}^* orbital of NO into the unoccupied d_{z^2} orbital of the low-spin iron(II) center. Hence, the resulting SOMO has mostly $\pi_{\text{h}}^*d_{z^2}$ character. Nevertheless, the admixture of some $\pi_{\text{h}}^*d_{xz}$ character into the SOMO of six-coordinate ferrous heme–nitrosyls complexes seems feasible as discussed above, and could be responsible for some of the weakening of the Fe–NO bond compared to the analogous five-coordinate species. This is reflected by the vibrational properties of these complexes (see Sect. 3.1). In addition, π -backbonding is mediated by the occupied d_{yz} orbital of iron(II) and the π_{v}^* orbital of NO (v = vertical; the π^* orbital of NO which is orthogonal to the Fe–NO plane) for both α and β spin in a quite similar way (i.e., spin-polarization effects on the π -backbond between d_{yz} and π_{v}^* are relatively small except for TPSSH*; see Table 4). Finally, additional contributions to the π -backbond arise from the interaction of the unoccupied β - π_{h}^* orbital of NO and β - d_{xz} of iron, which, however, is usually a weak interaction. This electronic structure leads to a spin-density distribution where most of the unpaired electron density is located on the NO ligand. Hence, six-coordinate ferrous heme–nitrosyls with axial N-donor coordination represent the prototype of complexes with a Fe(II)–NO(radical) type electronic structure [69].

In five-coordinate ferrous heme–nitrosyls the strength of the Fe–NO σ bond increases via increased donation from the α - π_{h}^* orbital of NO into the unoccupied d_{z^2} orbital of iron. This is caused by the absence of a *trans* ligand to NO, which lowers the d_{z^2} orbital of iron in energy and increases its interaction with α - π_{h}^* . In addition, the resulting SOMO is now a pure $\pi_{\text{h}}^*d_{z^2}$ orbital. Experimentally, this is reflected by a distinct increase in the Fe–NO and N–O stretching frequencies and force constants in

the five-coordinate compared to the six-coordinate case (see Sect. 3.1). The fact that both the Fe–NO and N–O bonds become stronger at the same time provides very strong evidence that this change in bonding in five-coordinate complexes is due to a change in σ -bonding (a change in π -backbonding would cause an inverse correlation) [69]. In the light of the above discussion, this direct correlation of the Fe–NO and N–O bond strengths constitutes further direct experimental evidence that the SOMO of heme–nitrosyls is in fact dominantly σ -bonding in nature. This increased donation from the NO ligand to iron(II) has also been taken as evidence that five-coordinate ferrous heme–nitrosyls have partial Fe(I)–NO⁺ character in the ground state [91].

Corresponding to this bonding model, an even stronger donating axial ligand, for example an axial thiolate ligand, should lead to a further weakening of both the Fe–NO and N–O bonds, and experimental and computational evidence support this idea (see Sect. 3.1) [95]. Further analysis of the wavefunction of these complexes shows that the axial thiolate ligand introduces a significant amount of Fe(III)–NO[−] character into the ground state of these complexes (about 20%) due to the fact that the anionic thiolate ligand stabilizes Fe(III) [126]. In contrast, the wavefunction of six-coordinate ferrous heme–nitrosyls with axial N-donor coordination is dominated by the Fe(II)–NO(radical) contribution (~90%) [126].

Recent CASSCF and CASPT2 calculations have been used to obtain further insight into the multi-configurational nature of the ground state of ferrous heme–nitrosyls [153]. These calculations predict that both five- and six-coordinate ferrous heme nitrosyls have ground state wavefunctions that are composed of roughly equal contributions of Fe(II)–NO(radical) and Fe(III)–NO(−) character, and that there is essentially no significant change with coordination number. However, since spectroscopic properties cannot be predicted from these correlated wavefunctions, it is not clear whether this balance accurately reflects the real complexes. Analysis of the spin contamination in DFT wavefunctions paints a different picture as described above where the Fe(II)–NO(radical) contribution to the ground state dominates. This point requires further study.

4.1.5 Biological Implications

The most important biological implication of the electronic structure of ferrous heme–nitrosyls is the *trans* effect of NO and its role in the activation of the mammalian NO-sensor protein sGC. The existence of the *trans* effect of NO was already proposed by Mingos in 1973 [149] (for analogous {CoNO}⁸ systems, but see also [164]), and its significance for the activation of sGC was recognized more than 20 years ago [159], but it was not until a few years ago that the underlying nature of this σ -*trans* effect was experimentally confirmed and quantified via extensive correlations of spectroscopic and theoretical results as described above [50, 69]. The mechanism of activation of sGC was recently reviewed in much detail by one of us [3], and because of this we will only briefly touch on this subject here. In short, sGC contains a 5C ferrous heme center with axial His coordination as the high-affinity sensor for NO. Upon coordination of NO, a corresponding 6C ferrous heme–nitrosyl

complex is formed as intermediate [165]. Due to the strong σ -*trans* effect of NO, the Fe–His bond is weakened and subsequently cleaved. This induces a conformational change that activates the catalytic domain of sGC for the production of cGMP, which then triggers smooth muscle relaxation in arteries, and cGMP is also involved in nerve signal transduction in the brain. While the *trans* effect of NO is the main player in this activation mechanism, it was recently proposed that the flattening of the heme upon NO binding could also contribute to this activation mechanism [166].

In addition, ferrous heme–nitrosyls are potentially involved as intermediates in the catalytic mechanism of NO reduction to N₂O by bacterial NO reductases (NorBC) [3], and also as intermediates in multiheme cytochrome *c* nitrite reductases (CcNIR) [53]. In order to understand the potential involvement of ferrous heme–nitrosyls in the mechanism of NorBC, a detailed understanding of the electronic structures of these species is necessary. In fact, the finding that ferrous heme–nitrosyls, especially in the 6C case, are best described as Fe(II)–NO(radical) complexes that show a large degree of radical character on NO supports a mechanism introduced by Girsch and de Vries, who proposed a radical type coupling between a heme- and a non-heme iron bound NO ligand [167]. Although this sounds feasible with respect to the heme–nitrosyl electronic structure, more recent results that particularly focus on the properties of the non-heme iron–nitrosyl complex indicate that this mechanism is unlikely [51, 168, 169]. Recent DFT studies favor mechanisms that are based on reductive coupling approaches (see Sect. 6.2).

In contrast, other transition metal complexes have been shown to facilitate radical type N–N bond formation as reviewed recently [170]. In particular, Onishi and coworkers reported that the {RuNO}⁶ complex [Ru(Tp)Cl₂(NO)], when treated with free pyrazole in the presence of base, forms a dimer that contains a neutral *cis*-ONNO ligand that results from the radical coupling of two coordinated NO molecules upon reduction of the complex [171]. The crystal structure of the product [{Ru^{II}(Tp)}₂(μ -Cl)(μ -pz)(μ - κ^2 -N₂O₂)] exhibits a long N–N distance of 1.861 Å, which is significantly longer than an N–N single bond, indicative of a neutral (NO)₂ ligand. Upon two-electron oxidation of the dimer, the N–N bond is broken, leading to reformation of two individual {RuNO}⁶ complexes that remain in a dimer arrangement. In this sense, the reaction is reversible. A more common scenario is a reductive coupling where N–N bond formation goes along with a two-electron oxidation of the coordinated metal center(s), leading to the formation of a hyponitrite (N₂O₂²⁻) bridged dimer, for example from [Co(NH₃)₆]²⁺ plus NO or from [Ni(NO)(bipy)₂]⁺ [172–175]. Importantly, ferrous heme–nitrosyls cannot catalyze the analogous reaction, and a corresponding hyponitrite-bridged dimer can only be obtained by reaction of a ferric heme precursor with hyponitrite directly [47], further adding credibility to the idea that the reduction of NO to N₂O has to be catalyzed in a different way in the enzyme NorBC. Interestingly, all these N₂O₂⁽²⁻⁾ complexes form N₂O upon treatment with acid, indicating that the N–N bond forming step is the real challenge in NOR catalysis, whereas the following decomposition of the formed hyponitrite intermediate to yield N₂O is a straightforward process. Mechanistic alternatives for NorBC are discussed in Sect. 6.2.

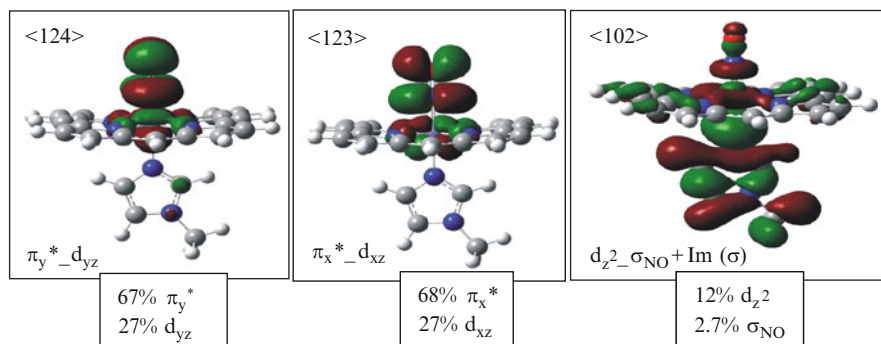


Fig. 23 Contour plots of key molecular orbitals of ferric heme–nitrosyls in the Fe(II)–NO⁺ ground state. Calculated for the optimized structure of [Fe(P)(MI)(NO)]⁺ using BP86/TZVP (reprinted with permission from [54]. Copyright 2008 American Chemical Society)

4.2 Ferric Heme–Nitrosyls

The electronic structure of ferric heme–nitrosyls with axial N-donor coordination is best described as a low-spin Fe(II) center with a bound NO⁺ ligand, in agreement with the structural and spectroscopic properties of these complexes [12]. As described above, these species are characterized by linear Fe–N–O units with very short Fe–NO bond lengths and N–O stretching frequencies around 1,900 cm^{−1}, which strongly supports this electronic structure description [42]. In addition, the coordinated NO⁺ ligand acts as an electrophile and reacts with hydroxide and other bases, and hence also shows typical NO⁺-type reactivity [33, 176]. The Fe(II)–NO⁺ ground state of ferric heme–nitrosyls is isoelectronic with Fe(II)–porphyrin CO complexes. Correspondingly, the Fe–NO interaction in this state is dominated by two strong π backbonds between Fe(II) and NO⁺, which are in fact stronger than the backbonds in the corresponding CO complexes. Figure 23 shows contour plots of the resulting antibonding MOs (left and middle), which have about 70% π^* and 30% d contributions. This further illustrates the strength of this interaction [54]. In contrast, the Fe–NO σ bond in these complexes is rather weak, as indicated by the corresponding antibonding MO in Fig. 23, right, which only has 3% NO contribution. The overall strength of the Fe–NO bond is reflected by the Fe–NO stretching frequencies in these complexes, which are typically observed in the 580–600 cm^{−1} range (see Sect. 3.2.1).

These properties of the Fe–NO⁺ ground state of ferric heme–nitrosyls are consistent, but lead to one puzzling question: if the Fe–NO bond is that strong in the ground state of these complexes, then why is the binding constant of NO to ferric hemes so small, making these complexes susceptible to NO loss? This apparent contradiction becomes clearly evident when the properties of ferrous and ferric heme nitrosyls are compared on the basis of either thermodynamic or spectroscopic criteria. As mentioned in Sect. 3.2 (first paragraph), experimental complex formation constants ($K_{\text{c}q}$) of ferrous compared to ferric heme–nitrosyls differ in general by four to five orders of magnitude.

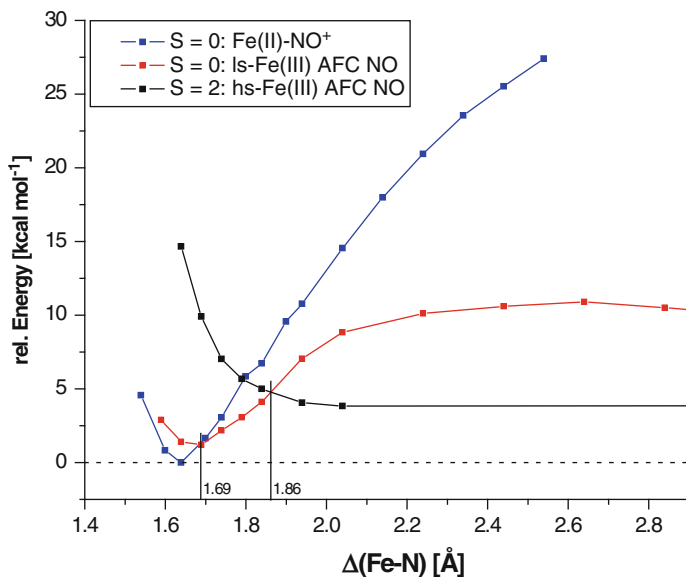


Fig. 24 Calculated potential energy surfaces for six-coordinate ferric heme–nitrosyls using the model system $[\text{Fe}(\text{P})(\text{MI})(\text{NO})]^+$ ($\text{P} = \text{porphine}^{2-}$; $\text{MI} = 1\text{-methylimidazole}$). The following states are considered: (a) closed shell $\text{Fe}(\text{II})\text{-NO}^+$ (blue); (b) low-spin (ls) $\text{Fe}(\text{III})$ antiferromagnetically coupled (AFC) to NO (open shell $S = 0$; red); and (c) high-spin (hs) $\text{Fe}(\text{III})$ antiferromagnetically coupled (AFC) to NO ($S = 2$; black) (reprinted with permission from [54]. Copyright 2008 American Chemical Society)

This translates to NO complex formation energies, ΔG° [according to (1)], that are about -15 to -16 kcal/mol for ferrous ($K_{\text{eq}} = 10^{11} - 10^{12} \text{ M}^{-1}$) versus -4 to -7 kcal/mol ($K_{\text{eq}} = 10^3 - 10^5 \text{ M}^{-1}$) for ferric heme–nitrosyls [177], and this trend is reproduced by DFT total energy calculations [54]. Therefore, the Fe–NO bond is thermodynamically much stronger in the ferrous compared to the ferric case. In contrast, the Fe–NO stretching frequency and force constant is 580 cm^{-1} and 3.92 mdyn/\AA for ferric $[\text{Fe}(\text{TPP})(\text{MI})(\text{NO})]^+$ compared to 437 cm^{-1} and 2.57 mdyn/\AA for ferrous $[\text{Fe}(\text{TPP})(\text{MI})(\text{NO})]$. This demonstrates that spectroscopically, the Fe–NO bond is stronger in the ferric compared to the ferrous case, which contradicts the observed thermodynamic trend. Hence, *NO is a weak ligand to ferric heme (from thermodynamics), but at the same time, makes a strong Fe–NO bond (from spectroscopy)*! This puzzling observation can be explained when the complete potential energy surface (PES) for the binding of NO to ferric hemes is considered [54].

4.2.1 NO Binding to Ferric Heme: A Multidimensional Problem (See [54])

Figure 24 shows the PES derived for the $\text{Fe}(\text{II})\text{-NO}^+$ ground state (blue curve, $S = 0$) of ferric heme–nitrosyls plus energy surfaces of two additional key states: the open shell singlet ls- $\text{Fe}(\text{III})\text{-NO}(\text{radical})$ alternative ground state, where low-spin (ls) $\text{Fe}(\text{III})$ is antiferromagnetically coupled to NO (red curve, $S = 0$), and the

corresponding high-spin (hs) state $\text{hs-Fe(III)-NO}(\text{radical})$ (black curve, $S = 2$), which corresponds to the product state upon dissociation of NO (since the 5C ferric heme–imidazole complex is high-spin). As evident from Fig. 24, the PES for the Fe(II)-NO^+ ground state is very steep with an estimated dissociation energy of >30 kcal/mol, which reflects the unfavorable dissociation of the complex into Fe(II) and NO^+ . Importantly, this explains the spectroscopically observed strength of the Fe–NO bond in ferric heme–nitrosyls: this is in fact a property of the Fe(II)-NO^+ ground state of these complexes.

Interestingly, the alternative ground state of ferric heme–nitrosyls, $\text{ls-Fe(III)-NO}(\text{radical})$ ($S = 0$), is observed surprisingly close in energy to the Fe(II)-NO^+ ground state (see Fig. 24). The optimized structure of the complex in this state shows again a linear Fe–NO unit, but a distinctively weaker Fe–NO bond. The DFT-calculated energy difference between the Fe(II)-NO^+ ground and the $\text{ls-Fe(III)-NO}(\text{radical})$ state is only ~ 1 kcal/mol. However, this is clearly an underestimate, as evident from the vibrational properties of the complexes, which do not indicate the presence of a low-lying excited state with a distinctively weaker Fe–NO bond close in energy to the ground state. In addition, the ground state is likely stabilized by configuration interaction (CI) via the corresponding, doubly excited electronic state within the Fe–NO π backbond. Based on these considerations, the energy surface of the Fe(II)-NO^+ ground state crosses that of the $\text{ls-Fe(III)-NO}(\text{radical})$ state at an Fe–NO distance of only about 1.70–1.76 Å, i.e., the ground state of the complex changes around that Fe–NO distance. This is accompanied by the transfer of one electron from Fe(II) back to NO^+ , forming a ls-Fe(III) center with a bound NO radical. If the dissociation of NO would be mediated by this $\text{ls-Fe(III)-NO}(\text{radical})$ state, then the predicted dissociation energy would be quite similar to that of ferrous heme–nitrosyls, so this result still cannot explain the distinctive thermodynamic weakness of the Fe–NO bond in the ferric case.

Upon a further elongation of the Fe–NO bond, the $\text{ls-Fe(III)-NO}(\text{radical})$ energy surface crosses that of the $\text{hs-Fe(III)-NO}(\text{radical})$ state ($S = 2$) at a Fe–NO distance of about 1.9 Å (see Fig. 24). This transition corresponds to a spin crossover of the iron(III) center and is related to the fact that the 5C ferric heme product is actually in the high-spin state. Importantly, *the $\text{hs-Fe(III)-NO}(\text{radical})$ energy surface is dissociative with respect to the Fe–NO bond.* This causes a dramatic drop in the thermodynamic stability of the ferric Fe–NO complex, from about -10 kcal/mol in the $\text{ls-Fe(III)-NO}(\text{radical})$ state to only about -4 kcal/mol (calculated) in the $\text{hs-Fe(III)-NO}(\text{radical})$ state. Therefore, *the properties of the $\text{hs-Fe(III)-NO}(\text{radical})$ energy surface determine the thermodynamic weakness of the Fe–NO bond in ferric heme–nitrosyls and the large dissociation rate constant of NO.* In other words, once the system is in the $\text{hs-Fe(III)-NO}(\text{radical})$ electronic state, the dissociative nature of the corresponding energy surface will actually drive the NO away from the metal center, causing a distinct increase in the NO dissociation rate compared to ferrous heme–nitrosyls. Hence, the experimentally derived Fe–NO force constant is *not* a measure for the stability of the Fe–NO bond in this case. These quantities are actually completely unrelated, because they depend on the properties of different

electronic states [54]. In this way, NO can form a strong Fe–NO bond and at the same time, be a weak ligand to a ferric heme.

4.2.2 Effect of Axial Thiolate and Other Anionic Ligand Coordination

As mentioned above, ferric heme–nitrosyls with axial imidazole or neutral N-donor coordination generally show linear Fe–N–O units. It was therefore a surprise when a bent Fe–N–O unit with an Fe–N–O angle of 161° was observed for the ferric NO adduct of fungal Cyt. P450 NO reductase via X-ray crystallography (see Fig. 18) [178]. This initial finding met some skepticism as to whether this result is real or due to an artifact, and whether the bending was induced by steric or electronic factors. The latter question was settled in 2006 when the first (and only) crystal structure of a corresponding model complex, $[\text{Fe}(\text{OEP})(\text{SR}-\text{H}_2)(\text{NO})]$, was published, which shows a similarly bent Fe–N–O unit as in the enzyme [74]. Directly analogous ferric {FeOEP} model complexes with axial imidazole coordination show linear Fe–N–O units in comparison [78]. DFT calculations further support the idea that the bending of the Fe–N–O unit in the presence of an axial thiolate ligand as well as the simultaneous weakening of the Fe–NO and N–O bonds (reflected by the corresponding vibrational stretching frequencies) are due to an electronic effect, i.e., a *trans* effect of the thiolate ligand [3, 137]. More recent work has shown that similar effects are also observed when other anionic ligands are bound *trans* to NO [81]. Hence, this is a general effect of proximal anionic ligand coordination, where the magnitude of the bending of the Fe–N–O unit and the decrease of the strength of the Fe–NO bond are directly correlated with the donor strength of the axial anionic ligand. This is nicely illustrated in Fig. 25, where trifluoroacetate (top, left) is the weakest donor with the most linear Fe–N–O unit and the strongest (shortest) Fe–NO and N–O bonds, and thiophenolate (bottom, right) is the strongest donor with the most bent Fe–N–O group and the weakest Fe–NO and N–O bonds. The calculated structures of $[\text{Fe}(\text{P})(\text{CF}_3\text{COO})(\text{NO})]$ and $[\text{Fe}(\text{P})(\text{SR}-\text{H}_2)(\text{NO})]$ are very close to the experimentally determined structures of corresponding TPP^{2-} and OEP^{2-} complexes, respectively, indicating that DFT is able to predict these properties with high accuracy [81, 137]. Further analysis of the computational results shows that the ground state of these complexes is best described as $\text{Fe}(\text{II})-\text{NO}^+$, just as in the case of the ferric heme–nitrosyls with axial imidazole or N-donor coordination [137]. Hence, the Fe–NO interaction is dominated by π backbonding between $\text{Fe}(\text{II})$ and NO^+ . However, the change in the Fe–NO bond as a function of the donor strength of an axially coordinated anionic ligand cannot correspond to a change in this π backbonding interaction, as this would lead to an inverse correlation of the Fe–NO and N–O bond strengths, and hence vibrational stretching frequencies. Figures 19 and 25 demonstrate that this is not the case, and that instead a direct correlation of the Fe–NO and N–O bond strengths (lengths) and vibrational stretching frequencies is observed. This raises the question which orbital interaction could be responsible for this curious observation.

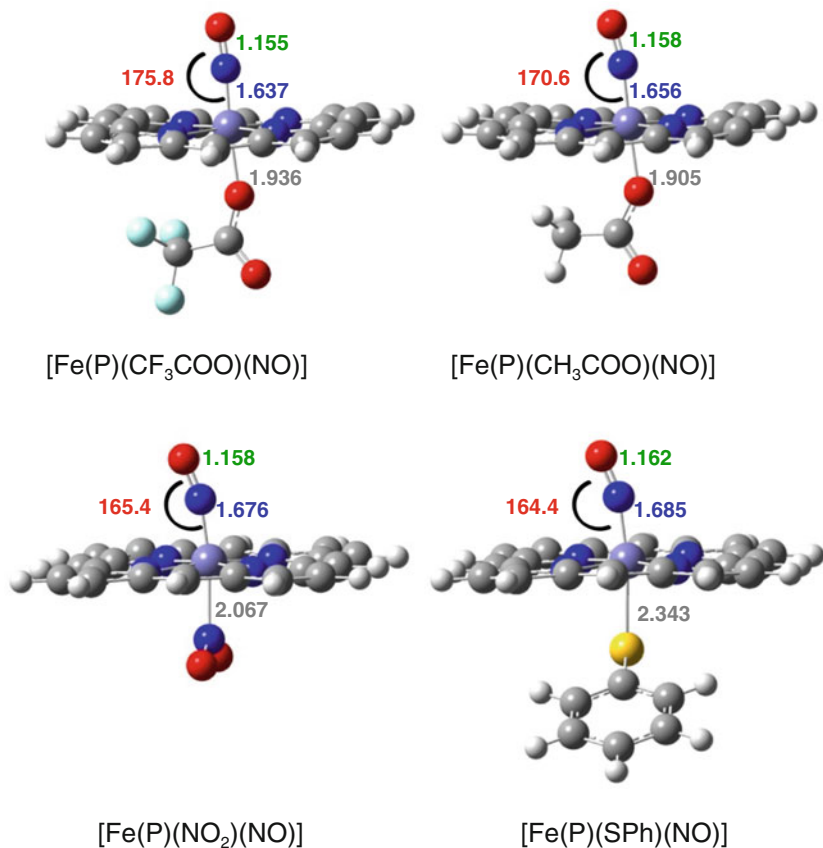


Fig. 25 BP86/TZVP calculated structures of [Fe(P)(X)(NO)] complexes (X = anionic ligand). Fe–N–O angles and Fe–NO, N–O and Fe–X bond distances are indicated. Adapted from [81]

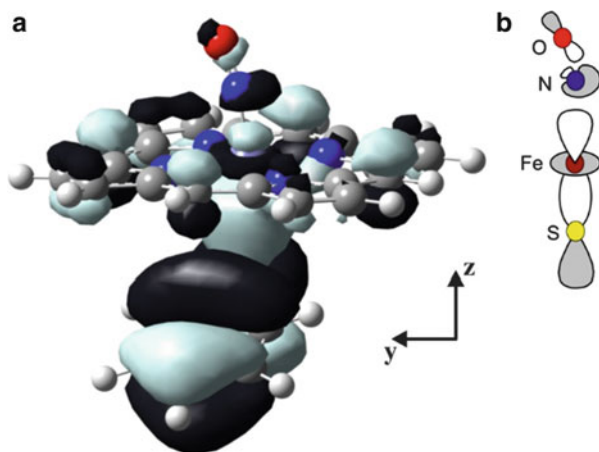


Fig. 26 Contour plot (left) and schematic drawing (right) of the key molecular orbital $A_{2u} + p_z(S)-d_{2z}-\sigma^*$ of [Fe(P)(SPh)(NO)] that illustrates the σ backbond into the σ^* orbital of the Fe–N–O subunit, mediated by the sulfur donor orbital p_z (reprinted with permission from [137]. Copyright 2007 American Chemical Society)

Detailed analysis and comparison of the obtained wavefunctions from the DFT calculations show that this effect is actually correlated to backbonding into a σ^* orbital of the Fe–N–O unit as illustrated in Fig. 26. This σ^* orbital is fully antibonding with respect to the Fe–N–O unit and normally unoccupied. However, this orbital becomes partially occupied by admixture into the occupied, low-lying σ donor orbital of the anionic *trans* ligand to NO (see Fig. 26). The stronger the σ -donor properties of the proximal ligand, i.e., the higher the corresponding donor orbital is in energy, the more pronounced this admixture becomes. An increase in occupation of this σ^* orbital via this indirect mechanism then causes an increase in the bending of the Fe–N–O unit and a concomitant weakening of the Fe–NO and N–O bonds (the latter is due to the fully Fe–N–O antibonding nature of this orbital) [137]. Analysis of the series of complexes shown in Fig. 25 further confirms this correlation [81]. Note that this unusual σ backbond into the σ^* orbital of the Fe–N–O unit, mediated by the σ -donor orbital of the anionic *trans* ligand to NO, is a new orbital interaction that has not been identified previously for any nitrosyl complexes. The biological implications of these results are discussed in the next paragraph.

4.2.3 Biological Implications

Although the electronic structure of ferric-heme nitrosyls with axial N-donor coordination had generally been considered to be of Fe(II)–NO⁺ type as described above, it was later proposed that in the nitrophorins (NO transport proteins) from *R. prolixus*, the corresponding ferric NO adducts could have an Fe(III)–NO(radical) type electronic structure [28]. However, recent investigations have shown that the Fe(III)–NO(radical) state would lead to a distinctively weaker Fe–NO bond, and lower Fe–NO and N–O stretching frequencies, whereas the spectroscopic properties of the ferric NO adducts of rNps are very similar to other {FeNO}⁶ complexes in heme proteins and model complexes [54]. Compared to experiment, it is therefore apparent that all ferric heme–nitrosyl complexes characterized so far fall into the regime of the Fe(II)–NO⁺ ground state. Calculations further show that the thermodynamic weakness of the ferric Fe–NO bond is not a property of the ground state of these complexes, but relates to the presence of the low-lying hs-Fe(III)–NO(radical) state, which is dissociative with respect to the Fe–NO bond. Hence, ferric heme–nitrosyls are intrinsically labile, since it can be expected that this hs state will always be present at low energy in these systems. This result is highly significant for the function of the NO transporter proteins mentioned above, but also NO producing enzymes such as NOS and heme *cd*₁ NIRs, since in all of these cases the enzyme–product complex corresponds to a ferric heme–nitrosyl. Without this lability of the ferric Fe–NO bond, these systems would not be able to efficiently release NO from their active sites, hence rendering these NO transporting and generating proteins inactive [3].

This is also true for complexes with bound axial anionic ligands like carboxylates, thiolates, and phenolates. However, in these cases an interesting σ -*trans* interaction

Table 5 Half wave potentials (in V versus Fc/Fc^+) for the one-electron reduction of ferrous porphyrin nitrosyl model complexes ($\text{Fc}/\text{Fc}^+ = 624 \text{ mV}$ versus SHE)

Complex	Solvent	$\{\text{FeNO}\}^7/\{\text{FeNO}\}^8$	References
$[\text{Fe}(\text{OEP})(\text{NO})]$	CH_2Cl_2	-1.59	[179]
$[\text{Fe}(3,5\text{-Me-BAFP})(\text{NO})]$	THF	-1.78	[64]
$[\text{Fe}(\text{To-F}_2\text{TPP})(\text{NO})]$	1,2-DCE	-1.18	[64]
$[\text{Fe}(\text{To}-(\text{NO}_2)_2\text{-}p\text{-}t\text{BuPP})(\text{NO})]$	1,2-DCE	-1.18	[64]
$[\text{Fe}(\text{TPP})(\text{NO})]$	CH_2Cl_2	-1.42	[179]
	THF	-1.47	[179]
$[\text{Fe}(\text{Tper-F}_5\text{TPP})(\text{NO})]$	1,2-DCE	-1.13	[64]
$[\text{Fe}(\text{TFPPBr}_8)(\text{NO})]$	CH_2Cl_2	-0.65	[180]

is observed that leads to a further weakening of the Fe–NO bond and a bending of the Fe–N–O unit. This explains the puzzling observations with respect to the geometric structures of ferric NO adducts in Cyt. P450s. The biological significance of this *trans* interaction lies in the observed further weakening of the Fe–NO bond. In NOS, oxidation of L-Arg generates the NO-bound ferric heme as the enzyme–product complex. In this sense, the presence of the axial thiolate helps to ensure a rapid release of NO. These aspects are discussed in detail in [3].

Finally, the presence of the proximal cysteinate ligand is crucial for the mechanism of fungal Cyt. P450 NOR [126]. This aspect is further discussed in Sect. 6.1.

5 Ferrous Heme–Nitroxyl Complexes

Ferrous heme–nitroxyl complexes, $\{\text{FeNO}\}^8$, are the one-electron reduced forms of ferrous heme–nitrosyls. These species have been proposed to be key intermediates in NO and nitrite reductase chemistry as discussed further in Sect. 6. In addition, in the light of the emerging biological role of HNO (the protonated form of the nitroxyl anion) [30, 31], the interaction of ferrous hemes with HNO has become of increasing interest. A number of corresponding $\{\text{FeNO}\}^8$ model complexes have been prepared, and in addition, the HNO adduct of ferrous Mb has been reported in the literature. This section provides a brief summary of the properties of these important species.

In model complexes, the unprotonated $\{\text{FeNO}\}^8$ species can be generated in a straightforward way from the corresponding ferrous heme–nitrosyls using electrochemical techniques. However, this requires very negative potentials as shown in Table 5. The only exception is the complex $[\text{Fe}(\text{TFPPBr}_8)(\text{NO})]$, which is substituted by a large number of electron withdrawing groups.

In initial studies, Kadish and coworkers demonstrated the reversible one-electron reduction of 5C ferrous heme–nitrosyls via UV–vis spectroelectrochemistry, utilizing TPP^{2-} and OEP^{2-} ligands, to generate the corresponding $\text{Fe}(\text{II})\text{-NO}^-$ complexes [179, 181]. Ryan and coworkers reported additional vibrational characterization of both $[\text{Fe}(\text{TPP})(\text{NO})]^-$ and $[\text{Fe}(\text{OEP})(\text{NO})]^-$ and related compounds [161, 182]. Finally, using the extremely electron withdrawing porphyrin $\text{H}_2\text{TFPPBr}_8$,

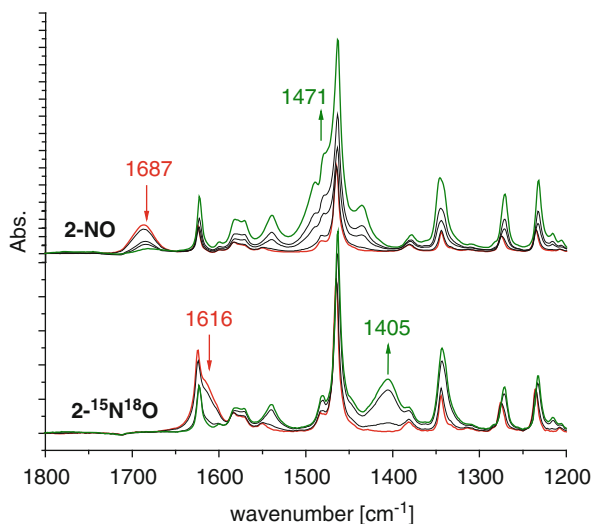
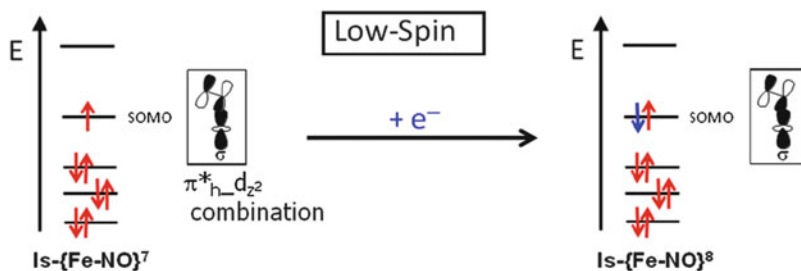


Fig. 27 Infrared spectra for the spectroelectrochemical reduction of $[\text{Fe}(\text{To-F}_2\text{PP})(\text{NO})]$ (*top*, natural abundance isotopes) and $[\text{Fe}(\text{To-F}_2\text{PP})(^{15}\text{N}^{18}\text{O})]$ (*bottom*) [64]



Scheme 3

Doctorovich and coworkers were able to isolate the corresponding 5C Fe(II)–NO[−] species, obtained by electrochemical or chemical reduction of the Fe(II)–NO starting material [180, 183]. As illustrated in Fig. 22, the one-electron reduction of the {FeNO}⁷ complexes causes a distinct drop in the N–O stretching frequency from 1,670–1,700 cm^{−1} to about 1,440–1,500 cm^{−1} in the {FeNO}⁸ products, which can be easily followed by spectroelectrochemical methods as illustrated in Fig. 27 for $[\text{Fe}(\text{To-F}_2\text{TPP})(\text{NO})]$ [64]. As discussed in detail in Sect. 4.1.2, the one-electron reduction of low-spin ferrous heme–nitrosyls essentially leads to a double occupation of the SOMO of the {FeNO}⁷ starting material as illustrated in Scheme 3. In the 5C case, the SOMO corresponds to the very covalent interaction between π^*_h and d_{2^2} (see above), and hence the resulting {FeNO}⁸ complex, formally of Fe(II)–NO[−] type, has an electronic structure that can be considered intermediate between Fe(II)–NO[−] and Fe(I)–NO [126]. Since the addition of one electron to the SOMO of the {FeNO}⁷ complexes

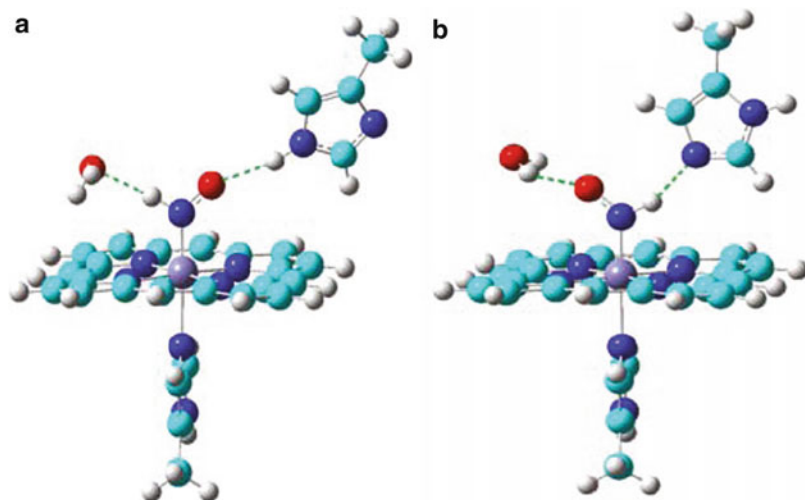


Fig. 28 Computational models for the Mb(II)–HNO adduct, showing two possibilities for the proposed, dual hydrogen bonding network of the coordinated HNO ligand (reprinted with permission from [188]. Copyright 2011 American Chemical Society)

causes a strengthening of the Fe–NO σ bond (as indicated by an increase of the *trans* effect of NO [64]), but also a loss of π backbonding and an increase in Coulomb repulsion between the doubly occupied π^* orbital of the bound ${}^1\text{NO}^-$ ligand and the occupied d_{xz} orbital of iron (in the coordinate system applied in Scheme 1), one would expect that the strength of the Fe–NO bond should only show small changes in $\{\text{FeNO}\}^7$ versus $\{\text{FeNO}\}^8$ complexes. This was confirmed by Ryan and coworkers, who identified the Fe–NO stretch of $[\text{Fe}(\text{TPP})(\text{NO})]^-$ at 525 cm^{-1} [161], close to the value of 532 cm^{-1} in $[\text{Fe}(\text{TPP})(\text{NO})]$ [69]. Unfortunately, all efforts to prepare the corresponding HNO complexes by treatment of the $\{\text{FeNO}\}^8$ model systems with acid failed, as this leads to disproportionation of the putative HNO complexes, generating the ferrous heme–nitrosyl starting materials plus H_2 [64, 161, 180].

So far, ferrous heme–HNO complexes could only be prepared in heme proteins, most famously by Farmer and coworkers in Mb via both reaction of deoxy-Mb with HNO donors, or by one-electron reduction of the Mb(II)–NO complex [184, 185]. The reduction potential for the Mb–NO adduct is about -650 mV versus NHE [186], which is at the borderline for biological systems [187]. Correspondingly, strong reductants like Cr(II) compounds are needed in order to effect the formation of the Mb(II)–HNO complex. Compared to the model complexes with TPP^{2-} and OEP^{2-} ligands, the reduction potential of the Mb(II)–NO species can be estimated to be several hundreds of millivolts more positive, in the range of the fluorinated complex $[\text{Fe}(\text{To-F}_2\text{TPP})(\text{NO})]$. The reason for this shift of the reduction potential of Mb(II)–NO toward positive values is likely the coupling of the reduction of this species to a proton transfer, leading directly to the generation of the HNO complex. This also indicates that the Fe(II)– NO^- species is very basic and easily picks up a proton, as predicted by DFT calculations [126]. Once formed, the Mb(II)–HNO

complex is very stable in solution [184], indicating that HNO is strongly coordinated to the ferrous heme center of Mb. Recent computational studies present evidence that this unexpected stability could also be due to a dual hydrogen bond formation where the coordinated HNO ligand acts both as a hydrogen bond donor and acceptor (involving the distal His and a nearby water molecule) as shown in Fig. 28 [188].

Although a crystal structure of the Mb(II)–HNO adduct is not available, extended spectroscopic characterization of this species by $^1\text{H-NMR}$, X-ray absorption, and resonance Raman spectroscopy has elucidated the geometric and electronic properties of this complex in detail [189, 190]. These results show that the Fe(II)–HNO complex is clearly N-protonated. This species exhibits Fe–NO and N–O stretching frequencies of 651 and $1,385\text{ cm}^{-1}$, respectively. Computational results further demonstrate that this N–O stretching frequency is also indicative of N-protonation of the bound nitroxyl ligand [126].

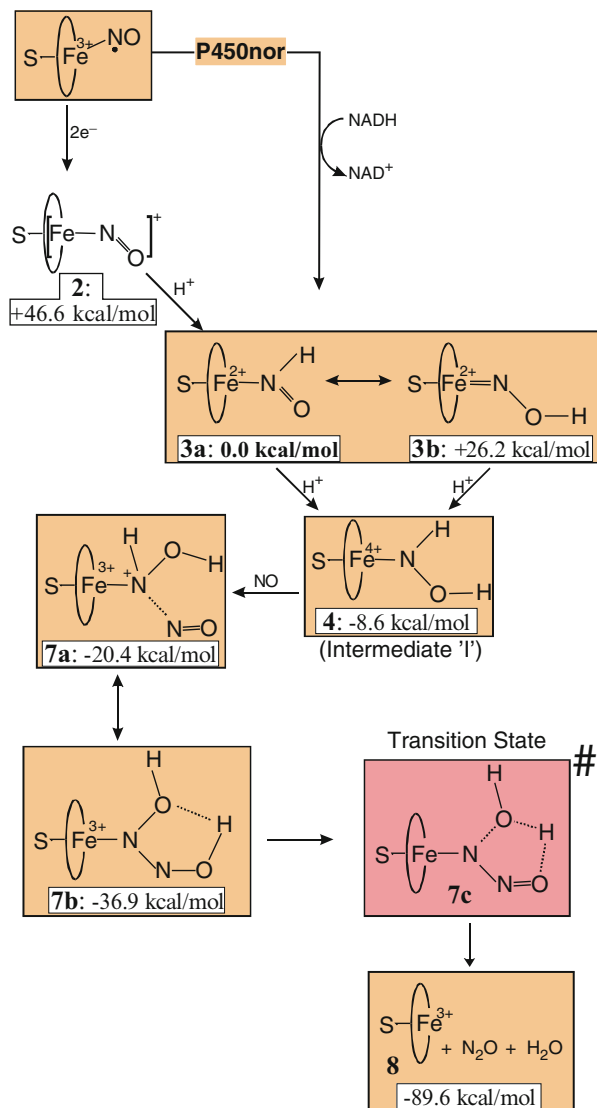
HNO itself is a weak σ -donor to a ferrous heme and acts mostly as a π backbonding ligand [42, 126, 191]. This has important implications with respect to recent proposals that HNO is able to activate sGC in a similar way as NO, i.e., by binding to the 5C ferrous heme in the sensor domain of this protein [192]. However, while NO is a strong σ -donor and hence binding of NO leads to a great labilization of the *trans* Fe–His bond (see above), recent computational work has shown that this is not the case for HNO [42]. These studies demonstrate that HNO behaves more similarly to CO and should therefore not be able to activate sGC to any significant degree via binding to its heme site [156].

6 Heme–Nitrosyl Complexes as Intermediates in Enzyme Catalysis: New Computational Insight

6.1 Fungal Nitric Oxide Reductase

In fungal cytochrome P450 NOR (P450nor), it has been shown that a ferric heme–nitrosyl complex is the first intermediate of catalysis. Experimentally, this species is then reduced by direct hydride transfer from NADH, leading to the generation of Intermediate I [193], which finally reacts with a second molecule of NO to generate N_2O [3, 24]. Following computational studies further refined the mechanistic picture as shown in Fig. 29 [126]. Direct hydride transfer to the bound NO in the ferric heme–nitrosyl complex generates a ferrous nitroxyl intermediate, which is N-protonated (species **3a** in Fig. 29). The analogous O-protonated form is 26 kcal/mol higher in energy and hence, energetically unfeasible. Importantly, the presence of the axial thiolate ligand increases the basicity of the bound HNO ligand: while in the Mb case, the Fe(II)–HNO complex is stable as described in Sect. 5, the computational results indicate that the proximal Cys ligand increases the basicity of the bound HNO ligand and leads to a further protonation of this species, generating a formally Fe(IV)–NHOH $^-$ complex. This species is identified as Intermediate I (species **4** in Fig. 29; see also [194]), which is reactive toward a second NO

Fig. 29 Proposed mechanism of Cyt. P450nor based on DFT calculations. Free energies, ΔG , are given relative to complex **3a** (set to 0.0 kcal/mol) (reprinted with permission from [42]. Copyright 2010 American Chemical Society)



molecule. This reaction can be envisioned as a two-step process where first the incoming NO reduces the Fe(IV) center, followed by addition of the generated NO^+ molecule to the N-atom of the bound NHOH-ligand, generating the N–N bond. Further tautomerism generates the relatively stable hyponitrite complex **7b**, which finally decomposes to N_2O and a water molecule. This mechanism is shown in Fig. 29 [126].

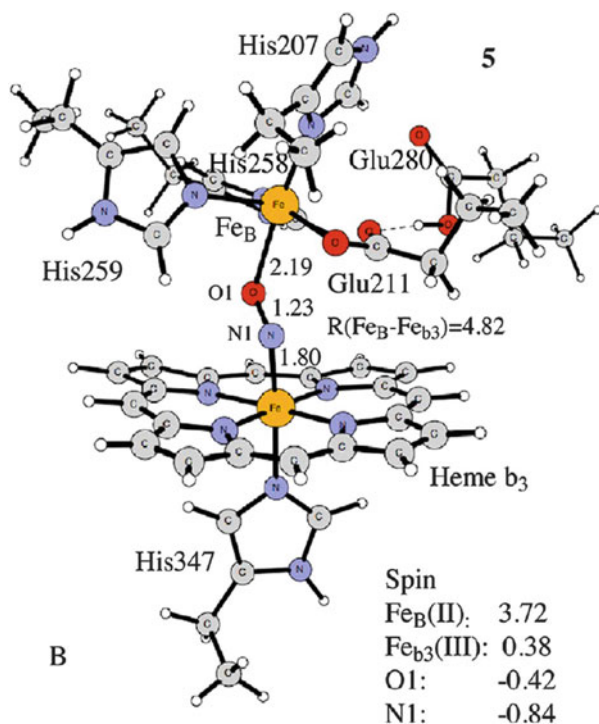
Most recently, Riplinger and Neese have reported large-scale QM/MM calculations on Cyt. P450nor [52]. In particular, they investigated the question whether the HNO or the corresponding protonated NHOH complex is more reactive

toward the second NO molecule in order to predict which one of these species would more likely correspond to the reactive Intermediate I. Their results have clarified further details of the mechanism of this enzyme. First, it is shown that the doubly protonated species is more reactive toward NO and therefore likely corresponds to Intermediate I as previously proposed. Importantly, the authors further evaluated different electronic descriptions of this species and concluded that Intermediate I is best described as Fe(III)–NHOH(radical) complex. This changes the mechanistic scenario for the following reaction with the second NO molecule, which should then be considered a radical recombination reaction that is responsible for N–N bond formation. Finally, in the QM/MM calculations the formed hyponitrite species does not remain bound to the ferric heme center, but dissociates into the heme active site pocket prior to spontaneous decomposition into N_2O and H_2O . This result from the QM/MM treatment is certainly surprising and contrasts the previous findings shown in Fig. 29. In summary, the combination of the experimental results for P450nor with the computational findings described in this section provides a very detailed picture of the mechanism of this enzyme, with only a few issues remaining to be resolved. Cyt. P450nor therefore constitutes the paradigm of how NO can be bound and activated by a single heme center.

6.2 Bacterial Nitric Oxide Reductase

In contrast to the detailed mechanistic insight accomplished for Cyt. P450nor, the mechanism of the respiratory bacterial NO reductase (NorBC) is much less understood [3, 22, 169]. The active site of this enzyme contains a His-ligated heme b_3 with a non-heme iron center (called Fe_B) in close proximity [23]. Initially, a *trans*-type mechanism was proposed, where both the ferrous heme and the non-heme iron center would bind one molecule of NO each, followed by radical coupling of the NO ligands to form the N–N bond and generate a hyponitrite intermediate [167]. As discussed in Sect. 4.1.5, although 6C ferrous heme–nitrosyls have the appropriate electronic structure for this type of radical reactivity, they do not spontaneously dimerize or couple with free NO, and hence, this reaction does not seem feasible for ferrous heme–nitrosyls. This is likely related to the fact that these species are thermodynamically very stable. In addition, ferrous non-heme iron–nitrosyls have an electronic structure best described as hs Fe(III) with a bound triplet NO^- , and hence, their electronic structure does not support the idea of a radical-type N–N bond formation [168]. Based on these considerations, and inspired by the mechanism of P450nor, researchers started to focus their attention on so-called *cis*-type mechanisms where one of the iron centers (either the heme or the non-heme iron) would bind one molecule of NO, which could then become activated, for example by reduction, before reaction with the second NO molecule occurs. Computational results by Yi, Shen, and Richter-Addo and coworkers suggest that a ferrous heme–nitrosyl only becomes reactive toward a second NO molecule if one additional electron and one proton are available [195]. In their DFT results, this leads to the formation of a ferric

Fig. 30 Computational model of the differerous form of the active site of NorBC with one NO molecule bound, which (in this proposed mechanism) bridges between the two metal centers. Spin densities and bond lengths are indicated (reprinted with permission from [51]. Copyright 2012 American Chemical Society)



hyponitrite species that closely resembles species **7b** in Fig. 29, except that the hyponitrite is only singly protonated. Transferring these findings back to NorBC would implicate a mechanistic picture where one NO would be bound to the ferrous heme center, followed by one-electron reduction (and potentially protonation) of the bound NO by electron transfer from the Fe_B site, and subsequent reaction with the second NO molecule. This scenario corresponds closely to the *cis*-heme *b₃* mechanism proposed previously for NorBC [22]. However, there is a key problem with this mechanism: as discussed in Sect. 5, the one-electron reduction of a ferrous heme–nitrosyl (even if coupled to a proton transfer) requires very negative potentials that are outside of the available redox potentials for the cofactors in NorBC. In particular, the Fe_B center seems to have a very positive redox potential [3, 196], which contradicts the idea that the ferrous Fe_B center could reduce the heme *b₃* NO adduct in the NorBC active site.

Recent DFT results by Blomberg and Siegbahn show a potential pathway how a *cis*-heme *b₃* type mechanism could nevertheless be achieved by utilizing the Fe_B site directly [51]. Here, the idea is that the first NO would bind to the ferrous heme *b₃* site in a way that it bridges to the ferrous Fe_B center, which coordinates to the O-atom of the NO molecule. The resulting structure is shown in Fig. 30. The polarization of the bridging NO ligand by the Fe_B center is proposed to induce an electronic structure that is of (heme)Fe(III)–NO[−] type, which makes this species reactive toward the second NO molecule. Note that such a polarization of a heme-bound NO molecule in

the presence of a divalent cation in close proximity has recently been reported (see Sect. 3.1.3) [119]. In this case, a second metal binding site has been engineered into the Mb active site to generate a model for NorBC. When NO is bound to the heme in the presence of Fe(II) or Zn(II), a drop of the N–O stretching frequency to $\sim 1,550\text{ cm}^{-1}$ is observed, indicating that the ferrous heme–nitrosyl complex adopts some Fe(III)–NO[−] character in the ground state. However, it is not clear whether the NO ligand bridges between the metal centers in this case, and whether the observed polarization of the heme-bound NO leads to an activation of this ligand. In the mechanism proposed by Blomberg and Siegbahn, the bridging NO complex in Fig. 30 reacts directly with the second NO molecule (without any protons required) to form a *cis*-hyponitrite intermediate that is coordinated with both O-atoms to the resulting ferric Fe_B center [51]. This species decomposes by release of N₂O, forming the diferric oxo-bridged form of the active site.

An alternative to this scenario would be a *cis*-Fe_B mechanism, where the first NO molecule binds to the Fe_B center instead of the heme [22]. This opens up a number of mechanistic possibilities as discussed in [169], for example a reduction of the ferrous Fe_B–NO complex by the heme *b*₃. At least in terms of the reduction potentials of ferrous heme versus non-heme iron–nitrosyls, this would be a much more feasible possibility [168]. Further work is necessary to fully elucidate the mechanism of NorBC.

6.3 *Multiheme Cytochrome c Nitrite Reductase*

Multiheme Cyt. *c* NIRs catalyze the six-electron reduction of nitrite to ammonia without the release of any detectable intermediates [197, 198]. Due to the large number of hemes present in these enzymes, it is very challenging to obtain experimental insight into their molecular mechanism [199]. It is thought that the first step of the reaction after binding of nitrite corresponds to the reduction of nitrite to NO, as observed for heme *cd*₁ NIRs and deoxy-Mb/Hb [3], generating a ferric heme–nitrosyl, {FeNO}⁶, intermediate. The further reduction of this species will then generate a ferrous heme–nitrosyl, {FeNO}⁷, as the next intermediate. However, generation of this species is problematic, as ferrous heme–nitrosyls are notoriously stable and unreactive, which is an underlying theme of this review. For example, in P450_{nor} the generation of a ferrous heme–nitrosyl is specifically avoided by direct two-electron reduction (via hydride transfer) of the corresponding {FeNO}⁶ intermediate (see above and Fig. 29). However, it seems that electron transfer in multiheme CcNIR occurs in one-electron steps [200], which makes the generation of a ferrous heme–nitrosyl as an intermediate unavoidable. Since ferrous heme–nitrosyls cannot be protonated, the next step of the reaction has to be another one-electron reduction to afford a ferrous heme–nitroxyl, {FeNO}⁸, level intermediate, which is likely protonated. As described in Sect. 5, the reduction of an {FeNO}⁷ complex to generate an Fe(II)–HNO species is challenging and requires very negative potentials. Recent DFT calculations by Bykov and Neese using an extended model of the enzyme's active site provide further ideas of how this reduction step could be mediated by CcNIRs [53].

The results from these calculations indicate that the unfavorable reduction energy of the $\{\text{FeNO}\}^7$ complex can be compensated by simultaneous proton transfer to amino acid side chains in the enzyme's active site. The energy gain from the protonation of the amino acid side chains then offsets the energetic "punishment" for reducing the $\{\text{FeNO}\}^7$ species. This is an interesting concept that provides a general strategy for enzymes to overcome unfavorable reduction reactions by proton-coupled electron-transfer (PCET) that involves not only the heme complex but also amino acid side chains of the active site. Further work is clearly necessary to better understand the complex reaction mechanism of CcNIRs.

7 Conclusions

Due to the extraordinary significance of nitric oxide in biological systems as a signaling molecule, immune defense (antimicrobial) agent and metabolite/intermediate in the global nitrogen cycle, the coordination chemistry of hemes with NO and its derivatives remains a primary research target, despite the fact that this topic has been studied for more than 30 years. Much progress has been made in our understanding of the geometric and electronic structures of ferrous and ferric heme–nitrosyls as a function of the properties of the heme, the *trans* ligand to NO, and the environment of the heme in a protein active site, and the recent developments are summarized in this review. A very good understanding of the properties of these systems has now been achieved, and this forms the basis for elucidating the roles that these species play in biology. Current research efforts focus on ferrous heme–nitroxyl complexes, the properties and reactivities of which are less well understood compared to their ferrous and ferric heme counterparts. In addition, in the light of the potential roles of HNO in biology, the interaction of this molecule with metal sites is a topic of strong current interest. Finally, current research efforts are focused on the elucidation of enzyme reaction mechanisms that involve NO and its derivatives, which is heavily based on computational methods. It can be expected that key breakthroughs in our mechanistic understanding of NO and (multielectron) nitrite reductases, NO – nitrite interconversions in mammals, and of multielectron oxidases that involve ammonia and hydroxylamine will be achieved in the coming years.

References

1. Kadish KM, Smith KM, Guillard R (2011) The handbook of porphyrin science. World Scientific, Hackensack
2. Cheng L, Richter-Addo GB (2000) Binding and activation of nitric oxide by metalloporphyrins and heme. In: Kadish KM, Smith KM, Guillard R (eds) The porphyrin handbook. Academic, New York, Vol. 4, p 219
3. Lehnert N, Berto TC, Galinato MGI, Goodrich LE (2011) The role of heme-nitrosyls in the biosynthesis, transport, sensing, and detoxification of nitric oxide (NO) in biological systems:

- enzymes and model complexes. In: Kadish KM, Smith KM, Guilard R (eds) *The handbook of porphyrin science*. World Scientific, Hackensack, Vol. 14, p 1
4. Stuehr DJ (1997) *Annu Rev Pharmacol Toxicol* 37:339
 5. Li H, Poulos T (2005) *J Inorg Biochem* 99:293
 6. Rousseau DL, Li D, Couture M, Yeh S-R (2005) *J Inorg Biochem* 99:306
 7. Martin NI, Woodward JJ, Winter MB, Beeson WT, Marletta MA (2007) *J Am Chem Soc* 129:12563
 8. Gorren ACF, Mayer B (2007) *Biochem Biophys Acta* 1770:432
 9. Cary SPL, Winger JA, Derbyshire ER, Marletta MA (2006) *Trends Biochem Sci* 31:231
 10. Boon EM, Marletta MA (2005) *Curr Opin Chem Biol* 9:441
 11. Galinato MGI, Fogle RS, III (2012) *Trends Inorg Chem* 13:1–22
 12. Averill BA (1996) *Chem Rev* 96:2951
 13. Cosby K, Partovi KS, Crawford JH, Patel RP, Reiter CD, Martyr S, Yang BK, Waclawiw MA, Zalos G, Xu X, Huang KT, Shields H, Kim-Shapiro DB, Schechter AN, Cannon RO, Gladwin MT (2003) *Nat Med* 9:1498
 14. Gladwin MT, Grubina R, Doyle MP (2009) *Acc Chem Res* 42:157
 15. Castello PR, Woo DK, Ball K, Wojcik J, Liu L, Poyton RO (2008) *Proc Natl Acad Sci USA* 105:8203
 16. Castello P, David P, McClure T, Crook Z, Poyton R (2006) *Cell Metab* 3:277
 17. Fukuda R, Zhang H, Kim JW, Shimoda L, Dang CV, Semenza GL (2007) *Cell* 129:111
 18. Gardner PR (2005) *J Inorg Biochem* 99:247
 19. Su J, Groves JT (2010) *Inorg Chem* 49:6317
 20. Su J, Groves JT (2009) *J Am Chem Soc* 131:12979
 21. Kurtikyan TS, Eksuzyan SR, Hayrapetyan VA, Martirosyan GG, Hovhannisyan GS, Goodwin JA (2012) *J Am Chem Soc* 134:13861
 22. Zumft WG (2005) *J Inorg Biochem* 99:194
 23. Hino T, Matsumoto Y, Nagano S, Sugimoto H, Fukumori Y, Murata T, Iwata S, Shiro Y (2010) *Science* 330:1666
 24. Daiber A, Shoun H, Ullrich V (2005) *J Inorg Biochem* 99:185
 25. Ruggiero CE, Carrier SM, Tolman WB (1994) *Angew Chem Int Ed Engl* 33:895
 26. Franz KJ, Lippard SJ (1998) *J Am Chem Soc* 120:9034
 27. Merkle AC, Lehnert N (2012) *Dalton Trans* 41:3355
 28. Walker FA (2005) *J Inorg Biochem* 99:216
 29. Bianchetti CM, Blouin GC, Bitto E, Olson JS (2010) *Proteins* 78:917
 30. Miranda KM (2005) *Coord Chem Rev* 249:433
 31. Doctorovich F, Bikiel D, Pellegrino J, Suárez SA, Larsen A, Martí MA (2011) *Coord Chem Rev* 255:2764
 32. Wyllie GRA, Scheidt WR (2002) *Chem Rev* 102:1067
 33. Ford PC, Lorkovic IM (2002) *Chem Rev* 102:993
 34. Wasser IM, de vries S, Moëne-Loccoz P, Schröder I, Karlin KD (2002) *Chem Rev* 102:1201
 35. Ford PC, Laverman LE (2005) *Coord Chem Rev* 249:391
 36. Walker FA, Simonis U (2005) *Iron porphyrin chemistry*. In: King RB (ed) *Encyclopedia of inorganic chemistry*, 2nd edn. Wiley, Chichester, p 2390
 37. Ghosh A (2005) *J Inorg Biochem* 99:1
 38. Roncaroli F, Videla M, Slep LD, Olabe JA (2007) *Coord Chem Rev* 251:1903
 39. Franke A, Roncaroli F, van Eldik R (2007) *Eur J Inorg Chem* 773
 40. Lehnert N, Scheidt WR (2010) *Inorg Chem* 49:6223
 41. Ghosh Dey S, Dey A (2011) *Dalton Trans* 40:12633
 42. Goodrich LE, Paulat F, Praneeth VKK, Lehnert N (2010) *Inorg Chem* 49:6293
 43. Ghosh A, Hopmann KH, Conradie J (2009) *Electronic structure calculations: transition metal–NO complexes*. In: Solomon EI, King RB, Scott RA (eds) *Computational inorganic and bioinorganic chemistry*. Wiley, Chichester
 44. Silvernail NJ, Olmstead MM, Noll BC, Scheidt WR (2009) *Inorg Chem* 48:971

45. Silvernail NJ, Pavlik JW, Noll BC, Schulz CE, Scheidt WR (2008) *Inorg Chem* 47:912
46. Silvernail NJ, Barabanschikov A, Sage JT, Noll BC, Scheidt WR (2009) *J Am Chem Soc* 131: 2131
47. Xu N, Campbell ALO, Powell DR, Khandogin J, Richter-Addo GB (2009) *J Am Chem Soc* 131:2460
48. Radoul M, Sundararajan M, Potapov A, Riplinger C, Neese F, Goldfarb D (2010) *Phys Chem Chem Phys* 12:7276
49. Gunn A, Derbyshire ER, Marletta MA, Britt RD (2012) *Biochemistry* 51:8384
50. Lehnert N, Sage JT, Silvernail NJ, Scheidt WR, Alp EE, Sturhahn W, Zhao J (2010) *Inorg Chem* 49:7197
51. Blomberg MRA, Sieghahn PEM (2012) *Biochemistry* 51:5173
52. Riplinger C, Neese F (2011) *Chemphyschem* 12:3192
53. Bykov D, Neese F (2012) *J Biol Inorg Chem* 17:741
54. Praneeth VKK, Paulat F, Berto TC, DeBeer George S, Näther C, Sulok CD, Lehnert N (2008) *J Am Chem Soc* 130:15288
55. Scheidt WR, Ellison MK (1999) *Acc Chem Res* 32:350
56. Scheidt WR, Reed CA (1981) *Chem Rev* 81:543
57. Scheidt WR, Frisse ME (1975) *J Am Chem Soc* 97:17
58. Ellison MK, Scheidt WR (1997) *J Am Chem Soc* 119:7404
59. Scheidt WR, Duval HF, Neal TJ, Ellison MK (2000) *J Am Chem Soc* 122:4651
60. Wyllie GRA, Scheidt WR (2003) *Inorg Chem* 42:4259
61. Nasri H, Haller KJ, Wang Y, Hyunh BH, Scheidt WR (1992) *Inorg Chem* 31:3459
62. Cheng L, Powell DR, Khan MA, Richter-Addo GB (2000) *Chem Commun* 2301
63. Wang J, Schopfer MP, Sarjeant AAN, Karlin KD (2009) *J Am Chem Soc* 131:450
64. Goodrich LE, Saikat R, Alp EE, Zhao J, Hu MY, Lehnert N (submitted)
65. Scheidt WR, Piciulo PL (1976) *J Am Chem Soc* 98:1913
66. Scheidt WR, Brinegar AC, Ferro EB, Kirner JF (1977) *J Am Chem Soc* 99:7315
67. Wyllie GRA, Schulz CE, Scheidt WR (2003) *Inorg Chem* 42:5722
68. Nasri H, Ellison MK, Huynh BH, Scheidt WR (1997) *J Am Chem Soc* 119:6274
69. Praneeth VKK, Näther C, Peters G, Lehnert N (2006) *Inorg Chem* 45:2795
70. Rath SP, Koerner R, Olmstead MM, Balch AL (2003) *J Am Chem Soc* 125:11798
71. Scheidt WR, Lee YJ, Hatano K (1984) *J Am Chem Soc* 106:3191
72. Ellison MK, Schulz CE, Scheidt WR (2000) *Inorg Chem* 39:5102
73. Linder DP, Rodgers KR, Banister J, Wyllie GRA, Ellison MK, Scheidt WR (2004) *J Am Chem Soc* 126:14136
74. Xu N, Powell DR, Cheng L, Richter-Addo GB (2006) *Chem Commun* 2030
75. Richter-Addo GB, Wheeler RA, Hixson CA, Chen L, Khan MA, Ellison MK, Schulz CE, Scheidt WR (2001) *J Am Chem Soc* 123:6314
76. Ellison MK, Schulz CE, Scheidt WR (1999) *Inorg Chem* 38:100
77. Ellison MK, Schulz CE, Scheidt WR (2002) *J Am Chem Soc* 124:13833
78. Ellison MK, Scheidt WR (1999) *J Am Chem Soc* 121:5210
79. Yi G-B, Chen L, Khan MA, Richter-Addo GB (1997) *Inorg Chem* 36:3876
80. Xu N, Powell DR, Richter-Addo GB (2011) *Angew Chem Int Ed* 50:9694
81. Xu N, Goodrich LE, Lehnert N, Powell DR, Richter-Addo GB (2013) *Angew Chem Int Ed* 52: asap (available online)
82. Scheidt WR, Hoard JL (1973) *J Am Chem Soc* 95:8281
83. Ellison MK, Scheidt WR (1998) *Inorg Chem* 37:382
84. Godbout N, Sanders LK, Salzmann R, Havlin RH, Wojdelski M, Oldfield E (1999) *J Am Chem Soc* 121:3829
85. Grande LM, Noll BC, Oliver AG, Scheidt WR (2010) *Inorg Chem* 49:6552
86. Scheidt WR, Hatano K, Rupprecht GA, Piciulo PL (1979) *Inorg Chem* 18:292
87. Zahran ZN, Jonghyuk L, Alguindigue SS, Khan MA, Richter-Addo GB (2004) *Dalton Trans* 44

88. Henry YA, Guissani A, Ducastel B (1997) Nitric oxide research from chemistry to biology: EPR spectroscopy of nitrosylated compounds. Landes Company, Austin
89. Lehnert N (2008) Electron paramagnetic resonance and low-temperature magnetic circular dichroism spectroscopy of ferrous heme nitrosyls. In: Ghosh A (ed) The smallest biomolecules: diatomics and their interactions with heme proteins. Elsevier, Amsterdam, p 147
90. Hayes RG, Ellison MK, Scheidt WR (2000) *Inorg Chem* 39:3665
91. Praneeth VKK, Neese F, Lehnert N (2005) *Inorg Chem* 44:2570
92. Patchkovskii S, Ziegler T (2000) *Inorg Chem* 39:5354
93. Berto TC, Praneeth VKK, Goodrich LE, Lehnert N (2009) *J Am Chem Soc* 131:17116
94. Utterback SG, Doetschman DC, Szumowski J, Rizos AK (1983) *J Chem Phys* 78:5874
95. Praneeth VKK, Haupt E, Lehnert N (2005) *J Inorg Biochem* 99:940
96. Radoul M, Bykov D, Rinaldo S, Cutruzzola F, Neese F, Goldfarb D (2011) *J Am Chem Soc* 133:3043
97. Neese F (2004) *Magn Reson Chem* 42:S187
98. Hori H, Ikeda-Saito M, Yonetani T (1981) *J Biol Chem* 256:7849
99. Morse RH, Chan SI (1980) *J Biol Chem* 255:7876
100. Copeland DM, Soares AS, West AH, Richter-Addo GB (2006) *J Inorg Biochem* 100:1413
101. Spiro TG, Ibrahim M, Wasbotten IH (2008) CO, NO, and O₂ as vibrational probes of heme protein active sites. In: Ghosh A (ed) The smallest biomolecules: diatomics and their interactions with heme proteins. Elsevier, Amsterdam, p 95
102. Vogel KM, Kozłowski PM, Zgierski MZ, Spiro TG (1999) *J Am Chem Soc* 121:9915
103. Lehnert N, Galinato MGI, Paulat F, Richter-Addo GB, Sturhahn W, Xu N, Zhao J (2010) *Inorg Chem* 49:4133
104. Leu BM, Zgierski MZ, Wyllie GRA, Scheidt WR, Sturhahn W, Alp EE, Durbin SM, Sage JT (2004) *J Am Chem Soc* 126:4211
105. Pavlik JW, Barabanschikov A, Oliver AG, Alp EE, Sturhahn W, Zhao J, Sage JT, Scheidt WR (2010) *Angew Chem Int Ed* 49:4400
106. Scheidt WR, Durbin SM, Sage JT (2005) *J Inorg Biochem* 99:60
107. Chottard G, Mansuy D (1977) *Biochem Biophys Res Commun* 77:1333
108. Stong JD, Burke JM, Daly P, Wright P, Spiro TG (1980) *J Am Chem Soc* 102:5815
109. Tsubaki M, Yu NT (1982) *Biochemistry* 21:1140
110. Benko B, Yu NT (1983) *Proc Natl Acad Sci USA* 80:7042
111. Tomita T, Hirota S, Ogura T, Olson JS, Kitagawa T (1999) *J Phys Chem B* 103:7044
112. Coyle CM, Vogel KM, Rush TS III, Kozłowski PM, Williams R, Spiro TG, Dou Y, Ikeda-Saito M, Olson JS, Zgierski MZ (2003) *Biochemistry* 42:4896
113. Zeng W, Silvernail NJ, Wharton DC, Georgiev GY, Leu BM, Scheidt WR, Zhao J, Sturhahn W, Alp EE, Sage JT (2005) *J Am Chem Soc* 125:11200
114. Silvernail NJ, Barabanschikov A, Pavlik JW, Noll BC, Zhao J, Alp EE, Sturhahn W, Sage JT, Scheidt WR (2007) *J Am Chem Soc* 129:2200
115. Paulat F, Berto TC, DeBeer George S, Goodrich LE, Praneeth VKK, Sulok CD, Lehnert N (2008) *Inorg Chem* 47:11449
116. Spiro TG, Wasbotten IH (2005) *J Inorg Biochem* 99:34
117. Ray GB, Li X-Y, Ibers JA, Sessler JL, Spiro TG (1994) *J Am Chem Soc* 116:162
118. Ibrahim M, Xu C, Spiro TG (2006) *J Am Chem Soc* 128:16834
119. Hayashi T, Miner KD, Yeung N, Lin Y-W, Lu Y, Moënne-Loccoz P (2011) *Biochemistry* 50: 5939
120. He C, Neya S, Knipp M (2011) *Biochemistry* 50:8559
121. Tangen E, Svadberg A, Ghosh A (2005) *Inorg Chem* 44:7802
122. Soldatova AV, Ibrahim M, Olson JS, Czernuszewicz RS, Spiro TG (2010) *J Am Chem Soc* 132:4614
123. Xu C, Spiro TG (2008) *J Biol Inorg Chem* 13:613
124. Yeung N, Lin YW, Gao YG, Zhao X, Russell BS, Lei L, Miner KD, Robinson H, Lu Y (2009) *Nature* 462:1079

125. Hu S, Kincaid JR (1991) *J Am Chem Soc* 113:9760
126. Lehnert N, Praneeth VKK, Paulat F (2006) *J Comput Chem* 27:1338
127. Zilberberg I, Ruzankin SP (2004) *Chem Phys Lett* 394:165
128. Zilberberg I, Ruzankin SP, Malykhin S, Zhidomirov GM (2004) *Chem Phys Lett* 394:392
129. Cooper CE (1999) *Biochim Biophys Acta* 1411:290
130. Miller LM, Pedraza AJ, Chance MR (1997) *Biochemistry* 36:12199
131. Tomita T, Haruta N, Aki M, Kitagawa T, Ikeda-Saito M (2001) *J Am Chem Soc* 123:2666
132. Ding XD, Weichsel A, Andersen JF, Shokhireva TK, Balfour C, Pierik AJ, Averill BA, Montfort WR, Walker FA (1999) *J Am Chem Soc* 121:128
133. Maes EM, Walker FA, Montfort WR, Czernuszewicz RS (2001) *J Am Chem Soc* 123:11664
134. Moeser B, Janoschka A, Wolny JA, Paulsen H, Filippov I, Berry RE, Zhang H, Chumakov AI, Walker FA, Schünemann V (2012) *J Am Chem Soc* 134:4216
135. Obayashi E, Tsukamoto K, Adachi S, Takahashi S, Nomura M, Iizuka T, Shoun H, Shiro Y (1997) *J Am Chem Soc* 119:7807
136. Hu S, Kincaid JR (1993) *J Biol Chem* 268:6189
137. Paulat F, Lehnert N (2007) *Inorg Chem* 46:1547
138. Kadish KM, Lançon D, Cocolios P, Guillard R (1984) *Inorg Chem* 23:2372
139. Guillard R, Lagrange G, Tabard A, Lancon D, Kadish KM (1985) *Inorg Chem* 24:3649
140. Hodge SJ, Wang L-S, Khan MA, Young VGJ, Richter-Addo GB (1996) *Chem Commun* 2283
141. Cheng L, Chen L, Chung H-S, Khan MA, Richter-Addo GB, Young VGJ (1998) *Organometallics* 17:3853
142. Xu N, Lilly J, Powell DR, Richter-Addo GB (2012) *Organometallics* 31:827
143. Zaczek MB, Zareba AA, Czernuszewicz RS, Montfort WR (2006) *J Porphyrins Phthalocyanines* 10:928
144. Pinakoulaki E, Gemeinhardt S, Saraste M, Varotsis C (2002) *J Biol Chem* 277:23407
145. Collman JP, Yang Y, Dey A, Decreau RA, Ghosh S, Ohta T, Solomon EI (2008) *Proc Natl Acad Sci USA* 105:15660
146. Hu C, Sulok CD, Paulat F, Lehnert N, Zatsman AI, Hendrich MP, Schulz CE, Scheidt WR (2010) *J Am Chem Soc* 132:3737
147. Enemark JH, Feltham RD (1974) *Coord Chem Rev* 13:339
148. Jørgensen CK (1966) *Coord Chem Rev* 1:164
149. Mingos DMP (1973) *Inorg Chem* 12:1209
150. Hoffmann R, Chen MML, Elian M, Rossi AR, Mingos DMP (1974) *Inorg Chem* 13:2666
151. Conradie J, Ghosh A (2007) *J Phys Chem B* 111:12621
152. Radon M, Pierloot K (2008) *J Phys Chem A* 112:11824
153. Radon M, Broclawik E, Pierloot K (2010) *J Phys Chem B* 114:1518
154. Boguslawski K, Jacob CR, Reiher M (2011) *J Chem Theory Comput* 7:2740
155. Siegbahn PEM, Blomberg MRA, Chen S-L (2010) *J Chem Theory Comput* 6:2014
156. Goodrich LE, Lehnert N (2013) *J Inorg Biochem* 118:179
157. Fujisawa K, Tateda A, Miyashita Y, Okamoto K, Paulat F, Praneeth VKK, Merkle A, Lehnert N (2008) *J Am Chem Soc* 130:1205
158. Merkle AC, Fry NL, Mascharak PK, Lehnert N (2011) *Inorg Chem* 50:12192–12203
159. Traylor TG, Sharma VS (1992) *Biochemistry* 31:2847
160. Leu BM, Silvernail NJ, Zgierski MZ, Wyllie GRA, Ellison MK, Scheidt WR, Zhao J, Sturhahn W, Alp EE, Sage JT (2007) *Biophys J* 92:3764
161. Choi I-K, Liu Y, Feng D, Paeng K-J, Ryan MD (1991) *Inorg Chem* 30:1832
162. Lahiri GK, Kaim W (2010) *Dalton Trans* 39:4471
163. Zhang Y, Gossman W, Oldfield E (2003) *J Am Chem Soc* 125:16387
164. Perutz MF, Kilmartin JV, Nagai K, Szabo A, Simon SR (1976) *Biochemistry* 15:378
165. Zhao Y, Brandish PE, Ballou DP, Marletta MA (1999) *Proc Natl Acad Sci USA* 96:14753
166. Muralidharan S, Boon EM (2012) *J Am Chem Soc* 134:2044–2046
167. Girsch P, de Vries S (1997) *Biochim Biophys Acta* 1318:202

168. Berto TC, Hoffman MB, Murata Y, Landenberger KB, Alp EE, Zhao J, Lehnert N (2011) *J Am Chem Soc* 133:16714
169. Berto TC, Speelman A, Zheng S, Lehnert N (2013) *Coord Chem Rev* 257:244
170. Arikawa Y, Onishi M (2012) *Coord Chem Rev* 256:468
171. Arikawa Y, Asayama T, Moriguchi Y, Agari S, Onishi M (2007) *J Am Chem Soc* 129:14160
172. Wright AM, Wu G, Hayton TW (2012) *J Am Chem Soc* 134:9930–9933
173. Gans P (1967) *J Chem Soc A* 943
174. Hoskins BF, Whillans FD, Dale DH, Hodgkin DC (1969) *J Chem Soc Chem Commun* 69
175. Villalba MEC, Navaza A, Güida JA, Varette EL, Aymonino PJ (2006) *Inorg Chim Acta* 359:707
176. Ford PC, Fernandez BO, Lim MD (2005) *Chem Rev* 105:2439
177. Kozlov A, Constantino G, Sobhian B, Szalay L, Umar F, Nohl H, Bahrami S, Redl H (2005) *Antioxid Redox Signal* 7:515
178. Shimizu H, Park S-Y, Gomi Y, Arakawa H, Nakamura H, Adachi S-I, Obayashi E, Iizuka T, Shoun H, Shiro Y (2000) *J Biol Chem* 275:4816
179. Lançon D, Kadish KM (1983) *J Am Chem Soc* 105:5610
180. Pellegrino J, Bari SE, Bikiel DE, Doctorovich F (2010) *J Am Chem Soc* 132:989
181. Olson LW, Schaeper D, Lancon D, Kadish KM (1982) *J Am Chem Soc* 104:2042
182. Wei Z, Ryan MD (2010) *Inorg Chem* 49:6948
183. Pellegrino J, Hübner R, Doctorovich F, Kaim W (2011) *Chem Eur J* 17:7868
184. Kumar MR, Fukuto JM, Miranda KM, Farmer PJ (2010) *Inorg Chem* 49:6283
185. Farmer PJ, Sulc F (2005) *J Inorg Biochem* 99:166
186. Bayachou M, Lin R, Cho W, Farmer PJ (1998) *J Am Chem Soc* 120:9888
187. Guo M, Sulc F, Ribbe MW, Immoos CE, Farmer PJ, Burgess BK (2002) *J Am Chem Soc* 124:12100
188. Yang L, Ling Y, Zhang Y (2011) *J Am Chem Soc* 133:13814
189. Sulc F, Fleischer E, Farmer PJ, Ma DJ, La Mar GN (2003) *J Biol Inorg Chem* 8:348
190. Immoos CE, Sulc F, Farmer PJ, Czarnecki K, Bocian DF, Levina A, Aitken JB, Armstrong RS, Lay PA (2005) *J Am Chem Soc* 127:814
191. Ling Y, Mills C, Weber R, Yang L, Zhang Y (2010) *J Am Chem Soc* 132:1583
192. Miller TW, Chemey MM, Lee AJ, Francoleon NE, Farmer PJ, King SB, Hobbs AJ, Miranda KM, Burstyn JN, Fukuto JM (2009) *J Biol Chem* 284:21788
193. Shiro Y, Fujii M, Iizuka T, Adachi S, Tsukamoto K, Nakahara K, Shoun H (1995) *J Biol Chem* 270:1617
194. Daiber A, Nauser T, Takaya N, Kudo T, Weber P, Hultschig C, Shoun H, Ullrich V (2002) *J Inorg Biochem* 88:343
195. Yi J, Morrow BH, Campbell ALOC, Shen JK, Richter-Addo GB (2012) *Chem Commun* 48:9041
196. Flock U, Reimann J (2006) *Biochem Soc Trans* 34:188
197. Fritz G, Einsle O, Rudolf M, Schiffer A, Kroneck PMH (2005) *J Mol Microbiol Biotechnol* 10:223
198. Clarke TA, Hemmings AM, Burlat B, Butt JN, Cole JA, Richardson DJ (2006) *Biochem Soc Trans* 34:143
199. Einsle O, Messerschmidt A, Huber R, Kroneck PMH, Neese F (2002) *J Am Chem Soc* 124:11737
200. Marritt SJ, Kemp GL, Xiaoe L, Durran JR, Cheesman MR, Butt JN (2008) *J Am Chem Soc* 130:8588

Medical Applications of Solid Nitrosyl Complexes

Phoebe K. Allan and Russell E. Morris

Abstract Solid nitrosyl compounds are under investigation as ways of delivering nitric oxide for medical applications. This contribution discusses the role of nitric oxide in biology and the need for solids that can be used to store and deliver the gas in biologically relevant amounts. The types of solid that make suitable gas storage media are discussed, as is the relationship between nitric oxide storage and other areas of gas storage research. The particular materials that show most promise for nitric oxide delivery are discussed in detail, including their preliminary medical applications on humans. Finally, a forward look is described as to how current nitric oxide technology is informing other potential gas delivery applications in medicine.

Keywords Gas adsorption · Medical applications · Metal–organic frameworks · Nitric oxide

Contents

1	Nitric Oxide in Biology	227
1.1	Endogenous Production of Nitric Oxide	229
1.2	Toxicity and Biological Activity of Nitric Oxide	230
1.3	Potential of Gasotransmitters as Therapeutics	231
2	Delivery of Nitric Oxide from Nitrosyl Complexes and Clusters	233
2.1	Gas Storage in Porous Materials	234
2.2	Methods of Gas Storage	235

P.K. Allan
Department of Chemistry, University of Cambridge, Lensfield Road, Cambridge CB2 1EW,
UK

R.E. Morris (✉)
EaStCHEM School of Chemistry, University of St Andrews, Purdie Building, St Andrews
KY16 9ST, UK
e-mail: rem1@st-andrews.ac.uk

2.3	Metal–Organic Frameworks	236
2.4	Synthesis and General Features	237
2.5	MOFs for Biological Applications	239
2.6	Porous Materials for Storage and Delivery of Nitric Oxide	239
2.7	Structural and Mechanistic Studies of Nitric Oxide Adsorption and Release	244
3	Looking Ahead: Other Gasotransmitter Molecules	245
3.1	Carbon Monoxide and Organ Transplantation	247
3.2	Hydrogen Sulfide and Suspended Animation	248
3.3	Interactions of the Gasotransmitters	248
4	General Implications and Future Directions	249
	References	249

Abbreviations

BET	Brunauer, Emmett, and Teller
btc	Benzenetricarboxylic acid
btt	1,3,5-Benzenetristetrazolate
CBS	Cystathionine- β -synthase
cGC	Cytosolic guanylate cyclase
cGMP	Cyclic guanosine-3,5-monophosphate
CO	Carbon monoxide
CORM	Carbon monoxide-releasing molecule
CSE	Cystathionine- γ -lyase
CUS	Coordinatively unsaturated sites
FAD	Flavin adenine dinucleotide
FMN	Flavin mononucleotide
GTP	Guanosine-5-triphosphate
H ₂ S	Hydrogen sulfide
Hb	Hemoglobin
HbCo	Carboxy-hemoglobin
HO	Heme oxygenase
MIL	Material of the Institute Lavoisier
mmol	Millimole
MOF	Metal–organic framework
NADP	Nicotinamide adenine dinucleotide phosphate
NO	Nitric oxide
NOS	Nitric oxide synthase
OxHb	Oxyhemoglobin
PBS	Phosphate buffer solution
PDF	Pair-distribution function
ppm	Parts per million
PTFE	Polytetrafluoroethylene
ROS	Radical oxygenating species
SBU	Secondary building unit
STP	Standard temperature and pressure

1 Nitric Oxide in Biology

Cells signal to each other in order to coordinate cellular actions. This intercellular signaling takes place through the use of neurotransmitters. Chemicals traditionally recognized as neurotransmitters are compounds produced by neurons and stored in vesicles until stimulation of the neurons trigger their release (Fig. 1, top). They bind to specific membrane receptors in a neighboring cell to produce a physiological effect. “Gasotransmitters” are a group of small gaseous molecules that exhibit a similar signaling function in the body but through a different mechanism. They function without receptors because they are freely permeable to cell membranes (Fig. 1, bottom) [1]. The term gasotransmitter was first used in a paper by Rui Wang [2], in order to distinguish the receptor-independent signaling nature of these molecules from that of traditional neurotransmitters. Wang suggested that for a molecule to be considered a gasotransmitter, a number of criteria must be met (Table 1) [1]. Most importantly, the molecule must be produced endogenously (within the body) for a specific biological function. The term gasotransmitter additionally serves to recognize the similarities between signaling methods employed by each of the gasotransmitter molecules and to group the molecules together.

To date, three gasotransmitter molecules have been proposed: nitric oxide, carbon monoxide, and hydrogen sulfide. Ironically, considering this biological role, the reputation of all of these gases is for being detrimental to health; inhalation of high concentrations of any of the three can be lethal. Nitric oxide is best known for being an atmospheric pollutant as part of NO_x , a component of smog. Carbon monoxide is a common household hazard produced by incomplete combustion of fossil fuels, and is undetectable by the human senses making it known as the “silent killer.” Hydrogen sulfide has a toxicity of similar potency to cyanide and is responsible for the characteristic smell of rotten eggs.

However dangerous large doses of these gases are, it has been shown that small amounts of all three gases are actually vital to human health. In fact, the body produces a small but biologically significant amount of all three gases and they are known to modulate cellular functions by influencing a range of intercellular signaling processes. The significance of this discovery was reflected in the award of the 1998 Nobel Prize for physiology to the three American scientists, Murad, Furchgott, and Ignarro for the discovery of the endogenous production of NO. In addition to the three accepted gasotransmitter molecules, recent reports suggest that the small gaseous sulfur dioxide molecule also plays a gasotransmitter role within the body [3, 4], and other gases such as carbonyl sulfide [5] and nitrous oxide [6] have been suggested for investigation.

Here, we consider the endogenous production and biological effects of nitric oxide before outlining the work done toward using exogenous dosage of nitric

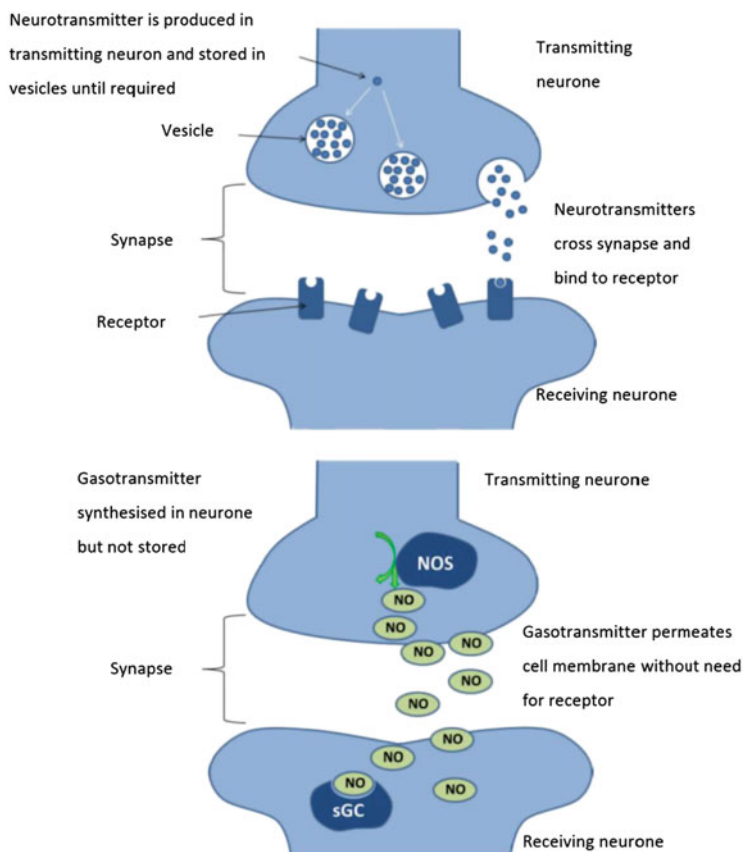


Fig. 1 Schematics of mechanism of neurotransmitter (1-1a, *top*) and gasotransmitter (1-1b, *bottom*) action

Table 1 Criteria for gasotransmitters

-
1. They are small, gaseous molecules
 2. They are freely permeable to cell membranes
 3. They are endogenously and enzymatically produced and regulated
 4. They have specific well-defined biological roles at specific concentrations
-

oxide as a medical device. We summarize work done using chemical donors – polymers, porous materials, particularly zeolites and metal–organic frameworks (MOFs) – as delivery vessels for this gas. Finally, we briefly consider the role that the other gasotransmitters could play and the *in vivo* interactions of the gases.

1.1 Endogenous Production of Nitric Oxide

Endogenous production of nitric oxide was suggested in 1987 when reports from the groups of Louis Ignarro and Salvador Moncada suggested that nitric oxide was responsible for the relaxation of endothelial cells¹ in blood vessels [7, 8]. Direct evidence that endogenous nitric oxide production was responsible for this effect was given shortly thereafter by the use of isotopic labeling of nitrogen in arginine in endothelium cell cultures [9].

It is now well established that the bulk of endogenous nitric oxide is formed by the reaction of the amino acid L-arginine (which provides the nitrogen of the NO) with oxygen gas to form citrulline and nitric oxide. The reaction is shown in Fig. 2. This reaction is catalyzed by the family of enzymes called nitric oxide synthase (NOS). There are several isoforms of NOS: the constitutive forms, eNOS and nNOS, which are expressed within tissues in all physiological conditions, and an inducible form, iNOS, which only exists when induced by the switching on of a central gene. All forms involve a central metal ion such as zinc, copper, or iron within a heme moiety.

The mechanism by which nitric oxide is formed is similar for all types of NOS [10]. Electrons are required for the conversion and these are provided by the chemical nicotinamide adenine dinucleotide phosphate (NADPH) which, while not part of the NOS enzyme itself, is essential to the enzyme activity. NOS has two distinct domains which take part in the conversion of L-arginine: reductase and oxygenase. The reductase domain contains two cofactors,² flavin mononucleotide (FMN) and flavin adenine dinucleotide (FAD), which receive the electrons from the NADPH and pass them, via calmodulin, to the oxygenase domain. The oxygenase domain contains, in addition to the NADPH, two cofactors: heme, where the substrate oxygen binds to the iron before reacting with the L-arginine, and BH₄, whose role is currently unknown. The electrons from the reductase domain activate the oxygen attached to the heme moiety and facilitate attack of the arginine. While most nitric oxide is produced by the method above, other sources of nitric oxide within the body are also known, such as S-nitrosothiols.

The endogenous concentration of nitric oxide has been estimated to be in the nanomolar concentration range [11], which is quite low for something to show significant biological activity. However, as NO is reactive and its lifetime in the body is thought to be a few seconds at the most, there would not be much free nitric oxide in tissues to be detected [7].

¹ In blood vessels, endothelial cells exist in the endothelium, which is the single-layer of cells between the hole through the middle of blood vessels where blood flows (the lumen) and the exterior wall of the blood vessel (smooth muscle layer). Relaxation of the muscle layer increases the size of the lumen and allows more blood to flow through the vessel, which is called dilation of the blood vessel (vasodilation).

² Cofactors are “helper molecules” for enzymes – chemical compounds which are not part of the enzyme itself but are required for the enzyme to catalyze biochemical processes.

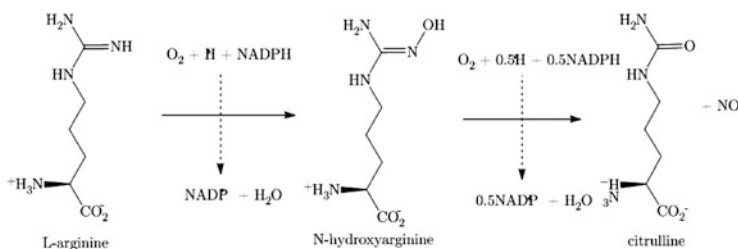


Fig. 2 Nitric oxide production via the conversion of L-arginine to citrulline

1.2 Toxicity and Biological Activity of Nitric Oxide

The direct toxicity of nitric oxide is modest, but is greatly enhanced by it reacting with superoxide to form peroxynitrite ($ONOO^-$) [12]. The generation of excess $ONOO^-$ leads to oxidative injury and lung damage culminating, at high dosages, in pulmonary edema. On contact with oxygen, NO spontaneously produces NO_2 which is considerably more toxic than nitric oxide itself.

The biological effects of nitric oxide appear to be ubiquitously present in the body. Research is only in its infancy, and in many areas there is not a clear consensus of the role NO performs, with many contradictory accounts of effects being reported. Part of the reason for this is that endogenous levels of the gases must strike a very fine balance; for example, nitric oxide deficiency can cause unwanted effects such as hypertension, thrombosis, and a reduced ability to fight infection and heal wounds [13] while overproduction of NO has been linked to conditions such as septic shock and inflammation [14].

NO produced in the endothelium prevents platelet aggregation in healthy blood vessels through a cGC-derived mechanism, implicating NO in wound healing and thrombosis [15]. When the endothelium of a blood vessel is damaged, the level of NO produced is lowered and platelet aggregation is no longer prevented. This leads to platelet aggregation clotting and healing of the vessel. NO is known to regulate the growth of new blood vessels and may regulate the production of new skin cells during wound healing [16]. This, coupled with the roles NO plays in fighting infection and in clotting, means that the endogenous dosage of nitric oxide has been suggested to improve wound healing, particularly in situations where the body's wound healing mechanisms are lowered (such as in diabetic ulcers). There are growing reports that H_2S , like nitric oxide, has therapeutic potential in the angiogenesis/wound healing area; *in vitro* studies demonstrate that hydrogen sulfide induces angiogenesis and stimulates gastric ulcer healing in rodent models [17–19].

In cases where platelet aggregation is not associated with a wound, there is a danger of clots which can prevent blood flow to key organs. This danger is increased when foreign matter, which does not produce NO , is inserted into the blood vessels, as is the case when stents are used to alleviate stenosis. Stenosis, the narrowing of the blood vessels by fatty lipid deposits, is a very dangerous condition which can increase blood pressure and strain on the heart. A stent at the end of a

catheter is inserted into the vessel and a balloon is inflated to increase the size of the lumen and increase blood flow. This procedure can damage the endothelium, lowering NO levels and increasing risk of clots on the surface of the stent, forming a thrombosis. Using stent materials which produce NO to mimic endothelial action could have a role in preventing thrombosis.

NO is a known antibacterial agent. Macrophages, which are scavenger cells and part of the immune system, protect the body from infection by killing and digesting microbes via the production of toxic chemicals to destroy the microbe cells. These chemicals are quickly removed from the body by enzymes, preventing them from damaging cells of the host tissue. NO is known to be one of the chemicals produced by macrophages and is involved in cell death, both necrosis³ and apoptosis,⁴ in its produced form and via conversion to peroxynitrite and nitrate [20]. NO-induced necrosis has also been suggested as the mechanism by which nitric oxide attacks tumor cells, although the role of nitric oxide in cancer is neither simple nor well understood at present [21].

The role of nitric oxide in inflammation is complex, and is both tissue- and concentration-dependent. Nitric oxide is generally labeled as pro-inflammatory, and the overproduction of NO by the inducible form of NOS (iNOS) has been implicated in pro-inflammatory conditions such as rheumatoid arthritis. Despite being pro-inflammatory, NO produced by eNOS is essential to wound repair and the growth of new blood vessels in the area affected by inflammation, meaning that therapies involving the inhibition of all NO production would not necessarily improve inflammatory conditions. Drugs which down-regulate iNOS-induced nitric oxide production without stopping production of eNOS-NO may possibly improve inflammatory conditions, and the subtle structural differences between the enzymes may mean that this level of selectivity is possible [22].

1.3 Potential of Gasotransmitters as Therapeutics

NO is an exciting potential therapeutic and the required concentrations of the gas for particular biological applications are starting to be realized. It is thought, for example, that for antiplatelet action very low concentrations of nitric oxide, of the order of nano- to pico-molar, are required [23]. For antibacterial action, much higher concentrations (millimolar) are needed. The biological effects are highly dependent on the concentration of the nitric oxide, meaning that potential therapies

³ Necrosis is cell death caused by factors external to the cell or tissue, such as infection, toxins, or trauma. It is generally “messy” leaving behind debris in the body, and is normally detrimental to tissue.

⁴ Apoptosis is programmed cell death. It results in cell fragments which can be engulfed and removed from the body before the contents of the cell can spill out onto surrounding cells and cause damage.

require a method that allows delivery of the exact amount of gas appropriate to the therapy at the desired rate.

There are number of difficulties with the dosage of nitric oxide; NO is a gas at room temperature and pressure. Secondly, it is lethal in high doses, meaning that the use of gas cylinders would have to be very tightly controlled and dosing an appropriately small amount would be awkward and difficult. Additionally, any exposure to oxygen causes immediate conversion to the extremely toxic NO₂. Inhalation of NO has been used extensively in biological experiments and, in fact, has met with some success in the treatment of infants with respiratory failure [24]. Recently, a delivery system specifically for dosing inhaled carbon monoxide (CO), NO's biologically signaling counterpart, has been developed by Ikaria to provide quantitative delivery of pharmaceutical-grade CO for inhalation in proportion to the subject's body weight [25].

The short lifetimes in vivo of NO mean that systemic delivery may not be able to dose the gas to the correct areas. Particularly for applications such as wound healing, direct delivery of the gas to a targeted area is desirable, and this would further avoid unwanted side effects of the gas's action in other parts of the body.

Outside of inhalation, chemical compounds which release the gas when exposed to a specific stimulus are the most widely researched source of gasotransmitters. NO donors are a growing area of research. Exogenous sources of NO have unwittingly been used as therapies for centuries; there are reports of potassium nitrate, which is broken down by NOS to produce NO, being used to treat the discomfort and pain associated with angina as early as 800 AD [20]. Glyceryl trinitrate, which is thought to be metabolized to form nitric oxide is the most common treatment for angina [26].⁵ Diazeniumdiolate compounds (NONOates) release nitric oxide in a first order, proton-mediated reaction, and the rate of gas release from compounds can be chemically controlled [27]. The drug Viagra works by prolonging the effect of NO in the penis, where the gas acts to relax the vessels, thereby enhancing blood flow [28]. S-nitrosothiols, when used as NO donor drugs, break down to form NO.

Some uses such as wound healing applications require topical delivery of the gas. Topical delivery of nitric oxide has received the most attention. Acidified nitrite creams have improved the wound healing time in both normal and diabetic mice, but there is some concern with regard to skin inflammation. Dressings with NO-releasing materials improved the wound healing time in diabetic mice [29]. Coatings for stents and catheters which release nitric oxide and better mimic endothelial nitric oxide production have been shown to decrease thrombosis formation [30–33]. This technology also requires materials which can release nitric oxide at a rate which mimics endogenous production.

⁵ Angina is a condition caused by constriction of the arteries supplying the heart, putting increased strain on the heart to maintain the same level of blood flow. Its symptoms are chest pain and choking.

2 Delivery of Nitric Oxide from Nitrosyl Complexes and Clusters

Some NO complexes of transition metals (metal nitrosyls) are photosensitive, that is, they release NO upon exposure to light. If NO release is of appropriate quantity and rate, these complexes could deliver NO in a site specific manner to malignant locations for applications such as apoptosis in tumor cells. Two main concerns for these complexes are a low quantum yield meaning that long exposures of UV light are required to release nitric oxide, which is harmful to tissues and low stability in aqueous media, limiting their implementation in real applications. Several groups have been active in the design of nitrosyl complexes which release nitric oxide exclusively on exposure to light [34, 35].

Choice of metal-oxidation state, spin configuration, and the spectator ligands in a complex can promote the release of nitric oxide and tailor the wavelength at which this nitric oxide is released as well as the stability of the complex in various media [35]. To increase the sensitivity of such compounds to visible light dyes have been added to the molecules or directly ligating a light-harvesting chromophore to the ruthenium center [36–38]. Initial work on iron and manganese complexes of the type $(\text{PaPy}_3)\text{M}(\text{NO})(\text{BF}_4)_2$ where PaPy_3 is the pentadentate ligand *N,N*-bis(2-pyridylmethyl)amine-*N*-ethyl-2-pyridine-2-carboxamide showed release exclusively on exposure to visible light with reasonable quantum yield, but both iron and manganese complexes are unstable in aqueous buffers when NO converts to NO_2 . The ruthenium complex $[(\text{PaPy}_3)\text{Ru}(\text{NO})](\text{BF}_4)_2$ showed much better stability but showed a lower quantum yield [38].

Recently, the photoactive manganese nitrosyl complex $\text{Mn}(\text{PaPy}_3)(\text{NO})(\text{ClO}_4)$ releases nitric oxide on exposure to visible light and is fairly stable to aqueous media [39]. Sensitivity of these compounds to wavelength can be adjusted by ligand replacement; in the case of $[\text{Mn}(\text{PaPy}_3)(\text{NO})](\text{ClO}_4)$ pyridine ring of the PaPy_3 -ligand frame with a quinoline moiety results in sensitivity in the near infrared region [40].

Photolytic delivery of nitric oxide in biological applications was actually implemented during the initial period when the role of nitric oxide in biology was emerging. Commercially available photolytic donors of nitric oxide were used as NO donors in biological experiments. For example, $[\text{Ru}(\text{NO})(\text{Cl})_5]^{2-}$ releases nitric oxide when exposed to light causing vasodilation in aortic rings, but NO release also occurs spontaneously from these compounds meaning that careful controls are required in any biological experiments [38]. In another example, clusters of $[\text{Fe}_4\text{S}_4(\text{NO})_4]$ irradiated with visible laser light were able to release NO both in solution and when contained in the endothelium. This nitric oxide was able to dilate rat arteries dependent of the length of exposure and wavelength of light used [41].

NO transfer to several proteins including hemoglobin, cytochrome *c* oxidase from $[(\text{PaPy}_3)\text{Ru}(\text{NO})](\text{BF}_4)_2$ within milliseconds of laser-pulse activation has been reported, as well as the activation of soluble granulate cyclase [35]. These materials require incorporation into release platforms to be used in real applications. NO released from photoactive nitrosyls has antibacterial action from a number of delivery platforms [34, 42–44]. $\text{Mn}(\text{PaPy}_3)(\text{NO})(\text{ClO}_4)$ can be incorporated into a sol–gel

matrix with a polyurethane coating and still shows a linear release of nitric oxide, which was further shown to have antibacterial actions against *Pseudomonas aeruginosa*, *Escherichia coli*, *Staphylococcus aureus*, and methicillin-resistant *S. aureus* [44, 45]. When incorporated into aluminosilicate MCM-41 the system has been reported to release micromolar concentrations of NO rapidly from the entrapped nitrosyl while the photoproducts are retained in the host structure [42]. Authors observed clearing of both drug-sensitive and drug-resistant strains of *A. baumannii*, showing antibacterial properties of the released nitric oxide. A layered delivery system using polydimethylsiloxane (PDMS) and Pluronic (R) F127 gel impregnated with, [Mn(PaPy3)(NO)]ClO₄ has recently been proposed for use in bandages [44].

In addition to reduction and photolysis, a method of NO release from ruthenium complexes using the body's mitochondria cells has recently been proposed. Mitochondria are able to facilitate the release of NO from nitrosyl ruthenium complexes because they are sources of reducing agents such as NADH, and this indicates that the role of nitric oxide in site specific cell death could occur in mitochondria-mediated processes and could find use in the treatment of tumors and skin cancers [46].

2.1 Gas Storage in Porous Materials

Gas storage is a topical issue; with the projected exhaustion of fossil fuels, the urgency of our search for new energy sources has increased, and porous materials have been highlighted as a possible storage medium. Gas storage in zeolites has been studied extensively, especially in those materials with extra-framework ions which can interact with guest species [47]. Some MOFs have large surface areas and high porosity and this means that they have the potential to store significant amounts of gas in their pores. Most work to date has concentrated on gas storage for environmental applications, and this can be broadly split into adsorption of potential fuel gases, hydrogen and methane [48–52], and the capture of carbon dioxide and other hazardous gases [53, 54].

There are several potential advantages of using MOFs for gas storage compared to gas cylinders. Firstly, there can be an increased storage density when compared with gas cylinders, zeolites, and activated carbons [50]. Secondly, in applications where only a small amount of gas is required, it could be easier to handle the gas in the form of solid pellets with adsorbed gas whose capacity can be tailored for application. Lastly, it might be safer to handle a gas when it is adsorbed in a solid, especially if higher pressures can be avoided. This is particularly applicable in the case of biological gases, where very controlled delivery of the gas is required.

Storage of a gas in a MOF requires large enough pore windows to allow the gas molecules to diffuse into the material and an ability to keep the molecule in the material through the interaction of the gas and the framework's internal surface. Storage implies that the gas can be removed when required, meaning the ability to trigger the release of the gas from the material is necessary. Gas adsorption capacity is generally reported as

adsorption isotherms, which quantify the amount of gas that a material adsorbs as a function of partial pressure of the gas. In general, few gas release experiments are performed, meaning that in reality if the delivery of gas is incomplete, the deliverable storage capacity may be less than the adsorption values reported.

2.2 Methods of Gas Storage

When gas molecules enter the material, they can bind to sites on its internal surface. This is adsorption. Adsorption is loosely divided into physical adsorption, or physisorption, and chemical adsorption, or chemisorption. Physisorption is generally weak, is due to induced or permanent dipoles and is generally observed at low temperatures with reduced capacity at higher temperature. Chemisorption involves the exchange of electrons (formation of chemical bonds) between adsorbate and adsorbant and is a much stronger interaction. While physisorption tends to be completely reversible on the decrease in partial pressure, species chemisorbed to a surface are likely to need an extra driving force such as heat for their removal.

For an uncharged gas molecule, the main interaction with the framework surface is via physisorption. Because of this, uptake is generally correlated with higher surface area, though this is not necessarily the only factor. The strength of interactions between the framework and gases can be reflected by isosteric heats of adsorption, Q_{st} [55]. When van der Waals interactions dominate, Q_{st} values are generally small; for hydrogen gas, for example, the Q_{st} for interaction with frameworks is typically in the range of 4–7 kJ mol⁻¹ [56]. For larger molecules such as methane, the Columbic portion of the interaction is larger, meaning that the gas is more “sticky.” The relatively weak interaction between the framework and the gas molecules is often the limiting factor with regard to gas adsorption capacity, but there are a number of ways in which this interaction energy can be increased through functionalization of the framework surface.

Unlike in zeolites, where metal ions exchanged into the framework sit extra- to the framework and are readily available for interaction with guest species, the metal ions within MOFs are an integral part of the structure. This means that in many cases their coordination sphere is made up entirely of strong ligand bonds and so they are unable to interact with guest species without breakdown of the framework. However, in some cases where one or more coordination site is taken up by solvent molecules from the synthesis, their removal leaves the structure with metals which are not coordinatively saturated. These metals with empty sites in their coordination spheres are named coordinatively unsaturated sites (CUS), or open metal sites. They can be very reactive with a high affinity for guest molecules and can become involved in chemisorption processes. CUS have been shown to enhance gas storage in a number of systems [48]. The Cu-framework HKUST-1 ([Cu₃(btc)₂(H₂O)₃]) shown at the bottom of Fig. 3 was the first example of functionalizable CUS. The aqua ligands from the Cu-site can be removed upon heating, and replaced by other groups such as pyridine [57]. The Mn-framework Mn₃[(Mn₄Cl)₃(BTT)₈]₂ (BTT = 1,3,5-benzenetristetrazolate) was reported by Dinca et al. to contain open Mn²⁺ coordination sites. Interaction with D₂

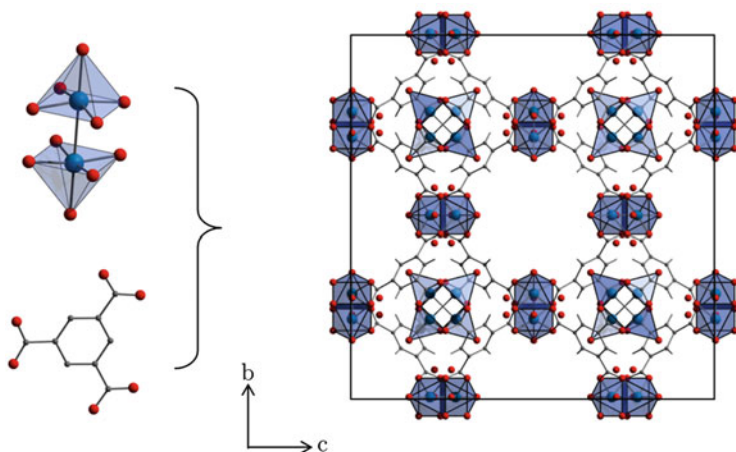


Fig. 3 $M_3(\text{btc})_2$ framework topology

gives a Q_{st} value of 10.1 kJ mol^{-1} at zero coverage at 77 K, with a Mn–D₂ bond length (2.27 Å) much shorter than would be expected for physisorption [58]. Similarly, the interaction of H₂ with the open Ni-sites in Ni-CPO-27 was shown to give $Q_{\text{st}} = 13 \text{ kJ mol}^{-1}$ at low coverages, the highest framework–H₂ interaction energy to date [59].

Interaction of a guest with the ligand can also increase the energy of adsorption. The higher methane capacity of IRMOF-6 compared to the other IRMOFs was ascribed to interaction with the cyclobutyl 1,4-benzenedicarboxylate ligand [60]. PCN-14, which combines both copper open metal sites and additional adsorption sites interacting with the anthracene ligand, shows the highest interaction energy and adsorption capacity for methane to date [61, 62]. Use of amine-based ligands has been shown to greatly increase the interaction of CO₂ with the framework. Interaction with organic groups can be increased further by grafting pendant functionalities onto the surface; this strategy to introduce alkylamine functionality onto bridging ligands or onto open metal sites can result in the increased uptake of carbon dioxide [54].

Gas storage by framework flexibility has been reported for several frameworks [63–69]. These transformations can include stretching, “breathing” and rotation and in some cases the selective induction of framework transitions can lead to selective gas adsorption properties through size selectivity or thermodynamic effects.

2.3 Metal–Organic Frameworks

MOFs, also known as coordination polymers, are extended materials which consist of metal ions or clusters which act as polyhedral “nodes,” connected by multi-dentate ligand molecules acting as linkers. Frameworks are formed by coordinate

bonds into infinite arrays, sometimes forming crystalline solids. The first MOF crystal structure was reported in 1959 [70], although significant research into the science and applications of MOFs started in the 1990s. To date, several thousand MOFs have been synthesized, usually via hydrothermal and solvothermal methods (Sect. 2.1) but increasingly using other techniques such as microwaves and electrochemistry [23].

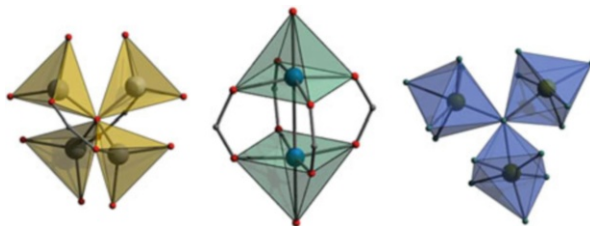
2.4 *Synthesis and General Features*

MOFs can exist as one-dimensional chains, two-dimensional sheets or three-dimensional frameworks. 2D and 3D structures can exhibit pores or channels running through them which are usually filled with solvent molecules from the synthesis. Many frameworks have fairly low thermal stability, but those which show higher stability can have guest molecules removed from pores by exposing the material to a vacuum or to heat. This results in materials with large pore volumes and high surface areas of thousands of square meters per gram. This compares favorably with several hundred square meters per gram for the most porous zeolites (the maximum surface area is zeolite Y, at $904 \text{ m}^2 \text{ g}^{-1}$) and activated carbons which have a theoretical maximum surface area of $2,630 \text{ m}^2 \text{ g}^{-1}$ [63]. The highest reported MOF surface area (BET) to date is $6,240 \text{ m}^2 \text{ g}^{-1}$, shown by MIL-200 [71].

The connectivities and topologies of MOF structures are dependent on coordination preferences of the synthetic conditions. Metals provide coordination sites for linkers and the geometry of the metal caused by oxidation states and coordination numbers determines the shape of the node and therefore the geometry of the framework. Linkers have multiple functional groups in order to act as a bridge between metal centers. The most common linker atoms are oxygen and nitrogen – carboxylates, phenol, pyridine, and imidazole donors are by far the most common donor groups reported, though the use of more “exotic” functional groups such as sulfonates, nitrates, and phosphonates are becoming increasingly common as the search for new frameworks continues. Rigid linkers, where the movement of the lone pair is restricted, increase the predictability of reactions and act as rods between metal nodes which can lead to robust frameworks with permanent porosity. Linkers with flexible binding modes have the potential to act as hemi-labile ligands and can lead to coordinative flexibility in the framework. Counter anions from reagents and solvents can act as reactants; both can take an active part in the framework, or act as template ions. Reaction conditions are also known to have a determining effect on the structure.

The range of metals and organic linkers available and the ability to change experimental conditions gives potential for a seemingly infinite number of framework topologies. However, in practice, the chemistry of these systems favor the in situ generation of particular polyatomic metal units, meaning that the same so-called “secondary building units” (SBUs) are seen over and over again

Fig. 4 Common secondary building units for MOFs: Zn_4O -cluster used in MOF-5 and IRMOFs (*left*); Cu-paddlewheel dimer seen in HKUST-1 (*middle*); Cr-trimer found in MIL-101 (*right*)



[72]. This is analogous to aluminosilicate zeolite chemistry, where a description of the structure can be given in terms of nine SBUs based on tetrahedral AlO_4 and SiO_4 primary building units [47]. Some common secondary building units – the Zn_4O -cluster, the copper paddlewheel dimer, and $Cr_3(OH)$ -trimer – are shown in Fig. 4.

It is possible to tailor the structure and properties of a framework. Firstly, knowledge of SBU formation can be applied in order to design frameworks with the same topology but utilizing different ligands, resulting in different pore sizes and surface areas. The best known example of this “isorecticular synthesis” is the IRMOFs reported by Yaghi and co-workers which use the same Zn_4O -cluster with different linkers to form a series of frameworks based on the same cubic topology but with different pore sizes and chemical functionality and thus varying gas adsorption properties [60, 73]. In a similar manner, the same framework topology can be created with different metals, as demonstrated by the M-CPO-27 framework where metals (Ni, Co, Zn, Mn, Mg, Fe) are linked by 2,5-dihydroxyterephthalic acid into a 3-D honeycomb framework, and the $[M_3(btc)_2]$ framework, based on M_2 -paddle-wheel units linked by benzenetricarboxylic acid (btc) which can be synthesized with $M = Cu$ (where it is commonly called HKUST-1) Fe, Cr, Mo (Fig. 3) [57, 74–76].

In addition to the range of frameworks which can be synthesized directly, it is also possible to modify the framework after the initial synthesis. This strategy of post-synthetic modification is frequently used to introduce functionalities to the pores and channels of the material required for specific purposes [77]. Post-synthetic modification can take several forms; removal of guest solvent molecules through the application of heat could be described as the most simple of post-synthetic modification procedures. Others include carrying out organic reactions on functional groups within the framework, grafting functional groups either onto the linker group or onto open metal sites in the material, or adding metal ions, clusters, or other species into the pores in order to enhance a particular characteristic of the material.

This ability to tailor a MOF’s structure to specific needs and requirements makes them exciting for a range of applications. Initially, the high porosity of the materials focused attention onto gas adsorption (see Sect. 2.2), but MOFs have since been suggested for potential applications in areas such as gas separation [78, 79], catalysis [80–82], luminescence and sensing [83, 84], magnetism [85], and medicine.

2.5 *MOFs for Biological Applications*

In recent years a growing area of research has involved MOFs for biological applications [23]. The use of MOFs for biomedical purposes is attractive for a number of reasons. MOFs are generally quite biodegradable because of the relatively labile nature of the coordination linkages holding the materials together, and this feature can be modified by the careful choice of metal and linker. Additionally, there is a wide range of MOFs available including those which use nontoxic components. This range lends itself to the idea that a MOF could be tailored for a specific therapeutic purpose.

Several ways in which MOFs could be used for biological applications have been suggested and this literature reviewed by Horcajada et al. [23]. Firstly, MOFs could be used as a container to store and deliver biologically active guests. Alternatively, the MOFs themselves could be biologically active or could be used as a diagnostic for applications such as imaging within the body.

2.6 *Porous Materials for Storage and Delivery of Nitric Oxide*

The exogenous dosage of gasotransmitter molecules has been shown to have beneficial medical effects. Unlike with gas storage and release for energy applications, it is not the amount of the gas stored but the release amounts and rate which are key [49].

Both zeolites and MOFs have been shown to store and release NO. There are two ways of storing NO in a structure (Fig. 5). The first is through the formation of diazeniumdiolate (or NONOates), which can deliver nitric oxide on exposure to water, and the second is by coordination of nitric oxide to a metal. The interaction of NO with zeolite materials is well characterized due to their use as deNO_x catalysts to remove the NO and NO_2 molecules from car exhaust fumes. Some of the NO is bound weakly by physisorption and some binds to the metal site making a strong, chemisorption interaction. The chemisorbed nitric oxide is not released from the material even at low pressures, making the adsorption irreversible. Both single-crystal experiments [86] and IR studies indicate that this chemisorption component involves the interaction of nitric oxide with the metal sites in the zeolite [86–88].

The different structures of zeolites give some measure of control over the kinetics of release. Work by Wheatley et al. [89, 90] probed the effect that zeolite topology and extra-framework cations had on NO adsorption and release, and concluded that the most effective framework topology was LTA. Different metal cations within the same zeolite framework topology (LTA) gave rise to differing adsorption capacities and rates of release, with cobalt showing the best characteristics – adsorption of 1.7 mmol g^{-1} of nitric oxide at 1 atm. of NO and at room temperature.

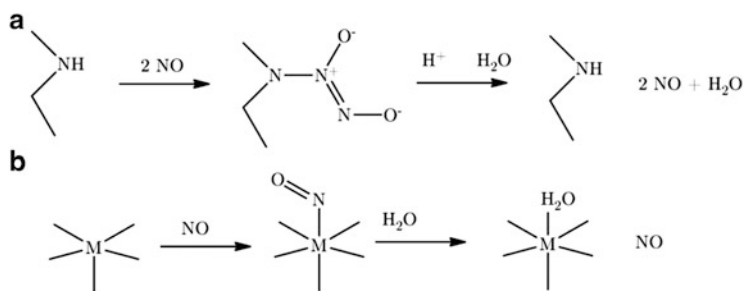


Fig. 5 Methods of storing nitric oxide in a zeolite or MOF. (a) Formation of diazeniumdiolates; (b) coordination to a metal ion

On the reduction of pressure, the weakly held physisorbed nitric oxide was removed leaving the irreversible chemisorbed content within the material. Upon exposure to moisture, water replaces the NO on the extra cation site and the nitric oxide is released. The zeolites show release of NO that is comparable in quantity to the adsorption process, although the total amount which is adsorbed is not released. The toxic nature of cobalt makes it unsuitable for some applications, so the much less toxic zinc framework, despite showing less ideal adsorption and desorption characteristics, has been used in several biological experiments.

NO-releasing zeolites show the expected biological activity. Wheatley et al. demonstrated anti-thrombosis activity on human platelet-rich plasma where a NO-loaded Co-exchanged zeolite-A sample completely inhibited platelet aggregation. When a NO scavenger was introduced to remove the NO from the system this inhibitory effect was removed, confirming the central role for NO in the inhibitory process and excluding the possibility that the effects of the NO-zeolite were merely cytotoxic. A sample of the Co-exchanged zeolite that has not been loaded with NO failed to inhibit aggregation. Figure 6 shows large platelet aggregants (PA) on the surface of the untreated zeolite which are not observed on the nitric oxide treated zeolite [89].

The well characterized low toxicity of zeolites makes them ideal for use in dermatological applications, and the sensitive nature of the delivery method compared favorably to other nitric oxide donors. Mowbray and co-workers have completed studies on human skin that show no significant inflammation of the skin on application of NO-releasing zeolites (Fig. 7), in contrast to chemically produced NO (from acidified nitrite creams), which is a competitor to gas storage materials for topical delivery [89].

Nitric oxide-loaded zeolite has also been shown to have antibacterial properties. A study by Fox et al. demonstrates the antibacterial properties of a NO-loaded Zn²⁺-exchanged zeolite material at a 50 wt.% composition in a polytetrafluoroethylene polymer against clinically relevant strains of bacteria, namely Gram-negative *P. aeruginosa* and Gram-positive methicillin-sensitive and methicillin-resistant *S. aureus* and *Clostridium difficile* [91]. NO-loaded zeolite treatments significantly reduced bacterial numbers compared to control NO-free zeolite control disks did not significantly reduce bacterial numbers in any of the samples measured. Wei

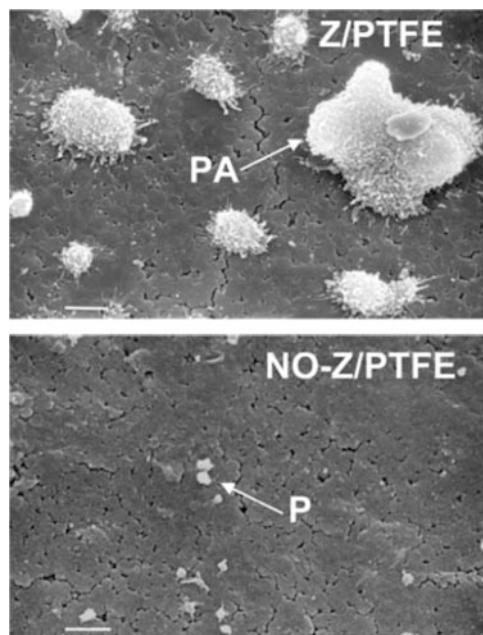


Fig. 6 Scanning electron micrographs of the surface of untreated Co-zeolite-A/PTFE disks (Z/PTFE) (*top*) and of NO-loaded Co-zeolite-A/PTFE disks (*bottom*). The *top* figure shows large platelet aggregants (PA) on the surface of the untreated zeolite/PTFE disk, while the *bottom* shows only a few, isolated platelets (P) on the surface of the NO-treated zeolite-PTFE disk. The scale bar is 10 μm . Reprinted with permission from J Am Chem Soc, 2006, 128 (2), pp 502–509. Copyright 2006 American Chemical Society



Fig. 7 Clinically visible cutaneous inflammation following topical acidified NO_2 , but not Ze-NO application. Reprinted with permission from Mowbray et al., J Investig Dermatol (2008) 128, 352

et al. recently demonstrated nitric oxide delivery from saturated zeolites as part of a multi-functional material which captured nitrosamine by alumina-modified zeolite samples in the gastric juice mimic [92].

Work by Wheatley et al. [89, 90] probed the effect that zeolite topology and extra-framework cations had on NO adsorption and release, and concluded that the

most effective framework topology was LTA. Different metal cations within the same zeolite framework topology (LTA) gave rise to differing adsorption capacities and rates of release, with cobalt showing the best characteristics – adsorption of 1.7 mmol g^{-1} of nitric oxide at 1 atm. of NO and at room temperature.

On the reduction of pressure, the weakly held physisorbed nitric oxide was removed leaving the irreversible chemisorbed content within the material. Upon exposure to moisture, water replaces the NO on the extra cation site and the nitric oxide is released. The zeolites show release of NO that is comparable in quantity to the adsorption process, although the total amount which is adsorbed is not released.

The toxic nature of cobalt makes it unsuitable for some applications, so the much less toxic zinc framework, despite showing less ideal adsorption and desorption characteristics, has been used in several biological experiments. The nitric oxide released from these materials has been shown to have antithrombotic effects [89]. The well characterized low toxicity of zeolites makes them ideal for use in dermatological applications, and the sensitive nature of the delivery method compared favorably to other nitric oxide donors; nitric oxide from a zeolite showed increased blood flow to the skin (due to the vasodilatory effect) without the redness from irritation found from acidified nitrate [93].

Several framework materials have been studied for nitric oxide adsorption and release. The storage of nitric oxide in MOFs can take place via either mechanism shown in Fig. 5. MOFs with open metal sites have shown much stronger adsorption of nitric oxide than those without [94]. This can be proven both structurally using X-ray diffraction or by infrared spectroscopy. Every MOF with open metal sites appears to store nitric oxide to some degree due to interaction of the gas molecule with the open metal site. The first studied MOF for NO adsorption, HKUST-1, adsorbs around 3 mmol g^{-1} of nitric oxide at room temperature and pressure [95].

The behavior of the CPO-27 isostructural series of frameworks for nitric oxide adsorption and release has been extensively studied [94]. McKinlay et al. report that both Ni-CPO-27 and Co-CPO-27 store considerable amounts of nitric oxide, with up to 8 mmol g^{-1} via coordination of the nitric oxide to the metal site resulting in octahedral geometry.

Other materials, such as the Fe-MIL-88 [64], Fe-MIL-100 [96], and Fe-MIL-101 also show good uptake of NO [97], and are of particular interest because of the redox chemistry that occurs on activation of the solids, with changes in activation energy that strongly affect the interaction of the NO with the open metal sites in the structure.

Storage of NO via the formation of diethylenetriamines, or NONOates was reported by Rosseinsky et al. who used post-synthetic modification of the open metal site of HKUST-1 [98]. However, on immersion in water, nitric oxide was released, but the amines were also leached from the metal sites. Cohen and co-workers use a similar method for functionalizing MOFs with NONOates by conversion of secondary amines from the functionalized ligands in MOFs rather than the open metal sites, thus improving the stability of the grafted amine species [99].

For biological applications, the release of nitric oxide is very important. In structures which chemisorb nitric oxide, reduction in gas pressure is not enough to induce release of the nitric oxide molecule. Nitric oxide can be released on heating the material, or photolytically, but the most common method of release is exposure to water. If the framework-nitrosyl compound is susceptible to water, water replaces the nitric oxide on the framework binding site and the nitric oxide is released. The amount of nitric oxide released is dependent on how susceptible the framework is to moisture. For example, HKUST-1, which chemisorbs 3 mmol g^{-1} of NO at room temperature, releases only a tiny fraction because the nitrosyl complex is too stable [90].

Both Ni-CPO-27 and Co-CPO-27 show exceptional release capabilities and the full adsorbed capacity is released on exposure to water [100]. Here, water replaced nitric oxide on the metal site in the structure, forcing the nitric oxide out of the structure to be released. The other members (Zn-CPO-27, Mn-CPO-27, and Mg-CPO-27) of the series also store and release nitric oxide but without the same exceptional release capacities [94]. The release capacities of these materials appear to be in some way correlated with the ease of dehydration and the stability of the open metal sites [23]. Between the two extremes of HKUST-1 and CPO-27 lie other MOFs with open metal sites which release a portion of their adsorbed amounts of nitric oxide.

Harding et al. recently reported the generation of nitric oxide via the MOF-catalyzed reaction of *S*-nitrosocysteine. At the peak of nitric oxide production, 200 picomolar concentrations were released whereas control experiments without the MOF present did not yield appreciable NO generation [101].

The use of MOF-nitrosyl complex released nitric oxide has concentrated on three areas: anti-thrombosis, antibacterial, and vasodilatory experiments. Each application requires a different release profile for the nitric oxide; antibacterial actions require a much larger dose of nitric oxide than the slow picomole dosage required for antiplatelet action. HKUST-1, which releases only a tiny percentage of the adsorbed nitric oxide, presumably because of the high stability of the copper-nitrosyl complex, was shown to be active in completely inhibiting the aggregation of platelets in human platelet-rich plasma (PRP). Aggregation was initiated using an exogenous agent, and after a short induction period no aggregation could be seen in the NO-loaded MOFs, whereas the MOF tested without NO loading showed no antiplatelet activity.

An investigation of NO-loaded MOF Zn-CPO-27 against methicillin-resistant *S. aureus*, *P. aeruginosa*, and *C. difficile* all showed significant bactericidal effects indicating that NO delivered in this way is very much a potential method of developing new technologies in this increasingly important field [46].

Vasodilatory actions of MOF-released nitric oxide were reported by McKinlay et al. [100]. Here, placement of pellets a distance of 2 mm from the vessel in the 10 mL organ bath resulted in rapid 100% relaxation of the vessel. The pellet could be seen to generate bubbles of gas for 10 min of submersion, although the relaxation remained maximal for >1 h. This effect was not observed when the pellet without nitric oxide loaded was placed in the same position.

Nitric oxide delivery from open framework sites has been developed further in an exciting strategy utilizing the tri-functionality of frameworks, where the fast release of nitric oxide from metal center on exposure to moisture can be combined with slower release of antibacterial drugs which fill up the space in the pores unoccupied by metal-bound nitric oxide. The third functionality is realized through using a bioactive metal such as zinc which is leached very slowly from the framework in buffer solution.

2.7 Structural and Mechanistic Studies of Nitric Oxide Adsorption and Release

The formation of stable nitrosyl complexes within active frameworks make these compounds ideal for studying mechanisms of gas adsorption, particularly selective adsorption. Ultraspecificity in frameworks can be tailored by the functional group present. In the case of the MOF Cu-SIP-3 [102], the dehydration process which activates the material toward gas adsorption takes place via a single-crystal to single-crystal thermally activated transition which goes via an amorphous intermediate and results in an essentially nonporous MOF. This material does not adsorb any of the common gases tried such as hydrogen or carbon dioxide but above a gate-opening pressure, nitric oxide can interact strongly enough with the framework to reverse the phase transition. Thus the material is effectively ultraspecific toward NO showing a 2.2 mmol g^{-1} uptake at 1 atm. of pressure. The nitric oxide uptake of this material was characterized by single-crystal and pair-distribution function analysis, which allowed probing of the ordered and disordered regions, respectively, and determine the order of atomic movements during the dehydration period. This, combined with in situ gas loading experiments using the two techniques was able to postulate that the formation of copper-nitrosyl complexes above the gate-opening pressure was responsible for the uptake and release of nitric oxide from the material [103, 104]. In another example of selectivity, a zinc-TCNQ MOF structure prepared by Kitagawa and co-workers displays nitric oxide selectivity over O_2 adsorption because of their ability to undergo electron transfer with the framework ligand [105].

In addition, the strong interaction of NO with some frameworks makes it useful as a selective probe molecule, especially for flexible frameworks where it can be used to induce changes in some parts of the framework. A prime example of this is in STAM-1, a copper-based MOF with two different channels: one pore lined only by organic groups rendering it hydrophobic while the other is hydrophilic and lined by potential open metal sites [106]. Which channel is accessible can actually be controlled by changing the activation conditions and the adsorption between the two channels can be switched. Here, the nitric oxide can interact relatively strongly with both types of surface, so is an excellent probe for such switchable adsorption. NO adsorption can be used to probe which pore is open as the strong interaction due

to the formation of nitrosyl at the open metal sites that are available leads to a steep increase in uptake at low pressure compared to that in the hydrophobic channel, which has no open metal sites.

3 Looking Ahead: Other Gasotransmitter Molecules

In addition to nitric oxide, there is increasing interest in carbon monoxide and hydrogen sulfide, two other accepted gaseous biological signaling molecules, and their role in biology. Like nitric oxide, the endogenous production mechanism of both gases has been discovered. In fact, the endogenous carbon monoxide production was postulated by Saint-Martin and Nicloux in 1898 [107], though the first experimental evidence was published in two papers by Sjostrand in 1949 and 1951 [108, 109]. It has also been known since the 1950s that breakdown of heme results in the production of carbon monoxide in the body, and in 1968 these facts were linked by the discovery of the enzyme heme oxygenase (HO), the main source of endogenous carbon monoxide, accounting for over 80% of endogenous production [110]. Carbon monoxide production is visible to anyone who has ever had a bruise. This process is illustrated in Fig. 8. Injury to a tissue results in free heme being released from hemoglobin forming a dark red patch (oxyhemoglobin). Free heme does not occur in healthy tissue and is toxic, so it is broken down by the body. HO catalyzes the oxidation of heme, producing first biliverdin (green) and then bilirubin (yellow) and carbon monoxide. This carbon monoxide coordinates to heme to give a bright red color. The blue color seen as the bruise develops is deoxygenated venous blood as the degradation of each heme requires three equivalents of dioxygen.

Most endogenous CO is part of the bloodstream, meaning that in the absence of significant ambient CO, blood Hb–CO levels are around 0.4–1% of the total Hb content [111]. The stability of carbon monoxide means that elimination of CO from the bodies of mammals occurs strictly through exhalation from the lungs with no further metabolism.

Hydrogen sulfide is produced within the body by both enzymatic and nonenzymatic pathways [112]. There are four enzymatic pathways which are known to produce hydrogen sulfide from cysteine derivatives. Of these, the bulk of endogenous H₂S is produced by the enzymes cystathionine- β -synthase (CBS) and cystathionine- γ -lyase (CSE) [113]. L-Cysteine is hydrolyzed by CBS to produce equimolar amounts of H₂S and L-serine. CBS is responsible for the bulk of H₂S production in the brain and central nervous system, whereas CSE is expressed largely in endothelial and smooth muscle cells in the cardiovascular system.

Several estimates of endogenous hydrogen sulfide levels have been made. Many of these show relatively high levels of hydrogen sulfide (50–160 μ M concentrations in brain tissue [114]), but figures should be approached with caution as their measurement involves an assay which is also sensitive to HS⁻ and S²⁻ [115, 116]. Recent estimates of H₂S put levels much lower, for example in a mouse brain the concentration is thought to be 15 nM [115, 117]. As for NO, these low

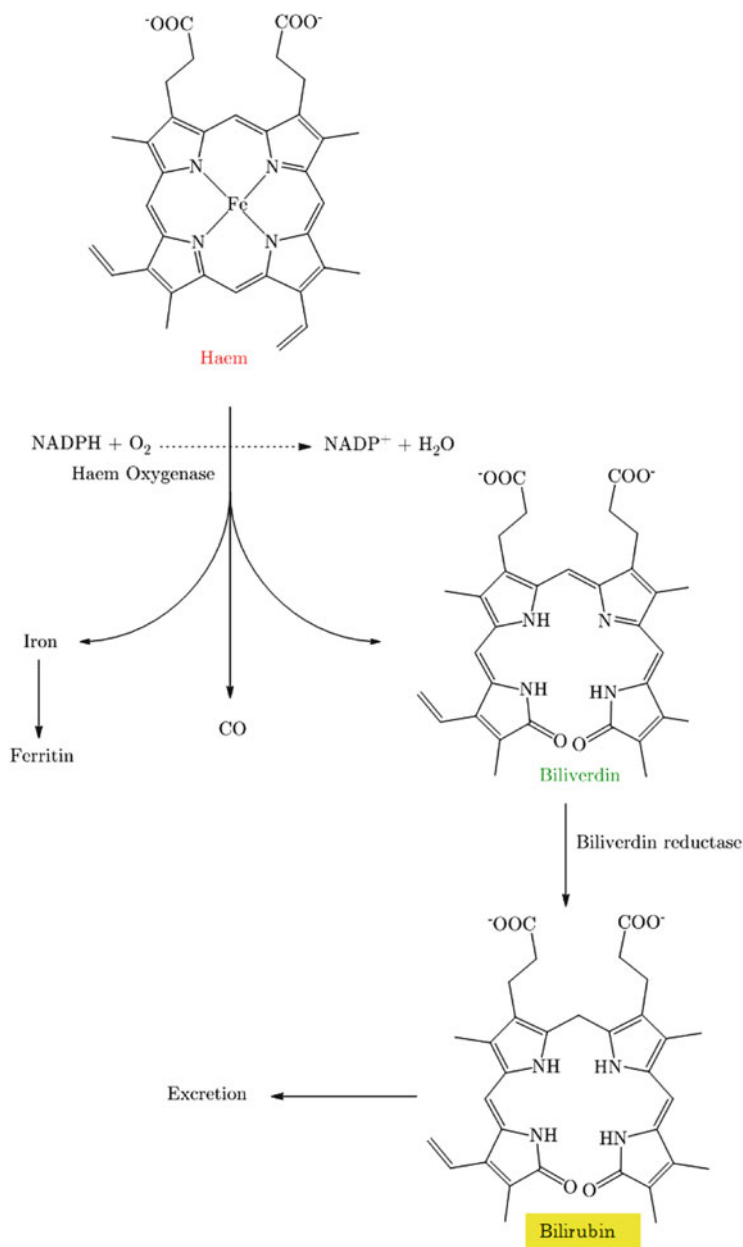


Fig. 8 Oxidation of heme to produce carbon monoxide as a by-product

levels are not necessarily a marker of biological inactivity, but are more of an indication that biological activity takes place rapidly upon production of the H_2S [7]. More accurate methods of measuring endogenous H_2S production is an area of current research [118].

Once produced, hydrogen sulfide is quickly metabolized by a number of pathways meaning that its lifetime in the body is fairly short with a half-life of the order of minutes [18]. Metabolism takes place mainly in the kidneys through oxidation by mitochondria yielding thiosulfate ($S_2O_3^{2-}$), sulfite (SO_3^{2-}), and sulfate (SO_4^{2-}), by methylation to dimethyl sulfide, or by reaction with metallo- or disulfide-containing molecules [2, 119]. One of these metalloproteins – the interaction with hemoglobin – is of particular interest, as this molecule is a common sink for both NO and CO. Interaction of H_2S with porphyrin forms the green sulfhemoglobin, and its formation could significantly alter the binding capacity for other gases [2].

3.1 Carbon Monoxide and Organ Transplantation

Organ transplantation is used routinely as a treatment for end-stage organ disease. A major challenge associated with the process of cold storage and warm reperfusion is ischemia/reperfusion injury⁶ (I/R injury) which affects the short-term and long-term outcomes of transplants. Lack of oxygen to the tissue leads to increased expression of anaerobic mediators which, when combined with reoxygenated blood can lead to an excess of oxygen and radical oxygenating species (ROS).⁷ This causes damage to the organ [120, 121] leading to chronic deterioration of the graft, infection and ultimately graft rejection [120–122]. A shortage of suitable donors leads to the use of more “marginal” organs [122] which are more susceptible to I/R injury and chronic deterioration, and makes patients more likely to suffer post-transplant complications.

The heme oxygenase system has been shown to have cytoprotective effects in transplantation using a number of disease models, and several papers have postulated that it is carbon monoxide generation which underlies this cytoprotective effect [122–124]. Transplants of organs from patients who have died from carbon monoxide poisoning have been successful and have shown reduced susceptibility to I/R injury [125]. Exogenous dosage of carbon monoxide has been shown to have a protective effect against I/R injury in many transplant models, including liver, intestinal, kidney, heart, and lung grafts. Increased survival rates in CO-dosed animals have been reported, indicating that carbon monoxide could be an exciting potential therapeutic in this area [122, 124, 126–129]. More recently, hydrogen sulfide has been suggested to have a similar role in I/R injury models [130, 131].

⁶ Ischemia is a state of tissue oxygen deprivation through loss of blood flow to an organ. Reperfusion is the restoration of blood flow to an ischemic tissue.

⁷ Reactive oxygenating species are intermediates formed by the incomplete one-electron reduction of molecular oxygen and include singlet oxygen, superoxides, peroxides, and hydroxyl radicals. They have crucial roles in oxidative stress, signal transduction, regulation of gene expression, and host defense.

3.2 *Hydrogen Sulfide and Suspended Animation*

Hydrogen sulfide has been shown to have an effect on metabolism and help survival in very low oxygen conditions. Administration of low levels (80 ppm) of hydrogen sulfide to mice led to a suspended animation or “H₂S hibernation” state where the body maintains a baseline metabolism that protects the vital organs from damage until energy supply levels and the heart rate returns to normal [132, 133]. These results indicate that H₂S may be able to protect against some of the effects of hypoxia,⁸ but experiments using larger animals such as sheep [134, 135] and piglets [136] have not seen the same effect, and whether H₂S could induce a hibernation-like state in humans is unknown.

3.3 *Interactions of the Gasotransmitters*

As more research appears in the literature it is becoming clearer that NO, CO, and H₂S all interact with each other and, to some extent, mediate the function of one another at many different levels [112]. There are at least two common sites of action for the three gases involving interaction with heme moieties; all three gases are known to bind to iron in hemoglobin and both CO and NO are known to interact with cGC, an enzyme involved in vasodilation. There are reports that the presence of more than one gasotransmitter has different effects to each gasotransmitter alone, depending on the location and conditions. Each gas appears to be able to regulate the expression of the other two gases, and the best known of these currently is that NO donors up-regulate HO-1, increasing the synthesis of carbon monoxide in blood vessels. The activity of CBS, an H₂S producing enzyme, can be directly inhibited by both nitric oxide and carbon monoxide [18]. H₂S can also induce an up-regulation of anti-inflammatory and cytoprotective genes including heme oxygenase. The interactions of the three gases are likely to be complex and highly dependent on the tissue and the absolute and relative concentrations of the gases involved.

There is less literature describing the interaction of carbon monoxide and hydrogen sulfide releasing media that for nitric oxide, and this reflects the less advanced stage at which biological research has reached to date. However, reports of carbon monoxide-releasing molecules (CORMs) based on transition metal carbonyl complexes, as well as the binding of carbon monoxide to metal centers in zeolites means that progress is being made in this area. The storage of hydrogen sulfide via coordination to the metal center in Ni-CPO-27 and Zn-CPO-27 has been reported crystallographically, and while there is not the exceptional release behavior observed for nitric oxide, the hydrogen sulfide which is released showed the

⁸ Hypoxia is a state when a tissue has an inadequate oxygen supply to allow normal cellular processes to take place.

expected vasodilatory actions [137]. Reports of hydrogen sulfide binding to other MOFs have been reported [138, 139], meaning that these frameworks are a real possibility of release method in this area.

4 General Implications and Future Directions

Since the discovery of the biological significance of NO in the body, the development of NO biology has been remarkable. The development of drug molecules that act as NO donors has perhaps been a little disappointing. However, the targeted delivery of NO from solids has the advantage of potentially avoiding the pitfalls associated with the systemic delivery of such a highly active molecule. However, there are still many challenges. Controlling the rate of release is the key to the development of real applications of solid nitrosyls – whether they are in the form of metal-containing polymers, MOFs or zeolites. Matching the rate and profile of the release to the required biological activity is by no means easy, and getting this right will be pivotal in achieving the desired efficacy of any therapy. However, controlling the release rate, either by changing the materials itself or by altering its formulation, is at least possible, and so there seems great promise that this approach may well in the medium term lead to successful products.

References

1. Wang R (2004) Signal transduction and the gasotransmitters: NO, CO, and H₂S in biology and medicine. Humana, Totowa
2. Wang R (2002) Two's company, three's a crowd: can H₂S be the third endogenous gaseous transmitter? FASEB J 16(13):1792–1798. doi:10.1096/fj.02-0211hyp
3. Mathew ND, Schlipalius DI (2011) Ebert PR (2011). Sulfurous gases as biological messengers and toxins. Comparative genetics of their metabolism in model organisms, J Toxicol. doi:10.1155/2011/394970
4. Wang XB, Jin HF, Tang CS, Du JB (2011) The biological effect of endogenous sulfur dioxide in the cardiovascular system. Eur J Pharmacol 670(1):1–6. doi:10.1016/j.ejphar.2011.08.031
5. Balazy M, Abu-Yousef IA, Harpp DN, Park J (2003) Identification of carbonyl sulfide and sulfur dioxide in porcine coronary artery by gas chromatography/mass spectrometry, possible relevance to EDHF. Biochem Biophys Res Commun 311(3):728–734. doi:10.1016/j.bbrc.2003.10.055
6. Gillman MA (1992) nitrous-oxide as neurotransmitter. Lancet 339(8788):307–307. doi:10.1016/0140-6736(92)91379-m
7. Palmer RMJ, Ferrige AG, Moncada S (1987) Nitric-oxide release accounts for the biological-activity of endothelium-derived relaxing factor. Nature 327(6122):524–526
8. Ignarro LJ, Buga GM, Wood KS, Byrns RE, Chaudhuri G (1987) Endothelium-derived relaxing factor produced and released from artery and vein is nitric-oxide. Proc Natl Acad Sci U S A 84(24):9265–9269. doi:10.1073/pnas.84.24.9265
9. Palmer RMJ, Ashton DS, Moncada S (1988) Vascular endothelial-cells synthesize nitric-oxide from l-arginine. Nature 333(6174):664–666. doi:10.1038/333664a0

10. Li HY, Poulos TL (2005) Structure-function studies on nitric oxide synthases. *J Inorg Biochem* 99(1):293–305. doi:[10.1016/j.jinorgbio.2004.10.016](https://doi.org/10.1016/j.jinorgbio.2004.10.016)
11. Hall CN, Garthwaite J (2009) What is the real physiological NO concentration in vivo? *Nitric Oxide* 21(2):92–103. doi:[10.1016/j.niox.2009.07.002](https://doi.org/10.1016/j.niox.2009.07.002)
12. Beckman JS, Koppenol WH (1996) Nitric oxide, superoxide, and peroxynitrite: the good, the bad, and the ugly. *Am J Physiol Cell Physiol* 271(5):C1424–C1437
13. Keefer LK (2003) Biomaterials – thwarting thrombus. *Nat Mater* 2(6):357–358. doi:[10.1038/Nmat913](https://doi.org/10.1038/Nmat913)
14. Loscalzo J, Welch G (1995) Nitric-oxide and its role in the cardiovascular-system. *Prog Cardiovasc Dis* 38(2):87–104. doi:[10.1016/s0033-0620\(05\)80001-5](https://doi.org/10.1016/s0033-0620(05)80001-5)
15. Radomski MW, Palmer RMJ, Moncada S (1991) Modulation of platelet-aggregation by an L-arginine nitric-oxide pathway. *Trends Pharmacol Sci* 12(3):87–88. doi:[10.1016/0165-6147\(91\)90510-y](https://doi.org/10.1016/0165-6147(91)90510-y)
16. Schaffer MR, Tantry U, Gross SS, Wasserkrug HL, Barbul A (1996) Nitric oxide regulates wound healing. *J Surg Res* 63(1):237–240. doi:[10.1006/jsre.1996.0254](https://doi.org/10.1006/jsre.1996.0254)
17. Papapetropoulos A, Pyriochou A, Altaany Z, Yang GD, Marazioti A, Zhou ZM, Jeschke MG, Branski LK, Herndon DN, Wang R, Szabo C (2009) Hydrogen sulfide is an endogenous stimulator of angiogenesis. *P Natl Acad Sci USA* 106(51):21972–21977. doi:[10.1073/pnas.0908047106](https://doi.org/10.1073/pnas.0908047106)
18. Szabo C (2007) Hydrogen sulphide and its therapeutic potential. *Nat Rev Drug Discov* 6(11):917–935
19. Wallace JL, Dickey M, McKnight W, Martin GR (2007) Hydrogen sulfide enhances ulcer healing in rats. *FASEB J* 21(14):4070–4076. doi:[10.1096/fj.07-8669com](https://doi.org/10.1096/fj.07-8669com)
20. Butler A, Nicholson R (2003) Life, death, and nitric oxide. RSC, Cambridge
21. Ryter SW, Alam J, Choi AM (2006) Heme oxygenase-1/carbon monoxide: from basic science to therapeutic applications. *Physiol Rev* 86(2):583–650. doi:[10.1152/physrev.00011.2005](https://doi.org/10.1152/physrev.00011.2005)
22. Pautz A, Art J, Hahn S, Nowag S, Voss C, Kleinert H (2010) Regulation of the expression of inducible nitric oxide synthase. *Nitric Oxide Biol Chem* 23(2):75–93. doi:[10.1016/j.niox.2010.04.007](https://doi.org/10.1016/j.niox.2010.04.007)
23. Horcajada P, Gref R, Baati T, Allan PK, Maurin G, Couvreur P, Férey G, Morris RE, Serre C (2011) Metal–organic frameworks in biomedicine. *Chem Rev*. doi:[10.1021/cr200256v](https://doi.org/10.1021/cr200256v)
24. Finer NN, Etches PC, Kamstra B, Tierney AJ, Peliowski A, Ryan CA (1994) inhaled nitric-oxide in infants referred for extracorporeal membrane-oxygenation – dose-response. *J Pediatr* 124(2):302–308. doi:[10.1016/s0022-3476\(94\)70324-8](https://doi.org/10.1016/s0022-3476(94)70324-8)
25. Motterlini R, Otterbein LE (2010) The therapeutic potential of carbon monoxide. *Nat Rev Drug Discov* 9(9):U724–U728. doi:[10.1038/nrd3228](https://doi.org/10.1038/nrd3228)
26. Chen ZQ, Zhang J, Stamler JS (2002) Identification of the enzymatic mechanism of nitroglycerin bioactivation. *Proc Natl Acad Sci U S A* 99(12):8306–8311. doi:[10.1073/pnas.122225199](https://doi.org/10.1073/pnas.122225199)
27. Keefer LK (1998) Nitric oxide-releasing compounds: from basic research to promising drugs. *ChemTech* 28(8):30–35
28. Boolell M, Allen MJ, Ballard SA, Gepi-Attee S, Muirhead GJ, Naylor AM, Osterloh IH, Gingell C (1996) Sildenafil: an orally active type 5 cyclic GMP-specific phosphodiesterase inhibitor for the treatment of penile erectile dysfunction. *Int J Impot Res* 8(2):47–52
29. Masters KSB, Leibovich SJ, Belem P, West JL, Poole-Warren LA (2002) Effects of nitric oxide releasing poly(vinyl alcohol) hydrogel dressings on dermal wound healing in diabetic mice. *Wound Repair Regen* 10(5):286–294. doi:[10.1046/j.1524-475X.2002.10503.x](https://doi.org/10.1046/j.1524-475X.2002.10503.x)
30. Zhao H, Feng Y, Guo J (2011) Polycarbonateurethane films containing complex of copper(II) catalyzed generation of nitric oxide. *J Appl Polym Sci* 122(3):1712–1721. doi:[10.1002/app.34056](https://doi.org/10.1002/app.34056)
31. Bohl KS, West JL (2000) Nitric oxide-generating polymers reduce platelet adhesion and smooth muscle cell proliferation. *Biomaterials* 21(22):2273–2278. doi:[10.1016/s0142-9612\(00\)00153-8](https://doi.org/10.1016/s0142-9612(00)00153-8)

32. Kushwaha M, Anderson JM, Bosworth CA, Andukuri A, Minor WP, Lancaster JR Jr, Anderson PG, Brott BC, Jun H-W (2010) A nitric oxide releasing, self assembled peptide amphiphile matrix that mimics native endothelium for coating implantable cardiovascular devices. *Biomaterials* 31(7):1502–1508. doi:[10.1016/j.biomaterials.2009.10.051](https://doi.org/10.1016/j.biomaterials.2009.10.051)
33. Riccio DA, Dobmeier KP, Hetrick EM, Privett BJ, Paul HS, Schoenfisch MH (2009) Nitric oxide-releasing S-nitrosothiol-modified xerogels. *Biomaterials* 30(27):4494–4502. doi:[10.1016/j.biomaterials.2009.05.006](https://doi.org/10.1016/j.biomaterials.2009.05.006)
34. Eroy-Reveles AA, Mascharak PK (2009) Nitric oxide-donating materials and their potential in pharmacological applications for site-specific nitric oxide delivery. *Future Med Chem* 1(8):1497–1507. doi:[10.4155/fmc.09.111](https://doi.org/10.4155/fmc.09.111)
35. Rose MJ, Mascharak PK (2008) Fiat Lux: selective delivery of high flux of nitric oxide (NO) to biological targets using photoactive metal nitrosyls. *Curr Opin Chem Biol* 12(2):238–244. doi:<http://dx.doi.org/10.1016/j.cbpa.2008.02.009>
36. Rose MJ, Fry NL, Marlow R, Hinck L, Mascharak PK (2008) Sensitization of ruthenium nitrosyls to visible light via direct coordination of the dye resorufin: trackable NO donors for light-triggered NO delivery to cellular targets. *J Am Chem Soc* 130(27):8834–8846. doi:[10.1021/ja801823f](https://doi.org/10.1021/ja801823f)
37. DeRosa F, Bu X, Ford PC (2005) Chromium(III) complexes for photochemical nitric oxide generation from coordinated nitrite: synthesis and photochemistry of macrocyclic complexes with pendant chromophores, trans-[Cr(L)(ONO)₂]BF₄. *Inorg Chem* 44(12):4157–4165. doi:[10.1021/ic048311n](https://doi.org/10.1021/ic048311n)
38. Rose MJ, Mascharak PK (2008) Photoactive ruthenium nitrosyls: effects of light and potential application as NO donors. *Coord Chem Rev* 252(18–20):2093–2114. doi:[10.1016/j.ccr.2007.11.011](https://doi.org/10.1016/j.ccr.2007.11.011)
39. Ghosh K, Eroy-Reveles AA, Avila B, Holman TR, Olmstead MM, Mascharak PK (2004) Reactions of NO with Mn(II) and Mn(III) centers coordinated to carboxamido nitrogen: synthesis of a manganese nitrosyl with photolabile NO. *Inorg Chem* 43(9):2988–2997. doi:[10.1021/ic030331n](https://doi.org/10.1021/ic030331n)
40. Eroy-Reveles AA, Leung Y, Beavers CM, Olmstead MM, Mascharak PK (2008) Near-infrared light activated release of nitric oxide from designed photoactive manganese nitrosyls: strategy, design, and potential as NO donors. *J Am Chem Soc* 130(13):4447–4458. doi:[10.1021/ja710265j](https://doi.org/10.1021/ja710265j)
41. Flitney FW, Megson IL, Thomson JLM, Kennovin GD, Butler AR (1996) Vasodilator responses of rat isolated tail artery enhanced by oxygen-dependent, photochemical release of nitric oxide from iron–sulphur–nitrosyls. *Br J Pharmacol* 117(7):1549–1557. doi:[10.1111/j.1476-5381.1996.tb15320.x](https://doi.org/10.1111/j.1476-5381.1996.tb15320.x)
42. Heilman BJ, St John J, Oliver SRJ, Mascharak PK (2012) Light-triggered eradication of *Acinetobacter baumannii* by means of NO delivery from a porous material with an entrapped metal nitrosyl. *J Am Chem Soc* 134(28):11573–11582. doi:[10.1021/ja3022736](https://doi.org/10.1021/ja3022736)
43. Halpenny GM, Heilman B, Mascharak PK (2012) Nitric oxide (NO)-induced death of gram-negative bacteria from a light-controlled NO-releasing platform. *Chem Biodivers* 9(9):1829–1839. doi:[10.1002/cbdv.201100320](https://doi.org/10.1002/cbdv.201100320)
44. Halpenny GM, Gandhi KR, Mascharak PK (2010) Eradication of pathogenic bacteria by remote delivery of NO via light triggering of nitrosyl-containing materials. *ACS Med Chem Lett* 1(4):180–183. doi:[10.1021/ml1000646](https://doi.org/10.1021/ml1000646)
45. Eroy-Reveles AA, Leung Y, Mascharak PK (2006) Release of nitric oxide from a Sol–Gel hybrid material containing a photoactive manganese nitrosyl upon illumination with visible light. *J Am Chem Soc* 128(22):7166–7167. doi:[10.1021/ja061852n](https://doi.org/10.1021/ja061852n)
46. Rodrigues FP, Pestana CR, Polizello ACM, Pardo-Andreu GL, Uyemura SA, Santos AC, Alberici LC, da Silva RS, Curti C (2012) Release of NO from a nitrosyl ruthenium complex through oxidation of mitochondrial NADH and effects on mitochondria. *Nitric Oxide* 26(3):174–181. doi:<http://dx.doi.org/10.1016/j.niox.2012.02.001>

47. Wright PA, Royal Society of Chemistry (Great Britain) (2008) Microporous framework solids. RSC materials monographs. RSC Publishing, Cambridge
48. Ma S, Zhou HC (2010) Gas storage in porous metal–organic frameworks for clean energy applications. *Chem Commun (Camb)* 46(1):44–53. doi:[10.1039/b916295j](https://doi.org/10.1039/b916295j)
49. Morris RE, Wheatley PS (2008) Gas storage in nanoporous materials. *Angew Chem Int Ed* 47(27):4966–4981. doi:[10.1002/anie.200703934](https://doi.org/10.1002/anie.200703934)
50. Mueller U, Schubert M, Teich F, Puetter H, Schierle-Arndt K, Pastre J (2006) Metal–organic frameworks–prospective industrial applications. *J Mater Chem* 16(7):626–636
51. Thallapally PK, Kirby KA, Atwood JL (2007) Comparison of porous and nonporous materials for methane storage. *New J Chem* 31(5):628–630. doi:[10.1039/b610321a](https://doi.org/10.1039/b610321a)
52. Suh MP, Park HJ, Prasad TK, Lim D-W (2011) Hydrogen storage in metal–organic frameworks. *Chem Rev.* doi:[10.1021/cr200274s](https://doi.org/10.1021/cr200274s)
53. Herm ZR, Swisher JA, Smit B, Krishna R, Long JR (2011) Metal–organic frameworks as adsorbents for hydrogen purification and precombustion carbon dioxide capture. *J Am Chem Soc* 133(15):5664–5667. doi:[10.1021/ja111411q](https://doi.org/10.1021/ja111411q)
54. Sumida K, Rogow DL, Mason JA, McDonald TM, Bloch ED, Herm ZR, Bae T-H, Long JR (2011) Carbon dioxide capture in metal–organic frameworks. *Chem Rev.* doi:[10.1021/cr2003272](https://doi.org/10.1021/cr2003272)
55. Rouquerol Fo, Rouquerol J, Sing KSW (1999) Adsorption by powders and porous solids : principles, methodology and applications. Academic, San Diego, London
56. Murray LJ, Dinca M, Long JR (2009) Hydrogen storage in metal–organic frameworks. *Chem Soc Rev* 38(5):1294–1314. doi:[10.1039/b802256a](https://doi.org/10.1039/b802256a)
57. Chui SSY, Lo SMF, Charmant JPH, Orpen AG, Williams ID (1999) A chemically functionalizable nanoporous material [Cu-3(TMA)(2)(H₂O)(3)](n). *Science* 283(5405):1148–1150
58. Dinca M, Long JR (2007) High-enthalpy hydrogen adsorption in cation-exchanged variants of the microporous metal–organic framework Mn-3[(Mn₄Cl)(3)(BTT)(8)(CH₃OH)(10)](2). *J Am Chem Soc* 129(36):11172–11176. doi:[10.1021/Ja072871f](https://doi.org/10.1021/Ja072871f)
59. Zhou W, Wu H, Yildirim T (2008) Enhanced H₂ adsorption in isostructural metal–organic frameworks with open metal sites: strong dependence of the binding strength on metal ions. *J Am Chem Soc* 130(46):15268–15269. doi:[10.1021/ja807023q](https://doi.org/10.1021/ja807023q)
60. Eddaoudi M, Kim J, Rosi N, Vodak D, Wachter J, O’Keeffe M, Yaghi OM (2002) Systematic design of pore size and functionality in isoreticular MOFs and their application in methane storage. *Science* 295(5554):469–472. doi:[10.1126/science.1067208](https://doi.org/10.1126/science.1067208)
61. Wu H, Simmons JM, Liu Y, Brown CM, Wang XS, Ma S, Peterson VK, Southon PD, Kepert CJ, Zhou HC, Yildirim T, Zhou W (2010) Metal–organic frameworks with exceptionally high methane uptake: where and how is methane stored? *Chemistry* 16(17):5205–5214. doi:[10.1002/chem.200902719](https://doi.org/10.1002/chem.200902719)
62. Ma S, Sun D, Simmons JM, Collier CD, Yuan D, Zhou H-C (2008) Metal–organic framework from an anthracene derivative containing nanoscopic cages exhibiting high methane uptake. *J Am Chem Soc* 130(3):1012–1016. doi:[10.1021/ja0771639](https://doi.org/10.1021/ja0771639)
63. Fletcher AJ, Thomas KM, Rosseinsky MJ (2005) Flexibility in metal–organic framework materials: impact on sorption properties. *J Solid State Chem* 178(8):2491–2510
64. Serre C, Mellot-Draznieks C, Surble S, Audebrand N, Filinchuk Y, Ferey G (2007) Role of solvent–host interactions that lead to very large swelling of hybrid frameworks. *Science* 315(5820):1828–1831. doi:[10.1126/science.1137975](https://doi.org/10.1126/science.1137975)
65. Tanaka D, Nakagawa K, Higuchi M, Horike S, Kubota Y, Kobayashi Tatsuo C, Takata M, Kitagawa S (2008) Kinetic gate-opening process in a flexible porous coordination polymer13. *Angew Chem Int Ed* 47(21):3914–3918
66. Fukushima T, Horike S, Inubushi Y, Nakagawa K, Kubota Y, Takata M, Kitagawa S (2010) Solid solutions of soft porous coordination polymers: fine-tuning of gas adsorption properties. *Angew Chem Int Ed Engl.* doi:[10.1002/anie.201002349](https://doi.org/10.1002/anie.201002349)

67. Horike S, Inubushi Y, Hori T, Fukushima T, Kitagawa S (2012) A solid solution approach to 2D coordination polymers for CH₄/CO₂ and CH₄/C₂H₆ gas separation: equilibrium and kinetic studies. *Chem Sci* 3(1)
68. Cheng Y, Kajiro H, Noguchi H, Kondo A, Ohba T, Hattori Y, Kaneko K, Kanoh H (2011) Tuning of gate opening of an elastic layered structure MOF in CO₂ sorption with a trace of alcohol molecules. *Langmuir* 27(11):6905–6909. doi:10.1021/la201008v
69. Uchida S, Kawamoto R, Tagami H, Nakagawa Y, Mizuno N (2008) Highly selective sorption of small unsaturated hydrocarbons by nonporous flexible framework with silver ion. *J Am Chem Soc* 130(37):12370–12376. doi:10.1021/ja801453c
70. Kinoshita Y, Matsubara, I, Higuchi T, Saito Y (1959) *Bull Chem Soc Japan* 32(11):1221
71. Furukawa H, Ko N, Go YB, Aratani N, Choi SB, Choi E, Yazaydin AO, Snurr RQ, O’Keeffe M, Kim J, Yaghi OM (2010) Ultrahigh porosity in metal–organic frameworks. *Science* 329(5990):424–428. doi:10.1126/science.1192160
72. Eddaoudi M, Moler DB, Li HL, Chen BL, Reineke TM, O’Keeffe M, Yaghi OM (2001) Modular chemistry: Secondary building units as a basis for the design of highly porous and robust metal–organic carboxylate frameworks. *Acc Chem Res* 34(4):319–330
73. Rosi NL, Eckert J, Eddaoudi M, Vodak DT, Kim J, O’Keeffe M, Yaghi OM (2003) Hydrogen storage in microporous metal–organic frameworks. *Science* 300(5622):1127–1129
74. Byrne PJ (2009) Structural studies of ionic liquids and ionothermally-prepared materials. University of St Andrews
75. Bloch ED, Murray LJ, Queen WL, Chavan S, Maximoff SN, Bigi JP, Krishna R, Peterson VK, Grandjean F, Long GJ, Smit B, Bordiga S, Brown CM, Long JR (2011) Selective binding of O₂ over N₂ in a redox–active metal–organic framework with open iron(II) coordination sites. *J Am Chem Soc* 133(37):14814–14822. doi:10.1021/ja205976v
76. An J, Farha OK, Hupp JT, Pohl E, Yeh JI, Rosi NL (2012) Metal-adeninate vertices for the construction of an exceptionally porous metal–organic framework. *Nat Commun* 3:604
77. Cohen SM (2011) Postsynthetic methods for the functionalization of metal–organic frameworks. *Chem Rev.* doi:10.1021/cr200179u
78. Li J-R, Kuppler RJ, Zhou H-C (2009) Selective gas adsorption and separation in metal–organic frameworks. *Chem Soc Rev* 38(5):1477–1504
79. Li J-R, Sculley J, Zhou H-C (2011) Metal–organic frameworks for separations. *Chem Rev.* doi:10.1021/cr200190s
80. Lee J, Farha OK, Roberts J, Scheidt KA, Nguyen ST, Hupp JT (2009) Metal–organic framework materials as catalysts. *Chem Soc Rev* 38(5):1450–1459
81. Yoon M, Srirambalaji R, Kim K (2011) Homochiral metal–organic frameworks for asymmetric heterogeneous catalysis. *Chem Rev.* doi:10.1021/cr2003147
82. Corma A, Garcia H, Llabres I, Xamena FX (2010) Engineering metal organic frameworks for heterogeneous catalysis. *Chem Rev* 110(8):4606–4655. doi:10.1021/cr9003924
83. Allendorf MD, Bauer CA, Bhakta RK, Houk RJT (2009) Luminescent metal–organic frameworks. *Chem Soc Rev* 38(5):1330–1352
84. Kreno LE, Leong K, Farha OK, Allendorf M, Van Duyne RP, Hupp JT (2011) Metal–organic framework materials as chemical sensors. *Chem Rev.* doi:10.1021/cr200324t
85. Kurmoo M (2009) Magnetic metal–organic frameworks. *Chem Soc Rev* 38(5):1353–1379
86. Cruz WV, Leung PCW, Seff K (1979) Crystal structure of nitric oxide and nitrogen dioxide sorption complexes of partially cobalt(II)-exchanged zeolite A. *Inorg Chem* 18(6):1692–1696. doi:10.1021/ic50196a059
87. Jeong GH, Kim Y, Seff K (2006) Crystal structures of the NO and NO₂ sorption complexes of fully dehydrated fully Mn²⁺-exchanged zeolite X (FAU). *Microporous Mesoporous Mater* 93 (1–3):12–22. doi:10.1016/j.micromeso.2006.01.020
88. Lee YM, Kim Y, Seff K (2005) Crystal structures of the NO and N₂O₄ sorption complexes of fully dehydrated fully Cd²⁺-exchanged zeolite X (FAU): coordination of neutral NO and N₂O₄ to Cd²⁺. *J Phys Chem B* 109(11):4900–4908. doi:10.1021/Jp040698t

89. Wheatley PS, Butler AR, Crane MS, Fox S, Xiao B, Rossi AG, Megson IL, Morris RE (2006) NO-releasing zeolites and their antithrombotic properties. *J Am Chem Soc* 128(2):502–509. doi:10.1021/Ja0503579
90. Wheatley PS, McKinlay AC, Morris RE (2008) A comparison of zeolites and metal organic frameworks as storage and delivery vehicles for biologically active nitric oxide. In: Antoine Gédéon PM, Florence B (eds) *Studies in surface science and catalysis*, vol 174, Part A. Elsevier, Amsterdam, Netherlands. pp 441–446. doi:10.1016/s0167-2991(08)80236-4
91. Fox S, Wilkinson TS, Wheatley PS, Xiao B, Morris RE, Sutherland A, Simpson AJ, Barlow PG, Butler AR, Megson IL, Rossi AG (2010) NO-loaded Zn²⁺-exchanged zeolite materials: a potential bifunctional anti-bacterial strategy. *Acta Biomater* 6(4):1515–1521. doi:http://dx.doi.org/10.1016/j.actbio.2009.10.038
92. Wei F, Yuan Yang J, Hou Q, Hua Zhu J (2010) Moisture-saturated zeolites – a new strategy for releasing nitric oxide. *New J Chem* 34(12):2897–2905
93. Mowbray M, Tan XJ, Wheatley PS, Morris RE, Weller RB (2008) Topically applied nitric oxide induces T-lymphocyte infiltration in human skin, but minimal inflammation. *J Invest Dermatol* 128(2):352–360. doi:10.1038/sj.jid.5701096
94. McKinlay AC (2010) New nitric oxide releasing materials. University of St Andrews, St Andrews
95. Xiao B, Wheatley PS, Zhao XB, Fletcher AJ, Fox S, Rossi AG, Megson IL, Bordiga S, Regli L, Thomas KM, Morris RE (2007) High-capacity hydrogen and nitric oxide adsorption and storage in a metal–organic framework. *J Am Chem Soc* 129(5):1203–1209. doi:10.1021/Ja066098k
96. Ferey G, Mellot-Draznieks C, Serre C, Millange F, Dutour J, Surble S, Margiolaki I (2005) A chromium terephthalate-based solid with unusually large pore volumes and surface area. *Science* 309(5743):2040–2042. doi:10.1126/science.1116275
97. Ohkubo T, Takehara Y, Kuroda Y (2012) Water-initiated ordering around a copper ion of copper acetate confined in slit-shaped carbon micropores. *Microporous Mesoporous Mater* 154:82–86. doi:10.1016/j.micromeso.2011.09.011
98. Ingleson MJ, Heck R, Gould JA, Rosseinsky MJ (2009) Nitric oxide chemisorption in a postsynthetically modified metal–organic framework. *Inorg Chem* 48(21):9986–9988. doi:10.1021/ic9015977
99. Nguyen JG, Tanabe KK, Cohen SM (2010) Postsynthetic diazeniumdiolate formation and NO release from MOFs. *Cryst Eng Comm* 12(8):2335–2338
100. McKinlay AC, Xiao B, Wragg DS, Wheatley PS, Megson IL, Morris RE (2008) Exceptional behavior over the whole adsorption-storage-delivery cycle for NO in porous metal organic frameworks. *J Am Chem Soc* 130(31):10440–10444. doi:10.1021/ja801997r
101. Harding JL, Reynolds MM (2012) Metal organic frameworks as nitric oxide catalysts. *J Am Chem Soc*. doi:10.1021/ja210771m
102. Xiao B, Byrne PJ, Wheatley PS, Wragg DS, Zhao X, Fletcher AJ, Thomas KM, Peters L, EvansJohn SO, Warren JE, Zhou W, Morris RE (2009) Chemically blockable transformation and ultrasensitive low-pressure gas adsorption in a non-porous metal organic framework. *Nat Chem* 1(4):289–294
103. Allan PK, Chapman KW, Chupas PJ, Hriljac JA, Renouf CL, Lucas TCA, Morris RE (2012) Pair distribution function-derived mechanism of a single-crystal to disordered to single-crystal transformation in a hemilabile metal–organic framework. *Chem Sci* 3(8):2559–2564. doi:10.1039/c2sc20261a
104. Allan PK, Xiao B, Teat SJ, Knight JW, Morris RE (2010) In situ single-crystal diffraction studies of the structural transition of metal–organic framework copper 5-sulfoisophthalate, Cu-SIP-3. *J Am Chem Soc* 132(10):3605–3611. doi:10.1021/Ja910600b
105. Shimomura S, Higuchi M, Matsuda R, Yoneda K, Hijikata Y, Kubota Y, Mita Y, Kim J, Takata M, Kitagawa S (2010) Selective sorption of oxygen and nitric oxide by an electron-donating flexible porous coordination polymer. *Nat Chem* 2(8):633–637
106. Mohideen MIH, Xiao B, Wheatley PS, McKinlay AC, Li Y, Slawin AMZ, Aldous DW, Cessford NF, Duren T, Zhao XB, Gill R, Thomas KM, Griffin JM, Ashbrook SE, Morris RE (2011) Protecting group and switchable pore-discriminating adsorption properties of a

- hydrophilic–hydrophobic metal–organic framework. *Nat Chem* 3(4):304–310. doi:10.1038/Nchem.1003
107. Wu LY, Wang R (2005) Carbon monoxide: endogenous production, physiological functions, and pharmacological applications. *Pharmacol Rev* 57(4):585–630. doi:10.1124/pr.57.4.3
 108. Sjostrand T (1951) Endogenous formation of carbon monoxide; the CO concentration in the inspired and expired air of hospital patients. *Acta Physiol Scand* 22(2–3):137–141
 109. Sjostrand T (1949) Endogenous formation of carbon monoxide in man. *Nature* 164(4170):580
 110. Tenhunen R, Marver HS, Schmid R (1968) The enzymatic conversion of heme to bilirubin by microsomal heme oxygenase. *Proc Natl Acad Sci* 61(2):748–755
 111. Von Burg DR (1999) Toxicology update. *J Appl Toxicol* 19(5):379–386. doi:10.1002/(sici)1099-1263(199909/10)19:5<379::aid-jat563>3.0.co;2-8
 112. Li L, Hsu A, Moore PK (2009) Actions and interactions of nitric oxide, carbon monoxide and hydrogen sulphide in the cardiovascular system and in inflammation – a tale of three gases! *Pharmacol Therapeut* 123(3):386–400. doi:10.1016/j.pharmthera.2009.05.005
 113. Awata S, Nakayama K, Suzuki I, Sugahara K, Kodama H (1995) changes in cystathionine gamma-lyase in various regions of rat-brain during development. *Biochem Mol Biol Int* 35(6):1331–1338
 114. Abe K, Kimura H (1996) The possible role of hydrogen sulfide as an endogenous neuromodulator. *J Neurosci* 16(3):1066–1071
 115. Wang H, Koster TK, Trease NM, Segalini J, Taberna PL, Simon P, Gogotsi Y, Grey CP (2011) Real-time NMR studies of electrochemical double-layer capacitors. *J Am Chem Soc* 133(48):19270–19273. doi:10.1021/ja2072115
 116. Albert T (2009) Measurement and biological significance of the volatile sulfur compounds hydrogen sulfide, methanethiol and dimethyl sulfide in various biological matrices. *J Chromatogr B* 877(28):3366–3377. doi:10.1016/j.jchromb.2009.05.026
 117. Furne J, Saeed A, Levitt MD (2008) Whole tissue hydrogen sulfide concentrations are orders of magnitude lower than presently accepted values. *Am J Physiol Regul Integr Comp Physiol* 295(5):R1479–R1485. doi:10.1152/ajpregu.90566.2008
 118. Sasakura K, Hanaoka K, Shibuya N, Mikami Y, Kimura Y, Komatsu T, Ueno T, Terai T, Kimura H, Nagano T (2011) Development of a highly selective fluorescence probe for hydrogen sulfide. *J Am Chem Soc* 133(45):18003–18005. doi:10.1021/ja207851s
 119. Beauchamp RO, Bus JS, Popp JA, Boreiko CJ, Andjelkovich DA (1984) A critical-review of the literature on hydrogen–sulfide toxicity. *CRC Crit Rev Toxicol* 13(1):25–97. doi:10.3109/10408448409029321
 120. Jaeschke H (1996) Preservation injury: mechanisms, prevention and consequences. *J Hepatol* 25(5):774–780
 121. Clavien PA, Harvey PRC, Strasberg SM (1992) Preservation and reperfusion injuries in liver allografts – an overview and synthesis of current studies. *Transplantation* 53(5):957–978
 122. Nakao A, Choi AMK, Murase N (2006) Protective effect of carbon monoxide in transplantation. *J Cell Mol Med* 10(3):650–671. doi:10.2755/jcmm010.003.16
 123. Abraham NG, Kappas A (2005) Heme oxygenase and the cardiovascular-renal system. *Free Radic Bio Med* 39(1):1–25. doi:10.1016/j.freeradbiomed.2005.03.010
 124. Nakao A, Otterbein LE, Overhaus M, Sarady JK, Tsung A, Kimizuka K, Nalesnik MA, Kaizu T, Uchiyama T, Liu F, Murase N, Bauer AJ, Bach FH (2004) Biliverdin protects the functional integrity of a transplanted syngeneic small bowel. *Gastroenterology* 127(2):595–606. doi:10.1053/j.gastro.2004.05.059
 125. Luckraz H, Tsui SS, Parameshwar J, Wallwork J, Large SR (2001) Improved outcome with organs from carbon monoxide poisoned donors for intrathoracic transplantation. *Ann Thorac Surg* 72(3):709–713
 126. Nakao A, Kimizuka K, Stolz DB, Neto JS, Kaizu T, Choi AM, Uchiyama T, Zuckerbraun BS, Bauer AJ, Nalesnik NA, Otterbein LE, Geller DA, Murase N (2003) Protective

- effect of carbon monoxide inhalation for cold-preserved small intestinal grafts. *Surgery* 134 (2):285–292. doi:10.1067/Msy.2003.238
127. Nakao A, Kimizuka K, Stolz DB, Neto JS, Kaizu T, Choi AMK, Uchiyama T, Zuckerbraun BS, Nalesnik MA, Otterbein LE, Murase N (2003) Carbon monoxide inhalation protects rat intestinal grafts from ischemia/reperfusion injury. *Am J Pathol* 163(4):1587–1598
 128. Nakao A, Toyokawa H, Kimizuka K, Kiyomoto T, Bailey RJ, Nalesnik MA, Murase N (2004) Carbon monoxide inhalation protects heart allograft from chronic rejection. *Am J Transplant* 4:461–461
 129. Nakao A, Toyokawa H, Tsung A, Nalesnik MA, Stolz DB, Kohmoto J, Ikeda A, Tomiyama K, Harada T, Takahashi T, Yang R, Fink MP, Morita K, Choi AMK, Murase N (2006) Ex vivo application of carbon monoxide in University of Wisconsin solution to prevent intestinal cold ischemia/reperfusion injury. *Am J Transplant* 6(10):2243–2255. doi:10.1111/j.1600-6143.2006.01465.x
 130. Wagner F, Asfar P, Calzia E, Radermacher P, Szabo C (2009) Bench-to-bedside review: hydrogen sulfide – the third gaseous transmitter: applications for critical care. *Crit Care* 13(3)
 131. Lowicka E, Beltowski J (2007) Hydrogen sulfide (H₂S) – the third gas for interest for pharmacologists. *Pharmacol Rep* 59(1):4–24
 132. Blackstone E, Morrison M, Roth MB (2005) H₂S induces a suspended animation-like state in mice. *Science* 308(5721):518–518. doi:10.1126/science.11108581
 133. Dangani R (2005) Torpor on demand – mice exposed to H₂S enter reversible state of suspended animation. *Chem Eng News* 83(17):8–8
 134. Haouzi P, Notet V, Chenuel B, Chalou B, Sponne I, Ogier V, Bihain B (2008) H₂S induced hypometabolism in mice is missing in sedated sheep. *Respir Physiol Neurobiol* 160(1):109–115. doi:10.1016/j.resp.2007.09.001
 135. Haouzi P, Bell H, Philmon M (2011) Hydrogen sulfide oxidation and the arterial chemoreflex: effect of methemoglobin. *Respir Physiol Neurobiol* 177(3):273–283. doi:10.1016/j.resp.2011.04.025
 136. Li J, Zhang G, Cai S, Redington AN (2008) Effect of inhaled hydrogen sulfide on metabolic responses in anesthetized, paralyzed, and mechanically ventilated piglets. *Pediatr Crit Care Med* 9(1):110–112. doi:10.1097/01.pcc.0000298639.08519.oc
 137. Allan PK, Wheatley PS, Aldous D, Mohideen MI, Tang C, Hriljac JA, Megson IL, Chapman KW, De Weireld G, Vaesen S, Morris RE (2012) Metal–organic frameworks for the storage and delivery of biologically active hydrogen sulfide. *Dalton Trans* 41(14):4060–4066
 138. Hamon L, Leclerc H, Ghoufi A, Oliviero L, Travert A, Lavalley J-C, Devic T, Serre C, Férey Gr, De Weireld G, Vimont A, Maurin G (2011) Molecular insight into the adsorption of H₂S in the flexible MIL-53(Cr) and rigid MIL-47(V) MOFs: infrared spectroscopy combined to molecular simulations. *J Phys Chem C* 115(5):2047–2056. doi:10.1021/jp1092724
 139. Hamon L, Vimont A, Serre C, Devic T, Ghoufi A, Maurin G, Loiseau T, Millange F, Daturi M, Férey G, De Weireld G (2009) Study of hydrogen sulphide adsorption on Mil-47(V) and Mil-53(Al, Cr, Fe) metal–organic frameworks by isotherms measurements and in-situ IR experiments. *Character Porous Solids VIII* 446(318):25–31

Index

A

Alkoxy ligands, 14
Alkylimido complexes, 14
Alkyloxy ligands, 14
Ambiphilic ligands, 1, 15
Ambivalency, 6
Amphoteric valence tautomerism, 1
Angina, 232
Aquacobalamin, 119
Arginine, 158, 229, 230
Aryl ligands, 14
Axial thiolate ligation, 188, 207, 213

B

Benzimidazole, 65
Bilirubin, 246
Bis(dinitrosyliron) derivatives, 61
Bis(2-pyridylmethyl)(benzyl)amine, 118

C

Calmodulin, 229
Carbon monoxide, 55, 89, 227, 232, 245, 248
Carbon monoxide-releasing molecules (CORMs), 248
Carbonyl sulfide, 227
Carbynes, 32
Ceruloplasmin, 126
Chelatable iron pool (CIP), 116
Chloroperoxidase, 188
Citrulline, 230
Cobalamin, 119
Cobalt, 173
Cobalt-porphyrin peroxyxynitrite, 159
Co-CPO-27, 243

Complementary spherical electron density model, 1, 20
Coordinatively unsaturated sites (CUS), 235
Copper, 99, 104, 109, 118, 137, 140
Crystallography, 155
Cu-SIP-3, 244
Cyclobutyl 1,4-benzenedicarboxylate, 236
Cystathionine- β -synthase (CBS), 245
Cystathionine- γ -lyase (CSE), 245
Cysteinate, 125, 158
Cysteine, 55, 64, 70, 78, 94, 245
Cytochrome *c*, 112, 121
Cytochrome *c* nitrite reductase (CcNIR), 203, 217
Cytochrome *c* oxidases (CcOs), 130, 158, 233
Cytochrome oxidase inhibition, 110
Cytochrome P450, 186, 188, 213

D

Deoxyhemoglobin, 117
DFT, 6, 9, 18, 46, 72, 155, 176, 214
Dialkylamido ligands, 14
Diazeniumdiolate compounds (NONOates), 232, 239
Dicarbonyldinitrosyl iron, 55
4,6-Dimethyl-2-mercaptopyrimidine, 71
Dimethyl sulfide, 247
Dinitrosyl iron complexes (DNICs), 53, 56, 70, 76, 92, 94, 103, 116
Dioxygen, 7, 128
Dynamic switching, 25

E

Effective atomic number rule (EAN), 5
Electronegativities, 4

Electron paramagnetic resonance (EPR), 104, 175

Electronic structure, 1, 4, 155

ENDOR, 141, 159, 178, 184

F

Ferric heme–nitrosyls, 169, 186, 204

Ferric porphyrins, 121

Ferroheme proteins, 114

Ferrohemoglobin NO adduct, 121

Ferrous heme–nitrosyls, 160, 174, 193, 210

Ferrous nitrosyl heme proteins, 114

Ferrous nitrosyl porphyrinato complexes, 114

Flash photolysis, 108

Flavin adenine dinucleotide (FAD), 229

Flavin mononucleotide (FMN), 229

Fluorescein, 126

G

Gas adsorption, 225

Gasotransmitters, 3, 227

therapeutics, 231

Gas storage, 234

Glutathione, 122

Graft rejection, 247

carbon monoxide, 247

Guanylyl cyclase, soluble (sGC), 43,

106, 158

Guanylyl monophosphate, cyclic (cGMP), 101

Guanylyl triphosphate (GTP), 101

H

Hafnium, 26

Heme, 99

models, 99, 110

oxidation, 246

Heme-copper oxidase, 138

Heme-hyponitrite dimer, 159

Heme–nitrosyls, 160

electronic structures, 193

Heme oxygenase (HO), 245, 247

Heme proteins, 155

Hemoglobin, 101, 106, 114, 117, 129, 233

Hibernation, hydrogen sulfide, 248

Histidine imidazole, 105

HKUST-1, 238, 242, 243

HNO, 155

Hydrogen sulfide, 227, 245, 248

Hypoxia, 248

I

Imidazoles, 64, 85, 94, 175, 187, 190, 205, 237

Imido complexes, isolobal, 1, 45

Innocent ligands 5

Iodine, 1, 8, 15, 18, 47

Iron, 99

Iron carbonyls, 24

Ironpentacarbonyl, 56

Iron (III) porphyrinate, 169

Iron porphyrins, 155

Iron–selenium nitrosyl cluster, 80

Iron sulfur cluster, 53

Iron–sulfur nitrosyl cluster, 80

Ischemia, 247

Isolobal analogy, 1

L

Lewis acid/bases, ambivalent, 1, 8

Ligands, ambivalent, 6, 9

Ligand-to-metal σ / π - donation, 120

Z-type, 20

Lipocalin, 159

M

Manganese, 173, 233

Manganese (III) tetraphenylporphyrinato complex, 104

Medical applications, 225

2-Mercapto-1-[2-(4-pyridyl)-ethyl]-benzimidazolyl, 79

Metal complexes, ambivalent, 20

Metal–hydrogen bond, 4

Metalloenzymes, 138

Metalloproteins, 99

Metal nitrosyls, 53

bonding, 101

formation and decay, 107

multinuclear, 85

protonation, 127

Metal–organic frameworks (MOFs), 225, 228, 234, 236

Metal-to-ligand backbonding, 120

2-Methyl-2-mercaptopyridine, 71

2-Methyl-2-propanethiolate, 71

6-Methyl-2-pyridyl, 71

Model complexes, 137

Mononitrosyl iron complexes (MNICs), 103

Mononitrosyls, 87

Multicopper enzyme nitrous oxide reductase, 139

Multiheme cytochrome c nitrite reductase, 217
Myoglobin (Mb), 108, 130, 158, 188

N

Neuroglobin, 114
Neurotransmitters, 3, 228
Nickel, 19, 89
Nicotinamide adenine dinucleotide phosphate (NADPH)
Ni-CPO-27, 248
Nitrate reductase, molybdopterin-containing, 138
Nitric oxide, 1, 39, 53, 101, 137, 157
 toxicity/biological activity, 230
Nitric oxide oxidase, 126
Nitric oxide reductase, 138
 bacterial (NorBC), 215
 fungal, 213
Nitric oxide synthase (NOS), 101, 157, 231
Nitrido complexes, 1, 32
Nitrite, 101, 137
 reduction, 121
Nitrite creams, acidified, 232
Nitrite reductases (NIR), 137, 158
Nitrobindin, 159
Nitrogen-based ligands, 64
Nitrogen dioxide, 101
Nitrophorins, 159
Nitroprusside, 103, 121, 127, 128
Nitrosoamines, 101
S-Nitrosocysteine, 117,
S-Nitrosoglutathione (GSNO), 117, 122,
Nitrosonium, 1, 102, 120
Nitrosothiols, 101, 117, 229
Nitrosylation, reductive, 120
Nitrosyls, 155
 bent, 1, 39
 isolobal analogies, 29
 linear, 1
 myoglobin, 130
 nonlinear, 1
Nitrous oxide, 227
Nitroxyls, 101, 120, 127, 155, 159, 193, 210
NO dioxygenation (NOD), 158
Non-heme iron, 116
Non-innocent ligands, 1, 5, 155
NO reductases (NOR), 158
Nuclear resonance vibrational spectroscopy (NRVS), 159

O

On/off reactions, 115
Organometallic metal nitrosyls, 92

Organ transplantation, carbon monoxide, 247
Oxyhemoglobin, 245
Oxymyoglobin, 129

P

P450nor, 188, 213
Peroxynitrite, 101, 129, 144, 158, 230
Phosphine spectator ligands, 44
Phosphorus based ligands, 56
Photodissociation, 111
Pincer ligands, 40
Poly-nitrido-oxo, isolobal, 45
Poly(nitrosyls), isolobal, 45
Porphinato, 110
Propanethiol, 71

Q

Quantum yield, 110

R

Radical oxygenating species (ROS), 247
Rhodium, 120
Roussin's black salt, 71, 80, 103, 116, 117
Roussin's red salt, 71, 103, 116
Roussin's red salt ester, 71, 103
Ruthenium, 90, 109
Ruthenium carbonyls, 24

S

Signatures, 15
Sodium nitroprusside, 121
Spectroscopy, 1, 155
STAM-1, 244
Sulfhemoglobin, 247
Sulfur-containing ligands, 70
Sulfur dioxide, 1, 15, 23
Suspended animation, hydrogen sulfide, 248
Symmetry signatures, 6, 9, 23

T

Technetium, 89
Tetrahydropterin, 158
Tetraphenylporphyrin, 43
Thiosulfate, 247
Thrombosis, 232
Titanium imido complexes, 44
Transplantation, carbon monoxide, 247
Trifluorosulfane, 7

Trinitrosyls, 87, 92

Tris(2-methylpyridine)amine (TPA), 70

Tris(2-pyridylmethyl)-amine, 118

U

Ultrasensitivity, 244

V

Valence shell electron pair theory (VSEPR), 9,
17, 20

Valence tautomerism, 14, 25

amphoteric, 1

Viagra, 232

Vibrational spectroscopy, 179, 187

Vitamin B₁₂, 119

Z

Zeolites, 228, 239

Zirconium, 12

Zn-CPO-27, 243, 248

Z-type ligands, 20